THE DESIGN AND LOW MACH NUMBER WIND-TUNNEL PERFORMANCE OF A MODIFIED NACA 23012 AEROFOIL, WITH AN INVESTIGATION OF DYNAMIC STALL ONSET

by

MARK WILLIAM GRACEY, B.Sc.

Dissertation submitted to the Faculty of Engineering,
University of Glasgow, for Degree of Doctor of Philosophy,
April 1991.

With thanks to my supervisor, Roderick Galbraith, for his help and patience over the many years during which this research was undertaken.

I am also grateful to Tom Beddoes of Westland Helicopters Limited and to the following current and former members of staff at the University of Glasgow for their advice and assistance :

Roger Angell	Liz Leitch
Frank Coton	Effie Murray-Smith
Emily Garman	Andy Niven
Robert Gilmour	David Perrins
Richard Gordon	Stratos Saliveros
David Herring	Tony Smedley
Jiang Dachun	David Whitelaw.
John Kitching	

Finally, I must express my gratitude to my parents and friends without whose persistent encouragement this dissertation would not have been completed.

The research described in this dissertation was funded by the S.E.R.C. under contract numbers GR/D/41064 (IG06) and GR/F/06760, and was performed by the author in the Department of Aerospace Engineering at the University of Glasgow during the period January 1986 to March 1991. The dissertation is original in content except where otherwise stated.

Mark William Gracey
Department of Aerospace Engineering
University of Glasgow
March 1991

ABSTRACT

In recent years, much of the research into aerodynamics performed at the University of Glasgow has considered the behaviour of helicopter and wind-turbine aerofoils in unsteady conditions. Theoretical predictive algorithms have not yet been developed fully and so there is still a great need to examine experimentally-recorded data. The present research was undertaken in an attempt to increase knowledge of the mechanism of trailing-edge dynamic stall at low Mach numbers. Consequently, the NACA 23012 aerofoil section has been modified over the trailing 75% chord to increase camber, and a model of the resulting aerofoil subjected to a series of wind-tunnel experiments.

This experimental investigation entails a four-stage procedure :

(i) design of the aerofoil section;
(ii) construction of a two-dimensional model of the aerofoil;
(iii) testing of the aerofoil in the University of Glasgow's "Handley-Page" wind-tunnel;
(iv) analysis of the data resulting from these tests.

Since the University began this research some years ago, efficient procedures have been established for stages (i) - (iii) : the aerofoil is designed with the aid of a suite of FORTRAN routines, many of which have been written during the course of the research described in this dissertation; the aerofoil models are built by a team of technicians using manual and computer-based techniques; the experiments, in which aerofoil motion is controlled and data are recorded by a computer system developed when previously testing other aerofoils, are performed in steady and unsteady conditions over a range of motion types and test parameters. The data, which are stored on the University of Glasgow's aerofoil database, have been analysed with the assistance of computer algorithms which have been coded specifically for the research under discussion.

The aerodynamic data for this aerofoil are compared with corresponding data for the NACA 23012 and another aerofoil which had previously been generated from that section by modifying over the trailing 75% chord to produce reflex camber at the trailing edge. In steady conditions, the influence of Reynolds number, Mach number and aerofoil geometry on the aerodynamic characteristics is examined. The unsteady experiments were performed under two types of motion : sinusoidal and constant-pitch-rate "ramps". The influence on the unsteady characteristics of mean angle of attack, amplitude, reduced frequency, reduced pitch-rate, Mach number, Reynolds number and aerofoil geometry is investigated and current hypotheses about aerofoil behaviour are supported by the results of this analysis.

There is evidence that, to examine unsteady aerodynamic characteristics in general rather than for only one particular type of motion, it is important to consider the maximum reduced pitch-rate which the aerofoil experiences during the test.

After this general review of the data, some particular aspects of dynamic stall are considered : the critical angle of attack which was defined by WILBY [91] is shown to be influenced by reduced frequency and Reynolds number as well as aerofoil geometry; negative aerodynamic damping, the condition which encourages stall flutter, is revealed as being less likely to occur on the aerofoils which possess more gentle trailing-edge separation characteristics; the mechanism of dynamic stall is shown to consist of a number of events, the timing of most but not all of which appear to be relatively independent of aerofoil motion.

For aerofoils experiencing trailing-edge stall at low Mach numbers, the earliest indication which can be detected from experimental data that dynamic stall has been initiated is when a deviation is first observed in the gradient of a pressure coefficient trace with respect to time. This incidence is shown to vary with Reynolds number, reduced pitch-rate and aerofoil geometry. Data from experiments on seven of the aerofoils tested at the University of Glasgow are employed to correlate the incidence of this deviation against reduced pitch-rate and Reynolds number. The incidence of static stall and the rate of trailing-edge separation in steady conditions are used as parameters to represent the aerofoil.

This correlation is compared to several criteria which are established as guides to the performance of aerofoils in unsteady conditions. Of these criteria, that which can be detected earliest is Wilby's critical angle. However, it can only be determined from oscillatory data. With the aid of the correlation and comparison of data from different motion types via the maximum attained pitch-rate, it is shown that an analogous incidence can be determined for ramps. This is achieved by means of a time-delay expressed in chordlengths of travel between an incidence which is equivalent to the critical angle of attack and that at which there is a deviation in the pressure cofficient trace. This equivalent critical angle of attack would seem to be an extremely important incidence to consider when comparing the unsteady aerodynamic behaviour of aerofoils.

Through this research another set of data has been added to the University of Glasgow's aerofoil database. Increasing the number of aerofoils tested over similar series of tests has enabled the details of unsteady aerodynamic behaviour to be examined. It has thus been possible to investigate the mechanism which governs the inception of dynamic stall on aerofoils experiencing trailing-edge stall at low Mach numbers.

CONTENTS

CHAPTER ONE

A BRIEF OUTLINE OF THE RESEARCH

1.1 INTRODUCTION

When a slender lifting surface, such as an aerofoil, is inclined to the freestream at an incidence greater than some critical angle of attack, the flow around the body no longer remains attached to the surface and breaks down, resulting in the phenomenon called stall. If the aerofoil is subjected to unsteady motion, it experiences a complex series of events which result in stall being delayed to angles of attack which are attained a significant length of time after passing through this static stall incidence. In such conditions, stall is followed by large deviations in lift and pitching-moment. This phenomenon is known as "dynamic stall" and appears on helicopter rotor blades, rapidly-maneuvering aircraft, wind turbines, jet engine compressor blades and insect wings.

Although much of the research on dynamic stall is relatively recent, the subject was under investigation in 1932 by KRAMER [53]. He observed that, when an aerofoil was pitched at significantly high rates, an increase in maximum lift was attained as a result of the boundary layer remaining attached to the surface at angles of attack greater than the incidence of stall in steady conditions.

The phenomenon was first identified on helicopters where it is necessary to balance the lift generated over the helicopter rotor disc. Relative to the freestream, the blade moves in the direction of flight at a greater velocity than when it is travelling in the opposite direction. As described by YOUNG [93], to compensate for the resulting difference in lift, the angles of attack on the retreating side of the rotor disc must be higher than at the corresponding position on the advancing side. An example of the relationship between azimuth angle and angle of attack is illustrated in Figure 1.1. As a consequence of this pitching motion, the helicopter blades are vulnerable to dynamic stall when operating close to the limits of their flight envelope.

In 1968, HARRIS AND PRUYN [43] concluded that if the incidence increases without interruption as the blade proceeds through the third quadrant of the rotor disc, blade lift stall will not occur. As illustrated by CARR [20] in Figure 1.2, further research indicated that it is the lift on the blade being greater than that predicted by steady flow which results in the helicopter rotor

experiencing extra lift during the time when the blade is retreating. Because stall on helicopters occurs when the blade is moving opposite to the direction of flight, dynamic stall is often termed "retreating blade stall". In addition, McCROSKEY AND FISHER [66] observed that, when the blade was advancing and during the onset of retreating blade stall, the forces and moments agreed with measurements on unsteady two-dimensional airfoils oscillating in pitch and there was no significant contribution by the three-dimensional effects associated with the flowfield around a helicopter rotor blade.

At the same time, HAM AND GARELICK [42] observed that at significantly large pitch-rates the aerodynamic loading on a two-dimensional wing was dominated by the influence of intense vorticity shed from the vicinity of the leading edge of the aerofoil. Dynamic stall occurred at an angle of attack substantially greater than the static stall angle, and, hence, the peak values which were attained for dynamic lift and moment were greater than those in steady conditions.

Much of the research into the dynamic stall phenomenon performed since the publication of the results described above has concentrated on examining the individual details. As well as studying the effect on helicopters, a large amount of recent research has considered the influence on wind turbines used for electric power generation. There have been two principal approaches to the investigation of the subject. The first

has been through analysis of data from aerofoil models during wind-tunnel and water-tunnel testing. It has thus been possible to examine the influence of each test parameter, in particular pitch-rate, on the aerodynamic characteristics. The second means of investigation has been through attempts to code accurate algorithms for predicting the characteristics of dynamic stall under any given test conditions. From the conclusions of these researchers, a general description of the events of dynamic stall is now widely accepted. This sequence of events is described in Section 1.2 and the methods of predicting the characteristics associated with the phenomenon are introduced briefly in Section 1.3.

At the University of Glasgow a methodical experimental investigation of dynamic stall has been performed in recent years. The particular research which is discussed in this dissertation is introduced in Section 1.4. The symbols which are used throughout the text and figures are listed in Section 1.5.

1.2 STALL EVENTS

As described in the previous section, stall proceeds according to whether the aerofoil is tested under steady or unsteady conditions. The different characteristics are described in this section.

1.2.1 Static Stall

Figure 1.3 depicts CRIMI AND REEVES's [27] illustrations of the three types of static stall which have been described by McCULLOUGH AND GAULT [68] : trailing-edge stall; leading-edge stall; thin-aerofoil stall.

Trailing-edge stall usually occurs on relatively thick aerofoils at comparatively high Reynolds numbers. As the angle of attack increases, the position of turbulent boundary-layer separation moves progressively closer to the leading edge of the aerofoil. As a result, there is a gradual decrease in lift (Figure 1.3(a)) and increase in drag.

Leading-edge stall is characterised by a more abrupt change in the aerodynamic loadings, as illustrated for lift in Figure 1.3(b). It is associated with the behaviour of the laminar separation bubble which is located on the upper surface of the aerofoil immediately downstream from the position of peak suction and has been described by, for example, HOUGHTON AND CARRUTHERS [50]. As incidence increases, the bubble moves forward, decreases slightly in length and grows thicker. As a result, probably because the leading-edge adverse pressure gradient becomes too great for the boundary layer to reattach downstream of the bubble, the flow suddenly separates from the entire upper surface (known as the "bursting" of the bubble) and the aerofoil experiences an abrupt loss of lift.

Thin-aerofoil stall, which occurs at comparatively low Reynolds numbers on thin aerofoils, is also characterised by a leading-edge bubble. In this case, however, as incidence increases the separation point remains fixed and the bubble grows progressively longer..

These three stalling classifications account for all aerofoil behaviour in steady conditions. Some cases correspond uniquely to one of the categories, whereas others combine two types of stall or are borderline cases.

1.2.2 Dynamic Stall

The stall mechanism in unsteady conditions is further complicated by the presence of the variable of time. The process has been described by McCROSKEY ET AL [64,67] and is illustrated by CARR ET AL [21] for a NACA 0012 aerofoil oscillating in pitch in Figure 1.4. The behaviour which is shown is characteristic of virtually any aerofoil experiencing full dynamic stall.

Dynamic stall is characterised by the shedding and passage over the upper surface of a vortex-like disturbance, known as the "dynamic stall vortex". The progress downstream of the dynamic stall vortex is revealed as a series of fluctuations in the pressure distribution, as illustrated for the NACA 23012 aerofoil in Figure 1.5. Yet, by returning to Figure 1.4, it can be seen that, because the aerofoil passes through the incidence of static

stall without any significant modification of the flow around the aerofoil, the dynamic stall process is initiated before the pressure distribution is affected by the vortex.

As the angle of attack increases further, the flow begins to reverse near the trailing edge of the aerofoil. This flow reversal progresses forward as a "tongue of reversed flow" until the dynamic stall vortex emerges near the leading edge. The vortex is then shed downstream. The resulting distortion to the pressure distribution induces strong pitching-moment effects on the aerofoil and a dramatic increase in drag. However, lift usually continues to rise until the vortex has travelled well past midchord. As the vortex nears the trailing edge, the airloads attain their greatest magnitudes and then drop dramatically, although, in general, the timing varies for each load. After the vortex travels into the wake, secondary vortices of greatly reduced strength are shed, causing further fluctuations. If the incidence begins to decrease after stall has been initiated, the flow reattaches to the leading edge at an angle of attack close to but slightly lower than the static stall incidence. **The reattachment point then moves towards the trailing-edge.**

The vortex shedding phenomenon is clearly defined when the amplitude, maximum incidence and rate of pitch (or oscillation frequency) are sufficiently high. These parameters along with aerofoil shape, Reynolds number, Mach number and three-dimensional effects influence the dynamic

stall process. In particular, the incidence of each stall event and the strength of airloads are determined by the magnitudes of such parameters.

Each of the events in the dynamic stall process develops over a finite length of time, the duration of which can be measured in terms of chordlengths of travel. Once stall has been initiated, the development of each event appears to be under negligible influence from the motion of the aerofoil. As a result, there is lag and asymmetry of the airloads with respect to the motion of the body, producing the hysteresis which is clearly illustrated in Figure 1.4.

Because the events which follow the initiation of stall are relatively independent of the aerofoil motion, a simple definition of stall is not easily realised. In this dissertation, the onset of stall will be considered to occur at the lowest incidence where, once it has been attained, no subsequent stall event can be prevented.

1.3 METHODS OF PREDICTING DYNAMIC STALL

A great deal of recent research has involved attempts to predict the aerodynamic characteristics of the dynamic stall phenomenon. The methods can be divided into four groups : Navier-Stokes calculations; discrete potential vortex methods; zonal methods; empirical correlation

techniques. Such methods have been reviewed comprehensively by, for example, McCROSKEY [64] and GALBRAITH [33].

The methods in the first of these categories employ numerical algorithms in an attempt to solve the full Navier-Stokes equations. They involve a great deal of computational time and storage space.

The discrete vortex models assume that the potential flow exists in the region external to the immediate vicinity of the aerofoil surface. The flow is considered to consist of parcels of vorticity which induce motion on each other. These vortices are generated empirically or by detailed boundary-layer calculation and are subsequently transported into the wake. It is necessary that the algorithms be coded in a form balancing the increased accuracy which is derived from modelling the flow with a large number of vortices and the greater efficiency which results when the number of vortices is reduced. A number of discrete vortex algorithms have been reviewed by LEONARD [60].

In zonal methods, the viscous region is modelled separately from the external potential flow. If incorporated in a numerical algorithm, these two zones are coupled by an iterative procedure.

Empirical correlation methods have been developed in the helicopter industry to estimate the airloads on

aerofoils in unsteady conditions. This is achieved by correlating against the parameters listed in Subsection 1.2.2 the timing of events and force and moment data which are obtained from wind-tunnel experiments. This category is very broad and the methods reveal many different approaches to the prediction of unsteady characteristics. Unlike Navier-Stokes methods, these predominantly empirical methods do not require a considerable amount of computational power. However large and expensive databases are necessary.

Algorithms for predicting unsteady aerodynamic characteristics are still being developed. Assessing their performance requires comparison with experimental data. In addition, the use of empirical methods would involve experimental data even if a universally-accepted algorithm existed. This fact highlights the necessity of acquiring unsteady aerodynamic data experimentally.

1.4 FRAMEWORK OF THE DISSERTATION

The previous section commented on the importance of experimental data when determining unsteady aerodynamic characteristics. As a result, in recent years, aerodynamic research at the University of Glasgow has involved collecting in the university's "Handley Page" low-speed wind-tunnel two-dimensional data which has been recorded under a variety of motion types and is stored on

an aerofoil database.

A number of aerofoils have been tested. They can be divided into two groups : the first is a family of cambered aerofoils generated from the NACA 23012 section and intended for the examination of transition from trailing- to leading-edge stall on helicopter blades; the second is a series of NACA four-digit symmetrical sections for use on vertical-axis wind turbines. The aerofoil which is discussed in this dissertation is a member of the cambered family. Its design and structure are discussed in Chapter Two. In addition, the reasons for choosing the NACA 23012 section as the generic shape are explained.

The experiments to which the aerofoil was subjected are described in Chapter Three. This chapter is divided into two main sections. In the first of these sections the mechanical and electronic components of the experimental apparatus are described. The aerofoil was tested under a number of types of motion. The procedure for each series of experiments, as well as the operations which were necessary before and after testing, are described in the second section.

In Chapter Four the data which were produced by these experiments are analysed in detail and compared to the data from similar experiments on the NACA 23012 and another modified aerofoil. After briefly introducing and assessing the data, the chapter is divided into four sections in which the results from each series of

experiments are discussed. The results in steady conditions are investigated in the first two sections : the separation characteristics and three-dimensional effects from flow-visualisation experiments and the influence of all relevant test parameters on the pressure data from static experiments. The discussion of the unsteady data is also divided into two sections. In the first section, the data from experiments in which the aerofoil was pitched periodically in a sinusoidal motion are examined. The influence of all relevant parameters, WILBY's [91] critical angle of attack and aerodynamic damping are all examined. By analysing the data perfomed during constant-pitch-rate "ramp" tests, the influence of pitch-rate on the dynamic stall characteristics is discussed in the second section. In addition to considering the influence of the other test parameters, there is an investigation of the timing of the dynamic stall events and how early it is possible to detect from experimental data if the stall process has begun. The influence of pitch-rate on the reattachment mechanism is discussed briefly. The final section of the chapter assesses the general performance of the test aerofoil.

A new correlation which indicates the incidence at which incipient dynamic stall can be detected from experimental data is introduced in Chapter Five. It is a function of static characteristics and is generated from data which were produced by all seven aerofoils possessing data on the University of Glasgow's aerofoil database at the time the analysis was performed. This correlation is then compared with other established stall criteria.

The final chapter reviews the topics which have been motivated by this research and suggests some areas which are worthy of further examination.

1.5 NOMENCLATURE

A :	constant in derivation of influence coefficients
A :	coefficient in correlation equation
A_{ij} :	coefficient from which influence coefficient is derived
B :	constant in derivation of influence coefficients
B :	coefficient in correlation equation
B_{ij} :	coefficient from which influence coefficient is derived
C :	constant in derivation of influence coefficients
C :	coefficient in correlation equation
C_1, C_2 :	constants in derivation of separation point equation
C_d :	coefficient of drag
C_{ij} :	influence coefficient for calculation of induced velocity
C_l :	coefficient of lift
C_m, $C_{m_{1/4}}$:	coefficient of pitching-moment about quarter-chord location
C_{mo} :	coefficient of pitching-moment at incidence of zero-lift
C_n :	coefficient of force normal to chord
C_n' :	ersatz coefficient of force normal to chord
C_{n_1} :	critical coefficient of force normal to chord
C_p :	coefficient of pressure
C_t :	coefficient of force tangential to chord and defined positive in direction towards leading edge
c :	length of chord
c_1, c_2, c_3 :	constants in derivation of correlation equation
D :	coefficient in correlation equation
E :	Young's modulus (Nm^{-2})
$F_1(.)$:	general function relating m_1 and m_2
f :	separation point in form of x/c
f_{max}, f_{min} :	constants in separation point equation
G :	modulus of rigidity (Nm^{-2})
I :	second moment of area (m^4)
i :	parameter in correlation equation
J :	torsion constant (m^4)
j :	parameter in correlation equation
K_1, K_2 :	constants in separation point equation
L_i :	length of aerofoil panel number i

L_1 norm : discrete norm defined as $\|f-a\|_1 = \sum_i w_i|f_i-a_i|$, for any real vectors f and a subject to real weight vector w

m_1, m_2 : constants in derivation of correlation equation

N : number of aerofoil panels

NC1 : number of aerofoil panel on upper surface downstream of which profile is modified

NC2 : number of aerofoil panel on lower surface downstream of which profile is modified

$\vec{n}_i$: unit vector normal to aerofoil panel i

p : Laplace variable

p : surface pressure

p.s.i. : pounds per square inch

R : $Re \times 10^{-6}$

Re : Reynolds number

r : reduced pitch-rate, calculated from $\dot{\alpha}c/2U_\infty$

$\vec{r}_{ji}$: vector from position on aerofoil panel j to mid-point of panel i

$\vec{r}_{n_{ji}}$: unit vector normal to $\vec{r}_{ji}$

S_1, S_2 : constants in separation point equation

S_j : distance along aerofoil panel j from (x_j, y_j)

T_p : pressure compensation time constant

t : time (s)

$\vec{U}$: velocity on surface of aerofoil

U_∞ : magnitude of freestream velocity (ms^{-1})

$\vec{U}_\infty$: vector of freestream velocity

$\vec{u}$: induced velocity on aerofoil surface

$\vec{u}_i$: induced velocity at mid-point of aerofoil panel i due to remainder of aerofoil

$\vec{u}_{ij}$: induced velocity at mid-point of aerofoil panel i due to panel j

$\vec{u}_{n_{ij}}$: vector normal to $\vec{u}_{ij}$

v : integration variable in derivation of induced velocity equation

X_1, X_2 : logarithmic functions of separation points

x : coordinate in direction of aerofoil chord

x_i : x-coordinate at edge of aerofoil panel i

x_p : x-coordinate of general point on aerofoil panel

xc_i : x-coordinate at mid-point of aerofoil panel i

y : coordinate in direction normal to aerofoil chord

y_i : y-coordinate at edge of aerofoil panel i

y_p : y-coordinate of general point on aerofoil panel

yc_i : y-coordinate at mid-point of aerofoil panel i

α : angle of attack

$\dot{\alpha}$: pitch-rate

α_1 : constant in separation point equation

α_a : amplitude of oscillatory cycle

α_c : critical angle of attack

α_{dm} : incidence of C_p deviation

α_m : mean angle of attack

α_{ss} : incidence of static stall

Ω : integration limit in derivation of induced velocity equation

Γ : temporary variable in derivation of induced velocity equation

γ : gamma function for Gormont model

γ : strength per unit length of vortex sheet

γ_j : strength per unit length of vortex sheet at (x_j, y_j)

γ_p : strength per unit length of vortex sheet at (x_p, y_p)

ΔC_m : deviation in pitching-moment coefficient

Δf : difference between f_{max} and f_{min}

Δt : time-delay (s)

$\Delta\alpha$: incidence delay

$\Delta\alpha_d$: incidence delay beween static and dynamic stall

δ : integration limit in derivation of induced velocity equation

ζ : pitch-damping parameter

η : temporary variable in derivation of induced velocity equation

θ : integration variable in derivation of induced velocity equation

μ, ν, ξ : temporary variables in derivation of induced velocity equation

τ : non-dimensional time-delay expressed in terms of chordlengths of travel as $\Delta t . U_\infty / c$

τ^* : non-dimensional time-delay between analogous critical angle of attack and incidence of C_p deviation

Φ, Ψ, Ω : temporary variable in derivation of induced velocity equation

CHAPTER TWO

DESIGN AND STRUCTURE OF TEST AEROFOIL

2.1 INTRODUCTION

As described in Chapter One, much of the research into aerodynamics performed at the University of Glasgow has been the systematic study, for aerofoil sections under dynamic conditions, of the transition from trailing to leading edge stall and the mechanism of reattachment. This study has involved the design of a series of aerofoil sections which are modifications of the NACA 23012 section. In this chapter, the design procedure and structure of one such aerofoil are described.

The NACA 23012 profile, together with its coordinates, is displayed in Figure 2.1. As may be gleaned from consulting the work of, for example, ABBOTT AND VON DOENHOFF [1], RIEGELS [79] and MILEY [70], a great deal of data for this aerofoil has been published. The

gradient of the NACA 23012's lift curve (Figure 2.2) varies little over angles of attack which are smaller than the angle at which maximum lift is obtained. Immediately above this angle, however, there is an abrupt decrease in lift. As indicated in Figure 2.3, this lift curve is typical of a leading edge stalling aerofoil. However, the correlation of GAULT [36], which employs the upper surface ordinate at the 1.25% chord station to characterise an aerofoil, suggests that the aerofoil should exhibit trailing-edge stall. It was this anomalous stalling behaviour which led to the NACA 23012 being chosen as the aerofoil section from which to produce a family of modified sections.

In order that the data for the modified aerofoils be compared with the data for the original aerofoil, a series of experiments was performed on the NACA 23012 by LEISHMAN [55] and SETO [82]. It was observed that, at an angle of attack of 14.2°, it experienced very rapid trailing edge boundary layer separation which resulted in it appearing to undergo leading edge stall. Gault had earlier postulated that the fact that the NACA 23012 did not conform to his correlation was due, in the case of this aerofoil, to stall being preceded by the very rapid forward progression of the turbulent boundary layer separation location. This observation made the aerofoil section most suitable for the purposes of this investigation.

The first modified aerofoil section, which was named the NACA 23012A and is compared with the original section

in Figure 2.4, was designed by NIVEN ET AL [73,75]. The profile of the NACA 23012A was identical to that of the NACA 23012 over the leading 25% chord, but the gradient of its camber over the trailing 75% chord was steeper and it possessed a reflex trailing edge. The consequence of this modification was to increase the theoretical pressure gradient as predicted from potential flow theory over the modified part of the aerofoil, as illustrated in Figure 2.5. It was intended that this pressure gradient distribution should encourage enhanced trailing edge separation characteristics. When the aerofoil was tested, it was discovered that this intention had been realised.

A second modified aerofoil section was then designed for comparison with both the NACA 23012 and NACA 23012A aerofoils. In keeping with the idea of a family of aerofoils, the aerofoil section was to be identical to the NACA 23012 over the leading 20% - 25% chord and the remainder of the aerofoil modified. The design procedure for this aerofoil section, which has previously been described in much greater detail by GRACEY AND GALBRAITH [38], is discussed in Section 2.2. In Section 2.3, the structure of the model for this aerofoil is described. The design of the model's spar is discussed in Section 2.4.

2.2 DESIGN PROCEDURE

The design procedure relied heavily on a panel method. This means that the donor and resultant aerofoils were represented by polygons, the corners of each side, or panel, of which lay on the surface of the aerofoil. The procedure was basically a sequence of three algorithms :

(i) forward process, which was a potential flow panel method arranging over the polygon a continuous vorticity distribution which varied linearly over each panel. The vorticity was calculated by employing the boundary conditions of surface flow tangency around the aerofoil and of Kutta at the trailing edge. From this vorticity distribution, the pressure gradient about the donor aerofoil, which was the NACA 23012, was calculated;

(ii) modification process, which modified this pressure gradient distribution;

(iii) inverse process, which was an iterative process generating the coordinates of an aerofoil which possessed this pressure gradient distribution. This was achieved by repeatedly modifying the elements in the panel influence coefficient matrix and using the influence coefficients of the donor aerofoil as the starting values.

The forward and inverse algorithms have already been described by LEISHMAN AND GALBRAITH [57] and VEZZA AND GALBRAITH [90] respectively, although the code for the forward process has since been updated to improve its efficiency. The derivation of the new algorithm is described in Appendix A.

An original aim was to design an aerofoil section which would experience more sudden trailing edge boundary layer separation than the NACA 23012. As explained by, for example, HOUGHTON AND CARRUTHERS [50], a larger positive pressure gradient retards the velocity of the boundary layer more severely and hence increases the likelihood of separation. It would therefore seem that, to encourage more sudden separation, a possible pressure gradient distribution over the upper surface of the aerofoil would be that illustrated in Figure 2.6. However, the profile of an aerofoil possessing such a pressure gradient distribution over the leading 25% chord could not be identical to the NACA 23012 profile over that part of the aerofoil. It was, therefore, decided to attempt to design an aerofoil section for which trailing edge separation would occur more gently.

Towards this goal, it was decided that the upper surface pressure gradient should be decreased at about the 25% chord station and increased towards the trailing edge, particularly over the trailing 10% chord. To implement these changes, process (ii) was divided into three sub-processes :

(iia) decide on an initial approximate shape for the pressure coefficient distribution graph. The pressure gradient distribution which was derived from this shape was later to be modified further to produce the required pressure distribution. This approximate distribution was formed in the following manner. Forward of the 25% chord station on the upper and lower surfaces, pressure coefficient values were equal to those for the NACA 23012. The designer then decided on a new value for the pressure coefficient at the 90% chord station on each surface. On the upper surface, this value was less than at the equivalent location on the NACA 23012. Straight lines were drawn from the pressure coefficient value at approximately 25% chord to the relevant value at approximately 90% chord. The pressure coefficient distribution then rose exponentially to a requested value at the trailing edge;

(iib) calculate the pressure gradient distribution for this pressure coefficient distribution;

(iic) based on this pressure gradient distribution, decide on the "requested" pressure gradient distribution. This involved smoothing the pressure gradient distribution and scaling the values over the trailing 75% chord in order that the total integrated pressure over the surface of

the requested aerofoil would be equal to that over the NACA 23012.

The aerofoil profile resulting from this modification is illustrated in Figure 2.7.

As can be seen, the resulting aerofoil section did not generate the requested pressure distribution. This was a consequence of the limitations of the inverse process. These limitations had also already restricted the amount of change which was attempted when modifying the pressure distribution. The problem is that the "adapted analysis" inverse method, which is iterative, does not converge. The profile which the process yields is that which possesses the best approximation to the requested induced vorticity distribution in the L_1 norm, but the distributions for the aerofoils in the sequence do not converge to this approximation.

To improve the results produced by this method, it is necessary that the iterative process should converge. This could be achieved through the "relaxation" of the iterative process. In this way, if the terms of a slowly convergent or divergent series, which, in essence, this method is, could be supplemented by some analytical information about the answer, an accurate approximation to the exact answer could be recovered from a few of these terms. A collection of several such methods has been compiled by, for example, BENDER AND ORSZAG [17].

It should, however, be appreciated that these methods work efficiently because they work for only certain cases. It follows, therefore, that, to find an effective algorithm, a great number of methods must be examined by incorporating each within the inverse process. This would be extremely time-consuming. For this reason, no attempt was made to modify the inverse process at the time of designing this aerofoil.

It had been discovered during earlier modification attempts that, although the aerofoil which was produced by the original design procedure did not yield the exact requested pressure gradient distribution, better results could be achieved by smoothing the surface panel distribution, mean camber-line and thickness distribution. It was, therefore, decided to continue by using such techniques.

Firstly, the distribution of the geometrical gradients of the panels was smoothed. Then the aerofoil was "normalised" by a transformation of the axes which resulted in the leading edge being located at (0,0) and the trailing edge at (1,0), with the thickness-to-chord ratio at every point remaining unaltered. This modified aerofoil was named DAT62D and is compared with the NACA 23012 in Figure 2.8. The leading 25% of this aerofoil was significantly different from the NACA 23012. This fault was overcome by merging the leading 25% of the NACA 23012 with the trailing 75% of the DAT62D. The resulting profile, named AERO4, is compared with the

NACA 23012 in Figure 2.9. Finally, this shape was normalised and, for practical reasons when building the model, the coordinates over the rear lower surface were modified so that the aerofoil possessed a finite trailing edge. The resulting aerofoil section was the NACA 23012C and it is illustrated in Figure 2.10.

The pressure gradient distribution yielded by the forward process for the NACA 23012C is compared with that for the NACA 23012 in Figure 2.11. As can be seen, the NACA 23012C did satisfy the original aims in the design of the aerofoil.

From the method of COTON [25], the integrated loads and boundary layer separation points were predicted at a number of angles of attack. A comparison between these values for the NACA 23012C and NACA 23012 aerofoils, as well as the experimental loads for the NACA 23012, can be found in Figures 2.12 and 2.13. The higher maximum lift coefficient, negative zero-lift angle and more gentle separation behaviour predicted for the NACA 23012C indicated that much could be learned from testing this aerofoil.

It was decided that a two-dimensional model with the cross-section of a NACA 23012C should be built and tested under static and dynamic conditions.

2.3 STRUCTURE OF AEROFOIL

The model, of span length 1.61m and chord length 0.55m, was built by a team of technicians using a standard procedure developed at the University of Glasgow. A diagram of such an aerofoil is illustrated in Figure 2.14.

The upper and lower parts of the aerofoil were each built separately, but in an identical manner. A female half-mould for each surface was constructed, in a temperature-controlled room, from a block of wax which was shaped by a cutting machine fitted with a router and follower. As a template, a mild steel plate which had been cut to a female outline of the aerofoil profile was used.

The first part of the model to be built was the instrumentation pod, which was required to be removable so that internal instrumentation could be accessed. The pod was 250mm wide, 10mm thick and situated at mid-span. The skin of the pod was a mixture of glass fibre woven roving and epoxy resin gel-coat, while its remainder was formed from a mixture of slate powder, chopped strand glass fibre and resin.

After this mixture had hardened, the remainder of the model was constructed. The skin was again composed of a glass fibre / epoxy resin mixture. Copper tubes of diameter 5mm, through which the pressure transducer wires

would be led, were laid from one edge of the pod at the approximate location of each pressure transducer (Figure 3.9) to the nearer edge of the model at approximately the quarter chord location. At each end of the model, balsa wood plugs, cut to fit the aerofoil shape, were glued to the surface, allowing space for the end plates and spar to be fitted later. An epoxy resin foam mixture was then poured into the model. On hardening, this mixture was machined flat and flush with each datum on the wax block and a groove in the shape of the spar (see Section 2.4) was cut into the foam.

The upper and lower parts and the aluminium spar were bonded together with epoxy resin. The spar was scratched and grooved to improve absorbtion of the shear stress from the foam. After the resin had set, an aluminium end plate was screwed, at each end, into the spar and through the balsa wood plugs into the foam.

Additional work was then performed on the pod, which had, by then, been split into two parts : a smaller part, for the lower surface, stretching from 30mm from the leading edge to 90mm from the trailing edge, and a larger part, for the upper surface, leading edge and trailing edge. Because the aerofoil was so thin at the tail, some assistance in the installation and removal of the pressure transducers at the trailing edge of the aerofoil was required. Therefore, a portion at mid-span of the trailing edge was cut away and replaced by an insert constructed from tufnol (Figure 2.15). This insert was to

house three transducers, each of which sat in a burrow of diameter 3mm drilled through the insert in a spanwise direction. The transducer wires were to be led to the main body of the aerofoil via grooves cut along each edge of the insert and the pressure on the surface was to be sensed by the transducers through holes of 1mm diameter drilled perpendicular to the surface.

The other twenty-seven transducers were individually housed at mid-span in perspex pockets which sat completely within hollows in the pod (Figure 2.16). Rising from each pocket to the surface of the aerofoil was a brass tube of inner diameter 1mm. Grooves were cut into the pod so that transducer wires could be led from the perspex pockets to the copper tubes running through the model.

In order that the aerofoil could rotate about the quarter chord location, a mild steel circular plate of diameter 175mm was connected at each end of the model. Each was connected to the spar with four screws and two dowel pins. As may be read in Section 2.4, the spar was not situated symmetrically about the chord-line of the aerofoil. Therefore, to ensure that the aerofoil did rotate about the quarter chord location, the screws and dowel pins were offset on the steel plate so that, although they lay along the principal axis of the spar, the aerofoil chord-line lay along the diameter of the plate. To enhance the smooth rotation of the aerofoil, a thin layer of felt was glued on to the aluminium end plate and the roof and floor of the tunnel were regularly sprayed with

silicon release agent and lubricant over the arc through which the aerofoil passed.

2.4 AEROFOIL SPAR

In designing the spar, which was constructed from aluminium, it was planned that it should be simple in shape and that it should imitate approximately the profile of the aerofoil. It was to be of a shape which gave sufficient rigidity in torsion and bending but with a small mass. These last two criteria were likely to conflict with each other and so some form of compromise was required.

After designing a number of shapes, that which is illustrated in Figure 2.17 was chosen. It can be seen that, because so little of the aerofoil lay below the chord-line and space had to be left for the pod, the spar lay totally above the chord-line.

As an indication of the strength of the spar and model, a series of standard calculations (see, for example, MEGSON [69] and STEPHENS [86]) were performed. The following values were calculated for the spar :

mass = 19.6kg

moment of inertia about

quarter chord position = 0.052kgm^2

GJ = 21600Nm^2

$$EI = 13400 Nm^2.$$

With the aid of these values, direct measurement and experiments performed previously on existing models, the following values were approximated for the entire model :

$$\text{mass} = 48kg$$

$$\text{moment of inertia about quarter chord position} = 0.41 kgm^2$$

$$GJ = 65000 Nm^2$$

$$EI = 75000 Nm^2.$$

From these values, it was calculated that, under conditions far more severe than those to which the aerofoil would be subjected, the aerofoil would experience the following :

$$\text{twist at mid-span} < 0.5^\circ$$

$$\text{bending deflection at mid-span} < 1mm$$

$$\text{natural frequency of torsion} > 50Hz$$

$$\text{natural frequency of bending} > 25Hz.$$

These results were regarded as being acceptable. In the case of the latter pair, this was on account of the fact that the aerofoil would experience fundamental driving frequencies no greater than 12.5Hz. It was on the basis of these calculations and the fact that the design criteria seemed to have been met satisfactorily that it was decided to fit this spar in the model. In order that, at the corners of the spar, the stress would be spread, these points were rounded.

2.5 CONCLUDING REMARKS

In order that the boundary layer separation characteristics of the NACA 23012 aerofoil could be enhanced, this aerofoil section was modified over the trailing 75% chord to produce the NACA 23012C aerofoil section. A two-dimensional model with the NACA 23012C profile was then built. This model was to be tested in a wind-tunnel under steady and unsteady conditions and the resulting set of data compared to those for the NACA 23012 and NACA 23012A aerofoils.

CHAPTER THREE

TESTING OF AEROFOIL

3.1 INTRODUCTION

Chapter Two described the design and construction of the NACA 23012C aerofoil. A series of experiments was then performed on this aerofoil under static and dynamic conditions. The present chapter, which describes these experiments, is divided into two main sections : Section 3.2 describes the experimental apparatus and Section 3.3 the test procedure. By the time the NACA 23012C aerofoil was tested, the test facility was well established, and much of the information contained in this chapter, particularly that in Section 3.2, has been described in more detail by LEISHMAN [55].

3.2 EXPERIMENTAL APPARATUS

A diagram of the data acquisition and control system which is described in this section is sketched in Figure 3.1, whilst the mechanical assembly is illustrated in Figure 3.2.

3.2.1 Mechanical Components

The experiments were performed in the University of Glasgow's low-speed "Handley-Page" wind tunnel (Figures 3.3 and 3.4), which has been described by HOUNSFIELD [51]. It is an atmospheric-pressure closed-return tunnel with a 5'3" x 7' (i.e. 1.61m x 2.13m) octagonal working section. When running the tunnel continuously, it was possible to obtain velocities of up to $40ms^{-1}$, which is equivalent to Mach and Reynolds numbers of approximately 0.11 and $1.5x10^6$ respectively. However, with intermittent use, a maximum velocity of $61ms^{-1}$ was possible (i.e. Mach number of 0.18; Reynolds number of $2.3x10^6$).

Dowelled and bolted to the tunnel framework were two transversely mounted steel support beams, on each of which the model was supported via a self-aligning bearing (Figure 3.5). The model's weight and fine positioning were taken and facilitated by a single thrust bearing on the top support.

The angle of attack was varied by rotating the

aerofoil about its quarter chord axis by means of an hydraulic actuator and crank mechanism, as illustrated in Figure 3.6. The actuator had a normal dynamic thrust of 6.1kN operated from a supply pressure of $7MNm^{-2}$. A MOOG Servo Valve with UNIDYNE Servo Controller System was used (Figure 3.7). Feedback was available via an angular displacement transducer (see Subsection 3.2.3) which was mounted horizontally below the working section. Input signals to the actuator controller were provided, for the static tests, by the 12-bit digital-to-analogue converter of the MINC microcomputer and, for the dynamic tests, by a BBC microcomputer and a 12-bit digital-to-analogue converter (see Subsection 3.2.2).

3.2.2 Microcomputer System

A DEC MINC-11 microcomputer was employed for data acquisition, data manipulation and monitoring and controlling external hardware. Storage space was available for software and data via an RX02 dual floppy disc system, a THORN EMI DATATECH D6100/48 Winchester disc drive and a THORN EMI DATATECH 9800 magnetic tape unit. A VT105 terminal was used for graphics output, with hard copies being produced via a RIVA PRINTGRAPHICS and ANADEX dot-matrix printer system.

Over and above standard interfaces, input to and output from the MINC computer were achieved by the addition of the following laboratory modules :

(i) an analogue-to-digital converter module, incorporated in which was a 16-channel multiplexer. This translated the instantaneous value of the input voltage into a binary value;

(ii) a 16-channel multiplexer module, which was used, in addition to the multiplexer in the analogue-to-digital converter, to increase the number of channels which could be sampled to thirty-two;

(iii) a programmable real-time clock module, with two Schmitt triggers, which was used to set the requested sampling frequency accurately. Data sampling was initiated via one of the Schmitt triggers by setting its reference voltage to a value corresponding to the output of the angular displacement transducer (Subsection 3.2.3) at the desired angle of attack;

(iv) a digital-to analogue converter module, housing four independent 12-bit digital-to-analogue converters which could be accessed via software. One of these was used to provide the command signal for the hydraulic actuator during static tests.

During the unsteady tests, where sampling and model motion were required simultaneously, the MINC was used only

to record the data. The input signal to the actuator controller was provided by a separate function generator, comprising of a BBC microcomputer and a 12-bit digital-to-analogue converter which transformed the digital output of the BBC into analogue form for the command input to the controller.

3.2.3 Angular Displacement Transducer

The instantaneous angle of attack of the aerofoil was determined by an angular displacement transducer which was geared to the model's spar (Figure 3.8). This was based on a wire-wound potentiometer mounted in an aluminium housing on sliding rails with anti-backlash springs. It was geared to the model's rotational axis in the ratio of 5:1. The output voltage from the potentiometer was fed into an amplifier / splitter to produce three signals for the following purposes :

(i) to record the instantaneous angle of attack of the aerofoil by connection to the MINC multiplexer via a sample-and-hold circuit (see Subsection 3.2.4) ;

(ii) to initiate data sampling via the Schmitt trigger when a preset angle was reached;

(iii) to act as a feedback signal to the hydraulic actuator controller.

A calibration of the transducer output voltage against angle of attack was performed before beginning this set of experiments (see Subsection 3.3.1).

3.2.4 Pressure Transducers and Signal Conditioning

The chordwise pressure distribution at mid-span of the aerofoil was measured by thirty ENTRAN EPIL-080B-5S ultra-miniature pressure transducers of excitation voltage 15V. These were sealed gauge transducers which employed a fully active wheatstone bridge as the sensing member. Each transducer's diaphragm, one side of which had been sealed at a reference pressure during manufacture, consisted of a silicon integrated circuit, resulting in extremely high frequency responses. For the experiments which were performed, each transducer had negligible sensitivity to acceleration and vibration in any of its axes and, due to the fact that it was fitted with a temperature compensation module, the change of zero offset and sensitivity with temperature was minimised.

Depending on its location, each transducer was housed just below the surface of the model in either the tufnol insert or a perspex pocket, as described in Section 2.3 and illustrated in Figures 2.15 and 2.16, and held in position with Silicon Rubber Compound. The locations of the transducers are illustrated and tabulated in Figure 3.9.

The pressure transducers were powered in parallel by a FARNELL "S" SERIES temperature-stabilised direct current voltage source with an excitation voltage of 15V. The output signals were conditioned by thirty amplifiers, a circuit diagram of one of which may be seen in Figure 3.10. Amplification could either be set to a pin-programmable gain of 1, 10, 100 or 1000 or to some other value by fine manual adjustment via secondary amplifiers which had a maximum gain of 11. Each signal then passed through a low-pass filter and a comparator, a circuit diagram of which is illustrated in Figure 3.11, so that the user would be informed whenever the voltage was greater than 5V in magnitude. This was the greatest voltage which could be received by the MINC analogue-to-digital converter module. From here, each signal passed through another low-pass filter into a 31-channel analogue sample-and-hold device. This device has been described by GALBRAITH ET AL [34]. It was designed so that, in the multiplexed analogue-to-digital conversion system, the time-skew errors between channels could be overcome. Due to the high time-dependence of the input signals, such errors would have been significant. This sample-and-hold device interfaced to the MINC multiplexed analogue-to-digital converter module.

At the time of manufacture, all the pressure transducers were factory calibrated in millivolts per p.s.i. However, since the signals were to be conditioned, it was considered more accurate to calibrate the system signals as recorded by the analogue-to-digital

converter. The procedures employed to achieve this and to adjust and record the gain values for the amplifiers are described in Subsection 3.3.1.

3.2.5 Measurement of Dynamic Pressure

The dynamic pressure in the wind tunnel was determined from the difference, as measured by a FURNESS FC012 micromanometer, between the static pressure in the settling chamber and that in the working section. The pressure in the working section was measured a distance of 1.2m upstream of the leading edge of the aerofoil through apertures of diameter 4mm on each side wall. In the settling chamber, it was measured in the same way, a distance 4.4m upstream of the aerofoil leading edge, on each side wall plus on the roof and floor.

As well as displaying the dynamic pressure in millimetres of water, the micromanometer provided a differential voltage output to the MINC multiplexed analogue-to-digital converter module via a low-drift operational amplifier circuit. A calibration of the voltage read by the analogue-to-digital converter against the dynamic pressure displayed by the micromanometer had previously been performed and the coefficients of the resulting least-squares cubic were used in the data reduction process (see Subsection 3.3.6).

3.3 EXPERIMENTAL PROCEDURE

A series of experiments was performed on the aerofoil by rotating it about the quarter chord axis under four types of motion : static, oscillatory (sinusoidal) and constant pitch-rate "ramp" motion in both positive and negative directions. The majority of tests were performed at a Reynolds number of approximately 1.5×10^6 (i.e. a Mach number of 0.11), but a small number were performed at Reynolds numbers of approximately 1.0×10^6 and 2.0×10^6 (i.e. Mach numbers of 0.075 and 0.15 respectively).

Data were recorded over a range of incidence by sweeping through the thirty-two channels of the MINC multiplexed analogue-to-digital converter and, hence, logging pressure values at thirty locations plus dynamic pressure and angle of attack. Each set of data was stored in an unformatted data file, the first 256-word block of which contained information which uniquely identified that test. After completing each experiment, this set of raw binary data was reduced to a set of real-valued pressure coefficients. Before testing the aerofoil, a number of components were calibrated for use in the data reduction procedure. In addition, a series of static flow visualistion experiments was performed at a Reynolds number of 1.5×10^6.

These procedures will be described in the remainder of this chapter. The main control programs were written in FORTRAN IV and MACRO 11 assembly language. Versions

have been documented, along with the contents of the run information block, by MURRAY-SMITH AND GALBRAITH [72].

3.3.1 Pre-test Procedure

Before erecting the aerofoil in the wind-tunnel, the amplifier settings (see Subsection 3.2.4) were adjusted and recorded. Both differential inputs were shorted and the resulting offset value, as recorded by the MINC analogue-to-digital converter, set to zero. A precision direct current calibrator was then employed to supply an accurate 20mV input to each amplifier and the new voltage reading was noted. Hence, the gain could be calculated. For each channel, in order that the output voltage did not rise above 5V, the amplification was set to a value of between 70 and 100. The exact values were written to a data file, which was read at the beginning of each test and re-written to the run information block of the file containing the raw recorded data.

As has been explained in Subsection 3.2.4, it was decided to re-calibrate the pressure transducers. This was achieved by applying suction to each transducer in turn with the aid of a suction pump. The magnitude of this suction was read in millimetres of mercury on a manometer and the voltage output was recorded by the MINC analogue-to-digital converter. A linear least squares fit was performed on this data (Figure 3.12) and, from the gradient of this line and making allowance for the

amplification of the signal, the sensitivity of the transducer, in volts per p.s.i., was calculated. These values were written to a data file for later inclusion in the run information block.

Before calibrating the angular displacement transducer, the threaded pushrod of the aerofoil pitch drive mechanism was adjusted for an angle of attack working range of between -20° and 50°. The transducer's voltage output was recorded by the MINC analogue-to-digital recorder and the incidence of the aerofoil was read from scaling provided on the wind tunnel floor. This was performed over a range of sixty-four angles, through which the aerofoil was swept via the MINC digital-to-analogue converter and hydraulic actuator controller. The best least squares cubic through these data points was calculated (Figure 3.13) and its coefficients were written into a data file along with the coefficients of the cubic produced by the dynamic pressure calibration (see Subsection 3.2.5).

Before beginning the series of tests on the aerofoil, the zero offset value for each transducer was manually adjusted so that it possessed a value as close as possible to zero. The precise values, calculated as the mean of five hundred readings sampled by the MINC analogue-to-digital converter at a frequency of 100Hz, were logged immediately before increasing the wind velocity from zero at the beginning of each test and stored in the run information block. It was discovered that, for the period

in which the entire series of these tests was performed (at temperatures of between 27°C and 32°C), there was negligible variation in the offsets.

All the calibration values acquired by these methods were used, after each test had been completed, when reducing the data (see Subsection 3.3.6).

3.3.2 Flow Visualisation Experiments

The first set of experiments to be performed on the NACA 23012C aerofoil was a series of flow visualisation tests at a Reynolds number of 1.5×10^6. All pressure orifices were sealed before beginning the experiments.

The flow visualisation was accomplished by using a mixture of saturn yellow "dayglo" powder, odina oil and paraffin. The aerofoil was first rotated about its quarter chord axis until it sat at the desired angle of attack. Then the upper surface was coated uniformly with a thin layer of the oil mixture, and the wind velocity was increased from zero to that which was equivalent to a Reynolds number of 1.5×10^6. Development of the flow pattern was allowed to proceed until either no further change was likely or, in regions of accumulated oil, gravitational effects began to distort the result. In order that the dayglo pigment would fluoresce in the visible range, the flow pattern was illuminated by ultra-violet light. To record the results, black and

white photographs were taken through a yellow filter.

3.3.3 Static Experiments

A number of experiments were performed under steady conditions. Once the wind velocity had reached the required value, the aerofoil was rotated about its quarter chord axis until it was positioned at the angle of attack at which the first set of data was to be recorded. Usually, this was approximately -2°. Through the MINC digital-to-analogue converter and hydraulic actuator controller, the incidence was then incremented in steps of approximately 0.5°. At each angle of attack, when the flow had stabilised, data were sampled. On each of one hundred occasions over a period of one second, the MINC clock overflowed, initiating a sampling sweep. Having averaged the data and written these values to buffer, the process was repeated. Data were recorded at 128 angles of attack : 64 when incidence was increasing and 64 when incidence was decreasing. At each angle of attack, integrated loads were calculated and displayed on the graphics terminal.

At the beginning of each set of experiments, a static test was performed at a Reynolds number of 1.5×10^{6}. If, over the unstalled range of incidence, the normal coefficient graphs for upstroke and downstroke could be superimposed, it was assumed that there was no temperature drift and that conditions had settled. Of these tests,

that which yielded the results which were most typical of the set as a whole was regarded as the standard test for analysis (i.e. the data from unsteady tests were to be compared with these data). In addition, static tests were performed at Reynolds numbers of 1.0×10^6 and 2.0×10^6.

So that, at any angle of attack, it was possible to examine the variation of pressure values with time, a number of "unsteady static" tests were performed at a Reynolds number of 1.5×10^6. This involved rotating the aerofoil to the desired incidence once the wind had reached the required velocity and, when the conditions had settled, manually initiating the sampling of 256 sweeps of data at a requested frequency. These experiments were performed over a range of incidence of between -7° and 32° at sampling frequencies of 100Hz and 500Hz (i.e. for fractionally over 2.5 seconds and 0.5 seconds respectively).

3.3.4 Oscillatory Experiments

The majority of oscillatory tests were performed at a Reynolds number of 1.5×10^6. At this Reynolds number, the parameters which varied were mean angle, amplitude and reduced frequency : mean angle between 3° and 20°; amplitude between 4° and 10°; reduced frequency between 0.01 and 0.175. In addition those runs with amplitude 8° and reduced frequency 0.100 were repeated at Reynolds numbers of 1.0×10^6 and 2.0×10^6. All oscillations were of

sinusoidal motion.

To generate the sine function, a BBC microcomputer and a 12-bit digital-to-analogue converter provided an input signal to the hydraulic controller. A second 12-bit digital-to-analogue converter was employed to enable software control of the maximum desired voltage for the given amplitude. The required output function was digitised into 512 equal time steps in two's complement code and stored in EPROM. The frequency of the function was controlled using the internal interrupts of the BBC computer.

The following test procedure was observed. When the wind velocity had reached the desired value, the aerofoil was rotated about its quarter chord axis until it was positioned at the mean angle. It was then set in motion via the BBC keyboard. After a small number of oscillations, the user instructed the MINC that data acquisition could begin. On the next occasion that the model passed through the mean angle, the MINC clock Schmitt trigger was fired and two cycles of data were sampled. These data were then written to a data file and the MINC awaited the firing of the Schmitt trigger again before sampling more data.

During each test, ten cycles of 128 sweeps were sampled at a frequency equivalent to the oscillation frequency multiplied by 128. This ensured that each cycle of data acquisition lasted for exactly one cycle of

oscillation.

3.3.5 Constant Pitch-rate Ramp Experiments

During a ramp test, the aerofoil was rotated about its quarter chord axis at a constant angular velocity. Most ramps were performed at a Reynolds number of 1.5×10^6. At this Reynolds number, thirty ramps were executed between -1° and 40° over a range of pitch rates between $0.75^\circ s^{-1}$ and $290^\circ s^{-1}$ (i.e. reduced pitch rates of between 0.0001 and 0.037). A similar series of tests was performed in the negative direction from 40° to -1°. In addition, a set of four ramps in the positive direction over the same range of angles and over a range of pitch rates between $30^\circ s^{-1}$ and $290^\circ s^{-1}$ were performed at Reynolds numbers of both 1.0×10^6 and 2.0×10^6.

The ramp function was also generated by the BBC microcomputer and 12-bit digital-to-analogue converter. The voltage was set via software for the desired arc length and the aerofoil's motion was controlled in a similar manner to that for sinusoidal motion.

The test procedure was as follows. When the wind velocity had reached the desired value, the aerofoil was rotated about its quarter chord axis to the angle of attack at which the ramp would begin. It was then set in motion via the BBC keyboard. As the aerofoil began to move, the MINC clock Schmitt trigger was fired and sweeps of data

were sampled at regular time intervals throughout the ramp. At the end of the data acquisition process, these values were written to a data file.

Five cycles of 256 sweeps were sampled during each test. Between each ramp, the model sat at the finishing angle for five seconds, moved smoothly back to the starting angle in five seconds and sat at this position for another five seconds. The sampling frequency was usually chosen so that 128 sweeps of data were sampled during motion and 128 sweeps while the model sat at the finishing angle. However, 550Hz was the maximum sweep frequency at which it was possible to sample data with the MINC. Therefore, for ramps executed at pitch rates of $176^{\circ}s^{-1}$ or greater, data was sampled at this frequency.

3.3.6 Data Reduction

The raw binary values were reduced to pressure coefficients before the data were analysed. At this stage, the outstanding values in the run information block were calculated.

The digitised raw values were initially converted to real-valued voltages, which were subsequently converted into the necessary form with the aid of the values obtained from the procedures described in Subsection 3.3.1. The angle of attack and dynamic pressure were obtained from their calibration cubics. The pressure coefficient at

each pressure transducer location was calculated from the equation

c_p = (voltage-offset)/(gain*sensitivity*dynamic pressure).

Although the input signal to the hydraulic controller is a linear function for ramp tests, there are slight non-linearities in the aerofoil's motion at the beginning and end of the ramp, as it builds up speed from rest and later returns to rest. Therefore, for ramp tests, it was necessary to calculate the pitch rate which was actually achieved over the range of angles for which the motion was linear. Having examined data from those aerofoils which had previously been tested with this system, it was accepted that this should be calculated by dividing the difference in angle of attack between 25% of the arc and 50% of the arc by the time taken to travel between these angles.

3.4 CONCLUDING REMARKS

A series of experiments, under steady and unsteady conditions, was performed on the NACA 23012C aerofoil in the University of Glasgow's "Handley-Page" wind tunnel using an existing data acquisition and control system. The data were recorded as binary values and later reduced to pressure coefficients. The reduced data files were transferred to a DEC VAX 750 computer, where they were

stored in the University of Glasgow aerofoil database, as described by LEITCH AND GALBRAITH [59]. The data were then analysed, and the results, with plots, are discussed in Chapters Four and Five.

CHAPTER FOUR

RESULTS OF EXPERIMENTS PERFORMED ON THE NACA 23012C AEROFOIL

4.1 INTRODUCTION

The NACA 23012C aerofoil was tested under steady and unsteady conditions using the apparatus and techniques which were described in Chapter Three. The resulting data have been presented by GRACEY AND GALBRAITH [39,40] and important aspects of these results are discussed in this chapter.

Unless otherwise stated, the data have been recorded during tests which were performed at a Reynolds number of approximately 1.5×10^6. Two comparisons are made with these data : they are compared with the data which were yielded by performing similar experiments on the NACA 23012 and NACA 23012A aerofoils at an approximate Reynolds number of 1.5×10^6 and they are also compared with the

corresponding data from the NACA 23012C at Reynolds numbers of approximately 1.0×10^6 and 2.0×10^6. The data for the NACA 23012 have previously been presented and discussed by LEISHMAN ET AL [55,58] and SETO ET AL [82,83,85], and the data for the NACA 23012A by NIVEN ET AL [73,76].

This chapter is divided into four main sections, in each of which are discussed the results from a particular series of experiments : the resulting photographs from the oil-flow visualisation tests are displayed and reviewed in Section 4.2; the data from static tests are discussed in Section 4.3; the data from oscillatory tests are considered in Section 4.4; the resulting data from those experiments which were performed under constant-pitch-rate "ramp" motions are examined in Section 4.5.

The reduced data are stored as pressure coefficients. By suitably integrating these values, it is possible to evaluate the coefficient of force in the direction normal to the aerofoil's chord line, the coefficient of pitching moment about the quarter chord position and the coefficient of force in the direction tangential to the aerofoil's chord line. This last force is defined as being positive when acting towards the leading edge of the aerofoil. These four loads form the basis of this investigation of the dynamic stall process. However, other forces are introduced when necessary.

When examining the figures in this dissertation, the following should be noted. A fault with the transducer at 10% chord caused it to appear to record more suction than it should. The data it provided were disregarded, along with those from the transducers over the trailing 10%, which, as has been typical of the other aerofoils tested with this apparatus, were also irregular.

Unless otherwise stated, all the data which are discussed in Sections 4.3 - 4.5 have been averaged over a

number of cycles : five cycles for ramp motion tests, ten for oscillatory tests and 100 for static tests. This is consistent with the treatment of the data which were recorded with the previously-tested aerofoils and with which these data will be compared. In averaging the data, the intention is that important features should be highlighted and erratic readings suppressed. As illustrated in Figure 4.1, it has been found that, over a number of cycles in unstalled conditions, there is little variation in the values which are recorded during corresponding data sweeps. In the stall regime, however, the level of duplication drops markedly. This is a result of the fact that, at higher angles of attack, vortices form and are shed periodically. It seems that the recorded strength of each vortex varies from cycle to cycle, and averaging may be invalidated. However, events tend to occur at the same data sweep of each cycle. As the principal area of interest in this dissertation is the incidence at which certain events influencing the onset of stall occur, and, because the absence of stray readings results in it being much simpler to locate such events, it was decided that averaged data were acceptable. However, additional examination of the effects of the variation in pressure readings between cycles will be considered in Sections 4.3 - 4.5.

The variation of the dynamic pressure in the working section with incidence is illustrated in Figure 4.2. It is shown in Figure 4.2(a), in which the variation of dynamic pressure is plotted for data from static tests over

a range of Reynolds numbers, that, as incidence is increased from 0° to 28° and blockage effects increase accordingly, dynamic pressure drops by approximately 20%. However the drop in dynamic pressure as the aerofoil is rotated from zero to the incidence of static stall is less than 4%.

It can be seen from Figures 4.2(b) - 4.2(d) that, in addition to these blockage effects, during unsteady experiments, there are other disturbances in the flow environment. The vortex which convects downstream during the dynamic stall process and, when the aerofoil is subjected to oscillatory motion, an induced periodic variation, which was first detected by LEISHMAN [55], both seem to affect dynamic pressure. The influence of both these unsteady effects are clearly illustrated in the greatly magnified graph in Figure 4.2(d). These effects do not become significant until stall has occurred and, for the main purpose of this dissertation, as described above, have little influence. The dynamic pressure was recorded during each data sweep, as described in Chapter Three, and this local value was used when reducing the pressure readings to pressure coefficient values.

There are regions of hysteresis in the dynamic pressure graphs. As will be described in Sections 4.3 and 4.5, these regions coincide with those at which there are hysteresis loops in the aerodynamic data. The dynamic pressure reading which was recorded at the beginning of an experiment, and from which the Reynolds number and Mach

number were calculated, was recorded when the aerofoil was sitting at an angle of attack of 0° and, hence, blockage effects were minimised.

4.2 FLOW VISUALISATION EXPERIMENTS

It was intended that two-dimensional characteristics should be obtained from the experiments which were performed on the NACA 23012C aerofoil. It was, therefore, necessary that the influence of any three-dimensional flow effects should be minimal. In particular, the data could be misinterpreted if, in the presence of induced downwash and cross-flow conditions, the chordwise pressure transducers did not lie in the region of two-dimensional flow. It has been reported by MOSS AND MURDIN [71] that three-dimensional effects were found at stall. The conclusion was that these effects seemed to be inherent in the aerodynamics of the stall itself and that only with great care should nominally two-dimensional data be considered for predicting the behaviour of helicopter rotors. These results were also observed by SETO ET AL [85] and NIVEN AND GALBRAITH [76] in similar series of experiments to that which was performed by the present author.

The method which was employed for this series of flow visualisation experiments was that which involved coating the surface of the aerofoil with a thin layer of oil

contaminated with a visible trace. As CHANG [24] explains, this coating of the aerofoil indicates the surface streamline or flow direction on the surface and, since a separation line is generally an envelope of surface streamlines, the locus of boundary layer separation points can be detected by this technique. It was, therefore, from these qualitative experiments, possible to compare experimentally-determined separation points with those predicted theoretically before preparing the apparatus for experiments involving pressure transducers.

A mixture of saturn yellow "dayglo" powder, odina oil and paraffin was used to coat the surface. The experimental technique is described in Subsection 3.3.2.

Before interpreting the results, an observation by WILBY [92] should be noted. The angle of attack had been set before the tunnel speed accelerated from zero to the desired velocity. Therefore, at high angles of attack, the initial flow was likely to be separated, with attachment resulting as Reynolds number increased. At a sufficiently high incidence, the flow would have failed to attach at the test conditions. In stalled conditions, it thus appears that these results correspond more closely to the downstroke of a static test. In addition, for the same reason, GREGORY ET AL [41] have claimed that static stall is a function not only of incidence and Reynolds number but also of the direction in which these parameters are changed. In order that these effects could be studied, NIVEN [73] performed a series of unsteady tests in

which, after the required tunnel speed had been attained, the aerofoil was pitched at a constant, but very slow, rate from zero to the desired incidence. It was concluded from these experiments that, because of the lack of sensitivity of the oil to subtle changes in the separated region, no significant change in the flow pattern or separation point resulted. It was, therefore, decided that the tests should be performed in the established manner.

It should be appreciated that, during these experiments, the model stood vertically. This resulted in gravitational effects giving a downward bias to the oil flow in regions of weak shear.

4.2.1 Oil-flow Characteristics for NACA 23012 and NACA 23012A Aerofoils

The flow development obtained on the upper surface of the NACA 23012 aerofoil over a range of angles of attack at a Reynolds number of 1.45×10^6 has been illustrated and discussed by SETO ET AL [85]. Similarly, the characteristics for the NACA 23012A over a similar incidence range at a Reynolds number of 1.5×10^6 have been described by NIVEN [73]. Several important points are noted.

For angles of attack of 10° and less, the flow about both aerofoils was primarily two-dimensional, with little or no flow separation at the junctions between the model

and the tunnel wall. The separation front of the NACA 23012 aerofoil became irregular as stall was approached. Between 14° and 15°, it experienced sudden and rapid trailing edge separation. For angles of attack greater than 14°, the flow was significantly three-dimensional and two distinct vortices formed at the outer span positions. This three-dimensionality seemed to have negligible significance for angles of attack which were lower than the stall incidence of 14.2°.

Between incidences of 10° and 13°, the separation front of the NACA 23012A moved towards the leading edge with a high degree of flow two-dimensionality. Between 13° and 17°, the boundary layer began to separate asymmetrically, with a larger separated region over the lower half-span. Separation was less sudden than it was for the NACA 23012 and, unlike the case of that aerofoil, the separation point did not become irregular as the stall incidence was approached. At an incidence of 17°, the flow pattern once again became symmetrical. However, the two-dimensionality of the flow pattern was not restored.

In the case of both aerofoils, transition from laminar to turbulent flow was shown via a laminar separation bubble. This bubble shortened and moved closer to the leading edge as the angle of attack was increased towards the stall incidence, but remained present up to and beyond stall. This indicated that the laminar separation bubble played no direct part in the stalling process of these aerofoils.

BIPPES AND TURK [18] have described how, on approaching the stagnation zone of an obstacle, the boundary layer separates and forms a vortex sheet. Hence, a vortex surrounds the obstacle in a horseshoe-like manner. At high angles of attack, the interference of this horseshoe vortex prevents flow conditions being symmetrical and results in the formation of an additional vortex on the upper surface near the tunnel wall. This theory is consistent with the observations which have been described above, and prompted Niven to illustrate the principal components of flow behaviour in Figure 4.3.

4.2.2 Oil-flow Characteristics for the NACA 23012C Aerofoil

The flow development over a range of angles of attack on the upper surface of the NACA 23012C aerofoil at a Reynolds number of 1.5×10^6 is illustrated in a series of photographs in Figure 4.4.

Because of the fact that, over the rear upper surface, and particularly at the trailing edge, the NACA 23012C has a greater adverse pressure gradient than both the NACA 23012 and NACA 23012A, the local velocity of the flow was retarded. Consequently, it can be seen that, even at low angles of attack, the oil pattern was significantly influenced by gravity. Indeed, at an incidence of 8°, the turbulent boundary layer had already begun to separate at the trailing edge. As incidence

increased, the separation front moved towards the leading edge. At lower angles of attack, the flow was reasonably two-dimensional. However, for angles of attack greater than 11°, the flow separated asymmetrically with a larger area of separated flow over the lower half-span than over the upper half-span. As the incidence increased to values greater than 14°, this asymmetry became significant and the degree of three-dimensionality increased. At an incidence of 18°, the separated region stretched over the trailing 60% of the aerofoil's upper surface and two vortices were apparent. For angles of attack of 19° and greater, in the presence of these vortices, the flow pattern became symmetrical.

A laminar separation bubble was detected at an angle of attack of 8°. As in the case of the other aerofoils, it shortened and moved towards the leading edge as incidence increased. The bubble was still present at an angle of attack of 24°, indicating, again, that it did not directly influence this aerofoil's stall process. There is an indication that the bubble still existed at incidences of 26° and 32°. However, at these angles of attack, the flow had fully separated at the leading edge and the photograph is probably revealing a region of oil which had accumulated as a result of the curvature of the surface of the model.

For any chordal position at mid-span on the upper surface of an aerofoil, there exists an angle of attack at which that position is the separation point of the

turbulent boundary layer. The variation of such angles of attack for the NACA 23012C, as determined from this series of flow visualisation experiments, is illustrated in Figure 4.5. The error bands demonstrate the difficulty in determining the separation point in the presence of oil accumulation. The trend was typical of an aerofoil which experiences trailing edge stall. A best least-squares curve fit was performed on the data points and has also been plotted on the graph. This curve consisted of two exponential functions which coincided at approximately the stall incidence. The reason for choosing this form for the equation of the curve is explained in Chapter Five. A comparison between this curve and similar curves which resulted from the experiments which were performed on the NACA 23012 and NACA 23012A is illustrated in Figure 4.6, along with the recorded separation points for the NACA 23012C. As was predicted in Chapter Two, the NACA 23012C possessed greatly enhanced trailing edge separation characteristics.

On the whole, the flow development on the NACA 23012C aerofoil was very similar to that for the NACA 23012 and, in particular, the NACA 23012A. Because of differences in the pressure distribution, the angle of attack at which each event occurred did vary. However, the degree of three-dimensionality appears to have been more closely related to the degree of turbulent boundary layer separation rather than the incidence. This supports the argument that three-dimensionality is a consequence of the stall process.

One more event should be explained. At the bottom of the aerofoil, particularly evident at an incidence of 14° (Figure 4.4(m)), another vortex was present. This was the result of a sink which had been caused by the failure to seal a gap adequately at the foot of the aerofoil, where additional packing had been required. This fault was corrected before beginning the series of quantitative experiments during which the data which are described in the following sections were recorded.

4.3 STATIC EXPERIMENTS

Typical data for an experiment which was performed on the NACA 23012C aerofoil at a Reynolds number of 1.5×10^6 are illustrated in Figure 4.7. For most angles of attack, the data which were recorded during the range of sweeps over which incidence was increasing differed negligibly from those which were recorded when incidence was decreasing. There was, however, slight hysteresis at the point of flow reattachment at the leading edge. This is typical of all such experiments which have been performed with this experimental apparatus. The delay in recovering the pre-stall conditions was of approximately 2°.

4.3.1 Pressure Coefficient Distribution

Graphs of the variation of pressure coefficient with chordal location as obtained from both potential flow prediction and experimental data are compared in Figure 4.8. The general trends were similar, but, at every position around the aerofoil, the theoretical value which was predicted for the pressure coefficient was greater in magnitude. The difference is primarily due to the presence of the boundary layer and wake, neither of which was modelled in the potential flow algorithm.

The pressure coefficient distributions which were predicted from potential flow for the NACA 23012C and NACA 23012 are compared in Figure 2.11. A similar comparison for the case of experimental data is illustrated in Figure 4.9. The graphs show similar trends, but examination of the peak suction at the leading edge reveals a slight disagreement. The pressure gradient at this position was very large for both aerofoils. Therefore, if a transducer were situated even slightly further from the location of peak suction on the NACA 23012C than the corresponding transducer on the NACA 23012, it could reduce the suction recorded on that aerofoil, in comparison to that on the NACA 23012, by a significant amount. As there were slightly fewer transducers located at the leading edge on the NACA 23012C than on the NACA 23012, this argument is plausible. However, when considering integrated loads, because of the short distances between the transducers which were situated at the leading edge, the significance

of this error is so greatly reduced that it may be ignored.

As displayed in Figure 4.7, for incidences between 8° and 10°, there was, in addition to that described in Section 4.1, a slight irregularity in the smoothness of the upper surface pressure distribution. It is thought that this was an indication of the existence of the laminar separation bubble. At higher angles of attack, it was no longer observed. This may have been due to the shortening of the bubble or to the fact that, as the leading edge suction increased, such small deviations could not be detected. Over the incidence range for which it could be observed, it was found that, as angle of attack increased, the bubble moved towards the leading edge and shortened. This behaviour was in accordance with the evidence of the flow visualisation experiments.

4.3.2 Separation Characteristics

From a chordwise pressure distribution graph, it is possible, by examining the extent of the constant base pressure over the separated region, to approximate the chordwise location of turbulent boundary layer separation. The angle of attack at which each transducer first appeared to be within the region of separated flow is plotted against the transducer's location in Figure 4.10. As in the case of the flow visualisation data, a best least-squares curve fit of exponential form was performed on the data. The error bands represent the distance of

the transducer from each adjacent transducer and the size of the step in incidence between each data sweep. The characteristics were typical of those possessed by an aerofoil experiencing trailing edge stall.

These data points and separation curve are compared to those which were determined from flow visualisation in Figure 4.11. The characteristics obtained from the flow visualisation experiments were more typical of enhanced trailing edge separation than those from pressure distribution. Because the extremities of the error bands do not overlap for many of the data points, the differences cannot be accounted for by the difficulty in determining the separation points from flow visualisation photographs. However, during the flow visualisation experiments, the accumulation of oil on the aerofoil surface may have provoked the transition of the boundary layer from laminar to turbulent flow, so that separation was delayed.

The separation characteristics for the NACA 23012C, NACA 23012 and NACA 23012A are compared in Figure 4.12. The rate of change of separation point with respect to angle of attack was greatest for the NACA 23012. The modified aerofoils separated at approximately equal rates, but the angle of attack at which any particular separation point was reached was approximately 2° lower for the NACA 23012A. Although, in view of their rate of separation, the separation characteristics for the modified aerofoils were more typical of aerofoils which experience trailing-edge stall than those of the NACA 23012, the

forward movement of the separation point between 70% chord and 20% chord was still rapid for these aerofoils. In contrast to what was observed from flow visualisation, it was evident that, for all the aerofoils, separation became steady for approximately 2° at about 10%-15% chord. This point is illustrated in Figure 4.10, where the point at 10% chord stands approximately 2° above the smooth exponential curve. This event indicated that flow remained attached around the leading edge until the bursting of the laminar separation bubble triggered the final collapse of leading edge suction. Figure 4.7 supports this explanation by the fact that, although leading edge suction initially dropped slightly at approximately 15°, it was not until the incidence reached 24° that it collapsed totally.

The separation characteristics of the NACA 23012C are compared to its reattachment characteristics in Figure 4.13. The delay of flow reattachment at the leading edge is indicated by the fact that the points do not coincide over the incidence range between 20° and 22°. In particular, over the incidence range for which the separation point remained constant on the upstroke, the boundary layer was still attached only at the extreme leading edge on the downstroke. This 2° delay is also related to a similar region of hysteresis in the tangential force characteristics (Figure 4.7). In all other respects, differences between the separation and reattachment characteristics were negligible. This confirms the view stated above that the most significant differences between the separation characteristics which

were yielded by the pressure coefficient distribution and by flow visualisation were the result of the differences in the experimental techniques, and not due to the observation, described in Section 4.2, that the results obtained from flow visualisation were more similar to the characteristics of reattachment.

4.3.3 Coefficient of Normal Force

Graphs of the variation of the coefficient of normal force with incidence for the NACA 23012C, NACA 23012 and NACA 23012A at a Reynolds number of 1.5×10^6 are compared in Figure 4.14. The differences between the characteristics for the NACA 23012C and NACA 23012 were very similar to those which were predicted in Chapter Two and illustrated in Figure 2.12.

The incidence of zero-lift was lowest for the NACA 23012C. According to standard calculation techniques, as described by, for example, ANDERSON [2], a more cambered aerofoil should possess a more negative incidence of zero-lift. This angle of attack being approximately -2.8° for the NACA 23012C and -0.7° for the NACA 23012 supports this prediction. However, the NACA 23012A possessed a positive zero-lift incidence of approximately 1.0°. It seems that this inconsistency was due to the effect of the aerofoil camber being exceeded by the effect of the pressure coefficient distribution over the region of reflex camber at the trailing edge. Over this region, the aerofoil experienced suction on the lower

surface and pressure on the upper surface.

ABBOTT AND VON DOENHOFF [1] have also argued that camber is the primary influence on the incidence of zero-lift, but that it is thickness which is the primary influence on the gradient of the lift curve. This opinion is supported by the fact that the gradients of the normal coeffient curves were approximately equal for the NACA 23012C and NACA 23012, which possess approximately equal thickness ratios at the position of maximum thickness. However, the NACA 23012A again failed to agree with the theory : its lift curve was steeper. NIVEN [73] also accounted for this abnormality with reference to the trailing edge.

PROUTY [78] has decribed how camber at the extreme leading edge provides an easier path for the upper surface streamline adjacent to the aerofoil, resulting in the leading edge suction peak being spread over a larger surface of the aerofoil and reduced in magnitude. Because of this, the pressure gradient behind the peak is less adverse and so the boundary layer is more stable. This allows a larger angle of attack to be reached before the aerofoil stalls and, hence, a larger maximum value of the normal coefficient to be achieved. As was explained in

Chapter Two, the design of the NACA 23012C required it to be rotated. Hence, although the geometry of the leading part of the NACA 23012C differed negligibly from that of the NACA 23012, its nose faces the wind at a lower

incidence than either of the other aerofoils and, therefore, is effectively more cambered at the leading-edge. Figure 4.15, which compares each aerofoil's pressure coefficient distribution at an angle of attack of approximately 12°, reveals that the suction peak of the NACA 23012C was indeed reduced and spread over more of the surface of the aerofoil than was the case for the other aerofoils. This fact could account for the larger magnitude of maximum normal coefficient which it possessed and for the higher angle of attack at which it occurred. It also supports Abbott and von Doenhoff's evidence that greater camber results in more lift. A number of experiments were performed on each aerofoil under steady conditions at a Reynolds number of 1.5×10^6. From examination of the results of all these experiments and taking into account the size of step in incidence between each data sweep, it was found that the maximum value of normal coefficient occurred at approximately 14.9° for the NACA 23012C, as opposed to 14.5° and 13.8° for the NACA 23012 and NACA 23012A respectively.

The normal coefficient collapsed from its maximum value more abruptly for the NACA 23012 than for the modified aerofoils. This was a direct consequence of its more abrupt separation characteristic. Abbott and von Doenhoff claim that more gentle stall is a result of the position of maximum camber being located further downstream. This claim was supported, in the case of these aerofoils, by the fact that maximum camber was located at approximately 50% chord on the NACA 23012C as

opposed to 15% for the NACA 23012.

4.3.4 Coefficient of Pitching Moment about Quarter Chord

Graphs of the variation of the coefficient of pitching moment about the quarter chord location with angle of attack for each aerofoil at a Reynolds number of 1.5×10^6 are compared in Figure 4.16. The differences between the characteristics for the NACA 23012C and NACA 23012 were very similar to those which were predicted in Chapter Two and illustrated in Figure 2.12.

These two aerofoils showed very similar trends. At low angles of attack, the pitching moment coefficient was reasonably constant, but increased slightly as suction grew at the leading edge. As the separation point moved towards the leading edge and caused the peak suction to drop, the pitching moment coefficient decreased. At a still higher incidence, at which the leading edge suction collapsed totally, the pitching moment coefficient again dropped sharply. The NACA 23012A behaved in a similar manner except that, between 0° and 5°, there was a distinct decrease in pitching moment. This was due to the drop in suction on the lower surface of the reflex trailing edge as incidence increased.

The clearest difference between the characteristics of the three aerofoils, however, was the amount by which the graphs were offset. The pitching moment coefficient

C_{mo} at each aerofoil's incidence of zero-lift approximated to -0.08, -0.01 and +0.04 for NACA 23012C, NACA 23012 and NACA 23012A respectively. In order that good control and vibration characteristics are maintained within the stall boundary, it would seem that C_{mo} should be as close as possible to zero. DAVENPORT AND FRONT [30] have described how leading edge camber can make C_{mo} more negative, but not necessarily unacceptable. They suggest that this problem can be overcome if the aerofoil possesses slight reflex camber at the trailing edge. It would seem that the reflex trailing edge of the NACA 23012A has over-compensated for the leading edge camber which is possessed by the NACA 23012. However such a modification could improve the pitching moment behaviour of the more highly cambered NACA 23012C.

4.3.5 Drag Characteristics

It is possible to calculate the coefficients of lift and drag which are due to the pressure distribution by resolving, in the directions of these forces, the coefficients of normal and tangential force. As can be seen from Figure 4.17, for the NACA 23012C, lift initially increased steadily at a cost of only a slight increase in drag. However, after stall, the lift coefficient decreased and drag increased significantly. Figure 4.18 indicates that the behaviour of drag did not differ significantly from aerofoil to aerofoil.

4.3.6 Unsteady Static Data

It may be observed from Figures 4.7, 4.14 and 4.16 that the variation of each integrated load with angle of attack became erratic after passing through the stall incidence. With reference to Section 4.2, this would seem to be due to flow turbulence resulting from separation and three-dimensional effects. In Figure 4.19, mean and standard deviation values for each integrated load and incidence are plotted. These values were calculated from the data resulting from the "unsteady static" experiments which were described in Subsection 3.3.3. Large values of standard deviation were detected after stall had occurred. Therefore, in the stall regime, the erratic values which resulted from averaged data were merely a reflection of the large variation of values which were recorded at a single angle of attack over a period of time.

Because of this result, it was hoped that the standard deviation of the pressure coefficient would reveal a perceptable degree of randomness resulting from the turbulence of the boundary layer. LORBER AND CARTA [61] successfully attempted a similar feat on data from unsteady experiments with the root mean square variation in pressure. However, as indicated in Figure 4.20, the variation in standard deviation was similar for all transducers on the upper surface, with negligible difference from sweep to sweep until stall occurred. This result again revealed that, during static experiments, the primary influence on the non-repeatability of data was the

effect of the stall process on the boundary layer. It also supported the opinion that averaging of the data was valid in pre-stall conditions. However, the position of turbulent boundary layer separation could not be determined from a consideration of the standard deviation of pressure coefficient values.

4.3.7 Influence of Reynolds Number

Static experiments were also performed on the NACA 23012C at Reynolds numbers of approximately 1.0×10^6 and 2.0×10^6. The results are displayed in Figures 4.21 and 4.22 respectively. Over this range of Reynolds number, the greatest local Mach number which was recorded on the surface of the aerofoil was less than 0.5. Therefore there were no compressibility effects, and any differences between the data of different experiments would seem to be due to Reynolds number rather than Mach number.

Because of the thicker boundary layer it should possess at lower Reynolds numbers, the flow is likely to separate from an aerofoil's surface at a lower incidence. From Figure 4.23, it seems that this is, in general, for separation up to the position of mid-chord, the case for these data. It also accounts for the fact that, as indicated in Figure 4.24, the maximum value of the coefficient of normal force increased as Reynolds number increased. One data point in Figure 4.23 which does not

agree with the general behaviour is at 90% chord for a Reynolds number of 2.0×10^6, where separation occurs earlier than for the lower Reynolds numbers. This may be due to the problems with data over the trailing 10% chord (described in Section 4.1). However, Figure 4.23 shows that the angle of attack at which the boundary layer separated at 50% chord was reasonably unaffected by Reynolds number. This property accounts for the fact that the incidence of maximum normal force was almost identical at all three Reynolds numbers. The incidence of zero-lift did not vary significantly with Reynolds number.

Under attached conditions, the gradient of the normal coefficient curve was almost identical at Reynolds numbers of 1.5×10^6 and 2.0×10^6. However, at a Reynolds number of 1.0×10^6, the normal coefficient curve was less steep. This may again be accounted for by the different boundary layer conditions at lower Reynolds numbers. The pressure coefficient distributions for each Reynolds number at an incidence of approximately 5° are plotted in Figure 4.25. Otherwise, the behaviour of the normal coefficient varied with incidence in a manner which reflected the behaviour of the separation characteristics : on the approach to the stall incidence, the rate of change with respect to angle of attack increased as Reynolds number increased.

Figure 4.26 plots the drag coefficient traces at each of the three Reynolds numbers. Although there is variation before stall, it is not important to the

discussion described herein.

From Figure 4.27, it can be seen that the angle of attack of pitching moment stall varied negligibly with Reynolds number. However, at a Reynolds number of $1.0x10^6$, the pitching moment coefficient was significantly closer to zero. As can be seen from Figure 4.25, the primary difference between the pressure coefficient distributions at Reynolds numbers of $1.0x10^6$ and $1.5x10^6$ occurred on the lower surface. It may be that, at this Reynolds number, there was no transition on the lower surface, but that, at higher Reynolds numbers, the flow became turbulent at the trailing edge. This hypothesis is supported by the results of the prediction code of COTON [25].

Increasing the tunnel speed to that which was required for a Reynolds number of $2.0x10^6$ took a length of time which was sufficient for the temperature on the surface of the model to rise significantly. Because of this, it is possible that the offset voltages of the transducers could have drifted. The fact that the graphs of the data from the experiment at a Reynolds number of $2.0x10^6$ did not always follow the trend which was set by the data which were recorded at the lower Reynolds numbers could have resulted from such offset drift. One such example is the lower surface pressure coefficient distribution in Figure 4.25, where the distribution for the experiment performed at a Reynolds number of $2.0x10^6$ was situated between those for data at the lower Reynolds

numbers. The fact that, in Figure 4.27, there was such a large difference in the values of c_{mc} which were recorded at Reynolds numbers of 1.0×10^6 and 1.5×10^6, and yet the values which were recorded at Reynolds numbers of 1.5×10^6 and 2.0×10^6 were almost identical, may also be due to offset drift at the highest Reynolds number. However, the effect of drift should not be significant in the analysis which is to follow. As explained above, this investigation will not concentrate primarily on the magnitudes of loads but on the incidences at which events occur. The values which are obtained for these incidences do not seem to have been affected by offset drift at a Reynolds number of 2.0×10^6.

4.4 OSCILLATORY EXPERIMENTS

In Subsection 3.3.4 was described a series of oscillatory experiments in which the parameters of mean incidence, amplitude, oscillation frequency and Reynolds number were varied in succession. The present section discusses the results of these experiments. Subsection 4.4.1 describes the stall regimes which were originally defined by McCROSKEY ET AL [64,67], while Subsections 4.4.2 - 4.4.5 examine the influence of each parameter on the typical unsteady characteristics of each regime. Two quantitative measurements - the critical angle for moment stall which was originally introduced by WILBY [91,92] and aerodynamic damping - which are peculiar

to oscillatory experiments, are considered in Subsections 4.4.6 and 4.4.7 respectively.

This section is an overview of the unsteady properties which are particularly associated with oscillatory experiments. The unsteady characteristics are examined further in Section 4.5 with the aid of data resulting from tests which were performed at a constant pitch-rate. The more general aspects of dynamic stall are discussed in that section.

In the figures which are compiled from several smaller graphs, a broken line illustrates the data from static experiments.

4.4.1 Degree of Stall

As discussed in Chapter One, McCROSKEY ET AL [64,67] have described how, in subsonic flow, the flow field around an oscillating aerofoil can be characterised by the degree or extent of flow separation and the shedding and convection over the upper surface of the aerofoil of a vortex-like disturbance. This "dynamic stall vortex", which, once initiated, is generally accepted as being independent of aerofoil motion, induces a highly non-linear, fluctuating pressure field. It was claimed that, for a given aerofoil, the primary parameter in determining the degree of such behaviour is the maximum attained angle of attack. Based on this parameter and the

behaviour of the coefficient of pitching-moment, four regimes of viscous / inviscid interaction were defined for oscillating aerofoils. From the oscillatory experiments which were performed on the NACA 23012C aerofoil at a Reynolds number of approximately 1.5×10^6, reduced frequency of 0.10 and oscillation amplitude of between 8.0° and 8.5°, typical data sets for each stall regime are plotted in Figures 4.28 - 4.31. The drag coefficient was approximated from the pressure distribution in the manner described in Subsection 4.3.5.

Figure 4.28 plots data from an experiment in which the maximum incidence was 11.5°. This is lower than the incidence of static stall. From the fact that there was a break in neither the pitching moment nor the gradient of the normal coefficient curve, it is clear that there was almost no turbulent boundary-layer separation throughout the cycle. However, as indicated by the slight, but distinct, hysteresis, with the data from neither the upstroke nor the downstroke lying on the graph of the static characteristics, the effects of boundary layer thickness were not completely negligible. These characteristics are typical for a test in the "regime of no stall". Increasing the maximum angle of attack to 13.5° (Figure 4.32) resulted in the boundary layer remaining attached at incidences where separation had begun in the static experiments, and this experiment was still typical of oscillations in the regime of no stall.

A further increase in the maximum incidence to 18.1°

(Figure 4.29) resulted in the boundary layer separating over the rear half of the aerofoil during the downstroke. This revealed itself at the top of the graph of pitching moment coefficient against angle of attack in the form of a slight distortion which was of the same order of magnitude as the inviscid effects. Therefore, there appeared to be no hysteresis at this part of the cycle. In addition, because of boundary-layer separation, there was a distinct hysteresis loop in the graph of normal coefficient against angle of attack, with a loss of lift on the downstroke. These data illustrate the limiting case for which maximum lift could be obtained without experiencing any significant penalty in pitching moment or drag. This condition is labelled "stall onset".

Any additional increase in the maximum incidence produced a major increase in the extent, severity and duration of the separation phenomenon. The effect became more marked as the maximum incidence was increased still further. Illustrated in Figure 4.30 is a typical example of the less severe conditions of the "light dynamic stall regime" in which the maximum incidence is only slightly greater than the stall onset incidence. In this case the maximum angle of attack was 20.0°. McCroskey et al described this as being the more common of the two higher stall regimes in helicopter applications and especially sensitive to aerofoil geometry, reduced frequency, maximum incidence and freestream wind velocity. The qualitative behaviour was described as being closely related to the boundary layer separation characteristics.

Examination of the pitching moment graphs reveals that there was an abrupt and well-defined change in characteristics when progressing from stall onset to light stall. The unsteady stall behaviour was characterised by large phase lags in the separation and reattachment of the viscous flow and, consequently, in the airloads. As can be seen, moment stall occurred quite abruptly when the boundary layer separated near maximum incidence. This event was followed by a negative contribution to the net aerodynamic pitch damping during the initial part of the downstroke where the greatest magnitude of pitching-moment coefficient was located. As a result, this regime was most susceptible to negative aerodynamic damping and, hence, stall flutter. This feature of dynamic stall is discussed in detail in Subsection 4.4.7. A large increase in drag was also observed.

The boundary layer remained attached at higher incidences than was the case under steady conditions, resulting in a large increase in the angle of attack at which there was a break in pitching-moment and in the lowest incidence of zero gradient on the normal force coefficient curve. This delay in boundary layer separation also enabled the magnitude of the normal force coefficient to be greater at the incidence of zero gradient than under steady conditions. When the normal coefficient gradient was negative, the influence of the dynamic stall vortex was first observed. The effect was revealed as a small disturbance in the three-dimensional pressure plots, but was much more clearly indicated in the normal

coefficient graph, where the gradient became positive again and reached a greater peak than at the earlier incidence of zero gradient. This phenomenon was not observed as being typical of the lift curve in the light stall regime by McCroskey et al : they found that the airloads were a direct extension of the static characteristics. However, their series of experiments was performed at a freestream Mach number of approximately 0.3. The consequence of the dynamic stall vortex which was observed in the series of experiments described in this dissertation was typical not only of all aerofoils which have been tested in the University of Glasgow's dynamic stall test rig but of low-Mach number experiments in general. The differences between data recorded at low Mach numbers and higher Mach numbers are well illustrated in, for example, the work of McALISTER ET AL [63]. The boundary between the two types of stall behaviour seems to be the air speed at which the greatest local Mach number becomes supersonic. For tests in which the maximum angle of attack was immediately greater than the incidence of dynamic stall onset, the effect of this phenomenon was not usually detectable, but, as the maximum incidence was increased, it became increasingly more distinct until, in the deep stall regime, it was most significant. In the light stall regime, the vortex was not observed until after the incidence had begun to decrease.

A typical set of data for the "deep dynamic stall regime" is illustrated in Figure 4.31, where the maximum incidence which was attained was 25.5°. In this regime,

which corresponds to the case of a fully-developed vortex, McCroskey et al described the qualitative results as being relatively independent of aerofoil geometry, Reynolds number and type of motion. The vortex was observed while the incidence was still increasing and its passage over the upper surface of the aerofoil resulted in each airload attaining values which were much greater in magnitude than those of their static counterparts. The shape and magnitude of the airloads' hysteresis loops changed dramatically from those observed in the other regimes. Although graphs of pitching moment coefficient against incidence appear to indicate that stall occurred least abruptly in the deep stall regime, this is a distortion resulting from the variation in pitch rate throughout the sinusoidal cycle. Examination of graphs of pitching-moment against non-dimensional time reveal that the abruptness of stall did not vary significantly through the stall regimes. This result supports the view that, once initiated, dynamic stall events can be regarded in terms of time constants which are independent of motion.

The dynamic stall vortex produced high drag, high lift and a negative pitching-moment coefficient which was large in magnitude. In addition to this greater lift, the vortex caused there to be a significant deviation in the gradient of the normal coefficient graph before the peak value was attained. As illustrated by McAlister et al, this phenomenon again seems to be much more pronounced at freestream velocities which are low enough for the local surface velocities to remain subsonic.

As the maximum incidence continued to be increased, the vortex strength increased, resulting in the greatest magnitude of each airload reaching larger values. As shown by the continuing variation of the hysteresis loops with increasing maximum incidence, the time histories of the aerodynamic coefficients and the phase in the cycle for boundary layer separation and reattachment also continued to change, and the formation and shedding of secondary vortices was clearly observed.

4.4.2 Influence of Reduced Frequency

Plots of the data resulting from experiments at an approximate mean incidence and amplitude of 13.5° and 8° respectively and reduced frequencies of 0.010, 0.102 and 0.151 are illustrated in Figures 4.33 - 4.35 respectively. Although the maximum incidence varied little between the experiments, it was observed that the aerofoil was more deeply in stall at the lowest oscillation frequency. In fact it was found that, as frequency was increased over its entire range in these experiments, so did the incidence which was required to be attained before entering each stall regime.

Comparisons between the tests illustrated in these figures show that the main differences are those between the experiment at a reduced frequency of 0.010 and those at the higher frequecies. Examination of the pressure

distributions reveals that the data recorded at the lowest frequency were most similar to those of the static test. One such characteristic was that, unlike the tests at higher frequencies, there was no evidence of the dynamic stall vortex. In addition, although, as in the static tests, at the low frequency the peak suction at the leading edge dropped in a two-step process, it collapsed completely at stall at the higher frequencies. The influence of the vortex also revealed itself at the higher frequencies in the deviation of the gradient of the normal coefficient graphs, resulting in a higher maximum value, and in the large maximum magnitudes of both pitching-moment coefficient and drag coefficient.

When considering the data over the entire range of mean incidence and reduced frequency at a Reynolds number of 1.5×10^6 and amplitude of between 8.0° and 8.5°, it can be seen that the results which are described above were typical of the oscillatory tests in general. The differences may be accounted for as being the consequence of the timing of events being dependent primarily on the freestream wind-speed. As a result, at greater oscillation frequencies, events such as separation occurred at higher incidences and, hence, the strength of the various loadings were greater in magnitude. In addition, it was observed that the maximum incidence which was required to be attained before entering each stall regime

increased as reduced frequency increased.

By examining the pressure distributions, it was seen that, in each stall regime, the peak suction at the leading edge increased with reduced frequency and that the suction did not collapse completely unless the reduced frequency was at least 0.05. Boundary-layer separation was progressively delayed as the frequency increased. It was not possible to witness a clear indication of the laminar separation bubble from pressure data. However, at reduced frequencies of 0.05 and greater, an irregularity in the smoothness of the pressure distribution in the neighbourhood of the eleventh transducer (see Figure 3.9) indicated that the dynamic stall vortex originated at approximately 27% chord. Its effect on the pressure distribution was clearly observed as it grew in strength and was shed downstream. As the frequency was increased, the influence of the vortex on the pressure distribution was first observed at a higher angle of attack and became much more pronounced, indicating that it grew in strength. Even at a reduced frequency of 0.025, in very deep stall with the maximum incidence of the order of 25°, there was, in addition to that resulting from trailing-edge boundary-layer separation, a very slight disturbance which would appear to indicate the presence of a weak vortex.

The influence of the dynamic stall vortex is also apparent in the graphs of normal force coefficient. With the exception, again, of the data recorded in the very deep stall regime at a reduced frequency of 0.025, there was no

deviation in the gradient of the normal coefficient graphs at reduced pitch-rates less than 0.05. However, as frequency was progressively increased from 0.05, this deviation in the gradient became more pronounced, indicating an increase in the strength of the vortex, and, as a result of the more abrupt and complete collapse of the peak suction at the leading edge of the aerofoil, the drop in the normal coefficient from its maximum value became more severe. Other than the characteristics which resulted from the presence of the dynamic stall vortex, there was no distinct variation with reduced frequency of the gradient of the normal coefficient graph. As a result of the delay in entering each stall regime as frequency increased, the trend was that there was an increase with frequency in the maximum value of the normal force coefficient attained in each regime.

Due to the increasing strength of the vortex, the maximum values of the pitching-moment and drag coefficients in the light- and deep-stall regimes increased with reduced frequency. In pre-stall conditions, however, there was little variation with frequency.

As described in Subsection 4.4.1, there is hysteresis in the integrated load traces. As would be expected, the degree of hysteresis increased as the oscillation frequency increased, particularly in the case of the pitching-moment coefficient trace.

4.4.3 Influence of Mean Angle of Attack and Amplitude

Because of the importance of the maximum angle of attack in determining the degree of separation, the mean incidence and amplitude cannot be considered as being completely independent of each other. It was shown in Subsection 4.4.1 that, when the mean angle of attack was progressively increased while the amplitude remained constant, the aerofoil travelled through all four stall regimes.

When the mean incidence remained constant and the amplitude was progressively increased, the significance of the maximum incidence was revealed again. Figure 4.36 illustrates the graphs of normal coefficient and piching-moment coefficient for four experiments in which the approximate values for mean incidence, reduced frequency and Reynolds number were 10.3°, 0.10 and 1.5×10^6 repectively. The amplitude was increased in steps of approximately 2° from 3.9° to 9.9°. As amplitude was increased, the data progressed from characteristics typical of the no-stall regime to stall onset at a maximum incidence of 17.9° and light stall for the highest maximum incidence plotted. All other characteristics at each reduced frequency were similar to those possessed in experiments at the same maximum incidence where mean varied and amplitude remained constant.

Figure 4.37 compares data from two tests at a reduced frequency of 0.10 in which the mean and amplitude differed

by 1° in such a way that the maximum incidence was approximately 24.5° in each test. The results were typical of data from tests in the deep stall regime and were very similar.

It can be shown that the maximum pitch rate during an oscillatory cycle is proportional to the product of the oscillation frequency and amplitude, and is not directly a function of the mean incidence. It is, therefore, interesting to compare data from experiments in which, although the amplitude and reduced frequency varied, the maximum pitch rates were approximately equal. Figure 4.38 plots data from three experiments in which the mean incidence was approximately 10.5°, the amplitude for each test was approximately 10.5°, 7.5° and 5.5° respectively, and the reduced frequency 0.051, 0.076 and 0.10 respectively. The results were again typical of those described in Subsection 4.4.1 : the characteristics seemed to be dependent on the maximum angle of attack and whether the incidence was increasing or decreasing when the dynamic stall vortex was formed (or if the vortex was formed at all). When the amplitude was 5.5°, the aerofoil did not attain an incidence which was large enough for the vortex to form. Increasing the amplitude to 7.5° resulted in the vortex-shedding phenomenon beginning only when the incidence was decreasing, and the characteristics were typical of light dynamic stall. Finally, when the amplitude was 10.5°, the vortex-shedding phenomenon began when incidence was increasing and the vortex was much stronger, as indicated by the significant deviation of the

gradient of the normal coefficient curve. As a result, the characteristics were typical of deep dynamic stall.

Another interesting comparison is illustrated in Figure 4.39. The parameters of the first test comprised mean, amplitude and reduced frequency of 11.1°, 10.5° and 0.126 respectively. For the second test, the parameters were 13.6°, 8.1° and 0.151 respectively. As Figure 4.39(a) illustrates, the incidence histories for these tests were very similar on the upper half of the cycle, where incidence was greater than that of static stall. In both experiments, the aerofoil experienced light dynamic stall. As the incidence increased towards the incidence of maximum normal force, the characteristics of the two tests were reasonably similar, but by no means identical : there was a distinct shift between the normal coefficient graphs on the upstroke. After forming at a similar angle of attack, the vortex grew more slowly and a lower maximum value of normal force coefficient was attained for the test with the larger amplitude and smaller reduced frequency. In unstalled conditions in the experiment in which the amplitude was larger, the data were very similar to those from the static test. It therefore seems possible that the differences were due, in the experiment in which the amplitude was smaller, to the minimum incidence not being low enough for fully-attached conditions to be restored. The pitching-moment traces were very similar : the traces on the upstroke were almost identical, as on the downstroke when the incidence was greater than the static stall incidence.

4.4.4 Influence of Reynolds Number

In the data presented by MCCROSKEY ET AL [64,67], it was revealed that, for each aerofoil, regardless of its low-Mach-number behaviour, there was a tendency towards leading-edge stall as the local Mach number grew to values greater than sonic conditions. No shock wave was detected with leading-edge supersonic flow. Over the range of tests discussed in the present dissertation, however, the local Mach number did not exceed a value of 0.7 and so the differences described in this section would seem to be a result of the effect of varying Reynolds number.

Data from experiments at Reynolds numbers of approximately 1.0×10^6 and 2.0×10^6 are plotted in Figures 4.40 - 4.43. In these experiments, the aerofoil was oscillated at a reduced frequency of 0.10, the amplitude was approximately 8.0° and the mean incidences were chosen to enable direct comparison with the graphs illustrated in Figures 4.30 and 4.31. It should be noted, however, that this section discusses the data from all the experiments at this amplitude and reduced frequency, and not just the data plotted in these figures. The trends were often an extension of the static characteristics which were discussed in Subsection 4.3.7.

It was observed that the maximum incidence which was required to be attained before entering each stall regime increased with increasing Reynolds number. As described in Subsection 4.3.7, this characteristic could have been a

result of the thicker boundary layer at lower Reynolds numbers encouraging separation at a lower incidence. The influence of aerofoil motion on separation characteristics is discussed in Section 4.5. As in steady conditions, the peak leading-edge suction increased as the Reynolds number increased and, at a reduced frequency of 0.10, the peak suction collapsed in one step at all Reynolds numbers. The indication from pressure traces of the dynamic stall vortex was first observed at the same chordwise location at all Reynolds numbers.

Comparing the traces of normal force coefficient reveals one very significant result : the influence of the vortex on the gradient of the normal coefficient graph was not as great at a Reynolds number of 2.0×10^6 as it was at the lower Reynolds numbers. This might at first be thought to indicate that the flow may have entered transonic conditions. However, as stated above, the greatest reading on any transducer corresponded to a local Mach number of less than 0.7. In addition, as will be seen in Section 4.5, during ramp tests in which the pitch-rate was greater than the maximum pitch-rate in any of the oscillatory tests, the greatest reading on any transducer corresponded to a local Mach number of closer to 0.8 and yet the influence of the vortex on the normal coefficient graph was similar to that in oscillatory experiments at the lower Reynolds numbers. It can also be observed from the pressure distributions that the characteristics were not typical of leading-edge stall.

It therefore seems likely that the problem lay elsewhere.

The time history of the normal coefficient resulting from the test which was illustrated in Figure 4.43 is plotted in Figure 4.44(a). This graph may be compared to the same test's dynamic pressure trace which is plotted in Figure 4.44(b). Superimposed on the dynamic pressure characteristics was an oscillatory function of approximately 15Hz, and the second peak of this graph coincided with the expected peak in the normal coefficient trace. As the data reduction process (see Subsection 3.3.6) involved dividing by the local dynamic pressure value, the effect of this dynamic pressure peak was to lower the maximum value of the normal coefficient. In addition, the trough between the first two peaks in the dynamic pressure graph increased the value which was calculated as the local normal coefficient at that time. This smaller peak is also illustrated in Figure 4.44(a). The influence of this variation in dynamic pressure on the airloads is illustrated in Figure 4.44(c), where, instead of the local value, the (constant) dynamic pressure reading which was used to determine the freestream velocity was employed in the calculation of the normal force coefficient. The resulting trace was much more similar to the characteristics of tests performed at the lower Reynolds numbers.

The reasons for this variation in the dynamic pressure are not, as yet, known and the problem must be investigated. For the purposes of this investigation,

however, it was decided to continue calculating the pressure coefficient values with the local dynamic pressure values : this seems to be the more conventional method of calculation, and, because the data from the experiments on the previously-tested aerofoils were calculated in this way, the comparisons with them are fairer. Only in the tests which were performed at a Reynolds number of 2.0×10^6 was the amplitude of oscillation in the dynamic pressure trace great enough to affect the values of the data significantly.

A consequence of this dependence of the pressure values on the position in the oscillatory cycle is that comparisons between similar experiments at different Reynolds numbers must be very arbitrary. The variation in magnitudes of airloads between tests at Reynolds numbers of 1.0×10^6 and 1.5×10^6 followed the trends which were set in steady conditions, but the tests at a Reynolds number of 2.0×10^6 did not. However, as was explained in Section 4.1, great caution must be taken when considering the magnitudes of the forces and so, in the present investigation, this problem may not be as serious as was feared. **This problem did not affect the incidences at which events relevant to this dissertation were observed.**

In the normal coefficient graphs, as in steady conditions, the maximum lift increased as the Reynolds number was increased from 1.0×10^6 to 1.5×10^6. As the Reynolds number increased over its full range, in another similarity to the static tests, there was a very slight

increase in the gradient of the normal coefficient graph, but, because of the problems involved in examining the behaviour around the position of maximum lift, it was not possible to compare fairly the rate at which the lift dropped.

Apart from the value of stall incidence, which is discussed in Subsection 4.4.6, the pitching-moment graphs differed negligibly : the magnitude of pitching-moment coefficient before incurring stall and at its maximum value, as well as the rate of stall, were all reasonably constant over the range of Reynolds numbers (although, for the reasons described above, the maximum magnitude decreased at a Reynolds number of 2.0×10^6). The drag characteristics were very similar in unstalled conditions. The maximum value increased as the Reynolds number was increased from 1.0×10^6 to 1.5×10^6, but, as was the case with the other airloads, decreased when the Reynolds number was increased further to 2.0×10^6. Because the reduced frequency was the same for all the tests, the degree of hysteresis did not vary significantly with Reynolds number.

4.4.5 Influence of Aerofoil Geometry

The unsteady characteristics resulting from oscillatory experiments on the NACA 23012C are now compared to those possessed by the NACA 23012 and NACA 23012A aerofoils. The experiments were performed at a Reynolds number, reduced frequency and amplitude of approximately

$1.5x10^6$, 0.10 and 8° respectively. Typical data for each aerofoil in each stall regime are illustrated in Figures 4.45 - 4.52. McCroskey et al found that, regardless of the static characteristics, all the aerofoils which they tested possessed trailing-edge separation characteristics. However, because all the aerofoils which are discussed in this dissertation possessed trailing-edge separation characteristics in steady conditions, it was not possible to examine this phenomenon.

As described in Subsection 4.4.1, dynamic stall onset represents the maximum stall-free lift which can be attained under unsteady conditions. A quantitative examination of a similar incidence over the entire range of reduced frequencies is discussed in detail in Subsection 4.4.6. The NACA 23012 and NACA 23012C aerofoils experienced a significant increase in the maximum value of the normal coefficient over that in steady conditions (Figures 4.46 and 4.29 respectively), with the increment being greater for the NACA 23012C. However, the maximum value for the NACA 23012A (Figure 4.50) differed negligibly from its static value : the incidence at which stall onset occurred was greater than the static stall incidence but a reduction in the gradient of the curve compensated for this. McCroskey et al claimed that the increments in lift are a direct consequence of the unsteady effects on boundary-layer separation characteristics.

In unstalled conditions, the degree of hysteresis was greatest for the NACA 23012C aerofoil. This appears to be

due to the NACA 23012C's more gentle pre-stall separation characteristics (illustrated for steady experiments in Figure 4.12) which resulted in a greater degree of separation being attained in unstalled conditions.

As in steady conditions, the angle of attack at which stall onset occurred was greatest for the NACA 23012C, with the NACA 23012A stalling at the lowest incidence. The difference between this incidence and that for static stall varied with aerofoil in a similar manner : approximately 3°, 2° and 0.5° for the NACA 23012C, NACA 23012 and NACA 23012A respectively. The reason for the large increment possessed by the NACA 23012C was also, as a result of its more gentle separation characteristics, the higher incidence which could be attained before the separation point suddenly moved forward.

As illustrated in Figures 4.29, 4.47 and 4.51, comparison of the data from experiments in which the maximum angle of attack was the same as the NACA 23012C's stall onset incidence reveals that the other two aerofoils possessed light stall characteristics. The maximum values of normal coefficient which were obtained by each aerofoil were very similar. Both the NACA 23012 and NACA 23012A aerofoils showed evidence of the dynamic stall vortex and typical trailing-edge separation characteristics.

Increasing the maximum incidence showed the NACA 23012C to be in the light stall regime (Figure 4.30). It also revealed evidence of the dynamic stall vortex and

typical trailing-edge separation characteristics. In all three cases, the maximum value of the normal force and magnitude of pitching-moment coefficients both occurred when the incidence was decreasing, supporting the theory that, once initiated, dynamic stall events proceed relatively independently of the motion of the aerofoil. The extra lift which was obtained from the vortex was greatest for the NACA 23012C, with the NACA 23012A showing only a slight increase. As was typical of all data recorded for these aerofoils, values of the pitching-moment coefficient differed in unstalled conditions. Otherwise, however, the graphs below each aerofoil's stall incidence were similar. The path from maximum to minimum value of pitching-moment coefficient was more gentle for the NACA 23012A. This may have been due to the shed vortex being stronger for the other aerofoils, as was indicated by the degree of deviation being greater in their normal coefficient graphs. NIVEN [73] claimed that the vortex-induced variation in the normal coefficient graph was less pronounced for the NACA 23012A because the dynamic-stall vortex coalesced with the effects of trailing-edge separation to create a more diffuse pressure wave. The rate of reattachment was similar for all the aerofoils. The first indication from the pressure coefficient graphs of vortex initiation on the three aerofoils was revealed by the adjacent transducers at 27% and 34% chord. The fact that the vortex was not detected until the light stall regime had been entered supports the opinion that vortex inception plays a fundamental role in the dynamic stall process.

When the mean incidence was increased further so that the maximum incidence was approximately 25°, all the aerofoils displayed characteristics which were typical of the deep stall regime. The characteristics of the three aerofoils were qualitatively similar, but there were differences in values. As in each of the other regimes, the maximum normal force attained by the NACA 23012C was greatest and that of the NACA 23012A smallest, with the additional lift resulting from the vortex and the incidence at which evidence of the vortex was first observed being ordered similarly.

Although the unstalled pitching-moment coefficient values were still offset by the amounts by which they were in steady conditions, the greatest magnitudes which were obtained after stall were very similar for all the aerofoils. The difference in the rates of pitching-moment break still existed but was less marked, in keeping with the fact that the influence of the dynamic stall vortex on the NACA 23012A's normal coefficient trace was more pronounced than in light stall but was still not as great as for the other aerofoils.

All three aerofoils now showed evidence of secondary vortices being shed. The peak leading-edge suction collapsed completely from its maximum value in one step rather than two. As described in Subsection 4.4.2, this did not occur at the lowest oscillation frequencies, and the lowest reduced frequency at which it did so was

approximately 0.05 for all aerofoils. The suction collapse did not occur until after vortex inception : indeed the vortex was already being shed downstream. As indicated by McCroskey et al, this indicated that the leading-edge bubble played no part in the dynamic stall process.

4.4.6 Calculation of Critical Angle

In Subsection 4.4.1, the incidence of stall onset for an aerofoil was defined as being the greatest maximum incidence through which it could be pitched without incurring moment stall. WILBY [91] reasoned that, in oscillatory conditions, aerofoil sections which exhibit the ability to attain high incidence values without involving a break in pitching moment would be beneficial to helicopter rotor performance. In order to calculate the maximum incidence to which an aerofoil could be pitched without incurring moment stall, he examined the data from a series of oscillatory experiments for which the mean angle of attack was methodically increased while the amplitude and reduced frequency were fixed at 8.5° and 0.10 respectively. For those tests in which the maximum incidence was sufficiently large for a break in pitching moment to be detected, the difference between the minimum value of pitching moment coefficient and its unstalled value was calculated. Extrapolating these differences to a value of zero yielded a clearly defined break point which indicated the maximum incidence which could be attained without

incurring moment stall. This incidence was termed the critical angle.

After pitching through the critical angle, a subsequent break in the pitching moment curve is unavoidable, since the stall process is no longer influenced by the motion of the aerofoil. This break need not occur immediately, and, if the aerofoil pitches through the critical angle at a high pitch-rate, it may be delayed significantly.

At the University of Glasgow, for a particular reduced frequency and Reynolds number, was performed a series of experiments over which the mean incidence was increased systematically and the amplitude was held approximately constant at a value of between 8.0° and 8.5°. The resulting data were used to calculate the critical angle for that reduced frequency, Reynolds number and aerofoil. The unstalled value of pitching-moment coefficient was defined to be the value at the maximum incidence in the test during which the greatest incidence was attained without pitching-moment stall being incurred. The extrapolation to a difference of zero was calculated by a suitable least-squares regression, as illustrated in Figure 4.53.

From those experiments which were performed at a Reynolds number of 1.5×10^6 the critical angle was calculated over a range of reduced frequencies for each aerofoil, and the results are plotted in Figure 4.54. At

any reduced frequency, the critical angle was greatest for the NACA 23012C and smallest for the NACA 23012A. This confirms the observation of the variation in incidence of pitching-moment break which is described in Subsection 4.4.5. Wilby described the difference between the stall incidence and zero-lift incidence as being the important angle for comparisons between aerofoils which are intended for use on helicopter rotor blades. With this in mind, the variation with reduced frequency of the difference between the critical angle and the zero-lift incidence is illustrated for each aerofoil in Figure 4.55. It can be seen that the differences which were illustrated in Figure 4.54 have been enhanced.

Wilby described how the critical angle could be regarded as the static stall incidence but that evidence at the time he was writing indicated that variation of oscillation frequency and amplitude combinations could result in variation of the critical angle. The data which are discussed in this dissertation showed negligible difference between the critical angle which was calculated in the manner described above and that which was calculated over a series of experiments in which the amplitude was approximately 2° larger. However, as has been illustrated in Figure 4.54, the critical angle did appear to be a function of reduced frequency. This would seem to contradict Wilby's opinion on the relationship between this angle and the static stall incidence if it were not for another of his observations. From a set of results which were similar to those described in Section 4.2, during his

series of quasi-static experiments, he detected flow separation at the junction between the model and the wind-tunnel wall as stall was approached. This reduced the effective incidence over the centre of the model with the result that the model attitude was no longer the true aerodynamic incidence. However, at higher frequencies, it was found that this end-separation was suppressed and conditions were much closer to two-dimensional flow. If, as Wilby suggests, the critical angle may be regarded as the static stall angle, then wind-tunnel effects may be causing its variation (i.e. it may be that the effective incidence is varying at the same rate as the critical angle of attack).

Unfortunately the test rig at the University of Glasgow is not, at present, equipped for flow visualistion of unsteady tests. However it may be possible to examine whether the flow behaves in the way described above by instrumenting the model with pressure transducers positioned across its span.

It is also possible that the variation is purely the result of the delay in the development of the boundary layer. If this is so, and bearing in mind what is written above, it may be possible to estimate the true (i.e. unconstrained or free-air) static stall incidence by extrapolating the critical values which were achieved at higher frequencies back to a reduced frequency of zero. In the case of these results (e.g. Figure 4.56), there is

very little difference from the recorded incidence for static moment stall.

As can be observed from Figure 4.57, the critical angle also varied with Reynolds number. This may be explained, as in Subsection 4.3.7, by the thicker boundary layer at lower Reynolds numbers encouraging separation at a lower incidence.

4.4.7 Aerodynamic Damping

TARZANIN [87] has described the aeroelastic self-excited pitching motion triggered by repeated submersion into and out of stall of a large portion of a helicopter blade which results in the existence of excessive torsional loads feeding into the control system. This phenomenon is commonly called stall flutter and is a consequence of attaining high angles of attack in order to achieve high gross weights and airspeeds. Strictly speaking, helicopter stall flutter occurs only in hover and does not become divergent. It does, however, cause extremely high loads which must be considered in the design of the rotor. In presenting his results, Tarzanin showed stall flutter to be fundamentally dependent on the dynamic stall delay. The relationship between aerodynamic damping and the hysteresis inherent in dynamic stall is also shown in Subsection 4.4.1 of this dissertation.

McCROSKEY ET AL [64,67] have described how each of the dynamic stall events described in Chapter One takes a finite amount of time to develop and, once initiated, tends to be relatively independent of aerofoil motion. As a result, there is lag and asymmetry of the airloads with respect to the motion of the body, producing the hysteresis illustrated in, for example, Figures 4.36 - 4.38.

Related to this point is the net aerodynamic work per cycle of oscillation, or "aerodynamic damping", and its relation to flutter. A measure of the aerodynamic damping for one complete cycle is provided by the pitch-damping parameter ζ, defined as

$$\zeta := -\oint C_m d\alpha / 4\alpha_a^2, \qquad (4.1)$$

where α is the angle of attack and α_a the amplitude of oscillation. The integral term in (4.1) represents the area inside the trace of the pitching-moment coefficient against incidence. It can be shown that the contribution to the pitch-damping parameter is positive from an anticlockwise loop of this trace and negative from a clockwise loop. If the pitch-damping parameter is negative (known as "negative damping"), the aerofoil extracts energy from the airstream, leading, if unrestrained, to the amplitude increasing and so to single-degree-of-freedom stall flutter of an elastic blade. This description and an examination of the pitching-moment coefficient graphs in each stall regime

(Figures 4.28 - 4.31) reveal that this stall flutter tends to occur when the aerofoil is oscillating into and out of stall. In such cases, if the contribution to the pitch-damping parameter from the clockwise loop is greater than the contribution from the anticlockwise loop(s), the oscillation becomes unstable unless restrained. Tarzanin described the blade response being naturally reduced by the reduction of negative damping, which occurs as the stall delay is reduced.

Plotted in Figure 4.58 is the variation of the pitch-damping parameter with maximum incidence for the NACA 23012C at each reduced frequency. In unstalled conditions, because the time-delay in the development of the boundary layer resulted in a greater single anticlockwise hysteresis loop, the pitch-damping parameter increased as reduced frequency increased. The traces show that in the light stall regime there was a decrease in the damping parameter, and it increased again in the deep stall regime.

The data from experiments performed in steady conditions (see Section 4.3) revealed that the boundary layer reattached at the leading edge of the aerofoil at an incidence approximately 2° lower than that at which it separated. This delay resulted in a small clockwise hysteresis loop at that position. Otherwise, there was negligible hysteresis. As described in Subsection 4.4.2, the data which were recorded at a reduced frequency of 0.010 were very similar to the data yielded by static

tests. Therefore, it follows that, at this frequency, the only significant contribution to the pitch-damping parameter came from a single clockwise hysteresis loop. Hence, for tests in which the aerofoil stalled, the pitch-damping parameter was negative. As the reduced frequency was increased, the delay in boundary layer development resulted in the existence of anticlockwise hysteresis loops which compensated for the effects of this clockwise loop and so the pitch-damping parameter remained positive over the complete range of maximum incidences. This remained the case until the reduced frequency reached a value of 0.151. This frequency was great enough for the delay in reattachment, which resulted from the finite amount of time required for the boundary layer to develop, to be of a large enough angle so that the anticlockwise loop was large enough for the pitch-damping parameter to become negative.

As demonstrated in Figures 4.59 and 4.60, these characteristics were typical of all three aerofoils. For both the NACA 23012C and the NACA 23012A, the pitch-damping parameter did not become negative again until the reduced frequency had reached a value of 0.130 for the NACA 23012A and 0.151 in the case of the NACA 23012C. However the NACA 23012 possessed regions of negative damping at all oscillation frequencies. This supports the observations of McCroskey et al and DADONE [28] who found that positive damping is favoured in conditions in which stall is gradual. To clarify this last point, a direct comparison at a reduced frequency of 0.10 is plotted in Figure 4.61.

The fact that negative damping is more likely at higher frequencies may also be related to the more abrupt stalling characteristics which are typical at such frequencies. At the higher frequencies, the maximum incidence did not reach high enough values for the second anticlockwise loop to appear in the pitching-moment coefficient trace and, as a result, there was no upturn in the pitch-damping parameter trace. With the exception of the experiments which were performed at a reduced frequency of 0.01 (and have been considered above), the incidence at which a particular aerofoil entered the domain of instability was approximately the same at any reduced frequency : 21° for the NACA 23012C; 18° for the NACA 23012; 18° for the NACA 23012A. At the higher frequencies, there was a brief upturn in the NACA 23012C graph. It appeared that, at these frequencies, the secondary vortex was strong enough to modify the anticlockwise loop of the pitching-moment coefficient graph by making its area slightly larger.

Figure 4.62 shows that, at a reduced frequency of 0.10, there was little influence of Reynolds number on the aerodynamic damping.

4.5 CONSTANT PITCH-RATE RAMP EXPERIMENTS

The data which were recorded from oscillatory experiments and described in the previous section were shown to be greatly dependent on the oscillation frequency. This fact, along with the influence of the other parameters, implied that a significant influence on the aerodynamic behaviour was imposed by the pitch-rate. In particular, the behaviour seemed to be dependent on the pitch-rate at the incidences of static stall and dynamic stall onset. However, the oscillatory experiments were characterised by variable pitch-rate. As a result, the onset of stall could be influenced by the pitch-rate of the aerofoil decreasing at that point of the cycle.

In order that the influence of pitch-rate could be investigated systematically, it was decided to perform a series of experiments in which the aerofoil was pitched about its quarter-chord axis at a constant rate. As was decribed in Subsection 3.3.5, in these "ramp" tests the aerofoil was pitched over a large arc at a constant rate and then held at the maximum incidence to allow the flow to relax to the steady condition.

Figure 4.63 illustrates the variation of incidence with non-dimensional time during an experiment in which the pitch-rate reached a steady value of approximately $290^{o}s^{-1}$. Although the pitch-rate was relatively constant for much of the experiment, there were regions of acceleration and deceleration at the beginning and end of

the motion respectively. However, the aerofoil was pitching at a constant rate before reaching the incidence at which trailing-edge separation was initiated in steady conditions. In addition, stall onset and other events of interest had occurred before the deceleration of the aerofoil became significant. SETO [82] considered thoroughly the influence of the non-linearity of the motion. Based on his investigation, it was decided that a ramp from -1° to 40° was ideal for analysing the influence of pitch-rate and that the linear pitch-rate which was achieved during the experiment should be determined from linear interpolation between 25% and 50% of the aerofoil's incidence range.

This section discusses the data which resulted from these ramps. Subsections 4.5.1 - 4.5.5 consider the experiments in which the pitch-rate was greater than zero. The influence of pitch-rate, Reynolds number and aerofoil geometry are examined in Subsections 4.5.1 - 4.5.3 respectively. Subsection 4.5.4 describes the criterion which is used to determine if dynamic stall has been initiated and the timing of dynamic stall events is discussed in Subsection 4.5.5. The general characteristics of experiments in which the pitch-rate was negative are outlined briefly in Subsection 4.5.6.

As in Section 4.4, the data from static experiments are illustrated by a broken line in the figures which are comprised of several graphs.

4.5.1 Influence of Pitch-rate

The dynamic stall characteristics of experiments performed on the NACA 23012C at a Reynolds number of 1.5×10^6 and five different pitch-rates are illustrated in Figures 4.64 - 4.68. At low pitch-rates (e.g. at a reduced pitch-rate of 0.002 in Figure 4.64), the normal coefficient gradient and the characteristics of pitching-moment and drag were qualitatively similar to those yielded by experiments in steady conditions. In particular, there was no evidence of the dynamic stall vortex, and the leading-edge suction collapsed in two steps. The data differed from those in steady conditions, however, in that the attached flow behaviour was extended to higher angles of attack. This behaviour was very similar to that revealed in the characteristics produced during oscillatory tests of high mean incidence and reduced frequency smaller than 0.05. Such characteristics are typical of the "quasi-static" stall regime, as described by SETO AND GALBRAITH [84].

During the experiments in which the pitch-rate was higher, the data was characteristic of Seto and Galbraith's "dynamic stall" regime, in which the dynamic stall vortex was evident and played a significant role in the stall process. Examination of the individual pressure traces indicates that the vortex was initiated in the region around 27% chord, as it did in the oscillatory experiments. Indeed, the data in this regime corresponded to those resulting from deep-stall oscillatory tests in which the

reduced frequency was greater than 0.025.

Over the range of tests in the dynamic stall regime the results were qualitatively very similar, but magnitudes varied progressively with all effects being enhanced by increasing the reduced pitch-rate. In attached flow, the characteristics were very similar in shape to those in the quasi-static regime except for the fact that the magnitudes of pressure coefficient and, hence, the integrated loads lagged behind the equivalent static and quasi-static values. As the angle of attack increased beyond the static stall value, the pressure distribution remained typical of attached-flow conditions and suction exceeded that in steady conditions. A further increase in incidence resulted in the aerofoil stalling. This was revealed over the front of the aerofoil as a pressure disturbance which, having originated at the 27% chord location, grew with time and convected downstream over the upper surface, creating strong suction peaks at each chordwise location as it did so. Seto and Galbraith noted that there was an inrush of air over the upper surface subsequent to the vortex being shed from the trailing-edge. It seems that, in a similar manner, this pressure wave initiated a secondary vortex which was observed as a weaker series of suction peaks. Several secondary vortices were detected. The strength of these vortices seemed to be related to the strength of the original dynamic stall vortex.

Once the aerofoil settled at its maximum incidence,

the separation characteristics became typical of a bluff body wake, with the boundary layer separating on the upper surface from the leading edge.

SCRUGGS ET AL [80] described how, in unsteady flow, boundary-layer separation and flow reversal are, in general, distinct phenomena. Reversal was described as referring to conditions at the inner part of the boundary layer, adjacent to the aerofoil surface, and its onset as corresponding to the wall shear stress vanishing. However, separation was described as the detachment of the outer flow from the aerofoil contour and characterised as the breakdown of the boundary-layer equations. By referring to the work of SEARS AND TELIONIS [81], it was suggested that separation would always occur later than reversal. The theoretically-based research of Scruggs et al predicted that the movement of the reversal point was delayed as reduced pitch-rate increased. This prediction has been supported by experimental investigations of the boundary layer (e.g. LEISHMAN [55], SETO [82] and NIVEN [73]).

By examining the root mean square variation in pressure between cycles of unaveraged data, LORBER AND CARTA [61] observed boundary layer turbulence. It was hoped that a similar indication may have been detected from the University of Glasgow data by means of the standard deviations of the pressure coefficient traces. Unfortunately, as can be seen in Figure 4.69, the only significant difference in the standard deviation occurred

at all transducer locations relatively simultaneously when the leading-edge suction collapsed.

When examining pressure coefficient distributions, it is not possible to detect flow reversal but it seems from the experimental analysis referred to above that the separation characteristics showed qualitatively similar trends. Figure 4.70 compares separation characteristics for the NACA 23012C during a static experiment and a ramp at a reduced pitch-rate of 0.034. It can be seen that the incidence at which the boundary layer separated at any chord location was significantly higher during the ramp. This incidence delay was found to increase with pitch-rate. However, after the dynamic stall vortex had been initiated, it became increasingly difficult to detect the separation point in the unsteady characteristics. It was therefore very difficult to determine the characteristics as the separation point moved closer to the leading edge. It was clear however that the rate of change of separation point with incidence was decreasing as reduced pitch-rate increased. Niven also found this to be a property of flow reversal. However, the drop in the coefficient of normal force at stall became more sudden as pitch-rate increased. Therefore, once boundary-layer separation has been initiated, it may not be the most significant factor in the dynamic stall process. It may be that the timing of the growth and shedding of the vortex is more influential.

This more sudden drop in the normal coefficient curve as pitch-rate was increased is illustrated in Figure 4.71.

The normal force coefficient is plotted in Figure 4.71(a) against angle of attack and in Figure 4.71(b) against non-dimensional time defined in chordlengths of travel. In this second graph the reference time has been defined in order that the lowest incidence of zero gradient occurred at the same non-dimensional time at each pitch-rate. It can be seen that the incidence to which events were delayed by pitch-rate was increased as reduced pitch-rate increased, and, as a result, the maximum value of normal force coefficient to be attained increased with reduced pitch-rate. All these characteristics were typical of those which were produced from oscillatory experiments as reduced frequency increased. Although the gradients of these curves were seen to be lower than the gradient of the the corresponding curve in steady conditions, it was difficult to see any other significant variation in gradient with pitch-rate. The range of frequencies over which the oscillatory experiments were performed also failed to reveal such a variation. It is, however, widely accepted that this gradient decreases with increasing pitch-rate (see, for example, BEDDOES [15]). Another characteristic of the normal force coefficient which was similar to the data from oscillatory experiments was that, while there was no deviation in the gradient of the curve in the quasi-static regime, at higher pitch-rates the incidence and degree of deviation increased with reduced pitch-rate, as did the incidence and magnitude of the force at the lowest incidence of zero gradient.

The variation of pitching-moment characteristics with

reduced pitch-rate also revealed many similarities to their variation with reduced frequency in oscillatory experiments. As a result of the dynamic stall vortex growing in strength as pitch-rate increased, the greatest magnitude of pitching-moment coefficient also increased with reduced pitch-rate. The pitching-moment coefficient traces for three different pitch-rates at a Reynolds number of 1.5×10^6 are compared in Figure 4.72. As a result of the delay in separation, the pitching-moment break was also delayed to higher angles of attack as reduced pitch-rate increased. The rate of stall with respect to non-dimensional time did not vary significantly, but the magnitude of pitching-moment coefficient increased as reduced pitch-rate increased. This feature was detected even when there was no boundary-layer separation. Figure 4.73 plots the pressure coefficient distributions for these three ramps at an incidence of approximately 10°. As can be seen, the only significant differences occurred at the leading edge where the growth of peak suction was increasingly delayed as pitch-rate increased and on the lower surface over the trailing 75% chord where pressure increased with pitch rate. This latter property would seem to have been a direct consequence of momentum theory. These phenomena combined to increase the magnitude of pitching-moment in the negative direction as demonstrated in Figure 4.72.

As in the oscillatory experiments, there was little variation in drag with reduced pitch before stall and, as a result of the increasing strength of the dynamic stall

vortex, the maximum value of drag increased with reduced pitch-rate.

It can be seen from Figures 4.65 - 4.72 that, on reaching the maximum incidence, the loadings were subject to oscillatory variations. This was the result of bluff-body vortex shedding. Due to the effect of averaging after stall had occurred, as described in Section 4.1, these events were not exactly in phase as reduced pitch-rate varied (Figures 4.71(b), 4.72(b)). However, it may be calculated that the Strouhal number was approximately 0.3 in all cases, as it was for all the other aerofoils whose data from experiments in this tunnel have been examined.

4.5.2 Influence of Reynolds Number

It was discovered that at Reynolds numbers of approximately 1.0×10^6 and 2.0×10^6 the variation of dynamic stall characteristics with reduced pitch-rate was seen to be qualitatively similar to that at a Reynolds number of approximately 1.5×10^6. As in oscillatory experiments, the trends were often extensions of the static characteristics. Data from experiments in which the reduced pitch-rate was approximately 0.016 or 0.017 and the Reynolds numbers were 1.00×10^6, 1.47×10^6 and 1.92×10^6 are plotted plotted in Figures 4.74, 4.75 and 4.76 respectively. As was also observed in the data from the static and oscillatory experiments, there were no significant compressibility

effects : the greatest local Mach number was less than 0.8.

The pressure coefficient distributions at approximately 14° for the experiments described above are compared in Figure 4.77. Comparing these data with those described in Subsection 4.3.7 and plotted in Figure 4.25 reveals many similar characteristics : no more than a very slight increase in peak suction with increasing Reynolds number and, in general, a similar variation with Reynolds number over the remainder of the aerofoil on both the upper and lower surfaces. It was not possible from pressure traces, however, to detect any variation of boundary-layer separation points with Reynolds number. It is possible that more could be gleaned from boundary-layer experiments such as flow visualisation or experiments with hot films.

The normal coefficient characteristics for these three experiments are compared in Figure 4.78. Before examining the graphs, however, it is necessary to consider the influence on these characteristics of the variation in dynamic pressure. In Subsection 4.4.4 (Figure 4.44), it was shown that an oscillatory function which was superimposed on the dynamic pressure trace had distorted the normal coefficient characteristics. The variation of dynamic pressure with incidence at each of the three Reynolds numbers is plotted in Figure 4.79. It can be seen that, although this superimposed function was not present in ramp experiments, there was a large amount of deviation after the aerofoil had stalled. However, if Figure 4.78 is compared to Figure 4.80, in which the normal

coefficient was calculated from the (constant) value of dynamic pressure which was used to determine the Reynolds number at which the experiment was performed, it can be seen that this variation in dynamic pressure did not significantly distort the normal coefficient characteristics until after the gradient of the trace had first become zero. Therefore, within the area of interest, it is possible to determine the normal force coefficient from the local value of dynamic pressure.

There was very little variation in the normal force coefficient with Reynolds number. The behaviour of the characteristics was very similar to that displayed in the oscillatory experiments. The earliest peak value for the normal coefficient was lower at a Reynolds number of 1.00×10^6 than at the higher Reynolds numbers. However, as explained in Section 4.1, because of the effect of averaging the data taken from discrete readings, care must be taken not to place too much emphasis on the magnitudes of forces which were yielded in these experiments. This feature could account for the fact that the peak did not increase with Reynolds number as it had in steady conditions. It can also be seen that in unstalled conditions the gradient of the normal coefficient trace increased very slightly with Reynolds number. The incidence at which there was a deviation in this gradient was lower at a Reynolds number of 1.00×10^6 than at the higher Reynolds numbers. The variation with Reynolds number of the incidence at which the vortex was formed, which is related to this property, is discussed in

Chapter Five.

The pitching-moment coefficient traces are compared in Figure 4.81. These traces were very similar in unstalled conditions and the rate of stall was also very similar. However, the incidence at which stall occurred increased as Reynolds number increased. This may have been an extension of the case described in Subsection 4.4.6, where critical angle was observed to increase with Reynolds number. In addition, the greatest magnitude of pitching moment increased with Reynolds number. However, because of the effects of averaging which have been discussed above and the fact that the fluctuations in dynamic pressure had become significant at such positions in the stall process, this property could not be examined precisely.

The drag characteristics and rate of bluff-body vortex shedding did not vary significantly with Reynolds number.

4.5.3 Influence of Aerofoil Geometry

The trends revealed by the NACA 23012C aerofoil over the range of reduced pitch-rates through which it was rotated were qualitatively similar to those experienced by the NACA 23012 and NACA 23012A aerofoils. Typical data for each of these aerofoils at a Reynolds number of 1.5×10^6 are plotted in Figures 4.82 - 4.85, and may be compared

directly with the data illustrated in Figures 4.65 and 4.67.

The separation characteristics which were determined from the pressure distributions at a reduced pitch-rate of 0.034 are compared in Figure 4.86. If this graph is compared to Figure 4.12, it can be seen that, in relation to each other, they were qualitatively similar in both steady and unsteady conditions, but that the incidence of separation at each chord location was much higher for each aerofoil in unsteady conditions. It is clear, however, that the NACA 23012 experienced a much more rapid forward movement of the separation point after the flow had remained fully attached to a higher incidence than either of the modified aerofoils. The NACA 23012A began to separate at the trailing-edge at a much lower incidence and at a much more gentle rate than either of the other aerofoils. However, after it had begun to separate significantly, the NACA 23012C's separation point moved at approximately the same rate as that for the NACA 23012A. All these characteristics were also typical of data from experiments in steady conditions.

The aerofoils' normal force coefficient characteristics at a reduced pitch-rate of between 0.023 and 0.024 are compared in Figure 4.87. The NACA 23012C was again found to have experienced the greatest force in the normal direction. The incidences at which this maximum value was attained and at which the gradient deviated were both greatest for the NACA 23012C. The

incidences of zero lift varied negligibly from their static values. All these characteristics were also typical of static and oscillatory experiments.

The pitching-moment coefficient traces are compared in Figure 4.88. The values in unstalled conditions were approximately the same as in steady conditions, and the incidences at which the pitching-moment curve broke increased with aerofoil in qualitatively the same manner as in the static experiments. As in oscillatory experiments, this break was much more gentle for the NACA 23012A than the other aerofoils and this could be associated with the fact that the deviation in the normal coefficient gradient was much more gentle for this aerofoil. This fact again indicates that the growth in strength of the dynamic stall vortex is significant in determining the rate of stall. The magnitude of pitching-moment after stall, particularly under the influence of the secondary vortices, was seen to be greatest for the NACA 23012C. This may have been a result of the stronger aerodynamic forces achieved when attaining extra lift. This supports the view (e.g. BEDDOES [16]) that the benefits, such as additional lift, which are yielded under dynamic stall conditions are transient and the enduring consequences of incurring dynamic stall are counter-productive. Therefore, to obtain the benefits of unsteady conditions, the aerofoil must perform in the incidence range between static stall and dynamic stall onset. The greater strength of the secondary vortices for the NACA 23012C are also clearly displayed in the normal force coefficient traces and in the

greater magnitude of drag which was created after stall was incurred.

It can be seen in Figures 4.87(b) and 4.88(b) that, having taken into consideration the inaccuracies of the averaging process, the rate of bluff body vortex shedding was very similar for the three aerofoils.

4.5.4 An Indication of Dynamic Stall Onset for Aerofoils Experiencing Trailing Edge Stall at Low Mach Numbers

In recent years, several methods have been employed to assess the timing of incipient dynamic stall. Some of these methods have involved the examination of airloads. Figure 4.89 illustrates the familiar characteristic time-dependent airloads which are associated with dynamic stall, and suggests possible locations which indicate the initiation of that process.

One such method was that of BEDDOES [12], who, by examining the results of 142 sets of experimental data, concluded that each dynamic stall event is governed by a distinct universal non-dimensional time constant, regardless of the time history of the motion. In particular, it was suggested that a time constant exists between the aerofoil pitching through the static stall incidence and experiencing both moment stall and maximum lift. The static stall incidence was defined as being the angle of attack at which there was an abrupt drop in the

pitching-moment curve.

WILBY [91] reasoned that aerofoil sections which, in oscillatory conditions, exhibit the ability to attain high incidence values without involving a break in pitching-moment would be beneficial to helicopter rotor performance. In order to calculate the maximum incidence to which an aerofoil could be pitched without occurring moment stall, he examined the data from a series of oscillatory tests for which the mean incidence was steadily increased. He then defined a critical angle of attack which was described and discussed in Subsection 4.4.6. This critical angle can only be calculated from oscillatory data. In order to investigate the dynamic overshoot of several new R.A.E. blade sections, he found it necessary, for ramp experiments, to define dynamic stall as occurring at the angle of attack where the coefficient of pitching moment had fallen by 0.05 from its maximum pre-stall value.

When analysing CARTA ET AL's [23] experimental data, SCRUGGS ET AL [80] defined dynamic stall onset as occurring at the incidence, on the upstroke, at which there is a sudden deviation in the gradient of the lift curve.

In the present procedure which has been described in Chapter Three, the airloads were calculated by suitably integrating the recorded pressure coefficient values around the aerofoil. As a consequence of this integration, early indications of incipient stall may be disguised or hidden : during vortex initiation it is likely that the formation of

any localised disturbance within the boundary layer would be indicated immediately by the response of the local pressure coefficient, whereas the integrated airloads would de-sensitise the inception point. It was, therefore, decided that the onset of stall should be examined in relation to individual pressure traces.

A number of such methods have been employed by other researchers. Indeed, the stall criteria which are described above have been modified to include the determination of stall from local pressure values.

WILBY [92] employed ramp data which were recorded at a freestream Mach number of 0.3 to investigate the effect of pitch-rate on an aerofoil's dynamic stall behaviour. He defined the stall incidence to be the angle of attack at which the pressure coefficient at 0.5% chord was at a minimum. It was observed that this was more clearly defined than a pitching-moment break.

BEDDOES [13] postulated that, under fully unsteady conditions, dynamic stall is triggered at the leading edge. As a result, to calculate an idealised static stall incidence, he employed EVANS AND MORT's [32] correlation in which aerofoils are assumed to experience leading-edge stall by the reseparation mechanism. This incidence is that at which the leading-edge becomes critical, and is calculated theoretically by suppressing all trailing-edge separation. It follows that, for aerofoils which experience leading-edge stall, this incidence is very close

to that of static stall. The dynamic stall onset incidence is then determined as the angle of attack which the aerofoil reaches after the expiry of the relevant non-dimensional time delay since pitching through the afore-mentioned equivalent static stall incidence. This static stall incidence is used for low Mach number cases in the latest version of Beddoes's algorithm, which has been described by LEISHMAN AND BEDDOES [56] and is discussed in Subsection 4.5.5.

DALEY AND JUMPER [29] performed a series of experiments in constant freestream flow over a Reynolds number range between 78300 and 301000. The aerofoil was pitched at a constant rate about its mid-chord axis. Stall was arbitrarily defined to occur at the incidence where the boundary layer separated at the quarter-chord. Smoke-flow visualisation and pressure data were used to determine this location.

Having displayed the pressure coefficient histories of their data in the manner described by CARTA [22], McCROSKEY ET AL [65,67] found that, while a thin layer of reversed flow on the rear half of the aerofoil was moving forward, a major boundary layer disturbance and vortex erupted out of the leading-edge region. Only later did these two distinct disturbances appear to meet at approximately mid-chord. These experiments revealed that the disturbances originated at approximately 25% chord and spread upstream and downstream from that general area.

SETO AND GALBRAITH [84] found similar results when testing a NACA 23012 aerofoil in the manner described in Chapter Three. These results were supported with experiments which were performed by SETO [82] and NIVEN [73] with hot-film gauges. Based on these results, Seto and Galbraith established a criterion for indicating that the stall process had been initiated. This criterion has been employed in the present analysis to locate the lowest incidence at which it is observed that stall onset has occurred, and is described in the remainder of this subsection.

Typical data from static and ramp tests have been described earlier in this chapter. It was noted that the ramp data could be divided into two regimes. At low reduced pitch-rates, where the characteristics are qualitatively similar to those in steady conditions with significant lift and moment overshoot, the response is labelled "quasi-static". The limit to this regime was observed to be at a reduced pitch-rate of 0.01. At higher reduced pitch-rates, the dynamic stall vortex plays a significant part in the stall process and the response is associated with "dynamic" stall.

Figure 4.90 illustrates, in the manner of Carta, the variation with non-dimensional time of the pressure coefficient at each transducer location over the upper surface. The first indication that the vortex which is associated with dynamic stall had been initiated was when a deviation in the gradient of one of the pressure

coefficient traces was observed. The incidence at which this deviation occurred was defined as being the incidence of intersection between two straight lines which had been determined from linear regression through data points before and after stall onset, as illustrated in Figure 4.91. The presence of this deviation in pressure coefficient distinguishes dynamic stall from quasi-static stall. The fact that the deviation is initially so small reveals why it is regarded as being more accurate to examine individual pressure traces than integrated airloads. Hereafter, this response will be referred to as C_p deviation.

The transducer location of the first C_p deviation was found to vary with aerofoil. Over the range of aerofoils for which results are discussed in this dissertation, this location was found to be between 25% and 60% chord. The reason for it occurring at a particular location on any aerofoil has not yet been determined. For the NACA 23012C aerofoil, C_p deviation occurred at 27% chord.

Illustrated in Figure 4.92 is the variation of C_p deviation with reduced pitch-rate for the NACA 23012C aerofoil. Using the current procedures and definitions of incipient dynamic stall, this C_p deviation (and its associated incidence) is the earliest indication which can be observed from the examination of the pressure histories that a consequence of dynamic stall which cannot be reversed has occurred. Evidence discussed by NIVEN [74] shows that this is not the stall trigger, but it is the

earliest indication which can be observed from experimental data based on pressure readings. A comparison in Figure 4.92 between this lowest angle of attack at which the vortex is detected and the angle of peak suction collapse confirms that the former did occur first for the NACA 23012C. However, in the quasi-static region, no vortex is formed and so it is necessary to determine the earliest indication of stall by a different method. In this case, the earliest indication was taken to be the collapse of the peak suction at the leading edge.

It should be stressed that the analysis which has been discussed above has only been performed on aerofoils experiencing trailing-edge stall at low Mach numbers (i.e. all local Mach numbers smaller than 0.8). Therefore, these results may only be typical of such cases.

The calculations which have been described in this subsection were performed on data from ramps. It is also possible to determine the incidence of C_p deviation from oscillatory experiments. The variation of this incidence with reduced frequency is illustrated in Figure 4.93. This figure also displays over the same range of reduced frequencies the critical angle which was defined by WILBY [91] and described in Subsection 4.4.6. It can be seen that the critical angle occurred before C_p deviation at all reduced frequencies. Therefore C_p deviation is not the earliest indication that the stall process has been initiated and cannot be reversed. However, the critical angle can only be determined from oscillatory data. For a

general type of motion, the C_p deviation is the earliest such indication of stall onset that has been observed from these data. It is, however, necessary to find an angle of attack, equivalent to the critical angle, which would indicate stall onset for any type of motion.

It was hoped that it would be possible, by correlating the oscillatory and ramp data via some parameter, to show this incidence to be independent of the type of motion. One such parameter yielded a far better correlation than all the others which were examined. Although involving a slight amount of subjective analysis, it may be defined in the following manner. If the mean incidence of the oscillatory cycle is chosen so that the pitch-rate through the incidence at which stall onset is deemed to to have occurred is still greater than zero and is not significantly lower than the maximum pitch-rate in the cycle then the maximum reduced pitch-rate which the aerofoil experiences in the cycle should be used as the parameter to represent each experiment. As illustrated in Figure 4.63, it should be remembered that, although nominally constant in such experiments, the pitch-rate varies during a ramp as well as an oscillatory cycle. This procedure was followed in order that the data for the aerofoils at the University of Glasgow could be correlated. The variation of the incidence of C_p deviation with maximum reduced pitch-rate for the NACA 23012C is illustrated in Figure 4.94. The amplitude of the oscillatory cycles and ramp arcs were approximately 8.5° and 41° respectively. In order to calculate the pitch-rate at each sweep the

angular transducer readings were filtered by taking the local average of three consecutive sweeps.

Plotting the incidence of C_p deviation against maximum reduced pitch-rate yielded similar results for all types of motions. At the University of Glasgow a number of experiments have been performed in order to study the behaviour of large-scale vertical-axis wind-turbines (see, for example ANGELL ET AL [5,8,11]). In a typical oscillation, a symmetrical aerofoil is pitched about an incidence of zero under a type of motion in which the pitch-rate on the upstroke differs from that on the downstroke. Figure 4.95 plots for the NACA 0015 aerofoil the magnitude of the incidence of C_p deviation against maximum pitch-rate for each half-cycle. The deviations on the downstroke occurred at negative angles of attack. A satisfactory correlation was again achieved.

The variation of the incidence of C_p deviation with reduced pitch-rate was a function of Reynolds number and aerofoil geometry. This behaviour is discussed in Chapter Five.

4.5.5 Timing of Dynamic Stall Events

For the NACA 23012C aerofoil at a reduced pitch-rate of 0.024, Figure 4.96 plots the variation with non-dimensional time, in the form of chordlengths of travel, of the coefficients of normal force,

pitching-moment about quarter-chord and pressure at the leading-edge, trailing-edge and 27% chord location. Several features can be observed. There was a distinct and steady increase with non-dimensional time in normal force, the magnitude of pitching-moment and leading-edge suction over the initial period of the ramp. After the boundary layer had begun to separate and the dynamic stall vortex had been initiated, the first indication of the influence of this vortex was revealed as a deviation of the pressure coefficient trace at the 27% chord location. As the motion continued, and the vortex grew in strength, there was a deviation in the gradient of the normal force coefficient trace. The suction at the leading edge then collapsed and the dynamic stall vortex was shed downstream. As the vortex moved towards the trailing-edge, each pressure transducer in succession registered a peak in the suction at its location, and the magnitude of pitching-moment at first increased and then was reduced. The maximum magnitudes of the coefficients of normal force and pitching-moment were attained while the vortex was being shed downstream.

The sequence of events described above summarises the dynamic stall process. However, if this process were to be modelled, it would be necessary to determine the time taken between each incident. Five important angles of attack which are easily measurable are those at which occur static stall, C_p deviation as described in Subsection 4.5.4, the maximum value of peak suction at the leading-edge, initiation of vortex shedding from the

location of its inception and the release of the dynamic stall vortex from the trailing-edge. The incidences at which these events occurred during the experiment described above are superimposed on distributions of the coefficients of normal force and pitching-moment in Figure 4.97. It was hoped that the dynamic stall process could be broken into a series of smaller subprocesses which were each related simply to or independent of the reduced pitch-rate of the aerofoil.

It has been claimed in the past (see, for example, McCROSKEY [64]) that each dynamic stall event takes a finite amount of time to develop and, once initiated, tends to be independent of aerofoil motion. Figure 4.98 illustrates the variation with reduced pitch-rate of the non-dimensional time which passed between the occurence of the events listed in the previous paragraph. It can be seen that these non-dimensional time delays were not in general independent of aerofoil motion. The delays between C_p deviation and both the shedding downstream of the dynamic stall vortex from that chord location and the maximum peak suction being attained at the leading edge were not constant. This property may have been related to the fact that the vortex seemed to grow in strength as reduced pitch-rate increased but that the rate of growth was relatively independent of aerofoil motion. This latter claim would seem to be supported by the fact that the trace of C_p deviation against reduced pitch-rate was observed to be approximately linear for all the aerofoils discussed in this dissertation, and, hence, the gradient

did not vary significantly with reduced pitch-rate. After making allowance for the errors, which have been discussed in detail in earlier passages of this chapter, involved in recording the data and determining values for events during data analysis, all subsequent non-dimensional time-delays were relatively independent of reduced pitch-rate. The non-dimensional time taken for the vortex to move downstream to any location, as indicated by suction peaks at each transducer, was observed to be independent of reduced pitch-rate. It can, therefore, be seen that, once C_p deviation was observed, the dynamic stall vortex grew in strength in proportion to the reduced pitch-rate for a non-dimensional time which was a linear function of reduced pitch-rate and was then shed downstream at a velocity which was independent of aerofoil motion.

It was also observed that the time which elapsed between passing through the static stall incidence and each of the other events occurring was not independent of pitch-rate. In particular, the delay between reaching the static stall incidence and the C_p deviation being observed was a linear function of the inverse of reduced pitch-rate.

After examining the relationship between static stall and dynamic stall in 142 test cases, BEDDOES [12] observed no significant dependence on the parameters of reduced frequency, pitch-rate, mean angle of attack, amplitude, Mach number or aerofoil geometry, whether the aerofoil was pitching or plunging. He found the mean non-dimensional time-delay between moment break in static and dynamic

conditions to be 2.44 with a standard deviation of 0.49. It was subsequently discovered [13], however, that, as a result of combinations of Mach number and aerofoil geometry for which the static stall data exhibited the characteristics of trailing-edge separation, this delay was being underestimated for less conventional aerofoils. He therefore superseded his previous definition of stall with a criterion, based on the correlation of EVANS AND MORT [32], in which dynamic stall is triggered at the leading edge. This criterion has been described in Subsection 4.5.4 and is used for low Mach number cases in the latest version of Beddoes's algorithm, as described by LEISHMAN AND BEDDOES [56]. The dynamic stall onset incidence is determined as the angle through which the aerofoil pitches after the expiry of the relevant non-dimensional time delay since pitching through this equivalent static stall incidence.

In practice, a critical normal force coefficient value C_{n_1}, associated with the incidence at which the leading-edge pressure criterion is invoked, denotes dynamic stall onset. From unsteady aerofoil tests, Beddoes has observed that, under nominally attached flow conditions, there is a lag in the leading-edge pressures with respect to the instantaneous normal force. He illustrated that the simplest representation of this behaviour was via a first order lag with a Mach-number dependent time constant T_p. As a result, it is possible to relate the pressure in the unsteady flow to that in steady conditions by applying a lag to the value of the normal force, producing a value

C_n'. In the Laplace domain, this relationship can be expressed as

$$C_n'(p)/C_n(p) = 1/(1+T_p p),$$

where p is the Laplace variable. In the time domain, the dynamic stall process is regarded as being initiated at the angle of attack where $C_n'(t)$ is equal to the critical normal force coefficient C_{n_1}. The non-dimensional time-delay between dynamic stall onset as defined by this criterion and the earliest observed indication of vortex initiation, C_p deviation, is plotted against reduced pitch-rate in Figure 4.99. It can be seen that the delay is approximately independent of aerofoil motion.

At a Reynolds number of 1.5×10^6, therefore, the dynamic stall phenomenon can be divided into a number of subprocesses. The delay between static stall and dynamic stall onset as defined by Beddoes seems to be dependent on Mach number, and the delay between incurring stall in this form and the vortex being observed is independent of reduced pitch-rate. As described above, the dynamic stall vortex then grows in strength in proportion to the reduced pitch-rate and is shed downstream at a velocity which is independent of aerofoil motion.

4.5.6 Data from Experiments at Constant Negative Pitch-rate

This section has discussed the influence of pitch-rate on an aerofoil's dynamic characteristics. In the preceding subsections, the effects due to a positive pitch-rate has been examined. However, it is also of interest to examine the influence of a negative pitch-rate over an incidence range chosen so that the aerofoil is initially in stall and moves into fully-attached conditions. A full series of these "ramp-down" experiments were performed over the same range of incidence and magnitude of pitch-rates as were the ramp-up experiments.

Figure 4.7 illustrates typical characteristics at a Reynolds number of 1.5×10^6 in steady conditions. As described in Section 4.3, there was only one area of hysteresis, occurring at the position of flow reattachment at the leading edge. Figures 4.100 - 4.102 reveal that this behaviour was enhanced as pitch-rate increased in magnitude.

At the most gentle reduced pitch-rate of -0.0017, the characteristics were qualitatively similar to those in steady conditions. The magnitude of the reduced pitch-rate was within the range of values which defined the quasi-static regime for ramps of positive pitch-rate. The

maximum loading around the static stall incidence was lower than that realised in steady conditions, but the static forces were attained again at an incidence only slightly lower. As in steady conditions, the flow reattached initially at the leading edge at approximately 22° and the boundary layer subsequently reattached along the upper surface towards the trailing edge.

At pitch-rates which were greater in magnitude, the reattachment process was modified. The establishment of the leading-edge loading was more gradual and continuous. The ensuing lower leading-edge suction resulted in a much smaller value for the normal force coefficient over a large incidence range until full reattachment over the upper surface was retained at an incidence which decreased with increasing magnitude of reduced pitch-rate. The pitching-moment characteristics were also significantly modified. A detailed discussion of the influence of pitch-rate on the reattachment process can be found by consulting SETO [82].

NIVEN ET AL [77] observed for a number of aerofoils that reattachment appeared to move downstream only after the suction at 2.5% chord began to rise. It was found that the incidence at which this occurred seemed to depend on the leading-edge geometry of the aerofoil, with the NACA 23012, NACA 23012A and NACA 23012C aerofoils all reattaching at the same incidence at all reduced pitch-rates. When examining the time-delay between the rise in suction and the establishment of fully-attached

flow over the aerofoil's upper surface it was observed that at pitch-rates of small magnitude there was a weak dependence on aerofoil motion, but at reduced pitch-rates greater in magnitude than 0.015 there was a constant non-dimensional time-delay of approximately 5 chordlengths of travel.

Detailed examinations of the data resulting from experiments performed at a constant negative pitch-rate at the University of Glasgow are discussed in detail by SETO [82], NIVEN ET AL [77] and HERRING [45].

4.6 CONCLUDING REMARKS

The NACA 23012C aerofoil was tested in the University of Glasgow's Handley-Page wind-tunnel under steady and unsteady conditions over a range of Reynolds numbers. The resulting data were compared to data from similar experiments performed on the NACA 23012 and NACA 23012A aerofoils. Established theories on aerofoil behaviour were supported.

In steady conditions, a number of properties were observed. As predicted when the aerofoil was designed (Chapter Two), the separation characteristics of the NACA 23012C were more typical of an aerofoil experiencing trailing-edge stall than those of the NACA 23012. The two modified aerofoils separated at a similar rate with respect

to incidence, but the angle of attack at which the separation point reached any chordal location was approximately 2° higher for the NACA 23012C. As a result of these separation characteristics and as would be expected of an aerofoil whose maximum camber was located further downstream, the NACA 23012C stalled less abruptly than the NACA 23012. Due to the NACA 23012C being the most highly cambered of the aerofoils, it possessed the lowest incidence of zero-lift, and, because they were of similar thickness, the NACA 23012C and NACA 23012 possessed similar gradients in the traces of normal force coefficient. However, as a result of the NACA 23012C being more highly cambered at the extreme leading edge, it experienced a higher maximum normal force, larger pitching-moment and higher stall incidence. The leading-edge bubble was found to play no significant part in the stall process.

It was observed that separation was slightly less sudden and that maximum normal force and normal force gradient were lower at a Reynolds number of 1.0×10^6 than at higher Reynolds numbers. However the stall incidence did not vary significantly with Reynolds number. As a result of there being no transition on the lower surface, the pitching-moment coefficient was closest to zero at the lowest Reynolds number.

Many of the characteristics of the data from unsteady

experiments were qualitatively extensions of those in steady conditions. This was particularly true of the variation with Reynolds number and aerofoil geometry. The most important parameters in the dynamic stall process were reduced pitch-rate and, in the case of oscillatory experiments, maximum incidence. As reduced pitch-rate increased, the magnitudes of the loads increased and the incidence at which events occurred was increasingly delayed. At a reduced pitch-rate of 0.01 or a reduced frequency of between 0.025 and 0.05, the dynamic stall vortex became evident in the form of a deviation in the gradient of the traces of the coefficients of normal force and pressure coefficient at the chord location of inception, and in a succession of suction peaks moving downstream over the upper surface with the vortex and secondary vortices. There appeared to be a correlation between the incidence of the C_p deviation and the maximum pitch-rate attained during tests of any type of motion. Of interest is the fact that the maximum reduced pitch-rate for a test at a reduced frequency of 0.03 is approximately 0.01. These values are approximately those at which the dynamic stall vortex began to play a prominant role in the dynamic stall process.

It seems that, once stall onset was encountered, the effects of stall could not be avoided. The dynamic stall process appeared to consist of a number of events which, with the exception of the growth of the dynamic stall vortex, which grew in strength over a period of

non-dimensional time proportional to reduced pitch-rate, lasted for non-dimensional periods of time (measured in chordlengths of travel) which were independent of aerofoil motion.

As the reduced frequency increased in oscillatory experiments, the degree of hysteresis increased and negative damping became more likely. The reduced frequency at which the modified aerofoil could pitch without suffering negative damping was much greater for the modified aerofoils than for the NACA 23012. The NACA 23012C could pass through an incidence 3° higher than the other aerofoils without suffering negative damping.

The critical angle of attack, which in oscillatory experiments is the incidence having passed through which a break in pitching-moment is unavoidable, was examined. This incidence was observed to increase with reduced frequency and Reynolds number, and was greatest for the NACA 23012C. It occurred before C_p deviation in oscillatory tests but could not be applied in ramps. The C_p deviation was the earliest indication from experimental data which could be detected under any type of motion that stall onset had occurred. Its variation with aerofoil geometry, reduced pitch-rate and Reynolds number is examined in the next chapter.

A great amount of information has been gleaned from testing the NACA 23012C aerofoil, and it possesses a number of favourable properties. Unfortunately, because of its

large pitching-moment magnitudes and its severe post-stall characteristics, it could not be employed in practice. However, it may be useful as a base from which to make further modifications.

It has been shown that trends in steady and unsteady conditions are linked. It would be useful if a relationship could be found so that, with the assistance of the large number of theoretical methods available for static characteristics, an indication of how an aerofoil might behave in unsteady conditions would be available before building and testing a model. This is examined in the next chapter.

CHAPTER FIVE

A CORRELATION INDICATING INCIPIENT DYNAMIC STALL

5.1 INTRODUCTION

Subsection 4.5.4 described how one method of detecting that the stall process has been initiated is the observation of a deviation in the gradient of the C_p trace with respect to non-dimensional time. This chapter proposes a new correlation which attempts to relate the incidence at which this C_p deviation occurs to particular parameters which describe its static stall behaviour. The motivation for the correlation came from two sources : a desire to make use of available theoretical techniques for predicting an aerofoil's steady characteristics and a desire to develop easily calculable procedures for predicting vortex initiation during dynamic stall. It is hoped that the correlation will assist in the preliminary design stages of an aerofoil geometry which is required to display a particular characteristic under unsteady

conditions.

Figure 5.1 illustrates the profiles of seven aerofoils which have been tested at the University of Glasgow in the manner described in Chapter Three. Data from the experiments on these aerofoils have been used as the basis of this correlation. The seven aerofoils are part of two families : the NACA four-digit series of symmetrical sections and a new family of four aerofoils developed at the University with the NACA 23012 as the generic shape. Of the four aerofoils in the NACA 23012 family, the original aerofoil and the modified aerofoils NACA 23012A and NACA 23012C have been described in great detail in this dissertation. The full set of data plots for these aerofoils are described by LEISHMAN ET AL [55,58], SETO ET AL [82,83,85], NIVEN ET AL [73,75,76] and GRACEY AND GALBRAITH [38,39,40]. The NACA 23012B aerofoil is a 16% thick composite aerofoil derived from the NACA 23012 and an RAE section, and has been described by HERRING ET AL [45,46,47,48,49]. A full set of data resulting from the experiments on the NACA 0015, NACA 0018 and NACA 0021 aerofoils are illustrated in reports by ANGELL ET AL [3,4,5,6,7,8,9,10,11].

In the dynamic stall regime, the variation of C_p deviation with reduced pitch-rate is approximately linear. However, as illustrated in Figure 5.2, the equation of the best least-squares straight line through these points varies significantly with aerofoil geometry. The aim of

this chapter is to find some method by which these lines may be represented by a single equation. This task must involve using parameters which are unique to each aerofoil. As will be seen, these data can be obtained from the results of experiments or predictive codes in steady conditions.

With the aid of a numerical boundary layer model, SCRUGGS ET AL [80] demonstrated that there was a high degree of correlation between the incidence at which significant flow reversal reached the 50% chord location and the experimentally-measured incidence of dynamic stall onset. This model also predicted that, with increasing pitch-rate, the extent of the delay in flow reversal increases and the subsequent forward movement of the flow-reversal point becomes progressively more rapid. However, it was stressed that this analysis did not imply that dynamic stall is simply the result of this forward movement of the flow-reversal point.

Water tunnel experiments by McALISTER AND CARR [62] revealed that, prior to vortex formation, a region of reversed flow momentarily appeared over the entire upper surface without any appreciable disturbance to the viscous-inviscid boundary. McCROSKEY ET AL [67] observed that, for aerofoils exhibiting gradual trailing edge stall, vortex initiation was preceded by a gradual forward movement of flow reversal in a thin layer at the bottom of the boundary layer. This behaviour was described as a "tongue of reversed flow" since no upper surface pressure

divergence, which would have indicated possible boundary-layer separation, was observed. CARR ET AL [21] also determined that the occurrence of surface flow reversals over the rear portion of the aerofoil are not necessarily equivalent to flow breakdown outside the boundary layer. The investigations of the boundary layer behaviour by SETO [82] and NIVEN [73] on the NACA 23012 and NACA 23012A aerofoils indicated that flow reversals may penetrate upstream to the 30% chord region prior to vortex formation.

These observations raise the question of whether such flow reversals are a prerequisite to vortex inception, and, if so, whether their behaviour is dependent on the aerofoil's static trailing-edge separation characteristics. One method of investigating this phenomenon would be to correlate the incidence at which vortex initiation is observed against a designated parameter representing the aerofoil's static trailing-edge separation characteristics. The results of McCROSKEY ET AL [65] imply that the incidence at which dynamic stall onset occurs is related to the abruptness of the aerofoil's static trailing edge separation. It therefore seemed reasonable to seek a parameter which describes this behaviour.

Section 5.2 describes how this parameter and the resulting correlation were derived. This correlation is compared to the results from several other predictive algorithms in Section 5.3.

5.2 THE CORRELATION

An approximation to the location of boundary layer separation at any angle of attack for an aerofoil experiencing trailing-edge separation has been described by BEDDOES [14]. The variation of the separation point with angle of attack was modelled by two exponential equations which coincided at the 70% chord location. These equations could not accurately model all types of separation characteristics, such as, for example, those possessed by the NACA 23012. It was therefore decided that these equations should be generalised to the form

$$f = f_{max} + K_1 \exp((\alpha - \alpha_1)/S_1), \quad \alpha \leq \alpha_1 \qquad (5.1a)$$

$$f = f_{min} + K_2 \exp((\alpha_1 - \alpha)/S_2), \quad \alpha > \alpha_1 \qquad (5.1b)$$

where α represents the angle of attack and f represents the separation point in the form of x/c, the ratio of the distance along the chord from the leading edge to the length of the chord. The remaining seven coefficients are constant for a particular aerofoil and Reynolds number under static conditions. An algorithm for approximating these constants for any set of data points $\{(\alpha, f)\}$ has been coded, and is derived in Appendix B. The resulting separation curves for the seven aerofoils are illustrated in Figure 5.3.

The larger range of values for f, including the region of the more sudden forward movement of the separation point, is included in Equation (5.1b). It

follows that, at this part of the separation process,

$$df/d\alpha = -S_2^{-1}K_2\exp((\alpha_1-\alpha)/S_2)$$
$$= -S_2^{-1}(f-f_{min}).$$

The constant f_{min} represents the location of bluff body separation, and is approximately equal for each aerofoil ($0 < f_{min} < 0.0025$). Therefore, for any given value of f in the range of abrupt separation and at the 50% chord location which SCRUGGS ET AL [80] examined when comparing aerofoils' separation characteristics, the rate of change of separation point with incidence is approximately proportional to S_2^{-1}. From the argument stated above, it would, therefore, seem that the statically-derived coefficient S_2 would be a suitable parameter to use when examining the influence of trailing edge separation on vortex inception. If this parameter does influence the formation of the vortex, it should be possible, in the light of what has previously been discussed, to use it when representing, in the form of single equation for all seven aerofoils, the incidence of the earliest indication from experimental data that stall onset had occurred.

In the fully dynamic stall regime, as illustrated in Figure 4.92, the angle of attack of C_p deviation α_{dm} varied linearly with reduced pitch-rate r. Therefore, this relationship can be expressed in the form

$$\alpha_{dm} = m_1 r + c_1, \qquad (5.2)$$

where m_1 and c_1 represent constants for a particular aerofoil. If the rate of separation influences the formation of the vortex, then it is possible that

$$m_1 = F_1(S_2)m_2,$$

where m_2 is a constant for all aerofoils and $F_1(S_2)$ is a function of S_2 and, hence, of aerofoil. By correlating m_1 against S_2, and with the intention that the function should be as simple as possible, it was decided that $F_1(S_2)$ should be of the form S_2^i, where i is a constant for all aerofoils. For each of a number of values of i, the set of values $\{m_1 S_2^{-i}\}$ over the range of aerofoils at a Reynolds number of approximately 1.5×10^6 was statistically examined, and the most suitable value of i was determined. **It was discovered that i=1/3 and i=1/4 resulted in a correlation which was acceptable at this stage.**

Because the static stall characteristic can be regarded as the characteristic of a ramp at zero pitch-rate, it seemed natural to consider the static stall angle α_{ss} as the aerofoil-dependent static parameter for determining the offset value c_1 in Equation (5.2). Regardless of how the static stall angle is defined, it is of the same order as c_1 and so a possible substitution seemed to be

$$c_1 = c_2 \alpha_{ss} + c_3,$$

where c_2 and c_3 are constants for all aerofoils. A

correlation of c_1 against α_{ss} supported the use of this substitution.

It follows that α_{ds} can be represented in the form

$$\alpha_{ds} = A + B\alpha_{ss} + C.S_2{}^{i}r, \qquad (5.3)$$

and values for A, B and C must be calculated.

In the dynamic stall regime for each aerofoil, the gradient and offset of the linear representation for the variation of α_{ds} with reduced pitch-rate were used in determining that the basic equation should be of the form in Equation (5.3). The gradient m_1 and offset c_1 in Equation (5.2) were calculated by least-squares regression through a set of data points for each individual aerofoil. These values, therefore, contained errors. In order to minimise these errors, once the basic form of the equation was known, all further curve fitting procedures were performed on all data points as one set, regardless of aerofoil, although the values of S_2 and α_{ss} were still dependent on aerofoil. For this purpose, an algorithm was coded to perform least-squares linear regression in two variables on the data points at a Reynolds number of approximately 1.5×10^6. These two variables were $S_2{}^{i}r$ and α_{ss}. For a given value of i, the algorithm calculated A, B, C and the least-squares error. Repeating the process with different values of i and comparing the resulting error values provided a suitable equation.

Initially, α_{ss} was regarded as being the first incidence at which the gradient of the normal force coefficient curve became zero. However, although a good correlation was achieved for each of the aerofoil families, the NACA 0021 data, which possessed very gentle separation characteristics, did not fit when correlating for all seven aerofoils. The incidence of pitching-moment break was then substituted and much better agreement resulted. This definition of the static stall incidence was employed in all further modifications of the correlation.

The correlation program yielded the most suitable results when i was assigned the value of 1/4. Because Equation (5.3) is the equation of a plane in three dimensions, any qualitative comparison of the original set of data points to those predicted by the equation with the aid of a three-dimensional diagram would be very difficult. Therefore, it was decided to illustrate the correlation as in Figure 5.4, by means of a two-dimensional graph, with the axes labelled $S_2{}^{i}r$ and $(\alpha_{ds} - B\alpha_{ss})$.

The resulting correlation was reasonable, but could have been more accurate : the general trend was not quite linear. In addition, it was decided that data points which resulted from quasi-static experiments should be included. The first indication of stall which was observed in the quasi-static regime was a drop in suction from its maximum value at the leading-edge. It was discovered that the inclusion of a square-root term was a simple and accurate modification, resulting in an equation

of the form

$$\alpha_{dm} = A + B\alpha_{mm} + C.S_2{}^{1}r + D(S_2{}^{1}r)^{1/2}. \quad (5.4)$$

The original program was modified to implement this change and a good correlation was achieved. This correlation is illustrated in Figure 5.5, in which a square-root scale is used on the $S_2{}^{1}r$ axis so that the data in the quasi-static regime can be compared more easily.

All the data which were used to form Equations (5.3) and (5.4) were recorded at a Reynolds number of approximately 1.5×10^6. The next modification to the program was the consequence of an attempt to include points at other Reynolds numbers. The influence of Reynolds number on static characteristics was discussed in Subsection 4.3.7. It was described how, at low Reynolds numbers, the flow was encouraged to separate from the surface at lower angles of attack. It therefore seems plausible that certain aspects of this phenomenon would be passed on to unsteady conditions. If vortex inception is influenced by the separation characteristics then it would follow that the C_p deviation would occur at a lower incidence. This theory is supported in the comparison of C_p deviation against reduced pitch-rate for the NACA 23012C over a range of Reynolds numbers in Figure 5.6.

It was hoped that the only necessary change to the

correlation would be to determine α_{ss} and S_2 at each Reynolds number. However, examination of the graphs which resulted from this modification indicated that the power to which S_2 is raised should be a function of Reynolds number, and that Equation (5.4) should be modified to the form

$$\alpha_{ds} = A + B\alpha_{ss} + C.S_2^{Rjr} + D(S_2^{Rjr})^{1/2}, \quad (5.5)$$

where $R = Rex10^{-6}$ and j is a constant for all aerofoils.

The final correlation is illustrated in Figure 5.7 and is compared with the data points which were recorded for the NACA 23012C in Figure 5.8. In this figure the correlation is compared to two sets of data points : data determined at 0% chord and data determined at 27% chord. In addition, in the quasi-static regime, the incidence at which the local peak suction collapsed at 27% chord is plotted : by the definition described in Subsection 4.5.4, in the quasi-static regime there was no C_p deviation of the form illustrated in Figure 4.91. The lowest incidence at which there was a distinct deviation in the pressure coefficient trace at the relevant location in this regime was that at which the gradient of the trace became negative. As would be expected, it can be seen that in the quasi-static regime the correlation refers to the peak suction collapse at 0% chord and in the dynamic regime to the C_p deviation at 27% chord.

As described in Chapter Four, McCROSKEY ET AL [67] found that, regardless of behaviour at low Mach number or

in the quasi-static regime, as the freestream Mach number was increased each aerofoil which they tested tended to exhibit characteristics typical of unsteady leading-edge stall. In such cases, a criterion based on trailing-edge separation may not be justified. It is, therefore, noted that the present correlation is restricted not only to aerofoils which experience trailing-edge separation, but also to test conditions in the low Mach number regime (i.e freestream Mach numbers of less than 0.2).

5.3 COMPARISON WITH EXISTING MODELS OF DYNAMIC STALL ONSET

This section compares the correlation which was derived in Section 5.2 and stated in Equation (5.5) with predictive algorithms which are already in use. Chapter One described how such algorithms can be divided into four groups : Navier-Stokes; discrete vortex; zonal; predominantly empirical. Of these four groups, only the last includes methods in which the onset of dynamic stall can be analysed without coding the entire algorithm. However, some of these empirical methods define stall onset implicitly and, for such cases, a comparison cannot be made without complete coding. Among these methods are those created by TRAN AND PETOT [88], who determined the loads from a system of ordinary differential equations whose coefficients were determined empirically, and GANGWANI [35] and BEDDOES ET AL [13,56] who have created time-delay models. However, as described in Section 4.5, a version

of Beddoes's algorithm has been coded at the University of Glasgow and so a direct comparison can be made between the incidences of stall onset as defined by his algorithm and by this correlation.

The basic idea of a time-delay model is that, regardless of the time history of the motion, each dynamic stall event is governed by a separate universal time-constant measured in chordlengths of travel. The comparison of Beddoes's prediction of stall incidence with the incidences of C_p deviation and correlation prediction for the NACA 23012C aerofoil at a Reynolds number of 1.5×10^6 is illustrated in Figure 5.9. It can be seen that, in the dynamic stall regime (where, as decribed in Subsection 4.5.4, reduced pitch-rate is greater than 0.01), Beddoes predicts that stall occurs earlier than C_p deviation was detected during experiments. As described in Subsection 4.5.5, the non-dimensional time-delay between these two events was approximately independent of aerofoil motion.

Another time-delay method has been created by CARLSON ET AL [19]. It was claimed that there exists a maximum quasi-static incidence at which the pressure distribution and boundary layer are in equilibrium. When the angle of attack has increased beyond this static stall incidence, there are finite time-delays before a redistribution of pressure, causing first a break and then a loss of lift corresponding to flow separation. The pitching-moment characteristics behave similarly.

McCROSKEY [64] reveals the non-dimensional time-delays between the static stall incidence and the angles of attack of moment stall and maximum lift to be 2.5 and 5.0 chordlengths of travel respectively. The resulting stall incidences are compared with the predictions of the correlation for the NACA 23012C aerofoil at a Reynolds number of 1.5×10^6 in Figure 5.10. No explicit definition of the behaviour in the quasi-static regime was provided and so the same definition was used at all reduced pitch-rates. It can be seen that, in the dynamic stall regime, the correlation predicts that C_p deviation would be detected at a lower incidence than Carlson predicts lift stall and at a higher incidence than moment break. Because of the gentle deviation of the moment characteristics, this definition of stall onset could not be detected easily from experimental data.

It should be noted that, as described in Subsection 4.5.5 and Section 5.2, the evidence of the data recorded at the University of Glasgow does not support the view that the delay between each event during dynamic stall consists of universal time-constants which are independent of aerofoil geometry and motion.

JOHNSON AND HAM [52] described the dynamic stall vortex being shed when the laminar separation bubble is burst. It was proposed that the dynamic stall delay results from the effect of the unsteady pressure gradient on the location of the transition point in the leading-edge bubble : the delay is caused by the delay of the bubble

reattachment point to move towards the leading-edge and encounter the large adverse pressure gradient. The incidence delay is given as a linear function of pitch-rate and is also dependent on the static stall incidence. In Figure 5.11 the resulting dynamic stall incidence is compared to the incidences observed for C_p deviation and predicted by the correlation for the NACA 23012C aerofoil at a Reynolds number of 1.5×10^6. This linear variation of stall incidence is only very approximately similar to the C_p deviation predicted by the correlation. It should be noted that, as described in Chapter Four and in support of earlier research (e.g. McCROSKEY ET AL [67]), there is a large amount of evidence which suggests that the leading-edge bubble does not play a significant part in the dynamic stall process.

ERICSSON AND REDING [31] described the separation-induced aerodynamic loads being affected by two distinctly different flow phenomena : one of quasi-steady behaviour which is associated with the dynamic delay of flow separation; the other of transient nature, associated with the upstream movement of the separation point during dynamic stall and the spillage and movement downstream of the leading edge vortex which follows this event. A time-delay is associated with each of these phenomena. The dynamic delay of flow separation is caused by a time-lag (divided further into circulation lag, convective viscous-flow time-lag and moving separation point effect) and boundary-layer improvement effects (split into accelerated flow and moving-wall effects). Of these two

effects, the former causes the corresponding static loads to lag the instantaneous flow environment and the latter produces an overshoot of the static stall characteristics. There is evidence that the maximum pitch-rate attained during the cycle is important in producing dynamic overshoot of the maximum lift coefficient.

The predicted incidence of dynamic flow separation is compared to the points of C_p deviation and the correlation prediction for the NACA 23012C aerofoil at a Reynolds number of 1.5×10^6 in Figure 5.12. Ericsson and Reding's predicted values are very close to those of the correlation, indicating that the two definitions of dynamic stall onset are not dissimilar. Also of interest is the fact that the position at which there is a change in the variation of this prediction, being composed of two linear distributions, is at a reduced pitch-rate of 0.01. As described in Section 4.5, this reduced pitch-rate has been observed as being that which divides the data between the regimes of quasi-static and dynamic stall in data produced at the University of Glasgow.

In the method developed by HARRIS ET AL [44] and GORMONT [37], the force and moment coefficients are constructed from static data using an equivalent angle of attack, which accounts for unsteady potential-flow effects, and a reference angle. In particular, the delay in incidence $\Delta\alpha_a$ between static stall and dynamic stall is determined from the equation

$$\Delta\alpha_d = \gamma\sqrt{\dot{\alpha}c/U_\infty},$$

where γ is a function of freestream Mach number and the maximum thickness of the aerofoil, and is different for lift and moment stall. These "gamma functions" were generated from a large amount of data obtained from wind-tunnel experiments by various aerofoils oscillating sinusoidally in pitch.

The resulting dynamic stall incidences for moment stall are compared to the correlation and incidences of C_p deviation for the NACA 23012C aerofoil at a Reynolds number of 1.5×10^6 in Figure 5.13. Both dynamic stall definitions are functions of the square-root of reduced pitch-rate and the results are very similar. The lack of a linear term in the equation tends to increase the curvature of the graph of Gormont's prediction. It seems that this definition of dynamic stall is very similar to C_p deviation, which is the earliest indication of dynamic stall which can be discerned easily from data recorded experimentally at the University of Glasgow.

In all the methods described in this section, the y-axis intercept is a function of the static stall incidence. However, the variation with reduced pitch-rate depends on parameters which vary with model : Carlson et al use a time-delay which is independent of aerofoil and wind-speed; Johnson and Ham's model varies as a function of the static stall incidence; Ericsson and Reding's parameters were derived from more elements than any of the

other models, but these parameters seem to be constant within various Reynolds number ranges; Beddoes bases his stall incidence on idealised static data (using EVANS AND MORT'S [32] correlation) based partly on aerofoil geometry with universal time-delays; Gormont's model varies as a function of aerofoil thickness and Mach number. However, as described in Section 5.2, correlation of the data at the University of Glasgow required the parameters of Reynolds number and separation characteristics for each aerofoil in steady conditions.

As described in Subsection 4.4.6, from purely experimental observation WILBY [91] has defined a critical angle signifying the highest incidence which can be attained before the consequences of dynamic stall become unavoidable. It can only be determined from oscillatory data. By a similar procedure to that described in Section 5.2, an equation was derived to correlate the data for the seven aerofoils illustrated in Figure 5.1 over the same range of Reynolds number as in the ramp tests. This correlation is illustrated in Figure 5.14.

As described in Subsection 4.5.4, the maximum pitch-rate can be used as a parameter to compare the incidence of C_{p} deviation for oscillatory and ramp tests. In order to compare the correlations illustrated in Figures 5.7 and 5.14, it would seem reasonable to use the maximum pitch-rate of a cycle to change the domain of the critical angle correlation from reduced frequency to reduced pitch-rate. These two definitions of stall onset

are compared in Figure 5.15. It can be seen that the critical angle of attack was reached significantly earlier than the incidence of C_p deviation at all pitch-rates.

The seven criteria which have been discussed in this chapter are compared in Figure 5.16. It can be seen that the critical angle of attack, as represented by the "WILBY" curve, occurs earliest and the C_p deviation (as represented by the "CORRELATION" curve), which, as stated above, was the earliest indication to be detected clearly from experimental data that the process of dynamic stall had been initiated, occurs among the latest of the stall definitions. Although based on experimental data, the other five definitions are theoretical and so cannot be detected easily when simply observing the data.

It was hoped when analysing the ramp data that it may have been possible to locate an incidence which was analogous to the critical angle in oscillatory data. This was not possible from simple observation of the data because, unlike oscillatory experiments, ramps take place at a constant pitch-rate and, hence, no change in pitch direction could be made when below the stall incidence. However, it may be possible to relate the two definitions of stall incidence theoretically.

As illustrated in Figures 4.56, 4.57, 4.92, 4.93, 5.2 and 5.4, in the dynamic regime the variation of these stall incidences with reduced pitch-rate is approximately linear. In these cases, the incidence α_{dm} of C_p deviation is given

by

$$\alpha_{d_{max}} = 0.152 + 1.210\alpha_{max} + 243.991 S_2^{R/6} r,$$

and the critical angle α_c by

$$\alpha_c = 7.389 + 0.487\alpha_{max} + 20.188 S_2^{R/6} r$$
$$\Leftrightarrow \alpha_c = 7.389 + 0.487\alpha_{max} + 144.586 S_2^{R/6} r,$$

where the critical angle correlation domain has been changed from reduced frequency to reduced pitch-rate by means of the maximum pitch-rate attained during the cycle. Therefore

$$\alpha_{d_{max}} - \alpha_c = (0.723\alpha_{max} - 7.237) + 99.405 S_2^{R/6} r.$$

Now the reduced pitch-rate r is defined as

$$r := \frac{\dot{\alpha} c}{2U_\infty} \cdot \frac{\pi}{180} = \frac{\pi c . \Delta\alpha}{360\, U_\infty . \Delta t} \qquad (5.6)$$

in the case of constant pitch-rate ramps, where $\Delta\alpha$ and Δt can be measured between any two points and where angle of attack is expressed in degrees. In particular, $\Delta\alpha$ and Δt can be measured between the critical angle and the incidence of C_p deviation and hence, employing Equation (5.6), the non-dimensional time-delay τ^* can be expressed as follows :

$$\tau^* := \frac{\Delta t . U_\infty}{c} = \frac{\pi . \Delta\alpha}{360\, r}$$

$$\Rightarrow \tau^* \approx \frac{0.00631}{r}\left(\alpha_{ss} - 10.0\right) + 0.868\, S_2^{R/6} \qquad (5.7)$$

In Figure 5.17, the variation of τ^* as defined in Equation (5.7) is compared with the measured time-delay between these two incidences being attained by the NACA 23012C at a Reynolds number of 1.5×10^6. The agreement is good.

5.4 CONCLUDING REMARKS

It has been shown that it is possible to predict the incidence of C_p deviation from the static characteristics of an aerofoil at a particular Reynolds number. The necessary statically-derived parameters are the incidence of pitching-moment stall and an additional parameter representing the incidence locus of the trailing-edge separation point. By examining static data which have been collected either from experiments or from one of the large number of accurate codes for predicting aerofoil characteristics in steady conditions, this correlation can be employed during the aerofoil-design process to provide an indication of an aerofoil's behaviour in unsteady conditions. However, much more research will be required before it is possible to answer with confidence the original question of whether flow reversal is a prerequisite to vortex inception.

Examination of various empirically-derived predictive

methods has revealed a large variation in the definition of the inception of dynamic stall. An analogous incidence to the critical angle defined by WILBY [91] from oscillatory data was observed to be the earliest indication yielded by the methods under investigation that the aerofoil had reached an incidence which, if exceeded, resulted in the initiation of the dynamic stall process. Between attaining this incidence and the angle of attack of C_p deviation, there exists a non-dimensional time-delay, expressed in chordlengths of travel, which is a simple function of reduced pitch-rate and the statically-derived parameters described above. This time-delay and the incidence of C_p deviation can be employed to predict the equivalent critical angle when examining experimental ramp data.

CHAPTER SIX

CONCLUSIONS AND RECOMMENDATIONS FOR FUTURE RESEARCH

Having modified the NACA 23012 aerofoil section to increase its camber, a two-dimensional model of the resulting aerofoil was built and tested in steady and unsteady conditions in the University of Glasgow's "Handley-Page" wind-tunnel. The data yielded by these experiments were compared to those provided by the original aerofoil and the NACA 23012A aerofoil, another modification of the NACA 23012 which was identical over the leading 25% chord but was reshaped downstream of that position to produce reflex camber at the trailing edge. Established hypotheses on aerofoil behaviour were supported and, in many respects, the NACA 23012C aerofoil compared favourably.

As in the case of the NACA 23012A, the separation characteristics of the NACA 23012C were more typical of an aerofoil experiencing trailing-edge stall than those of the

NACA 23012. As a result, stall was less abrupt. However the separation point reached each chord location on the NACA 23012C at an angle of attack approximately 2° higher than on the NACA 23012A. These two characteristics resulted in stall occurring at the highest incidence for the NACA 23012C. It also possessed the lowest incidence of zero-lift and, hence, the greatest difference in angle of attack between zero-lift and stall. The gradients of normal force did not vary significantly with aerofoil geometry and so the NACA 23012C experienced greatest lift.

The pitching-moment, which was consistently negative, was greatest in magnitude for the NACA 23012C both in unstalled and stalled conditions. Indeed the magnitudes were too great for it to be employed for practical purposes. However, observing the positive pitching-moment of the NACA 23012A before stall implied that, if the NACA 23012C were to be modified in a similar manner to the NACA 23012 when designing the NACA 23012A, a useful aerofoil may be produced. The data yielded from experiments on such an aerofoil could be of interest.

Reduced pitch-rate and, in the case of oscillatory experiments, maximum incidence were the greatest influences on dynamic stall. Increasing reduced pitch-rate resulted in an increase in the magnitudes of the loads and a larger delay in the incidences at which events occurred.

It was necessary to treat the magnitudes of the loadings with great care. There were two reasons for this

limitation. Firstly, pressure was recorded only at the discrete positions where transducers were located. In addition, for the reasons discussed in Section 4.1, the data had been averaged and, in certain conditions, peak values were not repeatable. With regard to this latter detail, a comprehensive inspection of unaveraged data would be beneficial. From such an examination, it might also be possible to quantify stall events, as, for example, LORBER AND CARTA [61] have done. With the large number of data sets available to researchers at the University of Glasgow, such techniques would increase efficiency to very powerful levels.

The former problem was a consequence of the necessity of positioning transducers at locations around all of the aerofoil's centre span. However, once a full series of tests has been performed on an aerofoil and the data has been analysed, it should be possible to repeat tests with transducers located over only a short length of the surface. Such a series of tests is now possible because the experimental rig at the University of Glasgow is being upgraded, enabling data to be recorded by more than thirty pressure transducers. This improvement will also permit data to be recorded at greatly increased sampling frequencies, with the result that a large amount of data could be recorded over a very short sweep of the aerofoil's arc. Before the tests are begun, this incidence range can be determined with the aim of recording data at some point of interest such as the critical angle of attack or incidence of C_p deviation, both of which are discussed

below.

It seems to be possible to compare data from different types of motion by considering the maximum incidence which is attained during the test. The dynamic stall vortex began to play a significant role when the aerofoil pitched at a sufficiently great rate. It was first detected at a reduced pitch-rate of 0.01. The reduced frequency at which this event occured in oscillatory experiments corresponded to the same reduced pitch-rate if calculated from the maximum pitch-rate over the cycle.

The leading-edge bubble did not appear to play a significant role in the mechanism of stall. In the flow visualisation experiments, three-dimensional effects were detected prior to stall. This phenomenon seemed to be a consequence of the stall process rather than incidence. Because the means were not available to perform flow visualisation experiments in unsteady conditions, it was not possible to observe the flow development associated with dynamic stall. However, it was observed by WILBY [92] that, when approaching stall in quasi-static experiments, separation induced at the junction of the model and wind-tunnel wall reduced the effective angle of attack at the centre of the model. As a result, the attitude of the aerofoil was no longer the true aerodynamic incidence. It is possible that flow visualisation apparatus for unsteady experiments will be assembled at the University of Glasgow in the near future. If so, the results of experiments on

the three-dimensional effects associated with the dynamic stall phenomenon would be of assistance when assessing the unsteady aerodynamic performance of an aerofoil.

The degree of hysteresis in oscillatory experiments increased with reduced frequency. As a result, negative damping became more likely. Because of their more gentle separation characteristics, the reduced frequencies at which the modified aerofoils could pitch without experiencing negative damping were much greater than for the NACA 23012. The NACA 23012C could pass through an incidence 3° higher than the other aerofoils without suffering the effects of negative damping.

The dynamic stall process appeared to consist of a number of events. The dynamic stall vortex grew in strength over a period of non-dimensional time, measured in chordlengths of travel, proportional to reduced pitch-rate. However each of the other events lasted for a length of time which was independent of aerofoil motion.

WILBY's [91] critical angle of attack, which in oscillatory experiments is the highest incidence which can be attained while avoiding a break in pitching-moment, was observed to increase with reduced frequency and Reynolds number, and was consistently greatest for the NACA 23012C. The first indication from ramps that dynamic stall had been initiated was when there was a deviation in the gradient of one of the pressure coefficient traces. The incidence at which this event occurred revealed a similar variation with

reduced pitch-rate, Reynolds number and aerofoil geometry as that displayed for the critical angle. In oscillatory experiments, it occurred later than the critical angle of attack was attained. Stall could not be prevented after either of these events had been detected.

The chord location at which the first deviation in the pressure trace was detected varied with aerofoil. Although it is suspected that this phenomenon may result from the tongue of reversed flow interfering with the adverse pressure gradient, the reason for this variation in its location on the aerofoil surface is not yet known and should be the subject of future research. There was also some evidence that this chord position may also have varied with reduced pitch-rate. However, to be certain that it does vary, it would be necessary for the transducers to be more closely spread about the location under review. If they were to be distributed in this way, it would also be possible to detect more precisely if this location varied with Reynolds number.

A correlation was derived to indicate the incidence of C_p deviation from the static characteristics of an aerofoil at a particular Reynolds number. The necessary statically-derived parameters were the incidence of pitching-moment stall and an additional parameter representing the rate of trailing-edge separation. This correlation could be used when designing an aerofoil section to suggest how it would perform in unsteady conditions. It suggests that there is a connection

between an aerofoil's trailing-edge separation characteristics and the mechanism of dynamic stall as well as between its steady and unsteady characteristics. However, much more research will be essential before it is possible to determine indisputably whether flow reversal is a prerequisite to vortex inception.

Several empirically-derived criteria which are established as indicating how an aerofoil performs in unsteady conditions were examined. One of these criteria was the critical angle of attack. It was compared with data from ramp experiments by considering the maximum pitch-rate which was attained during its oscillatory cycle, and was observed to be reached earliest. WILBY [92] has declared the most important angle to consider when assessing aerofoil behaviour as being the difference between the critical angle of attack and the incidence of zero-lift. However the critical angle can only be calculated from oscillatory data. It was therefore hoped that it could be determined from pitch-rate and, hence, from any type of motion. This was achieved by means of a time-delay, which was a simple function of reduced pitch-rate and the static aerofoil parameters used in the correlation, between an analogous critical angle of attack and the incidence of C_p deviation.

All of the aerofoils which have been tested at the University of Glasgow have possessed characteristics of trailing-edge stall. In examining the transition from trailing-edge to leading-edge stall, it would be

interesting to compare the results produced by the aerofoils described in this dissertation with those of aerofoils which reveal characteristics of leading-edge stall in steady conditions. Such tests would also enable an investigation of McCROSKEY ET AL's [67] claim that, regardless of their static characteristics, all aerofoils experience trailing-edge separation characteristics in unsteady conditions.

One practical method of analysing data is to attempt to recreate experimental data by means of a computer algorithm which has been determined theoretically but with the aid of a small number of empirically-derived parameters. If the algorithm is to agree with the experimental data, a number of constraints are necessary. These constraints should reveal some information about the aerodynamic performance. For example, VEZZA [89] discovered a great deal about the reattachment process while attempting to model unsteady characteristics with the aid of a discrete vortex algorithm which was typical of those described in Chapter One. The constraints should also reveal the influence of the physical limits resulting from the fact that the tests are being performed in a wind-tunnel. From this latter feature, it should be possible to determine "correction coefficients" in order to predict from the wind-tunnel data how the aerofoil would behave in field conditions. This form of research should be pursued further to discover more about the mechanism which influences the inception of dynamic stall.

An aerofoil section has been designed which, although impractical for use on a helicopter blade, does possess many favourable aerodynamic characteristics. By analysing the data produced by a series of experiments performed on this aerofoil, a great deal of information has been gathered about the mechanism of dynamic stall. The importance of investigating unsteady aerodynamic characteristics by experimental techniques has been demonstrated, and any further research on the prediction of these characteristics by means of theoretical algorithms will require the support of experimental data.

REFERENCES

[1] ABBOTT, I.H. and VON DOENHOFF, A.E. Theory of wing sections. Dover Publications, New York, 1959. ISBN 486-60586-8.

[2] ANDERSON, J.D. Fundamentals of aerodynamics. McGraw-Hill, New York, 1985. ISBN 0-07-001656-9.

[3] ANGELL, R.K., MUSGROVE, P.J. and GALBRAITH, R.A.McD. Collected data for tests on a NACA 0021 aerofoil. Volume I : Pressure data from ramp function tests, with photographs of oil-flow visualisation tests. Glasgow University Aero Report 8802, June 1988.

[4] ANGELL, R.K., MUSGROVE, P.J. and GALBRAITH, R.A.McD. Collected data for tests on a NACA 0021 aerofoil. Volume II : Pressure data from oscillatory tests. Glasgow University Aero Report 8802, June 1988.

[5] ANGELL, R.K., MUSGROVE, P.J. and GALBRAITH, R.A.McD. Collected data for tests on a NACA 0021 aerofoil. Volume III : Pressure data relevant to the study of large scale vertical axis wind turbines. Glasgow University Aero Report 8802, June 1988.

[6] ANGELL, R.K., MUSGROVE, P.J. and GALBRAITH, R.A.McD. Collected data for tests on a NACA 0015 aerofoil. Volume I : Pressure data from ramp function tests, with photographs of oil-flow visualisation tests. Glasgow University Aero Report 8803, February 1988.

[7] ANGELL, R.K., MUSGROVE, P.J. and GALBRAITH, R.A.McD. Collected data for tests on a NACA 0015 aerofoil. Volume II : Pressure data from oscillatory tests. Glasgow University Aero Report 8803, February 1988.

[8] ANGELL, R.K., MUSGROVE, P.J. and GALBRAITH, R.A.McD. Collected data for tests on a NACA 0015 aerofoil. Volume III : Pressure data relevant to the study of large scale vertical axis wind turbines. Glasgow University Aero Report 8803, February 1988.

[9] ANGELL, R.K., MUSGROVE, P.J. and GALBRAITH, R.A.McD. Collected data for tests on a NACA 0018 aerofoil. Volume I : Pressure data from ramp function tests, with photographs of oil-flow visualisation tests. Glasgow University Aero Report 8815, September 1988.

[10] ANGELL, R.K., MUSGROVE, P.J. and GALBRAITH, R.A.McD. Collected data for tests on a NACA 0018 aerofoil. Volume II : Pressure data from oscillatory tests. Glasgow University Aero Report 8816, September 1988.

[11] ANGELL, R.K., MUSGROVE, P.J. and GALBRAITH, R.A.McD. Collected data for tests on a NACA 0018 aerofoil. Volume III : Pressure data relevant to the study of large scale vertical axis wind turbines. Glasgow University Aero Report 8817, September 1988.

[12] BEDDOES, T.S. A synthesis of unsteady aerodynamic effects, including stall hysteresis. Vertica, Volume 1, pp 113-123, 1976.

[13] BEDDOES, T.S. Onset of leading edge separation effects under dynamic conditions and low Mach number. 34th Annual National Forum of the American Helicopter Society, Washington D.C., May 1978.

[14] BEDDOES, T.S. Representation of airfoil behaviour. Vertica, Volume 7, Number 2, pp 183-197, 1983.

[15] BEDDOES, T.S. Practical computation of unsteady lift. Vertica, Volume 8, Number 1, pp 55-71, 1984.

[16] BEDDOES, T.S. Private communication, 1988.

[17] BENDER, C.M. and ORSZAG, S.A. Summation of series. Chapter 8 in Advanced mathematical methods for scientists and engineers. International series in pure and applied mathematics. McGraw-Hill, New York, 1978. ISBN 0-07-004452-X.

[18] BIPPES, H. and TURK, M. Half model testing applied to wings above and below stall. In Unsteady turbulent shear flows (Ed. Michel, R., Cousteix, J., Houdeville, R.). Springer-Verlag, New York, 1981.

[19] CARLSON, R.G., BLACKWELL, R.H., COMMERFORD, G.L. and MIRICK, P.H. Dynamic stall modeling and correlation with experimental data on airfoils and rotors. Paper Number 2, NASA SP-352, 1974.

[20] CARR, L.W. Progress in analysis and prediction of dynamic stall. Journal of Aircraft, Volume 25, Number 1, pp 6-17, January 1988.

[21] CARR, L.W., McALISTER, K.W. and McCROSKEY, W.J. Analysis of the development of dynamic stall based on oscillating airfoil experiments. N.A.S.A. Technical Note D-8382, January 1977.

[22] CARTA, F.O. Analysis of oscillatory pressure data including dynamic stall effects. N.A.S.A. Report CR-2394, 1974.

[23] CARTA, F.O., COMMERFORD, G.L., CARLSON, R.G. and BLACKWELL, R.H. Investigation of airfoil dynamic stall and its influence on helicopter control loads. U.S.A.A.M.R.D.L. Technical Report Number 72-51, September 1972.

[24] CHANG, P.K. Control of flow separation. Hemisphere Publishing Corporation, Washington, 1976. ISBN 0-07-010513-8.

[25] COTON, F.N. Contributions to the prediction of low Reynolds number aerofoil performance. Glasgow University Aero Report 8818, September 1988.

[26] CRIMI, P. Analysis of helicopter rotor blade torsional oscillations due to stall. N.A.S.A. Report CR-2573, September 1975.

[27] CRIMI, P. and REEVES, B.L. A method for analyzing dynamic stall. A.I.A.A. 10th AerospaceSciences Meeting, San Diego, California, January 1972.

[28] DADONE, L. Rotor airfoil optimization : an understanding of the physical limits. 34th Annual National Forum of the American Helicopter Society, Washington D.C., May 1978.

[29] DALEY, D.C. and JUMPER, E.J. Experimental investigation of dynamic stall for a pitching airfoil. Journal of Aircraft, Volume 21, Number 10, October 1984.

[30] DAVENPORT, F.J. and FRONT, J.V. Airfoil sections for helicopter rotors - a reconsideration. 22nd Annual National Forum of the American Helicopter Society, May 1966.

[31] ERICSSON, L.E. and REDING, J.P. Fluid mechanics of dynamic stall. Part I : Unsteady flow concepts. Journal of Fluids and Structures, Volume 2, pp 1-33, 1988.

[32] EVANS, W.T. and MORT, K.W. Analysis of computed flow separation parameters for a set of sudden stalls in low speed two-dimensional flow. N.A.S.A. Technical Note D-85, 1959.

[33] GALBRAITH, R.A.McD. Comments on the prediction of dynamic stall. Glasgow University Aero Report 8501, March 1985.

[34] GALBRAITH, R.A.McD., BARROWMAN, J. and LEISHMAN, J.G. Description of the sample-and-hold circuits for the Glasgow University dynamic stall facility. Glasgow University Aero Report 8208, 1982.

[35] GANGWANI, S.T. Synthesized airfoil data method for prediction of dynamic stall and unsteady airloads. Vertica, Volume 8, pp 93-118, 1984.

[36] GAULT, D.E. A correlation of low-speed, airfoil-section stalling characteristics with Reynolds number and airfoil geometry. N.A.C.A. Technical Note 3963, March 1957.

[37] GORMONT, R.E. A mathematical model of unsteady aerodynamics and radial flow for application to helicopter rotors. U.S. Army AMRDL - Eustis Directorate Report TR-72-51, 1972.

[38] GRACEY, M.W. and GALBRAITH, R.A.McD. An account of the design procedure of aerofoil section GU23012-MOD B. Glasgow University Aero Report 8608, January 1987.

[39] GRACEY, M.W. and GALBRAITH, R.A.McD. Data for a NACA 23012C aerofoil pitched about its quarter chord axis. Volume I : Pressure data from static and ramp function tests, with photographs of oil-flow visualistion tests. Glasgow University Aero Report 8901, January 1989.

[40] GRACEY, M.W. and GALBRAITH, R.A.McD. Data for a NACA 23012C aerofoil pitched about its quarter chord axis. Volume II : Pressure data from oscillatory tests. Glasgow University Aero Report 8902, January 1989.

[41] GREGORY, N., QUINCEY, V.G., O'REILLY, C.L. and HALL, D.J. Progress report on observations of three-dimensional flow patterns obtained during stall development on aerofoils, and on the problem of measuring two-dimensional characteristics. A.R.C. C.P. 1146, 1970.

[42] HAM, N.D. and GARELICK, M.S. Dynamic stall considerations in helicopter rotors. Journal of the American Helicopter Society, Volume 13, Number 2, pp 49-55, April 1968.

[43] HARRIS, F.D. and PRUYN, R.R. Blade stall - half fact, half fiction. Journal of the American Helicopter Society, Volume 13, Number 2, pp 27-48, April 1968.

[44] HARRIS, F.D., TARZANIN, F.J. and FISHER, R.K. Rotor high speed performance : theory versus test. Journal of the American Helicopter Society, Volume 15, Number 3, July 1970.

[45] HERRING, D.G.F. Ph.D. Dissertation, University of Glasgow, United Kingdom. (In preparation).

[46] HERRING, D.G.F. and GALBRAITH, R.A.McD. The collected data for tests on a NACA 23012B aerofoil. Volume 1 : Description, pressure data of static tests with oil flow visualistion. Glasgow University Aero Report 8808, June 1988.

[47] HERRING, D.G.F. and GALBRAITH, R.A.McD. The collected data for tests on a NACA 23012B aerofoil. Volume 2 : Description and pressure data of oscillatory tests. Glasgow University Aero Report 8809, June 1988.

[48] HERRING, D.G.F. and GALBRAITH, R.A.McD. The collected data for tests on a NACA 23012B aerofoil. Volume 3 : Description and pressure data of ramp function tests. Glasgow University Aero Report 8810, June 1988.

[49] HERRING, D.G.F. and GALBRAITH, R.A.McD. The collected data for tests on a NACA 23012B aerofoil. Volume 4 : Description and pressure data of arbitrary motion tests. Glasgow University Aero Report 8811, June 1988.

[50] HOUGHTON, E.L. and CARRUTHERS, N.B. Aerodynamics for engineering students. Third Edition. Edward Arnold, London, 1982. ISBN 0-7131-3433-X.

[51] HOUNSFIELD, F.R.S. The Handley-Page low-speed wind tunnel. Aircraft Engineering, July 1940.

[52] JOHNSON, W. and HAM, N.D. On the mechanism of dynamic stall. Journal of the American Helicopter Society, October 1972.

[53] KRAMER, M. Increase in the maximum lift of an aerofoil due to a sudden increase in its effective angle of attack resulting from a gust. N.A.C.A. Technical Memorandum 678, 1932.

[54] LEISHMAN, J.G. A user guide for the Glasgow University potential flow computer programs. Glasgow University Aero Report 8103, May 1981.

[55] LEISHMAN, J.G. Contributions to the experimental investigation and analysis of aerofoil dynamic stall. Ph.D. Dissertation, University of Glasgow, United Kingdom, March 1984.

[56] LEISHMAN, J.G. and BEDDOES, T.S. A semi-empirical model for dynamic stall. Journal of the American Helicopter Society, Volume 34, Number 3, July 1989.

[57] LEISHMAN, J.G. and GALBRAITH, R.A.McD. An algorithm for the calculation of the potential flow about an arbitrary two-dimensional aerofoil. Glasgow University Aero Report 8102, May 1981.

[58] LEISHMAN, J.G., SETO, L.Y. and GALBRAITH, R.A.McD. Collected data for sinusoidal tests on a NACA 23012 aerofoil. Glasgow University Aero Report 8600, March 1986.

[59] LEITCH, E.L. and GALBRAITH, R.A.McD. Guide to the Glasgow University aerofoil database - Version I. Glasgow University Aero Report 8700, February 1987.

[60] LEONARD, A. Vortex methods for flow simulation. Journal of Computational Physics, Volume 37, pp 289-335, 1980.

[61] LORBER, P.F. and CARTA, F.O. Unsteady stall penetration experiments at high Reynolds number. United Technologies Research Center Report R87-956939-3, April 1987.

[62] McALISTER, K.W. and CARR, L.W. Dynamic stall experiments on the NACA 0012 airfoil. N.A.S.A. Technical Paper 1100, January 1978.

[63] McALISTER, K.W., PUCCI, S.L., McCROSKEY, W.J. and CARR, L.W. An experimental study of dynamic stall on advanced aerofoil sections. Volume 2 : Pressure and force data. N.A.S.A. Technical Memorandum 84245, USAAVRADCOM TR-82-A-8, September 1982.

[64] McCROSKEY, W.J. The phenomenon of dynamic stall. Von Karman Institute for Fluid Dynamics Lecture Series 1981-4 : Unsteady airloads and aeroelastic problems in separated and transonic flow, March 1981.

[65] McCROSKEY, W.J., CARR, L.W. and McALISTER, K.W. Dynamic stall experiments on oscillating airfoils. AIAA Journal, Volume 14, Number 1, pp 57-63, January 1976.

[66] McCROSKEY, W.J. and FISHER, R.K., jnr. Detailed aerodynamic measurements on a model rotor in the blade stall regime. Journal of the American Helicopter Society, Volume 17, Number 1, pp 20-30, January 1972.

[67] McCROSKEY, W.J., McALISTER, K.W., CARR, L.W., PUCCI, S.L., LAMBERT, O. and INDERGAND, R.F. Dynamic stall on advanced airfoil sections. Journal of the American Helicopter Society, Volume 13, Number 1, pp 40-50, January 1981.

[68] McCULLOUGH, G.B. and GAULT, D.E. Examples of three representative types of airfoil-section stall at low speed. N.A.C.A. Technical Note 2502, September 1951.

[69] MEGSON, T.H.G. Aircraft structures for engineering students. Edward Arnold, London, 1977. ISBN 0 7131 3393 7.

[70] MILEY, S.J. A catalog of low-Reynolds-number airfoil data for wind-turbine applications. Department of Aerospace Engineering, Texas A&M University, February 1982.

[71] MOSS, G.F. and MURDIN, P.M. Two-dimensional low-speed tunnel tests on the NACA 0012 section, including measurements made during pitching oscillations at the stall. R.A.E. Technical Report ARC CP 1145, May 1968.

[72] MURRAY-SMITH, E. and GALBRAITH, R.A.McD. User manual for the Glasgow University unsteady aerodynamic facility software. Glasgow University Aero Report 8800, February 1988.

[73] NIVEN, A.J. An experimental investigation into the influence of trailing edge separation on an aerofoil's dynamic stall performance. Ph.D. Dissertation, University of Glasgow, United Kingdom, September 1988.

[74] NIVEN, A.J. Preliminary comparisons between a semi-empirical dynamic stall model and unsteady aerodynamic data obtained from low Mach number wind-tunnel tests. Glasgow University Aero Report. (In preparation).

[75] NIVEN, A.J. and GALBRAITH, R.A.McD. The design procedure to modify the trailing edge upper surface pressure gradient of a given aerofoil. Glasgow University Aero Report 8408, July 1984.

[76] NIVEN, A.J. and GALBRAITH, R.A.McD. An investigation into the three-dimensional stall developments on modified NACA 23012 aerofoil. Glasgow University Aero Report 8414, November 1984.

[77] NIVEN, A.J., GALBRAITH, R.A.McD and HERRING, D.G.F. Analysis of reattachment during ramp down tests. Vertica, Volume 13, Number 2, pp 187-196, 1989.

[78] PROUTY, R.W. A state-of-the-art survey of two-dimensional airfoil data. Journal of the American Helicopter Society, Volume 20, Number 10, pp 14-24, October 1975.

[79] RIEGELS, F.W. (translated Randall, D.G.) Aerofoil sections, results from wind-tunnel investigations, theoretical foundations. Butterworths, London, 1961. UDC 533.6.01.

[80] SCRUGGS, L.Y., NASH, J.F. and SINGLETON, R.E. Analysis of dynamic stall using unsteady boundary layer theory. N.A.S.A. Report CR-2462, October 1974.

[81] SEARS, W.R. and TELIONIS, D.P. Unsteady boundary-layer separation. In Recent research on unsteady boundary layers (Proceedings of the I.U.T.A.M. Symposium, Quebec, 1971), edited by Eichelbrenner, E.A., Presses de L'universite Laval, Quebec, 1972.

[82] SETO, L.Y. An experimental investigation of low speed dynamic stall and reattachment of the NACA 23012 aerofoil under constant pitch motion. Ph.D. dissertation, University of Glasgow, United Kingdom, August 1988.

[83] SETO, L.Y. and GALBRAITH, R.A.McD. The collected data for ramp function tests on a NACA 23012 aerofoil. Volume 1: Description and pressure data. Glasgow University Aero Report 8413, November 1984.

[84] SETO, L.Y. and GALBRAITH, R.A.McD. The effect of pitch-rate on the dynamic stall of a NACA 23012 aerofoil. 11th European Rotorcraft Forum, Paper Number 34, London, September 10-13, 1985.

[85] SETO, L.Y., LEISHMAN, J.G. and GALBRAITH, R.A.McD. An investigation of the three-dimensional stall developments on NACA 23012 and NACA 0012 aerofoils. Glasgow University Aero Report 8300, January 1983.

[86] STEPHENS, R.C. Strength of materials : theory and examples. Edward Arnold, London, 1970. ISBN 0 7131 3211 6.

[87] TARZANIN, F.J., jnr. Prediction of control loads due to blade stall. 27th Annual National Forum of the American Helicopter Society, May 1971.

[88] TRAN, C.T. and PETOT, D. Semi-empirical model for the dynamic stall of airfoils in view of the application to the calculation of responses of a helicopter blade in forward flight. 6th European Rotorcraft and Powered Lift Aircraft Forum, Bristol, September 16-19, 1980.

[89] VEZZA, M. Numerical methods for the design and unsteady analysis of aerofoils. Ph.D. dissertation, University of Glasgow, United Kingdom, April 1986.

[90] VEZZA, M. and GALBRAITH, R.A.McD. A comparison of two new methods for the design of aerofoils with specific pressure distributions. Glasgow University Aero Report 8303, June 1983.

[91] WILBY, P.G. The aerodynamic characteristics of some new RAE blade sections, and their potential influence on rotor performance. Vertica, Volume 4, pp 121-133, 1980.

[92] WILBY, P.G. An experimental investigation of the influence of a range of aerofoil design features on dynamic stall onset. 10th European Rotorcraft Forum, Paper Number 2, August 28-31, 1984.

[93] YOUNG, W.H., jnr. Fluid mechanics mechanisms in the stall process for helicopters. N.A.S.A. Technical Memorandum 81956, USAAVRADCOM TR 81-B-1, March 1984.

APPENDIX A

DERIVATION OF INFLUENCE COEFFICIENTS FOR THE CALCULATION OF POTENTIAL FLOW ABOUT AN ARBITRARY AEROFOIL

This model is based on the algorithm of LEISHMAN AND GALBRAITH [57]. It makes use of a continuous and piecewise-linear distribution of panel vorticity. The important points of interest are illustrated in Figures A.1 and A.2.

The aerofoil profile is replaced by a polygon of N sides, or panels, the corners of which lie on the surface of the aerofoil. The co-ordinates of each corner point are

$$(x_i, y_i), \quad i=1,2...,N+1.$$

The point (x_1, y_1) is located at the upper surface trailing edge and the indices of all subsequent points increase monotonically with travel around the polygon in an anti-clockwise direction.

The i^{th} panel stretches from (x_i, y_i) to (x_{i+1}, y_{i+1}). At the mid-point of the i^{th} panel lies the

i^{th} control point (xc_i, yc_i). It follows that

$$xc_i=(x_i+x_{i+1})/2 \tag{A.1a}$$

$$yc_i=(y_i+y_{i+1})/2. \tag{A.1b}$$

The length L_i of the i^{th} panel is given by

$$L_i = \sqrt{(x_{i+1} - x_i)^2 + (y_{i+1} - y_i)^2}\ .$$

The unit vector $\vec{n_i}$ normal to the i^{th} panel is given by

$$\vec{n}_i = (y_{i+1} - y_i,\ x_i - x_{i+1}) / L_i. \tag{A.2}$$

Now consider the j^{th} panel, which is, in general, distinct from the i^{th} panel. The co-ordinates (x_p,y_p) at any position on this panel are given by

$$x_p = x_j + (x_{j+1} - x_j)\ S_j / L_j \tag{A. 3a}$$

$$y_p = y_j + (y_{j+1} - y_j)\ S_j / L_j, \tag{A. 3b}$$

where S_j represents the distance along the j^{th} panel from (x_j, y_j).

The aerofoil contour is replaced by a vortex sheet of unknown variable strength. The strength per unit length of this vortex sheet at (x_j, y_j) is represented by γ_j and the value of γ is assumed to vary linearly along each panel. Therefore, at the point (x_p,y_p), the vortex sheet strength γ_p is given by

$$\gamma_p = \gamma_j + (\gamma_{j+i} - \gamma_j)S_j/L_j. \tag{A.4}$$

This vortex strength is defined as being positive in the clockwise direction.

The vector $\vec{r}_{ji}$ is defined as being the vector from the point (x_p,y_p) to the i^{th} panel control point,

i.e. $\vec{r}_{ji} = (xc_i - x_p,\ yc_i - y_p)$.

Therefore, the distance $|r_{ji}|$ between these points is given by

$$|r_{ji}| = \sqrt{(xc_i - x_p)^2 + (yc_i - y_p)^2}. \qquad (A.5)$$

The unit vector normal to $\vec{r}_{ji}$ in the plane of the aerofoil profile is represented by $\vec{r}_{n/i}$. Therefore

$$\vec{r}_{n/i} = (yc_i - y_p, x_p - xc_i)/|r_{ji}|. \qquad (A.6)$$

The fluid velocity $\vec{U}$ at any point is given by

$$\vec{U} = \vec{U}_\infty + \vec{u},$$

where $\vec{U}_\infty$ represents the uniform freestream velocity and $\vec{u}$ represents the perturbation velocity induced at that point by the vortex sheet. If the angle of attack of the aerofoil is represented by α, then

$$U_\infty = (|U_\infty|\cos\alpha, |U_\infty|\sin\alpha). \qquad (A.7)$$

The induced velocity $\overrightarrow{du}_{ij}$ at the control point on the i^{th} panel due to an element dS_j on the j^{th} panel is given by

$$\overrightarrow{du}_{ij} = (\gamma_p dS_j \vec{r}_{n/i})/(2\pi|r_{ji}|).$$

Therefore, the induced velocity $\vec{u}_{ij}$ at the control point on the i^{th} panel due to the entire aerofoil is given by

$$\vec{u}_{ij} = (1/2\pi)\int_0^{Lj} \gamma_p \vec{r}_{n/i}/|r_{ji}|.dS_j. \qquad (A.8)$$

It follows that the induced velocity $\vec{u}_i$ at the control point on the i^{th} panel due to the entire aerofoil is given by

$$\vec{u}_i = \sum_{j=1}^{N} \vec{u}_{ij}$$

$$= (1/2\pi)\sum_{j=1}^{N}\int_0^{Lj} \gamma_p \vec{r}_{n/i}/|r_{ji}|.dS_j.$$

From (A.2) and (A.8), it follows that the component of $\vec{u}_{ij}$ normal to the i^{th} panel is given by

$$u_{nij} := \vec{u}_{ij}.\vec{n}_i$$

$$= (1/2\pi)\int_0^{Lj} \gamma_p(\vec{r}_{nji}.\vec{n}_i)/|r_{ji}|.dS_j . \qquad (A.9)$$

In addition, from (A.2) and (A.7), it follows that the component of freestream velocity normal to the i^{th} panel is given by

$$\vec{U}_\infty.\vec{n}_i = |U_\infty|[(y_{i+1}-y_i)\cos\alpha - (x_{i+1}-x_i)\sin\alpha]/L_i \qquad (A.10)$$

Therefore, the component of fluid velocity normal to the surface of the aerofoil at the i^{th} control point is given by

$$\vec{U}_i.\vec{n}_i = \vec{U}_\infty.\vec{n}_i + \sum_{j=1}^{N} u_{nij},$$

as defined by equations (A.9) and (A.10). The boundary condition of zero flow normal to the surface is applied at each control point and so

$$\vec{U}_i.\vec{n}_i = 0,\ i = 1,2...,N. \qquad (A.11)$$

A set of N equations in N+1 unknown variables can be formed from (A.11). These variables are the vortex strength values γ_i at the corner points of each panel. In order that a unique set of solutions for γ be found, an additional condition must be imposed. This is the Kutta condition of zero loading at the trailing edge, and results in

$$\gamma_1 + \gamma_{N+1} = 0. \qquad (A.12)$$

Before solving the system of equations (A.11) and (A.12), equation (A.9) must be simplified. The special case of j = i will be considered later. However, when $j \neq i$, the substitution of (A.2), (A.3), (A.4), (A.5) and (A.6) into (A.9) yields

$$u_{n\,ij} = \frac{1}{2\pi Li}\int_0^{Lj} \frac{\{L_j\gamma_j + (\gamma_{j+1}-\gamma_j)S_j\}\{[(yc_i-y_j)L_j-(y_{j+1}-y_j)S_j][y_{i+1}-y_i]+[(x_j-xc_i)L_j+(x_{j+i}-x_j)S_j][x_i-x_{i+1}]\}}{\{[(xc_i-x_j)L_j-(x_{j+i}-x_j)S_j]^2+[(yc_i-y_j)L_j-(y_{j+1}-y_j)S_j]^2\}}dS_j$$

$$= \frac{1}{2\pi Li}\int_0^{Lj} \frac{(\gamma_{j+1}-\gamma_j)\mu S_j^2+[\gamma_{j+1}\upsilon+\gamma_j(\mu-\upsilon)]L_jS_j+\gamma_jL_j^2\upsilon}{(L_jS_j-\xi)^2+\eta^2}dS_j, \qquad (A.13)$$

where

$$\mu := (x_i - x_{i+1})(x_{j+1} - x_j) + (y_i - y_{i+1})(y_{j+1} - y_j)$$

$$\upsilon := (x_i - x_{i+1})(x_j - xc_i) + (y_i - y_{i+1})(y_j - yc_i)$$

$$\xi := (xc_i - x_j)(x_{j+1} - x_j) + (yc_i - y_j)(y_{j+1} - y_j)$$

$$\eta := (yc_i - y_j)(x_{j+1} - x_j) - (xc_i - x_j)(y_{j+1} - y_j).$$

By making the substitution

$$\theta = \tan^{-1}((L_j S_j - \xi)/\eta),$$

(A.13) becomes

$$u_{n\,ij} = (1/2\pi Li)\int_{\beta}^{\delta} (A\tan^2\theta + B\tan\theta + C)/L_j^3\,\eta.d\theta, \qquad (A.14)$$

where

$$\beta := \tan^{-1}(-\xi/\eta)$$

$$\delta := \tan^{-1}((L_j^2 - \xi)/\eta)$$

$$A := (\gamma_{j+i} - \gamma_j)\mu\eta^2 \qquad (A.15)$$

$$B := 2(\gamma_{j+i} - \gamma_j)\mu\xi\eta + L_j^2[\gamma_{j+i}\upsilon + \gamma_j(\mu - \upsilon)]\eta \qquad (A.16)$$

$$C := (\gamma_{j+i} - \gamma_j)\mu\xi^2 + L_j^2[\gamma_{j+i}\upsilon + \gamma_j(\mu - \upsilon)]\xi + \gamma_j L_j^4\upsilon. \qquad (A.17)$$

Integrating the right hand side of (A.14) yields

$$u_{n\,ij} = [A(\tan\beta - \tan\alpha) + B\ln|\sec\beta/\sec\alpha| + (C\text{-}A)(\beta - \alpha)]/(2\pi L_i L_j^3\eta)$$

$$= [AL_j^2/\eta + B\ln|\sqrt{(L_j^2 - \xi)^2 + \eta^2}/\sqrt{\xi^2 + \eta^2}| + (C\text{-}A)(\delta - \beta)]/(2\pi L_i L_j^3\eta)$$

$$= \{\gamma_j[-\mu + (\mu - \Gamma)\Phi + (L_j^2\upsilon + \mu\xi - \Psi)\Omega] + \gamma_{j+i}[\mu + \Gamma\Phi + \Psi\Omega]\}/(2\pi L_i L_j), \qquad (A.18)$$

where

$$\Gamma := (2\mu\xi + L_j^2\upsilon)/L_j^2$$

$$\Phi := \ln|\sqrt{(L_j^2 - \xi)^2 + \eta^2}/\sqrt{\xi^2 + \eta^2}|$$

$$\Psi := [\mu(\xi^2 - \eta^2) + L_j^2\upsilon\xi]/L_j^2$$

$$\Omega := (\delta - \beta)/\eta$$

and where equations (A.15), (A.16) and (A.17) have been employed. Equation (A.18) may be rewritten as

$$u_{n\,ij} = (A_{ij}\,\gamma_j + B_{ij}\,\gamma_{j+1})/(2\pi L_i), \tag{A.19}$$

where

$$A_{ij} := [-\mu + (\mu - \Gamma)\Phi + (L_j^2\upsilon + \mu\xi - \Psi)\Omega]/L_j \tag{A.20a}$$

$$B_{ij} := [\mu + \Gamma\Phi + \Psi\Omega]/L_j\,. \tag{A.20b}$$

When j=i, the method which has been described above fails as a consequence of the discontinuity in equation (A.9) at the control point. Therefore, this special case must be treated separately. It can be seen that

$$\overrightarrow{r_{nii}}\,.\,\overrightarrow{n_{ii}} = 1 \text{ for } S_i < L_i/2$$

$$\overrightarrow{r_{nii}}\,.\,\overrightarrow{n_{ii}} = -1 \text{ for } S_i > L_i/2.$$

Therefore,

$$u_{n\,ii} = (1/2\pi)\int_0^{L_i/2} \gamma_p/\left|r_{ii}\right|.dS_i \; - (1/2\pi)\int_{Li/2}^{Li} \gamma_p/\left|r_{ii}\right|.dS_i$$

$$= (I+J)/2\pi, \tag{A.21}$$

where, by employing (A.4), (A.5) and (A.3),

$$I := \int_0^{L_i/2} \frac{[\gamma_i + (\gamma_{i+1} - \gamma_i)S_i/L_i]dS_i}{\{[xc_i - x_i - (x_{i+1} - x_i)S_i/L_i]^2 + [yc_i - y_i - (y_{i+1} - y_i)S_i/L_i]^2\}^{1/2}}$$

$$J := \int_{Li/2}^{Li} \frac{[\gamma_i + (\gamma_{i+1} - \gamma_i)S_i/L_i]dS_i}{\{[xc_i - x_i - (x_{i+1} - x_i)S_i/L_i]^2 + [yc_i - y_i - (y_{i+1} - y_i)S_i/L_i]^2\}^{1/2}}\,.$$

In I, let

$$v = S_i/L_i$$

and, in J, let

$$v = 1 - S_i/L_i\,.$$

Equation (A.21) then becomes

$$u_{n\,ii} = (1/2\pi)\int_0^{1/2} (\gamma_i - \gamma_{i+1})(1-2v)/(1/2-v).dv$$

$$= \lim_{R \to 1/2} (1/2\pi)\int_0^R (\gamma_i - \gamma_{i+1})(1-2v)/(1/2-v).dv$$

$$= \lim_{R \to 1/2} [(\gamma_i - \gamma_{i+1})/2\pi]\int_0^R 2dv$$

$$= (A_{ii}\gamma_i + B_{ii}\gamma_{i+1})/2\pi L_i), \qquad \text{(A.22)}$$

where

$$A_{ii} := L_i \qquad \text{(A.23a)}$$

$$B_{ii} := -L_i \qquad \text{(A.23b)}$$

and where equation (A.1) has been employed.

From equations (A.19) and (A.22), it follows that

$$\sum_{j=1}^{N} u_{n\,ij} = (1/2\pi L_i)\sum_{j=1}^{N}(A_{ij}\gamma_j + B_{ij}\gamma_{j+1})$$

$$= (1/2\pi L_i)[A_{i1}\gamma_1 + \sum_{j=2}^{N}(A_{ij} + B_{i,j-1})\gamma_j + B_{iN}\gamma_{N+1}]$$

$$= (1/2\pi L_i)\sum_{j=1}^{N+1} C_{ij}\gamma_j, \qquad \text{(A.24)}$$

where

$$C_{i1} := A_{i1}$$

$$C_{ij} := A_{ij} + B_{i,j-1},\ j = 2,...,N$$

$$C_{i,N+1} := B_{iN}.$$

and where the values of A_{ij} and B_{ij} are determined from equations (A.20) and (A.23). The terms C_{ij} are the influence coefficients, and depend only on the geometry of the aerofoil.

Substituting (A.10) and (A.24) into (A.11) yields

$$\left|U_\infty\right|[(y_{i+1} - y_i)\cos\alpha - (x_{i+1} - x_i)\sin\alpha]/L_i + (1/2\pi L_i)\sum_{j=1}^{N+1} C_{ij}\gamma_j = 0,\ i = 1,2,...,N$$

$$\Rightarrow \sum_{j=1}^{N+1} C_{ij}\gamma_j = 2\pi\left|U_\infty\right|[(x_{i+1} - x_i)\sin\alpha - (y_{i+1} - y_i)\cos\alpha],\ i=1,2,..,N, \qquad \text{(A.25)}$$

subject to Kutta condition (A.12).

A FORTRAN 77 subroutine has been coded in order that the system of equations (A.25) and (A.12) be created and solved. When compared to the original code by LEISHMAN [54] over the range of panels which are generated for current research (i.e. $50 \leq N \leq 100$), the calculation time is found to have been reduced to as little as 30% of its original value. The solutions yielded by the two algorithms are identical.

APPENDIX B

DETERMINATION OF COEFFICIENTS IN SEPARATION POINT EQUATIONS

An approximation to the location of boundary layer separation at any angle of attack for an aerofoil experiencing trailing edge separation has been described by BEDDOES [14]. The variation of the separation point with angle of attack is modelled by two exponential equations which coincide when the boundary layer separates at the 70% chord location. It was decided that these equations should be generalised to the form

$$f = f_{max} + K_1 \exp((\alpha - \alpha_1)/S_1), \text{ for } \alpha \leq \alpha_1 \quad \text{(B.1a)}$$

$$f = f_{min} + K_2 \exp((\alpha_1 - \alpha)/S_2), \text{ for } \alpha \geq \alpha_1, \quad \text{(B.1b)}$$

where α represents the angle of attack and f represents the separation point in the form of x/c, the ratio of distance along the chord from the leading edge to the length of chord. The remaining seven coefficients are constant for a particular aerofoil and Reynolds number, and are evaluated for any set of data points $\{(\alpha, f)\}$ by the following method.

The values of f_{max} and f_{min} are simply the respective maximum and minimum values of f which are recorded over the range of data points. When $\alpha = \alpha_1$, the values of f which are obtained from equations (B.1a) and (B.1b) must be equal. Therefore

$$f_{max} + K_1 = f_{min} + K_2$$

$$\Rightarrow \quad K_2 = K_1 + \Delta f, \tag{B.2a}$$

where

$$\Delta f := f_{max} - f_{min}. \tag{B.2b}$$

If f_{max} and f_{min} are to be the maximum and minimum values, it follows, from equation (B.1), that $K_1 < 0$ and $K_2 > 0$. It may also be noted that $\Delta f \approx 1.0$.

Now, for $\alpha \leq \alpha_1$,

$$f = f_{max} + K_1 \exp((\alpha - \alpha_1)/S_1)$$

$$\Rightarrow \quad \alpha = \alpha_1 + S_1 \ln((f - f_{max})/K_1)$$

$$= [\alpha_1 - S_1 \ln(-K_1)] + S_1 \ln(f_{max} - f)$$

$$= C_1 + S_1 X_1; \tag{B.3}$$

where

$$C_1 := \alpha_1 - S_1 \ln(-K_1) \tag{B.4}$$

$$X_1 := \ln(f_{max} - f). \tag{B.5}$$

For $\alpha \geq \alpha_1$,

$$f = f_{min} + (K_1 + \Delta f) \exp((\alpha_1 - \alpha)/S_2)$$

$$\Rightarrow \quad \alpha = \alpha_1 - S_2 \ln((f - f_{min})/(K_1 + \Delta f)$$

$$= [\alpha_1 + S_2 \ln(K_1 + \Delta f)] - S_2 \ln(f - f_{min})$$

$$= C_2 - S_2 X_2, \tag{B.6}$$

where

$$C_2 := \alpha_1 + S_2 \ln(K_1 + \Delta f) \tag{B.7}$$

$$X_2 := \ln (f - f_{min}). \qquad \text{(B.8)}$$

The set of data points are now split into two mutually exclusive subsets: one consisting of points for which $\alpha \leq \alpha_1$ and one of points for which $\alpha > \alpha_1$. Obviously it is impossible to know the value of α_1 before it is calculated. Therefore it is necessary to repeat the following procedure over the entire possible range of distribution of the subsets. After performing the procedure, the least- squares error between the recorded values of f and those calculated from the obtained coefficients is calculated. The set of coefficients which yields the smallest error is regarded as being the solution set.

For each subset, the value of X_1 or X_2 is calculated from equation (B.5) or (B.8). Hence, the values of C_1, C_2, S_1, and S_2 are approximated from least-squares regression and equations (B.3) and (B.6). It is possible to assign suitable weight values to the data points. From equations (B.4) and (B.7), it follows that

$$\begin{aligned} C_2 - C_1 &= S_1 \ln (-K_1) + S_2 \ln (K_1 + \Delta f) \\ &= \ln((-K_1)^{S_1}(K_1 + \Delta f)^{S_2}) \\ \Rightarrow \quad (-K_1)^{S_1} &+ (K_1 - \Delta f)^{-S_2} \exp (C_2 - C_1) = 0. \end{aligned} \qquad \text{(B.9)}$$

A value for K_1 in equation (B.9) can be approximated by a numerical algorithm (e.g. Newton's Method, Bisection Method) and, hence, values can be assigned to the coefficients in equation (B.1) via equations (B.2), (B.4) and (B.7).

As described above, the accuracy of these coefficients is evaluated and the process repeated over the range of all possible subsets of the original data set.

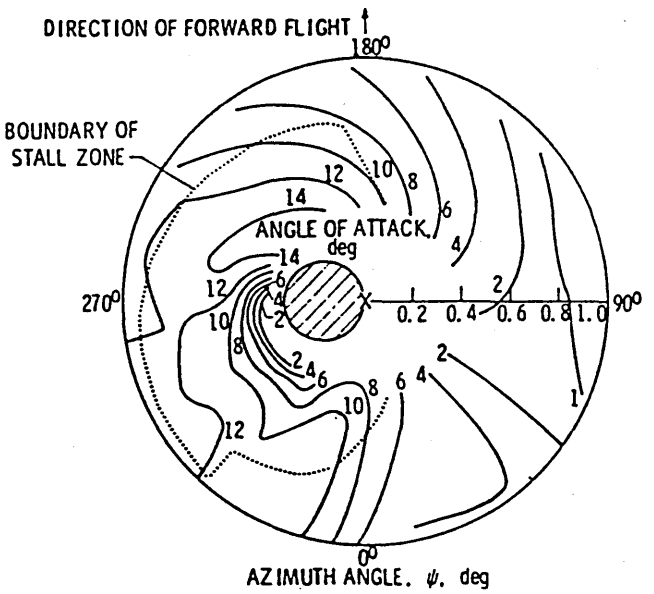

Figure 1.1 : Computed angle of attack distribution for helicopter rotor. (from CRIMI [26])

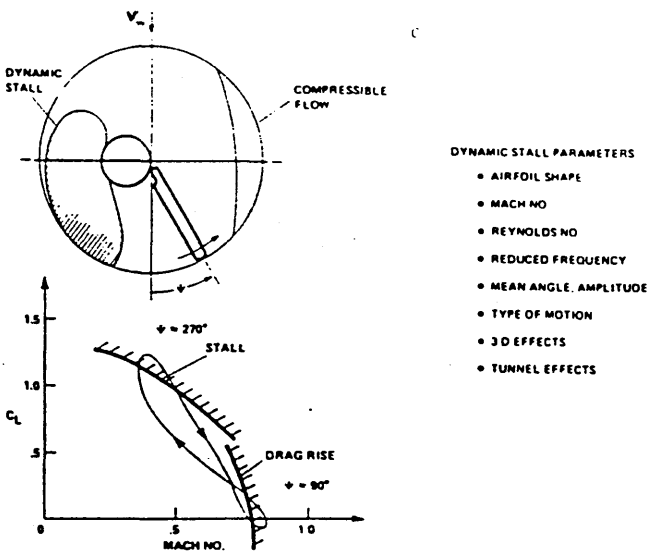

Figure 1.2 : Helicopter rotor aerofoil requirements. (from CARR [20])

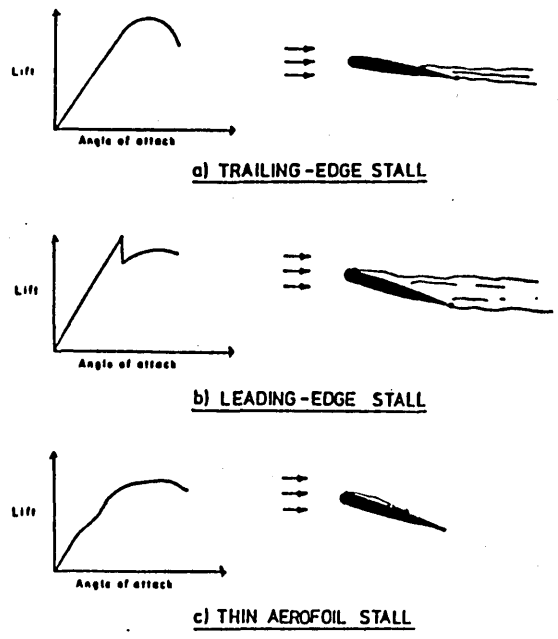

Figure 1.3 : The three types of basic static stall for aerofoils.
(from CRIMI AND REEVES [27])

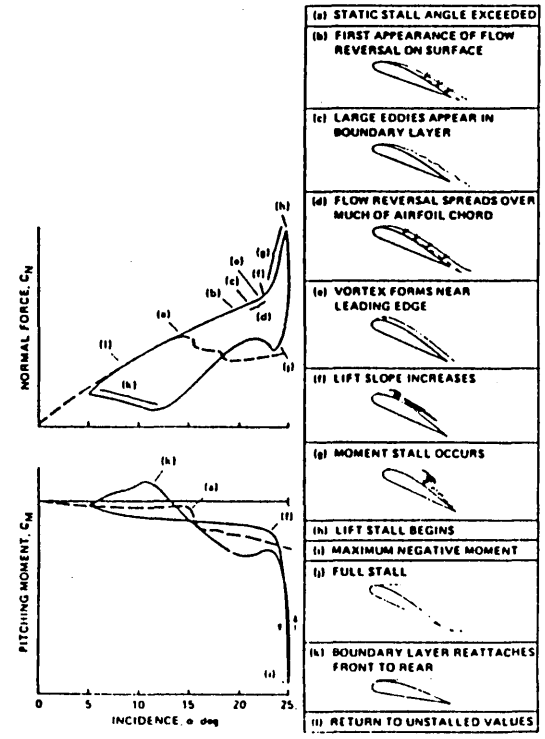

Figure 1.4 : Events of dynamic stall on the NACA 0012 aerofoil.
(from CARR [20])

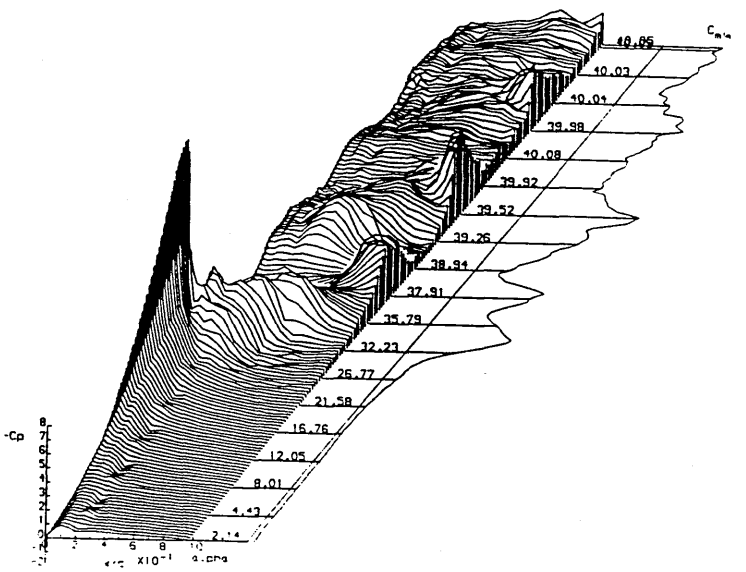

Figure 1.5 : Variation of pressure coefficient distribution with time for the NACA 23012 aerofoil.

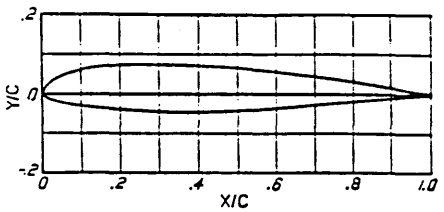

NACA 23012
(Stations and ordinates given in per cent of airfoil chord)

Upper surface		Lower surface	
Station	Ordinate	Station	Ordinate
0	.....	0	0
1.25	2.67	1.25	− 1.23
2.5	3.61	2.5	− 1.71
5.0	4.91	5.0	− 2.26
7.5	5.80	7.5	− 2.61
10	6.43	10	− 2.92
15	7.19	15	− 3.50
20	7.50	20	− 3.97
25	7.60	25	− 4.28
30	7.55	30	− 4.46
40	7.14	40	− 4.48
50	6.41	50	− 4.17
60	5.47	60	− 3.67
70	4.36	70	− 3.00
80	3.08	80	− 2.16
90	1.68	90	− 1.23
95	0.92	95	− 0.70
100	(0.13)	100	(− 0.13)
100	.....	100	0

L.E. radius: 1.58
Slope of radius through L.E.: 0.305

Figure 2.1 : NACA 23012 aerofoil profile and coordinates.
(from ABBOTT AND VON DOENHOFF [1])

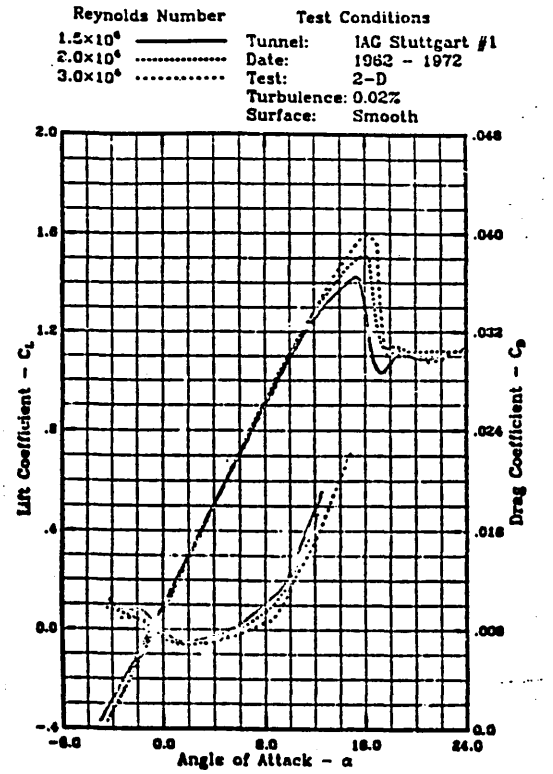

Figure 2.2 : Static lift and drag coefficients for the NACA 23012 aerofoil.
(from MILEY [70])

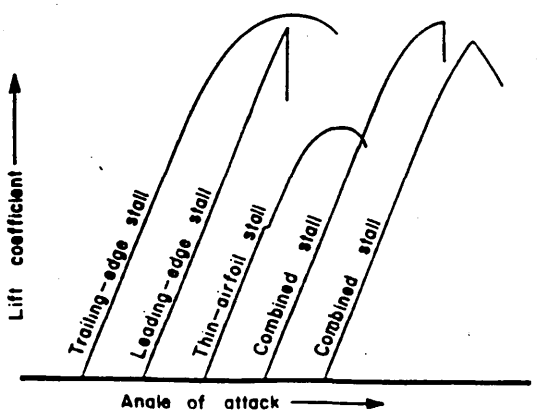

Figure 2.3 : Basic static stall lift characteristics.
(from GAULT [36])

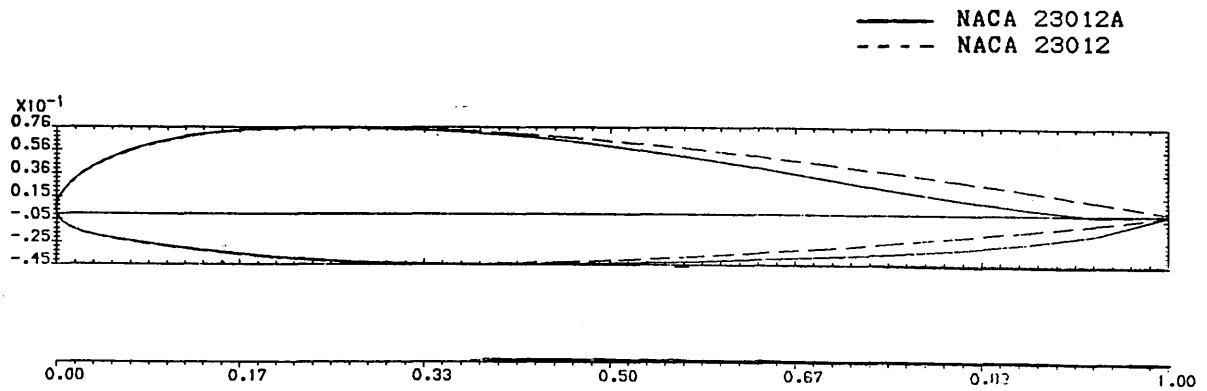

Figure 2.4 : Comparison of profiles of NACA 23012 and NACA 23012A aerofoils.

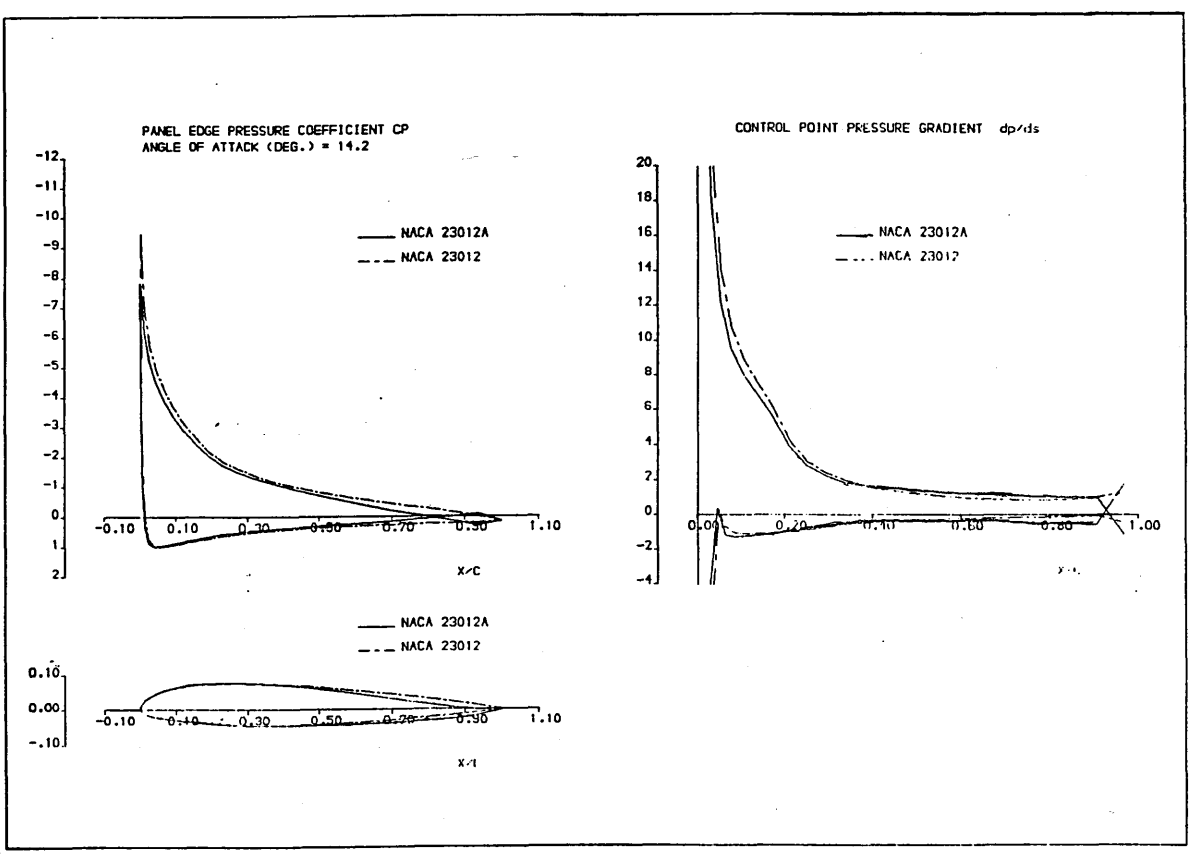

Figure 2.5 : Comparison of pressure distributions of NACA 23012 and NACA 23012A aerofoils.

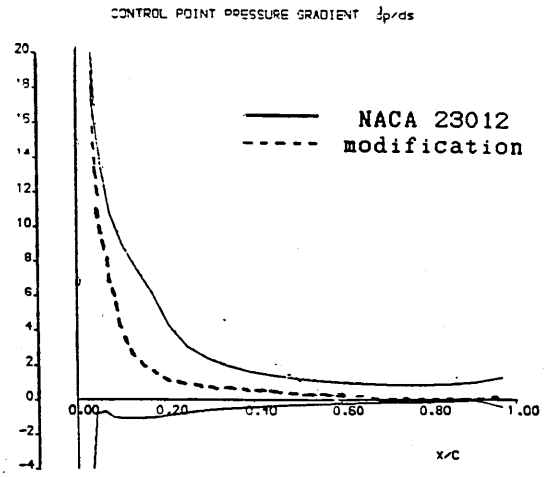

Figure 2.6 : Possible pressure gradient to encourage more sudden stall than for NACA 23012 aerofoil.

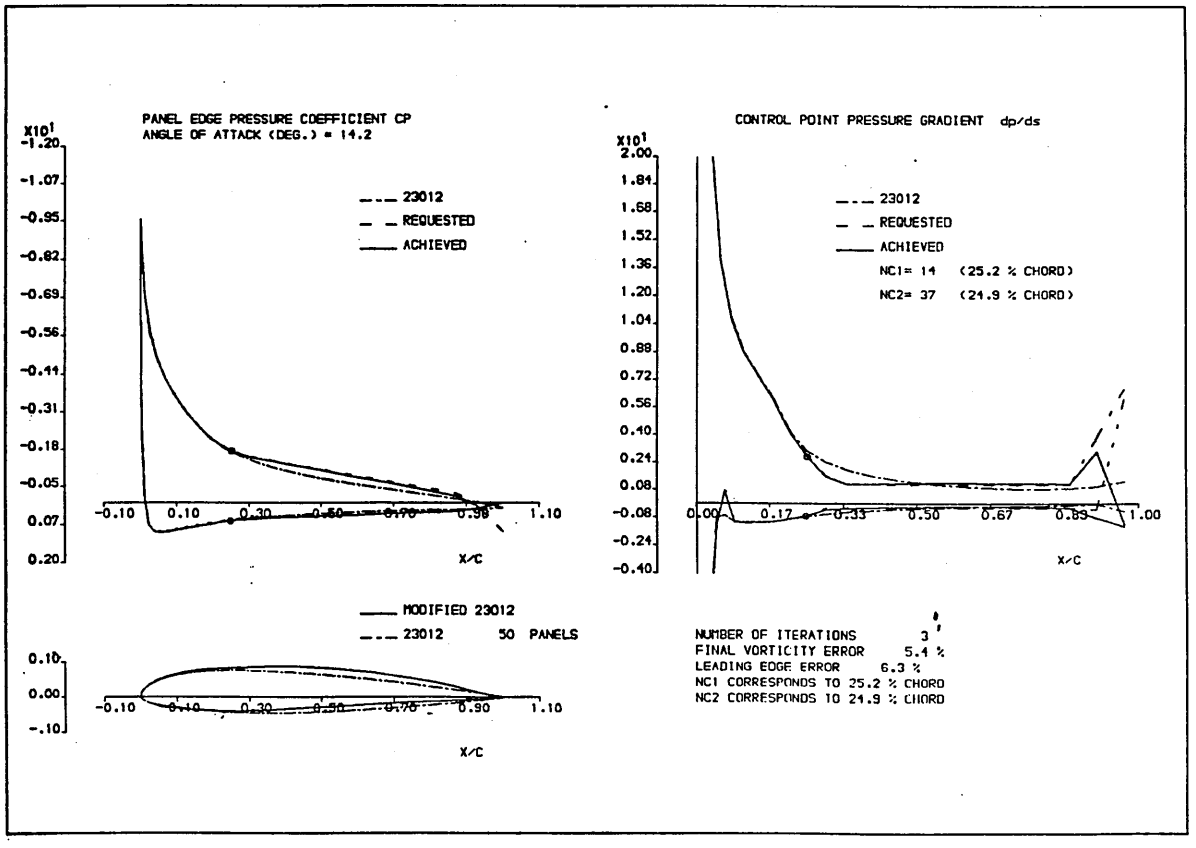

Figure 2.7 : Modifications to NACA 23012 aerofoil which were requested and achieved.

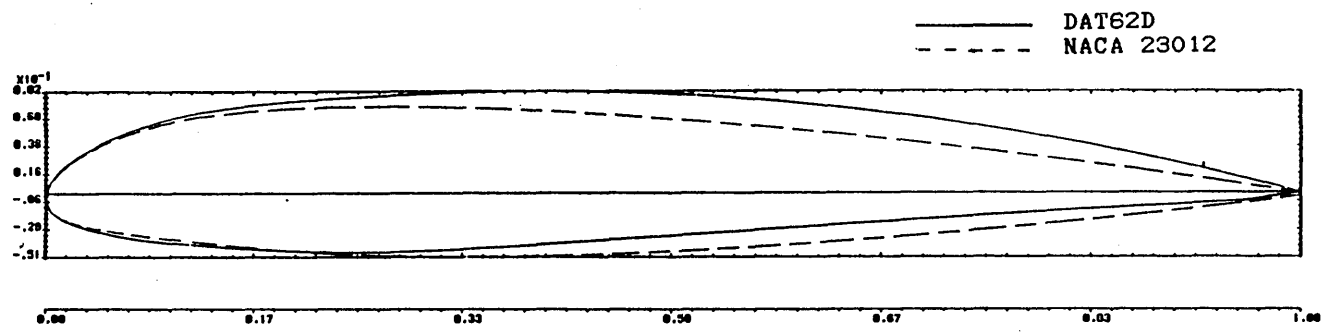

Figure 2.8 : Comparison of profiles of NACA 23012 and DAT62D aerofoils.

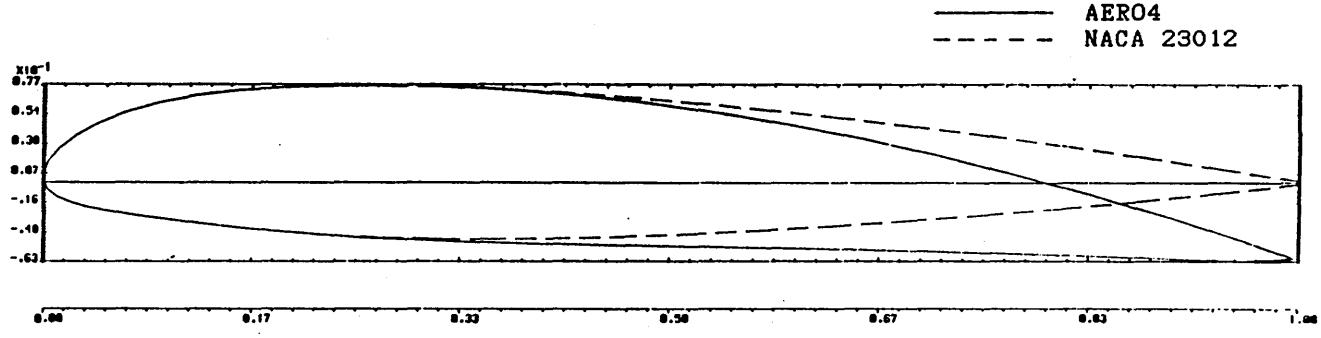

Figure 2.9 : Comparison of profiles of NACA 23012 and AERO4 aerofoils.

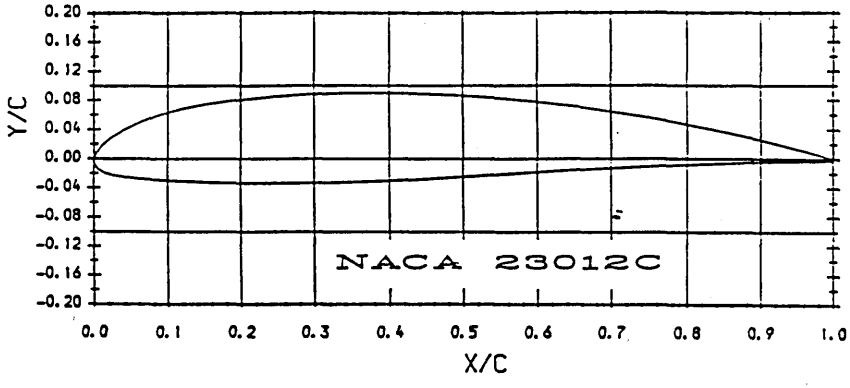

Upper Surface		Lower Surface	
Station	Ordinate	Station	Ordinate
0.000	0.000	0.000	0.000
0.341	0.917	0.657	-1.453
1.124	1.932	1.472	-1.948
2.366	3.009	2.614	-2.310
4.071	4.097	4.064	-2.568
6.232	5.135	5.811	-2.757
8.826	6.072	7.854	-2.905
11.813	6.862	10.206	-3.038
15.139	7.489	12.892	-3.167
18.741	7.965	15.942	-3.291
22.585	8.339	19.393	-3.386
24.873	8.529	23.243	-3.401
29.023	8.783	29.525	-3.345
33.467	8.942	33.969	-3.245
38.184	8.985	38.681	-3.062
43.156	8.914	43.641	-2.830
48.362	8.702	48.829	-2.515
53.782	8.335	54.223	-2.187
59.395	7.803	59.803	-1.857
65.178	7.105	65.546	-1.533
71.108	6.243	71.429	-1.224
77.162	5.222	77.429	-0.931
83.316	4.046	83.523	-0.657
89.547	2.684	89.686	-0.419
95.829	1.136	95.892	-0.340
100.000	0.000	100.000	-0.288

Figure 2.10 : NACA 23012C aerofoil profile and coordinates.

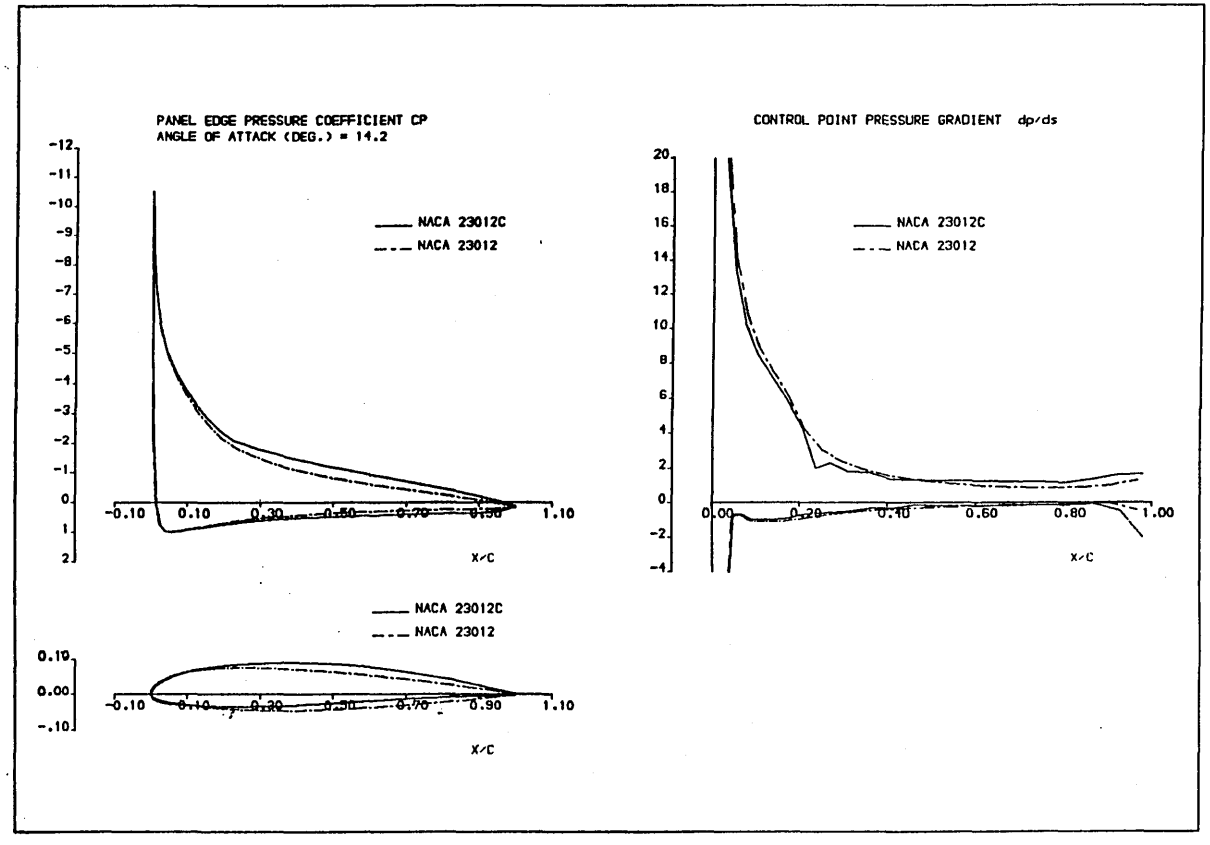

Figure 2.11 : Comparison of pressure distributions of NACA 23012 and NACA 23012C aerofoils.

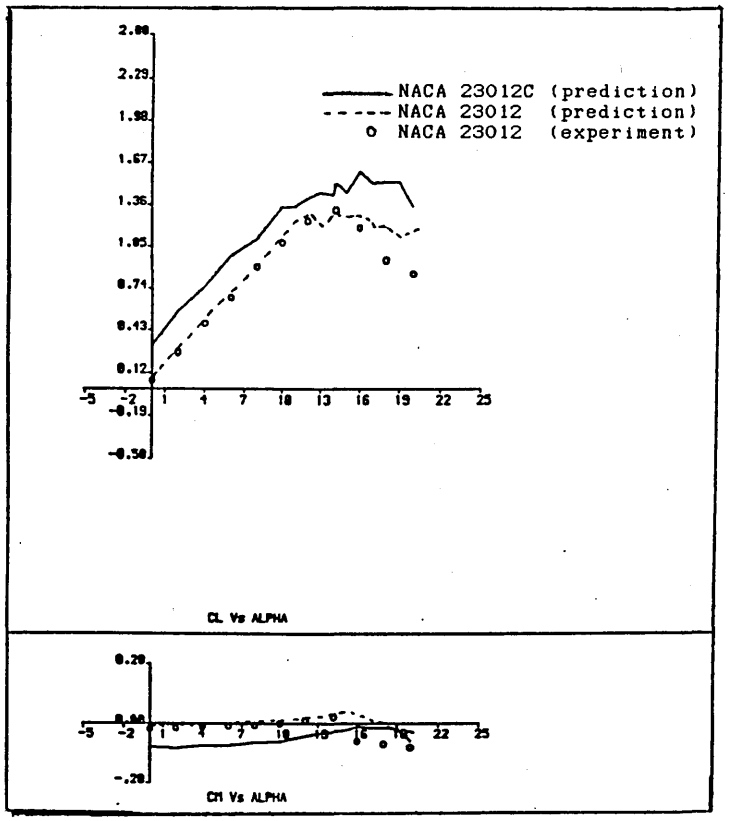

Figure 2.12 : Comparisons between predicted aerodynamic loadings for NACA 23012 and NACA 23012C aerofoils.

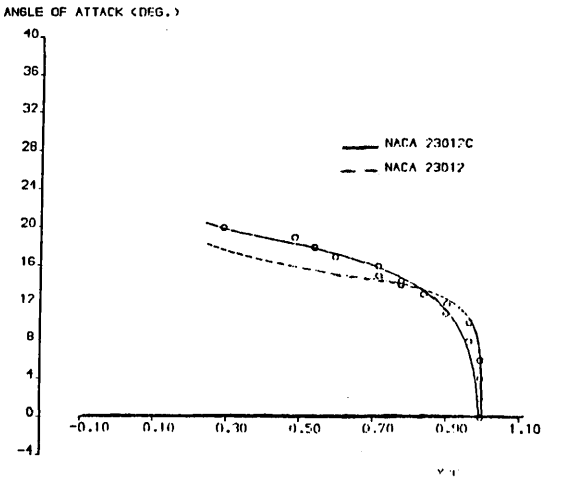

Figure 2.13 : Comparison of predicted separation characteristics for the NACA 23012 and NACA 23012C aerofoils.

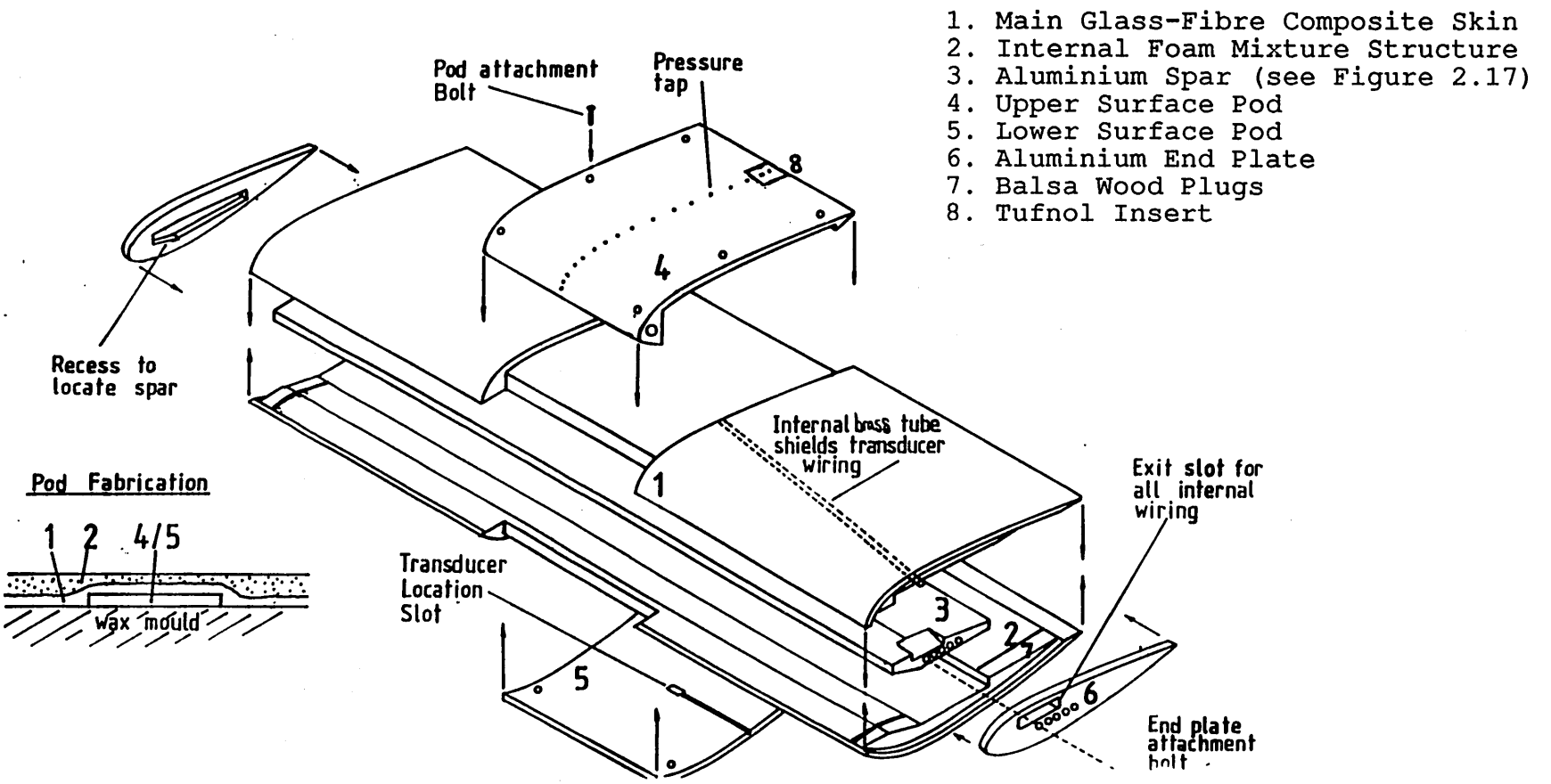

Figure 2.14 : Structure of test aerofoil.
(modified from NIVEN [73])

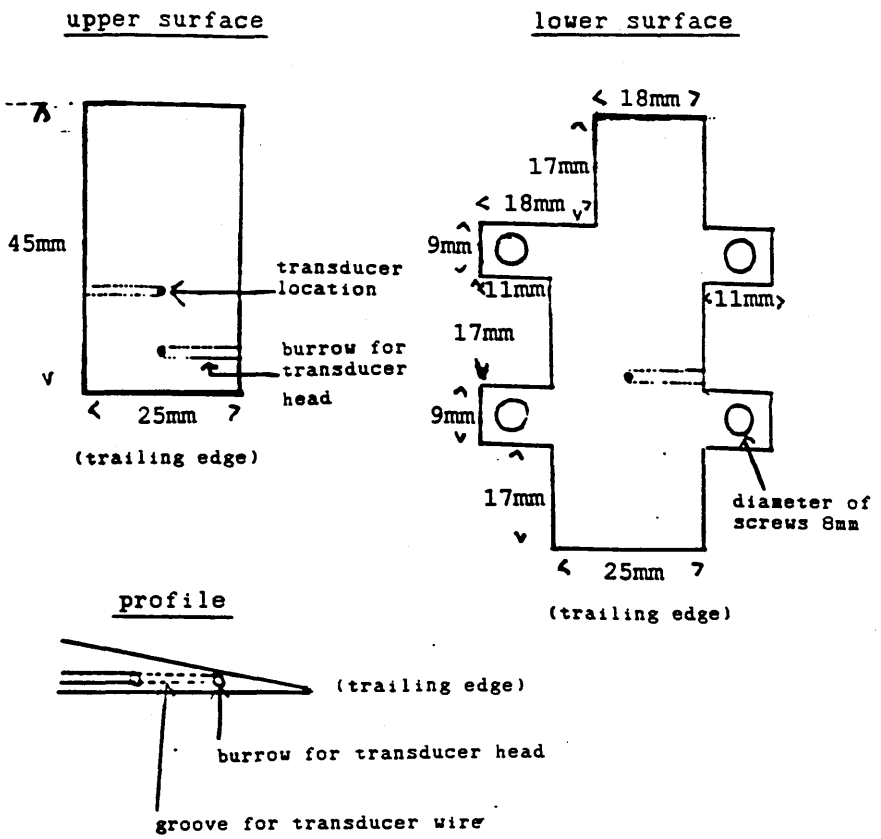

Figure 2.15 : Trailing-edge tufnol insert.

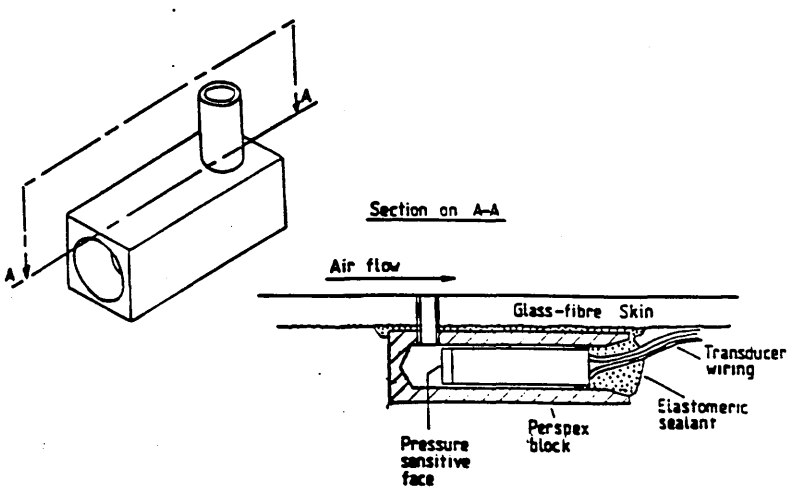

Figure 2.16 : Perspex pockets for housing pressure transducers.
(from NIVEN [73])

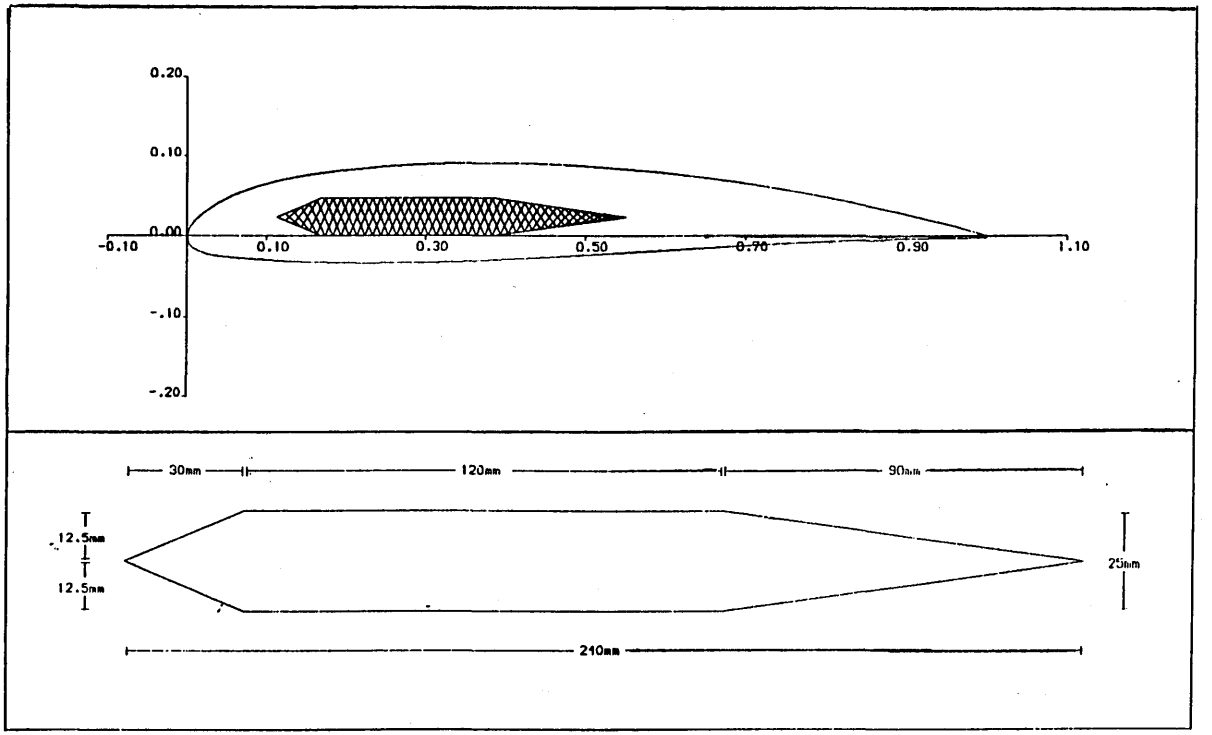

Figure 2.17 : Profile of spar for NACA 23012C aerofoil.

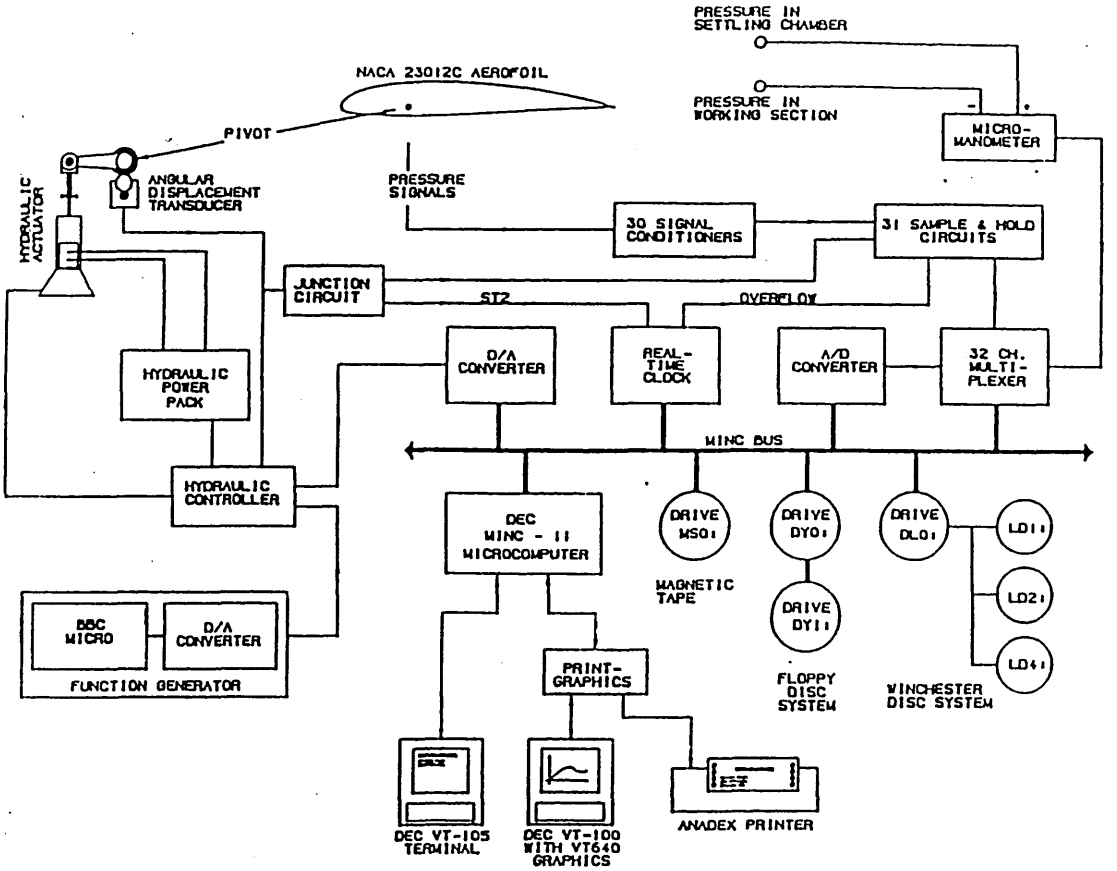

Figure 3.1 : Flow diagram of data acquisition and control system.

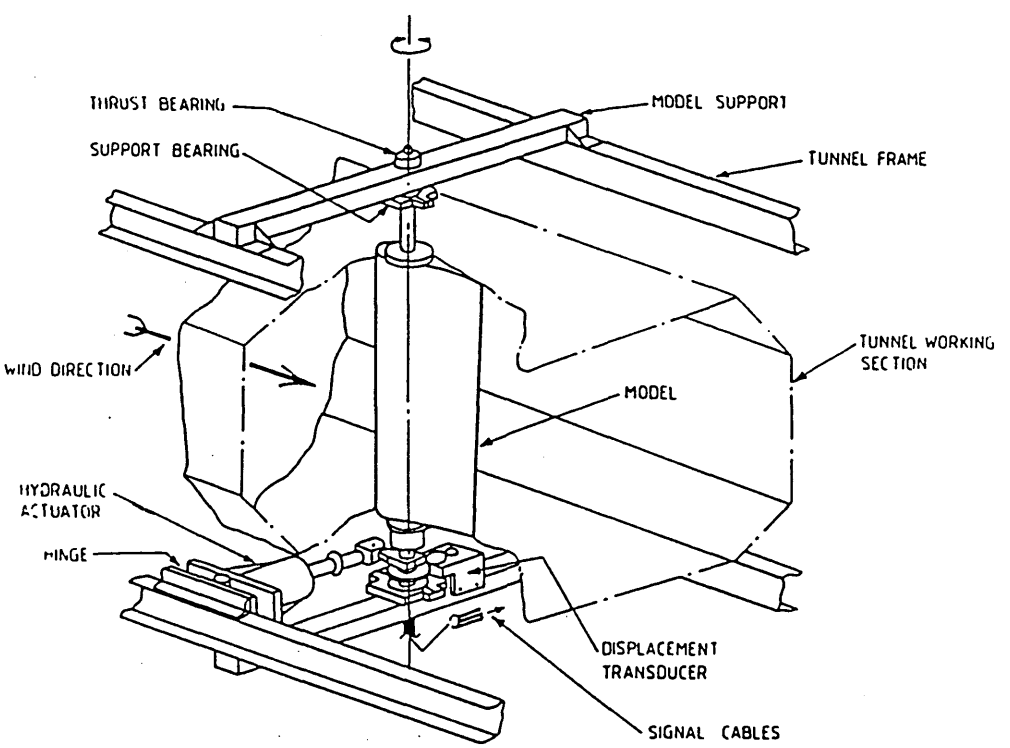

Figure 3.2 : Dynamic stall rig at the University of Glasgow.

(from LEISHMAN [55])

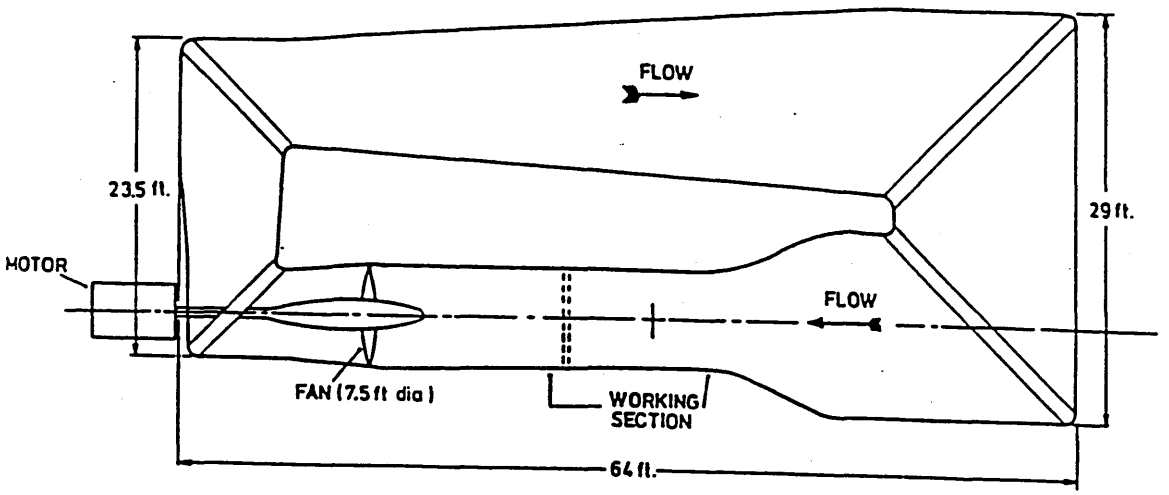

Figure 3.3 : Plan view of the University of Glasgow's 7'x5'3" "Handley-Page" wind-tunnel. (from LEISHMAN [55])

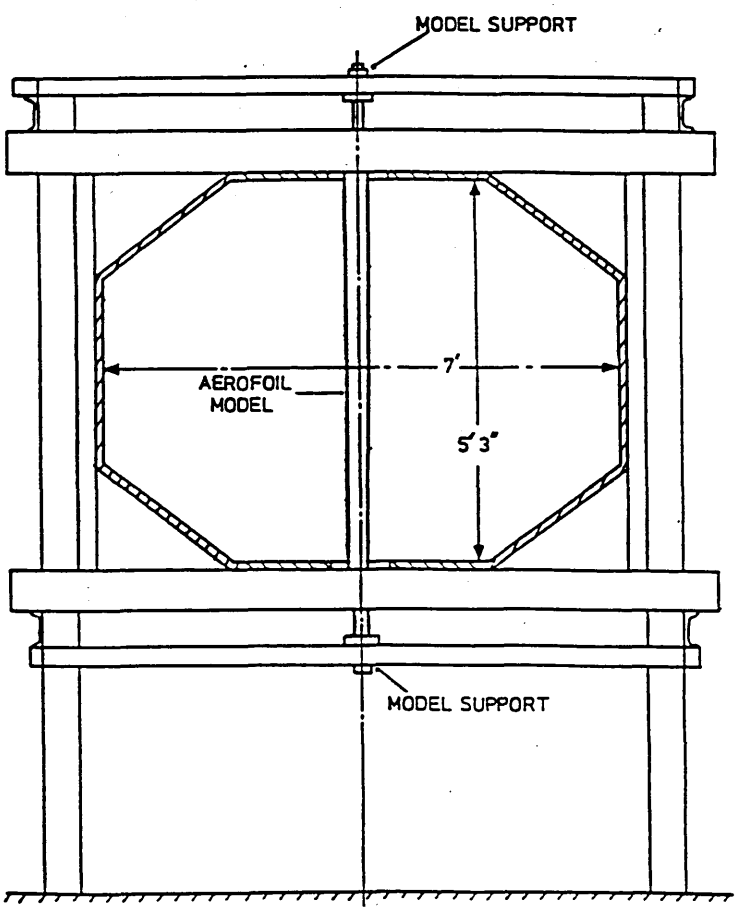

Figure 3.4 : Detail of the University of Glasgow's "Handley-Page" wind-tunnel working section. (from LEISHMAN [55])

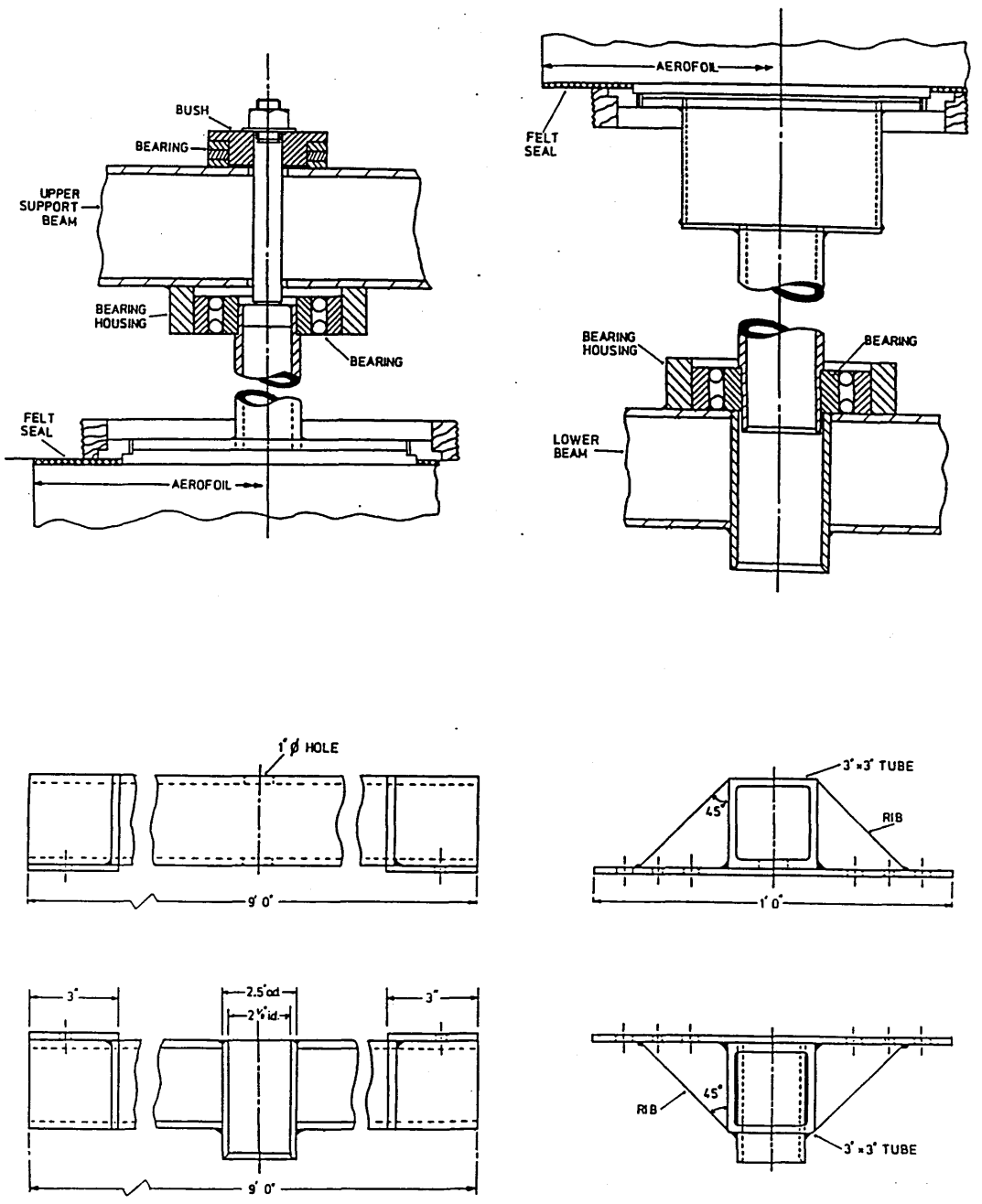

Figure 3.5 : Detail of the University of Glasgow's wind-tunnel model support structure. (from LEISHMAN [55])

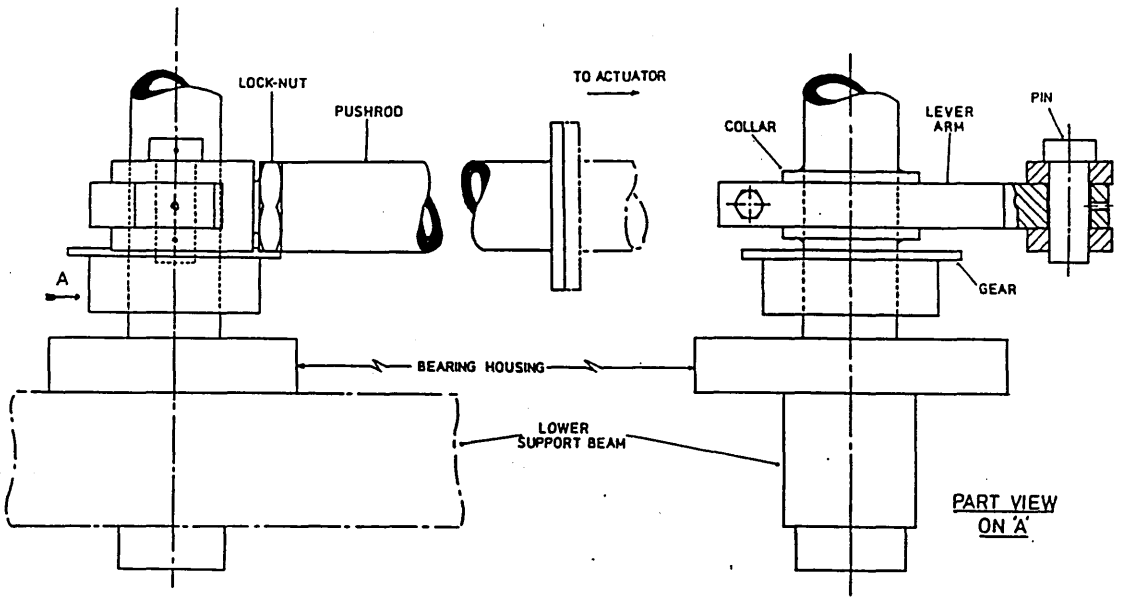

Figure 3.6 : Detail of the aerofoil pitch-drive mechanism.
(from LEISHMAN [55])

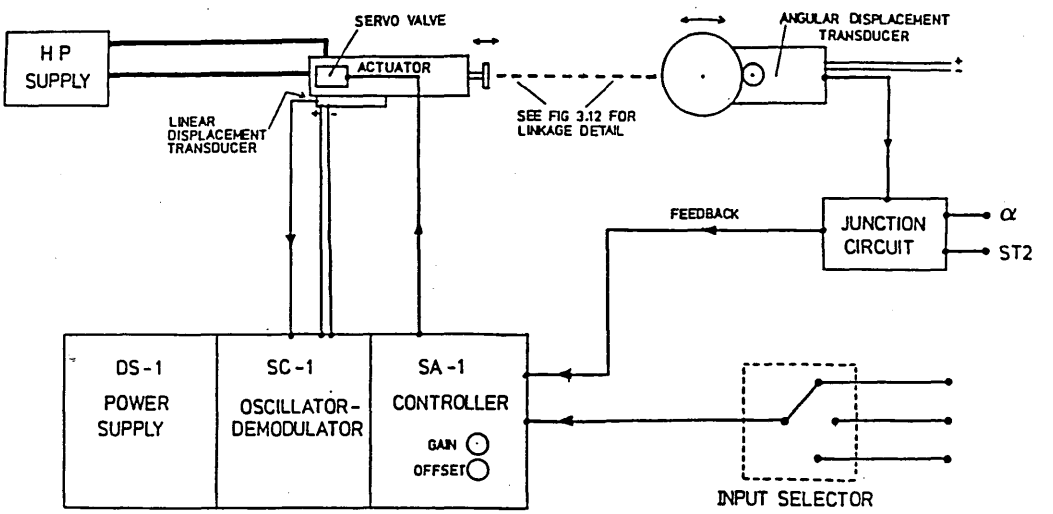

Figure 3.7 : Schematic of the servo actuator control system.
(from LEISHMAN [55])

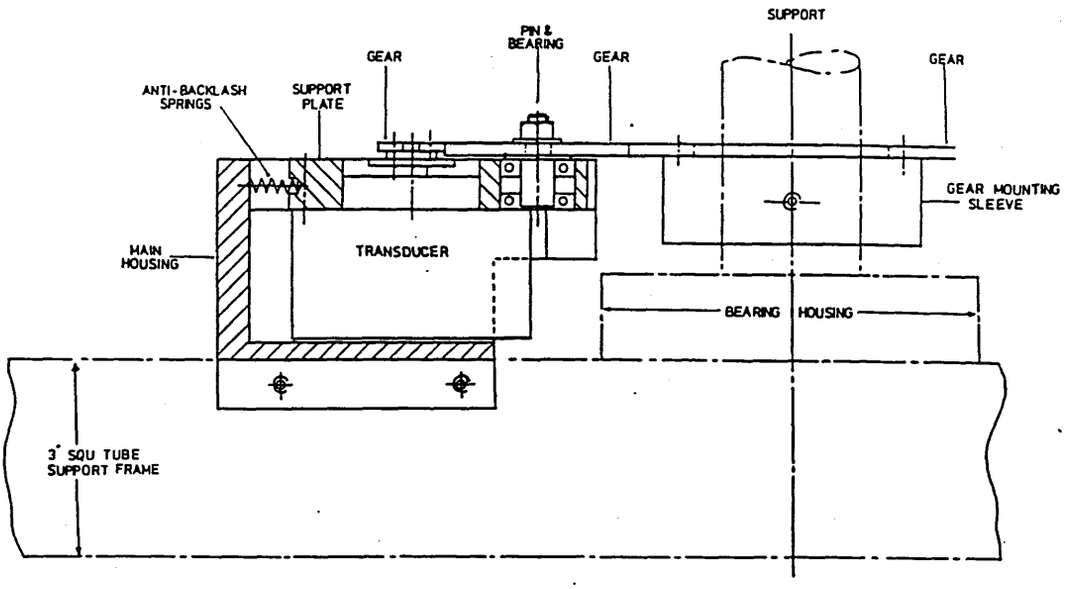

Figure 3.8 : Cross-section of the angular displacement assembly.
(from LEISHMAN [55])

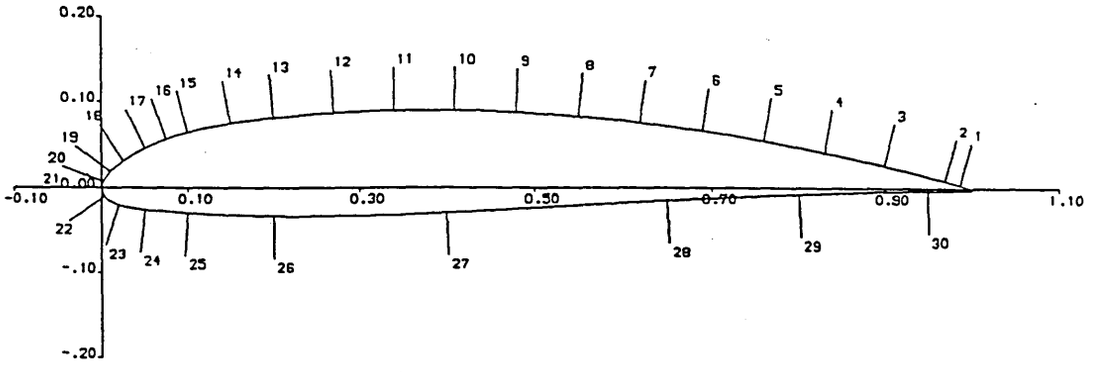

X(1)/C= 0.9875	X(11)/C= 0.3400	X(21)/C= 0.0000
X(2)/C= 0.9700	X(12)/C= 0.2700	X(22)/C= 0.0040
X(3)/C= 0.9000	X(13)/C= 0.2000	X(23)/C= 0.0200
X(4)/C= 0.8300	X(14)/C= 0.1500	X(24)/C= 0.0500
X(5)/C= 0.7600	X(15)/C= 0.1000	X(25)/C= 0.1000
X(6)/C= 0.6900	X(16)/C= 0.0750	X(26)/C= 0.2000
X(7)/C= 0.6200	X(17)/C= 0.0500	X(27)/C= 0.4000
X(8)/C= 0.5500	X(18)/C= 0.0250	X(28)/C= 0.6500
X(9)/C= 0.4800	X(19)/C= 0.0100	X(29)/C= 0.8000
X(10)/C= 0.4100	X(20)/C= 0.0025	X(30)/C= 0.9500

Figure 3.9 : Pressure transducer locations
for the NACA 23012C aerofoil.

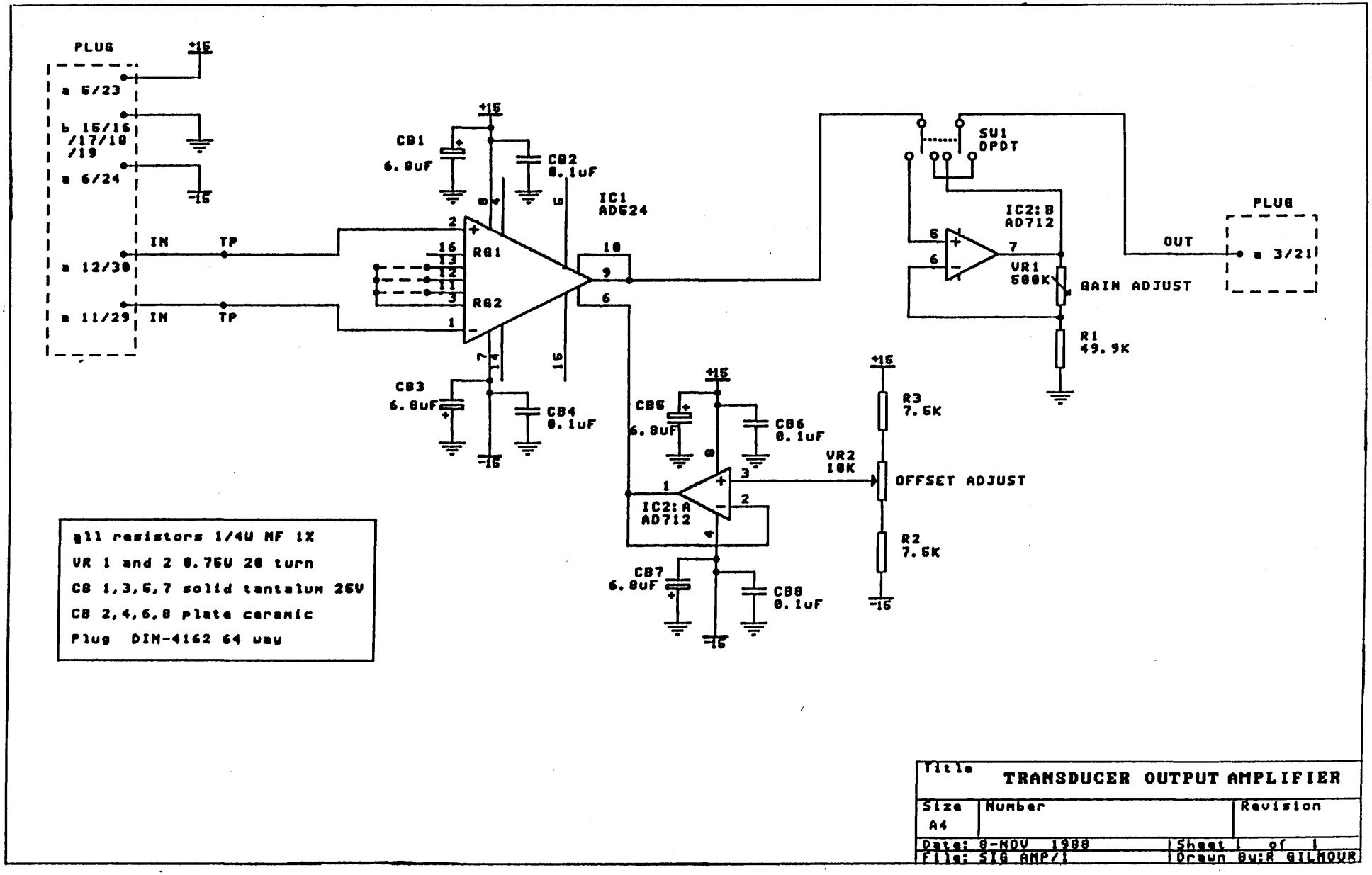

Figure 3.10 : Circuit diagram of a transducer output amplifier.

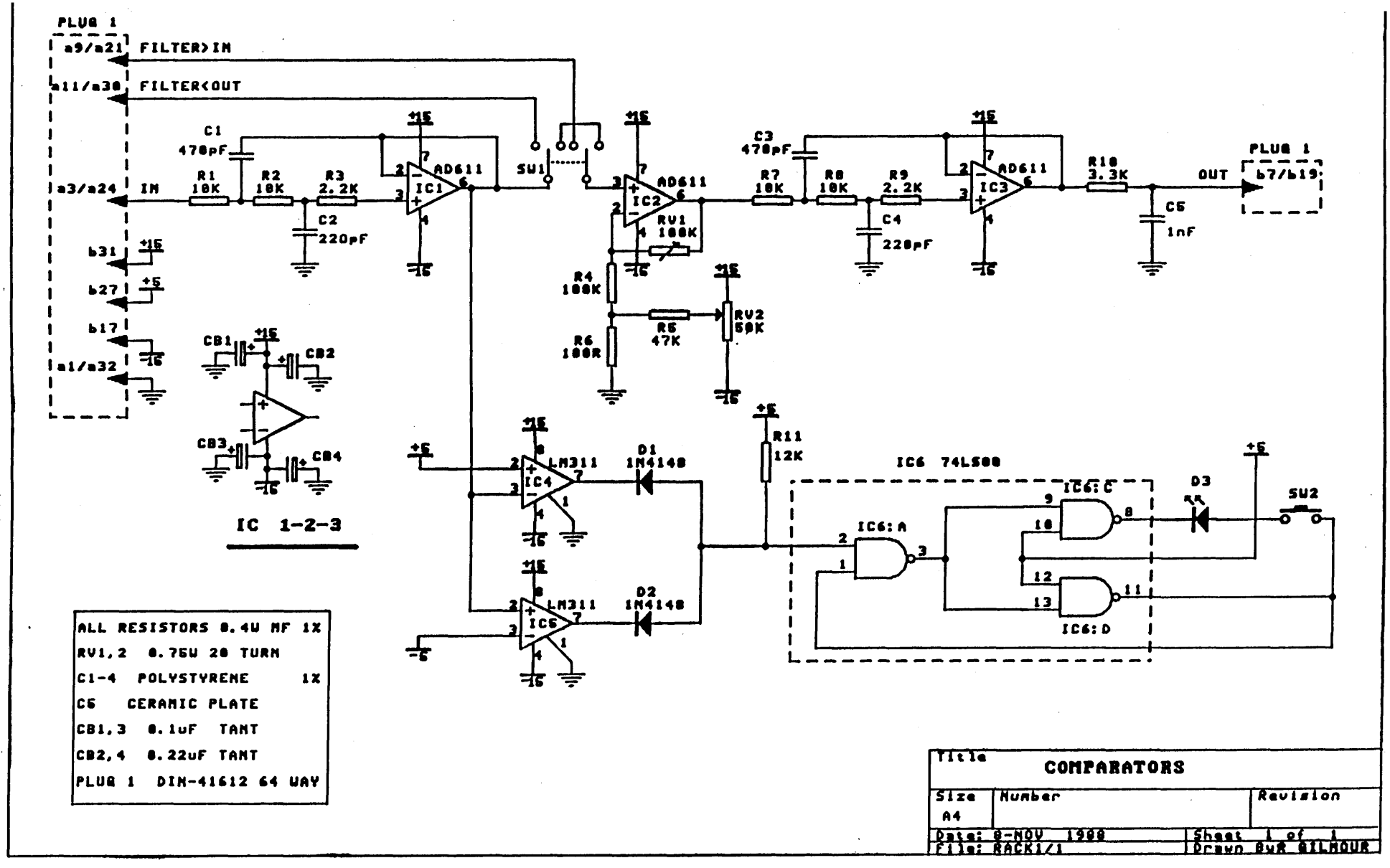

Figure 3.11 : Circuit diagram of a comparator.

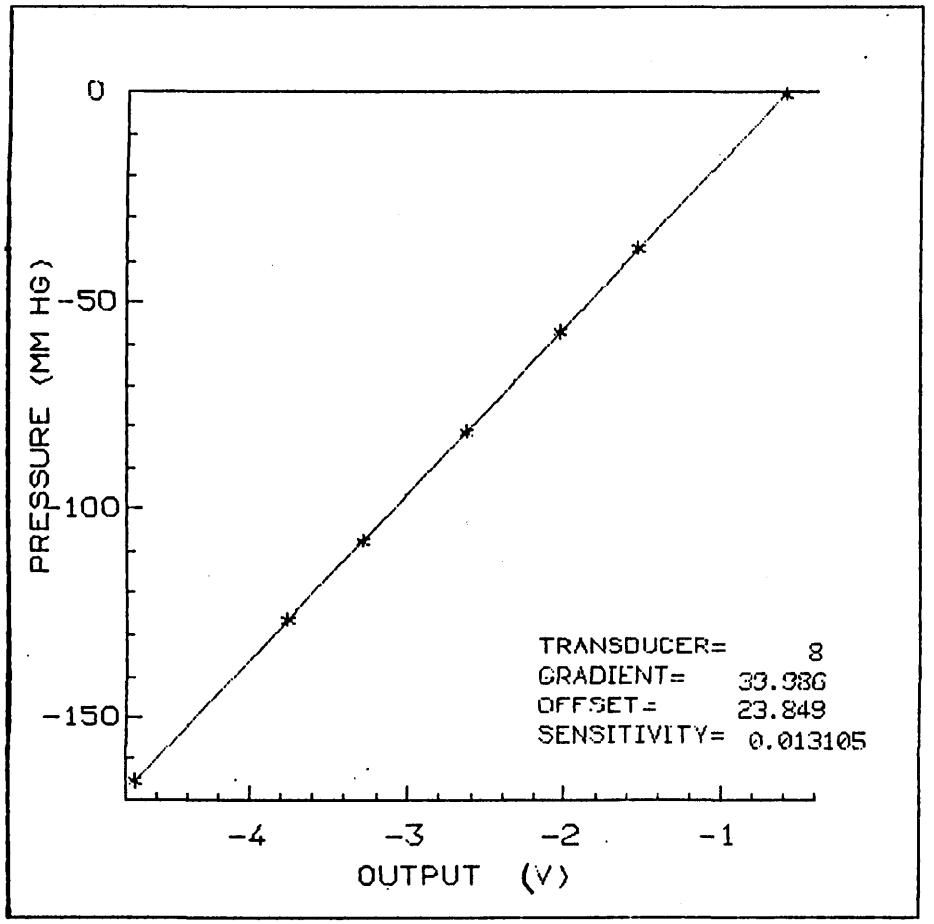

Figure 3.12 : Calibration graph for pressure transducer.

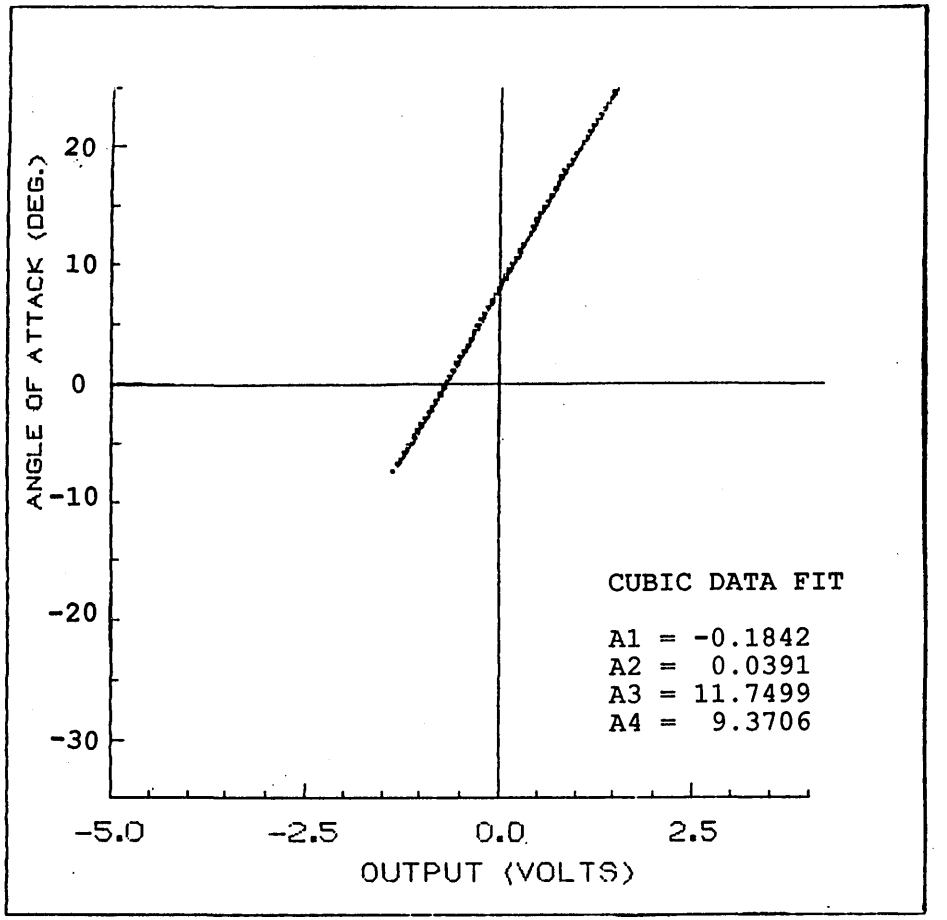

Figure 3.13 : Calibration graph for angular displacement transducer.

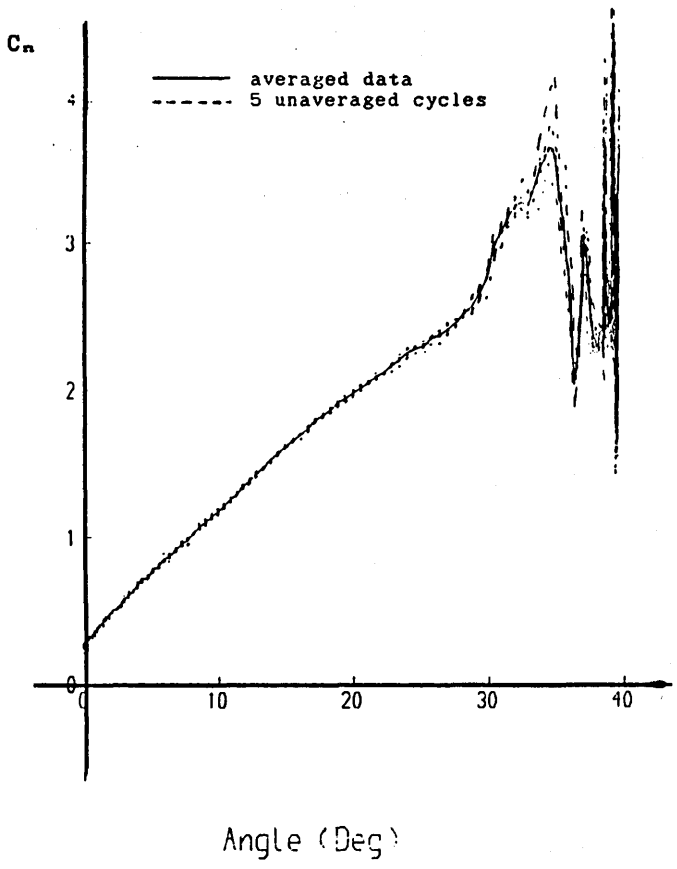

(a) Ramp data :
normal coefficient versus incidence.

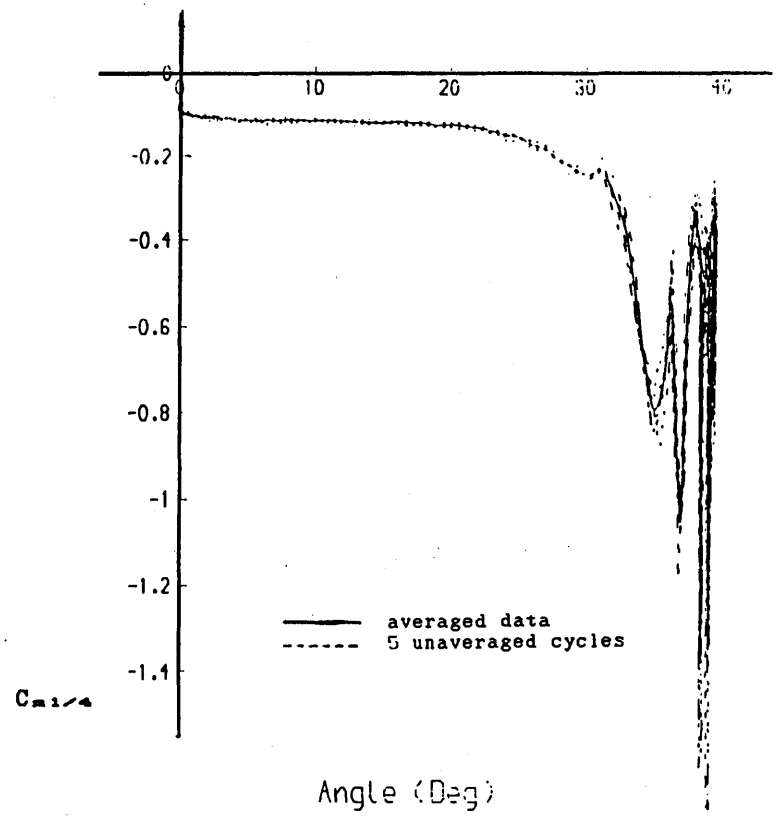

(b) Ramp data :
pitching-moment coefficient versus incidence.

Figure 4.1 : Comparison between averaged data and unaveraged sweeps.

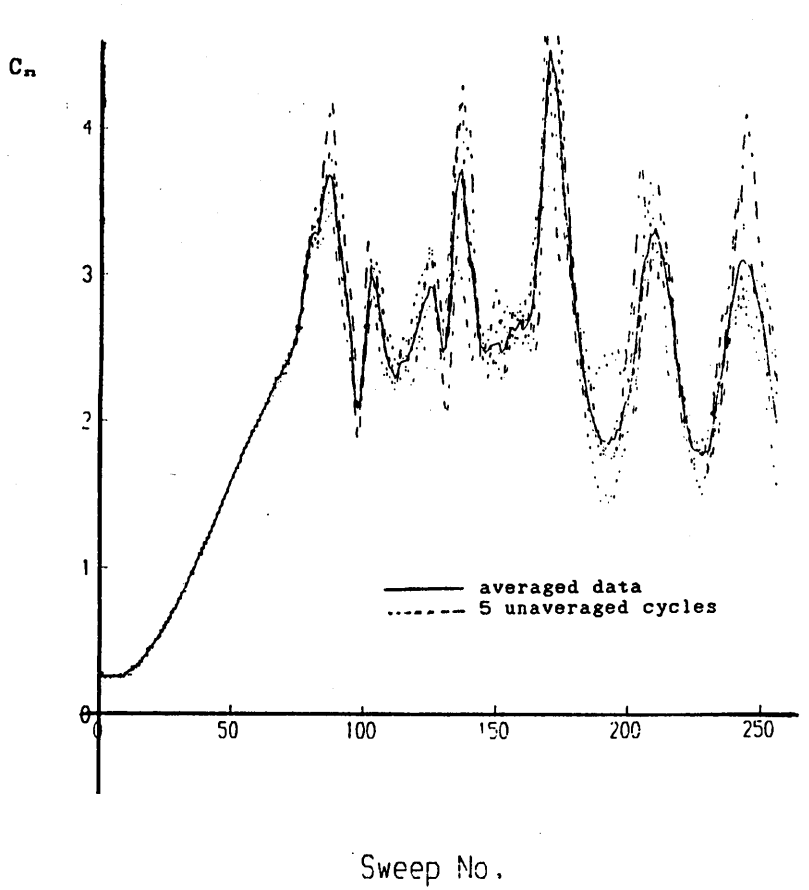

(c) Ramp data :
normal coefficient versus sweep number.

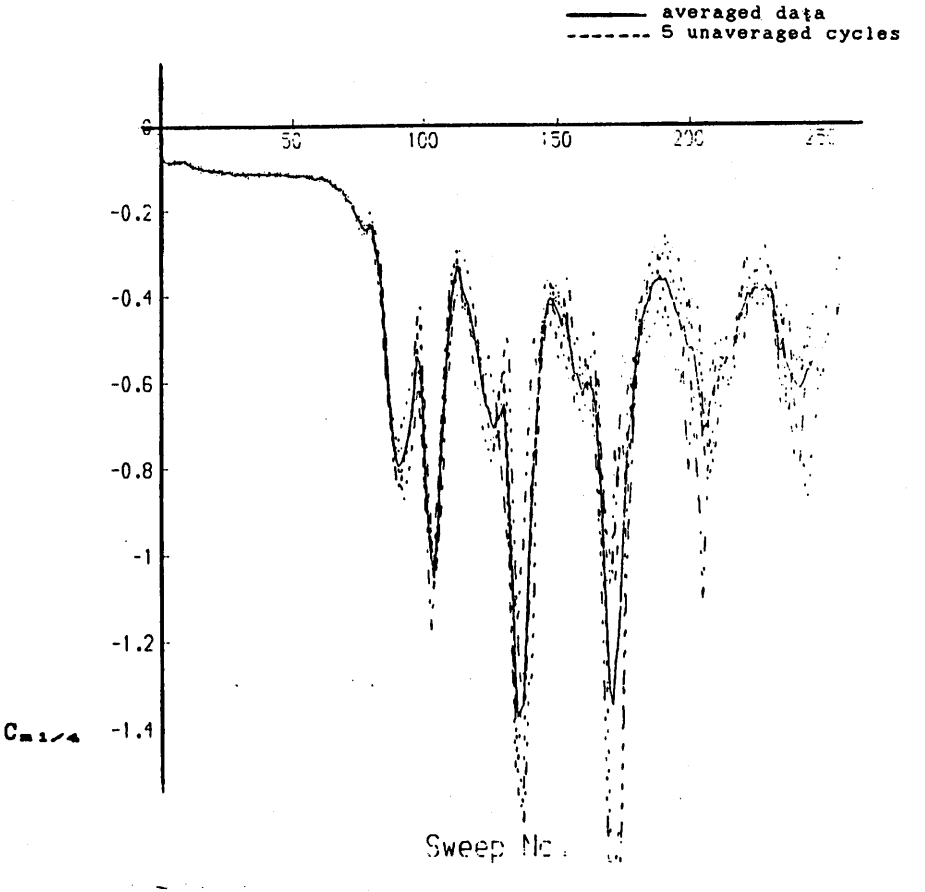

(d) Ramp data :
pitching-moment coefficient versus sweep number.

Figure 4.1 : Comparison between averaged data and unaveraged sweeps.
(continued)

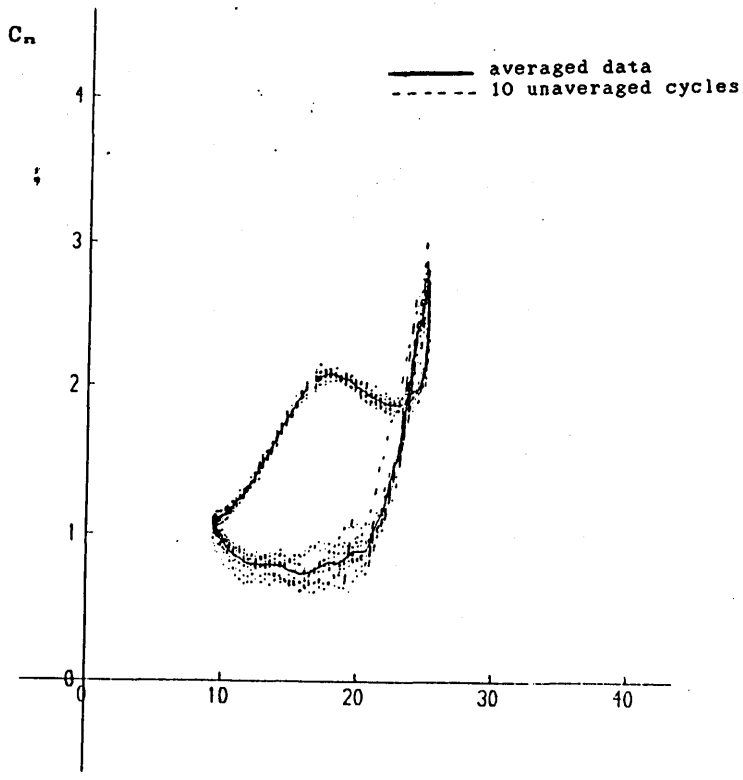

(e) Sinusoidal data :
normal coefficient versus incidence.

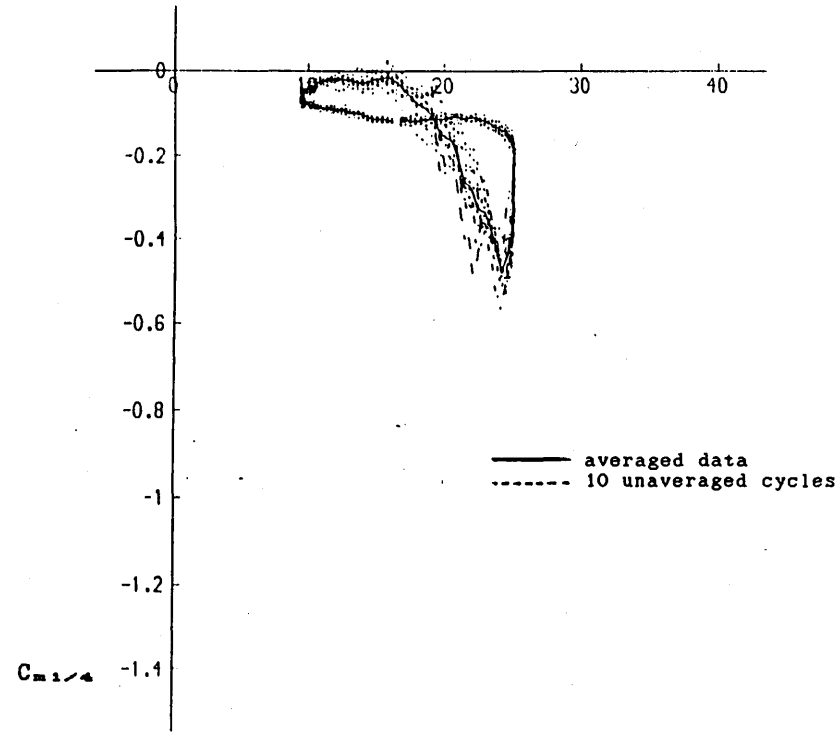

(f) Sinusoidal data :
pitching-moment coefficient versus incidence.

Figure 4.1 : Comparison between averaged data and unaveraged sweeps.
(continued)

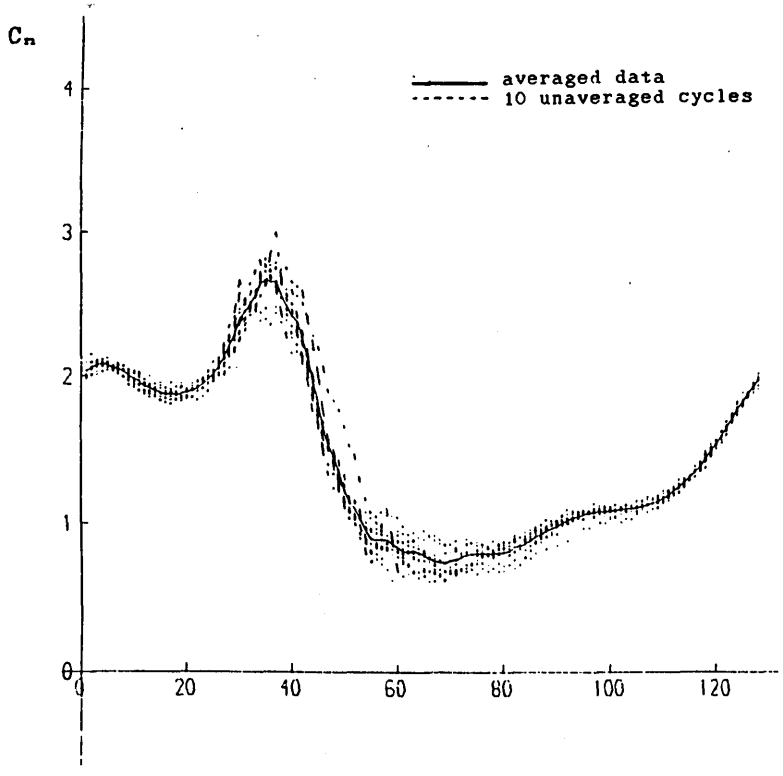

(g) Sinusoidal data :
normal coefficient versus sweep number.

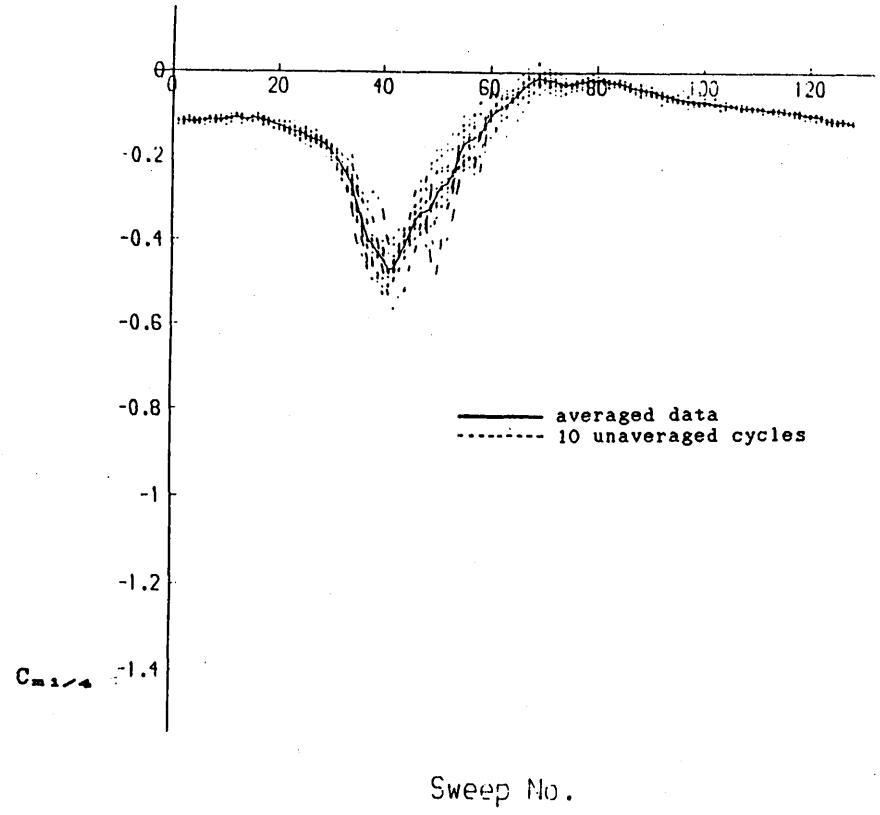

(h) Sinusoidal data :
pitching-moment coefficient versus sweep number.

Figure 4.1 : Comparison between averaged data and unaveraged sweeps.
(concluded)

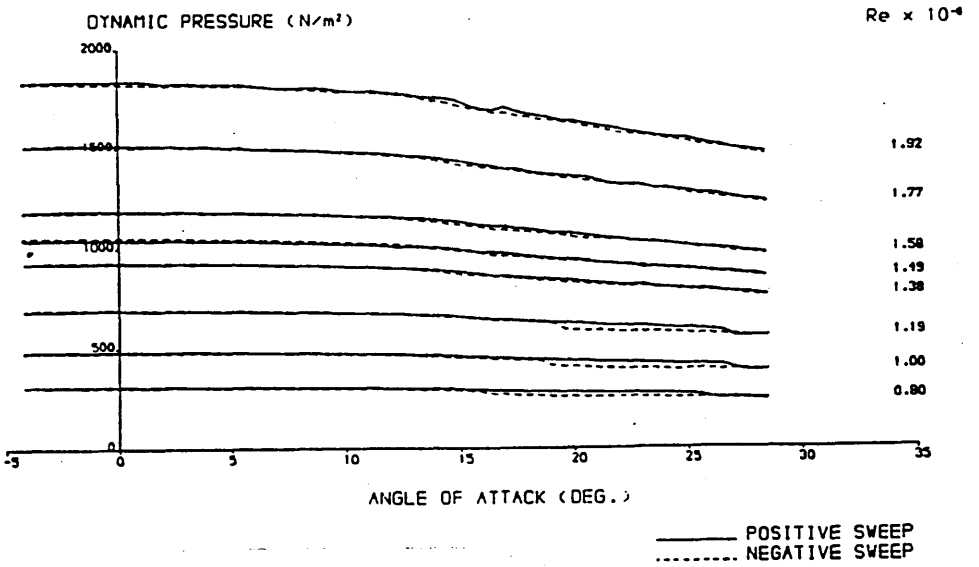

(a) Static experiments :
Reynolds number differs.

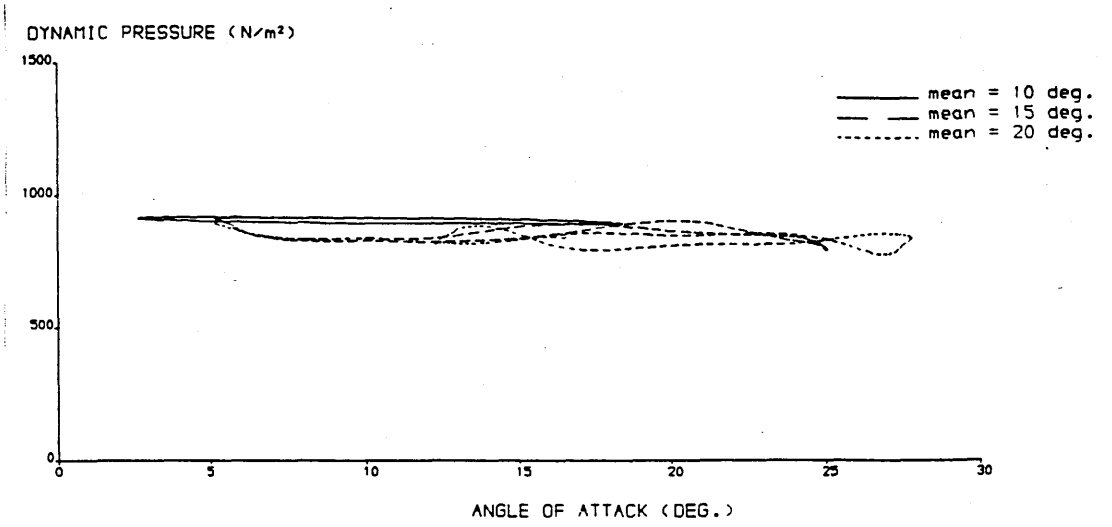

(b) Sinusoidal experiments :
mean incidence differs (k=0.10).

Figure 4.2 : Variation of dynamic pressure with incidence over series of experiments in which only one parameter differs between tests.

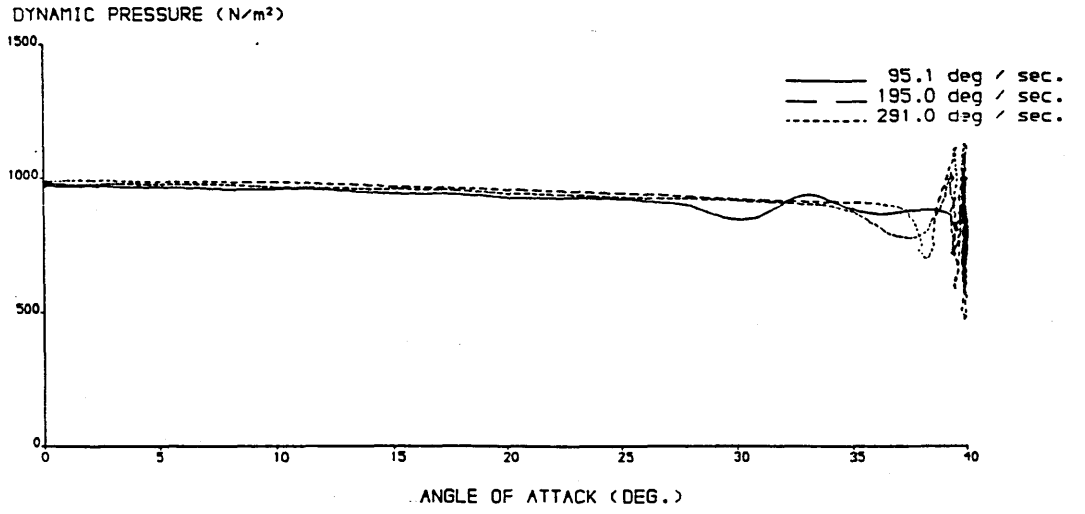

(c) Ramp experiments :
pitch-rate differs.

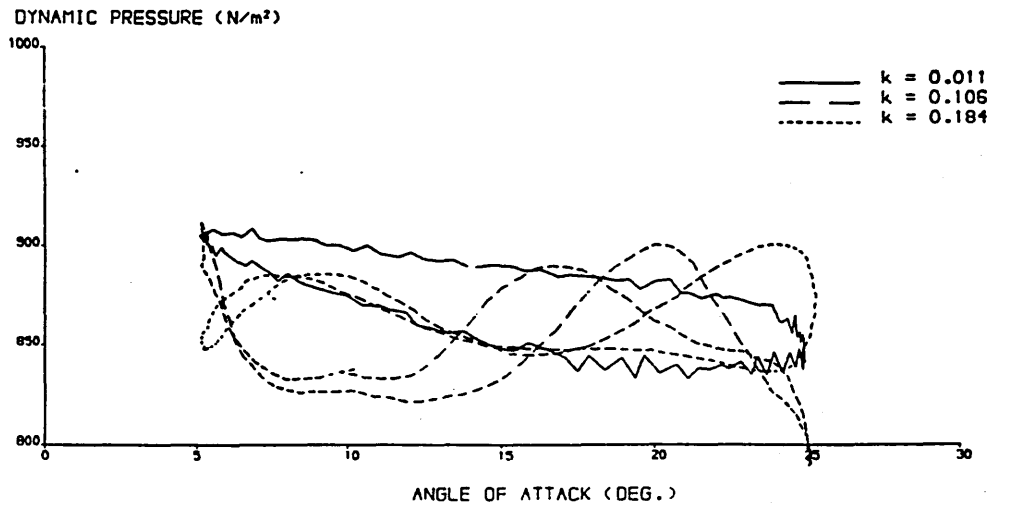

(d) Sinusoidal experiments :
reduced frequency differs.

Figure 4.2 : Variation of dynamic pressure with incidence over series of experiments in which only one parameter differs between tests.

(concluded)

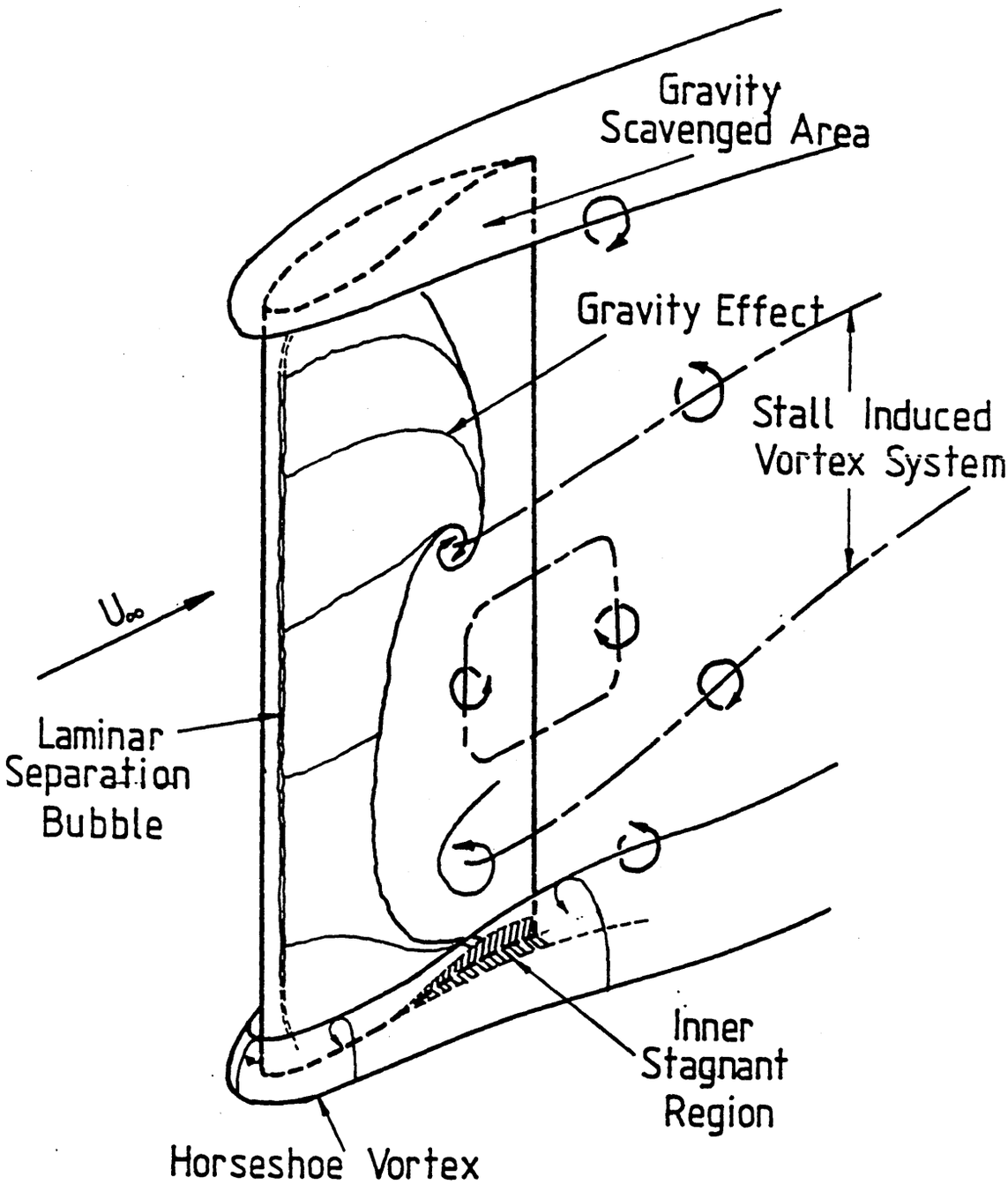

Figure 4.3 : Flow behaviour on an aerofoil as indicated by oil-flow visualisation. (from NIVEN [73])

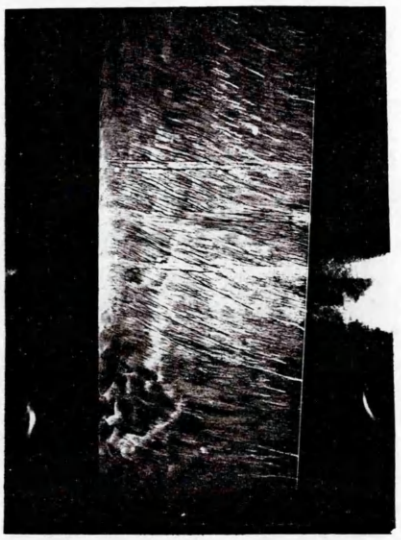

(a) approximately -8°

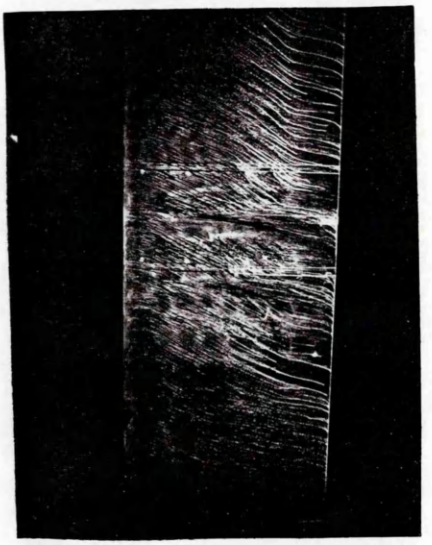

(b) approximately -4°

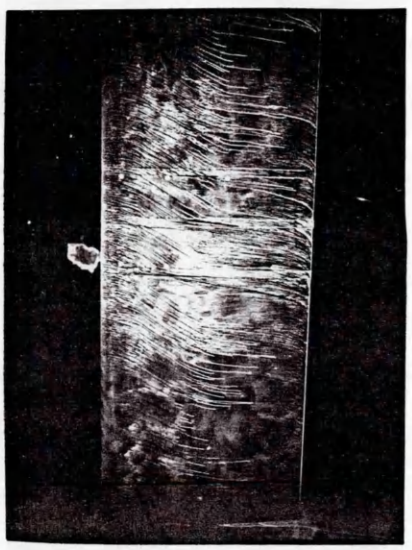

(c) approximately 0°

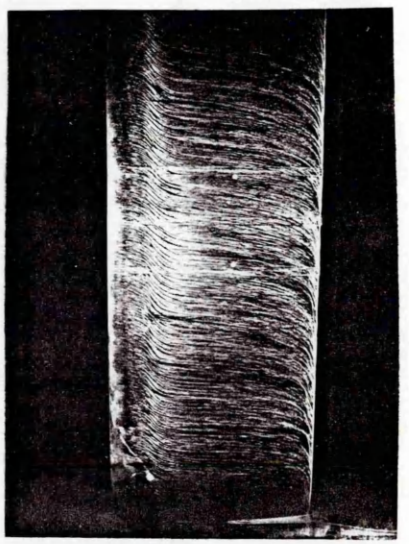

(d) approximately 2°

(wind blowing from left to right)

Figure 4.4 : Oil-flow characteristics for the NACA 23012C aerofoil at a Reynolds number of approximately 1.5×10^6.

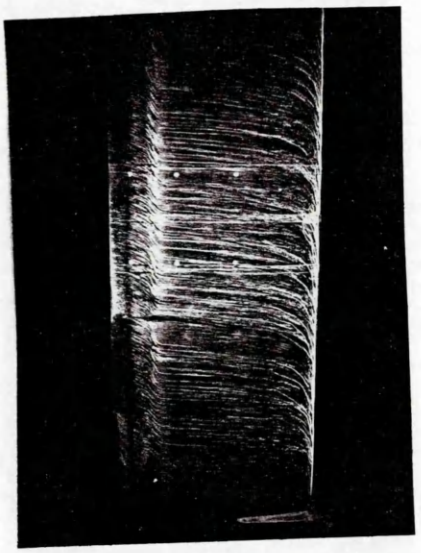

(e) approximately 4°

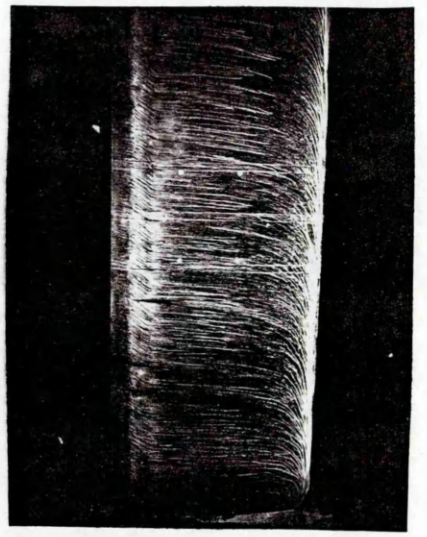

(f) approximately 6°

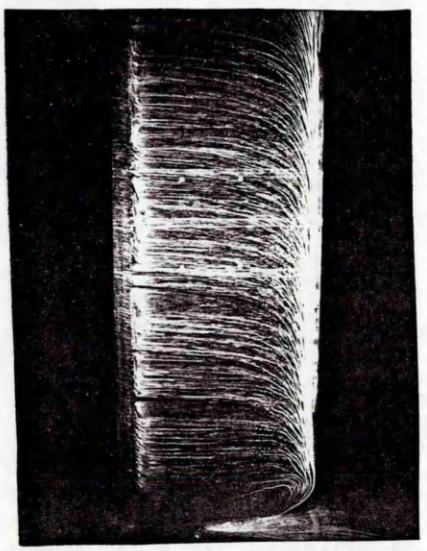

(g) approximately 8°

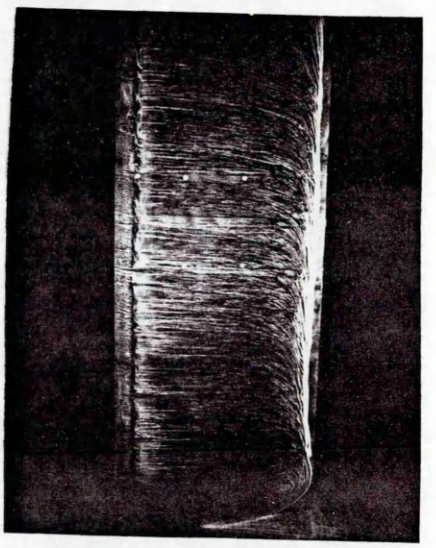

(h) approximately 9°

(wind blowing from left to right)

Figure 4.4 : Oil-flow characteristics for the NACA 23012C aerofoil at a Reynolds number of approximately 1.5×10^6. (continued)

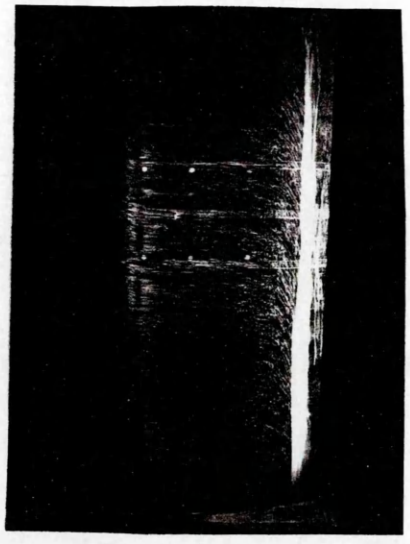

(i) approximately 10°

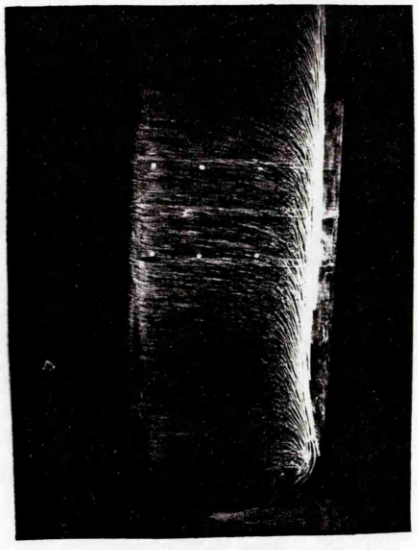

(j) approximately 11°

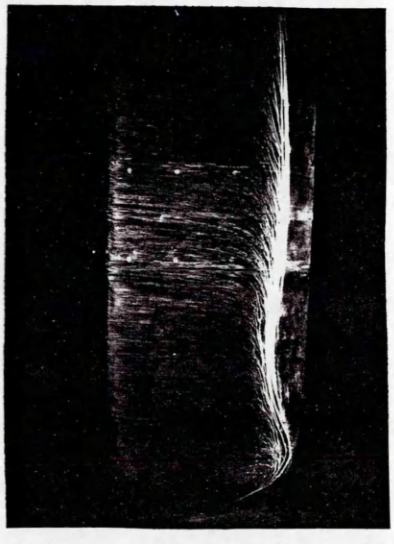

(k) approximately 12°

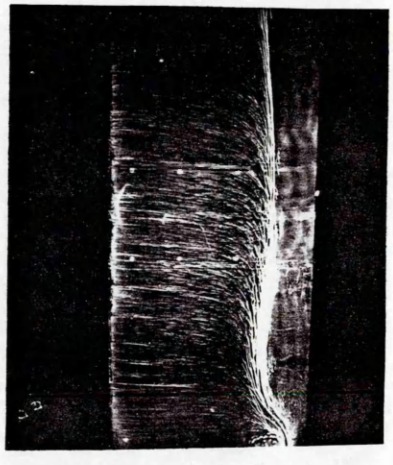

(l) approximately 13°

(wind blowing from left to right)

Figure 4.4 : Oil-flow characteristics for the NACA 23012C aerofoil at a Reynolds number of approximately 1.5×10^6. (continued)

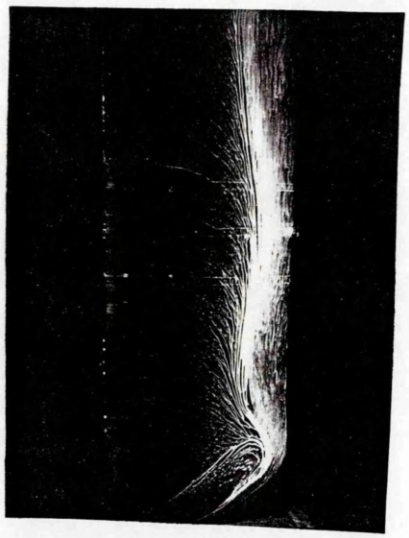

(m) approximately 14°

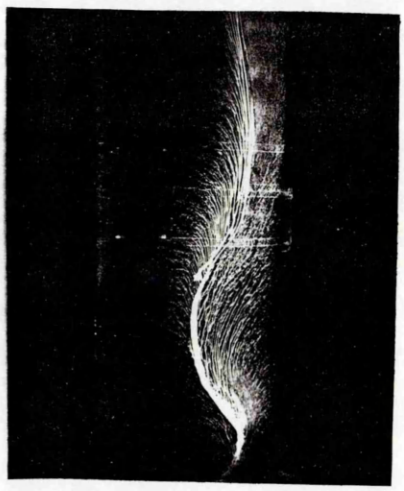

(n) approximately 15°

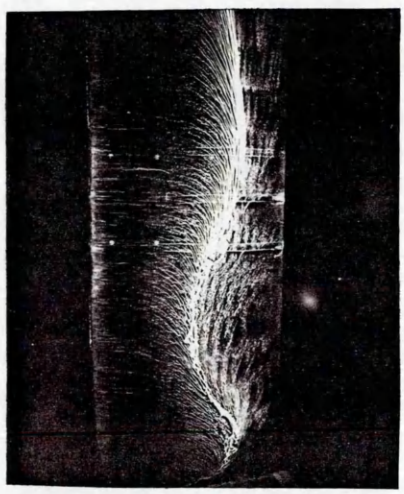

(o) approximately 16°

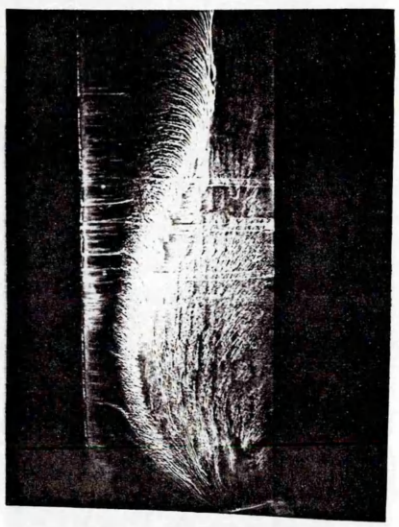

(p) approximately 17°

(wind blowing from left to right)

Figure 4.4 : Oil-flow characteristics for the NACA 23012C aerofoil at a Reynolds number of approximately 1.5×10^6. (continued)

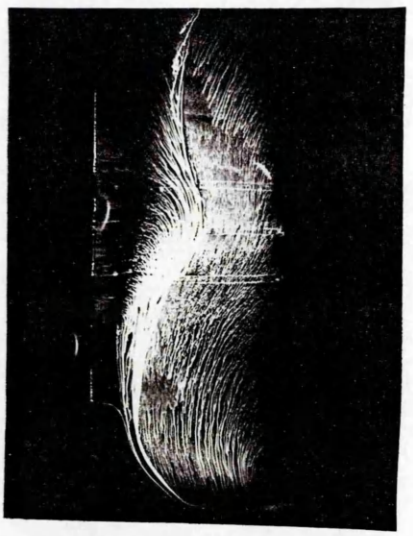

(q) approximately 18°

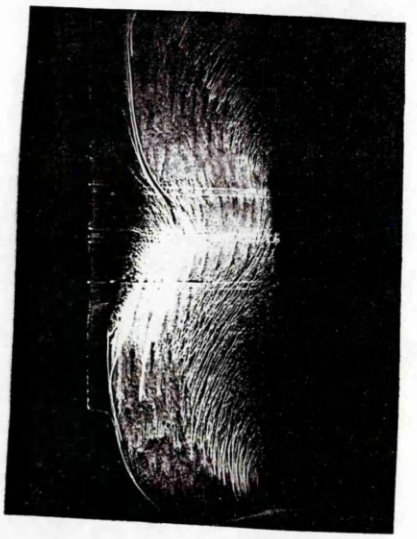

(r) approximately 19°

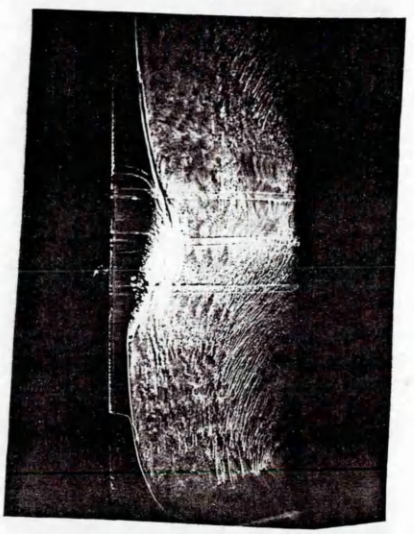

(s) approximately 20°

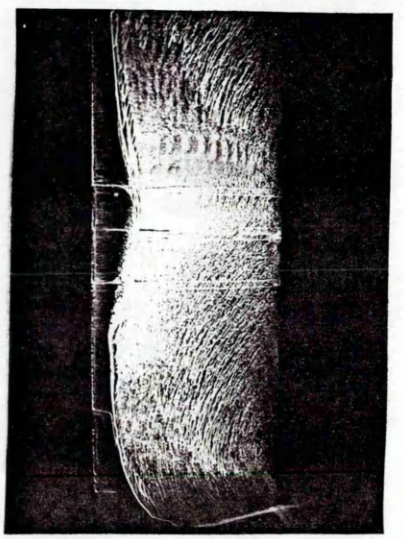

(t) approximately 21°

(wind blowing from left to right)

Figure 4.4 : Oil-flow characteristics for the NACA 23012C aerofoil at a Reynolds number of approximately 1.5×10^6. (continued)

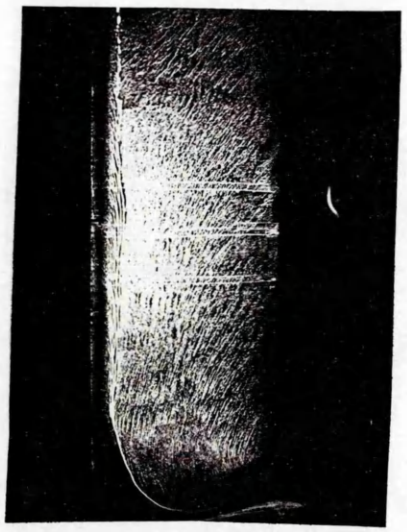

(u) approximately 22°

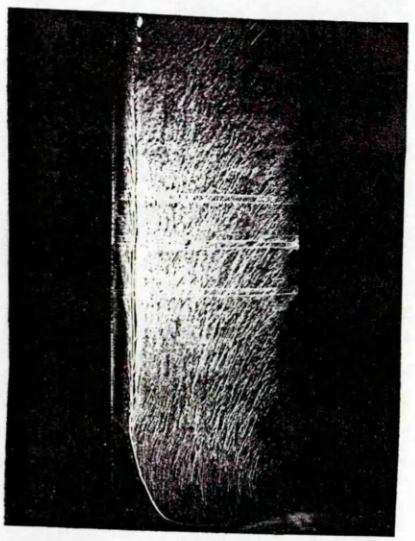

(v) approximately 23°

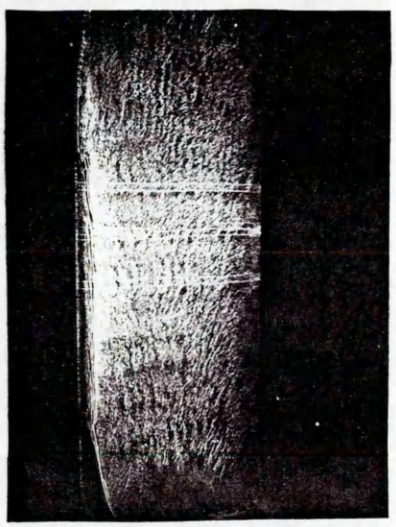

(w) approximately 24°

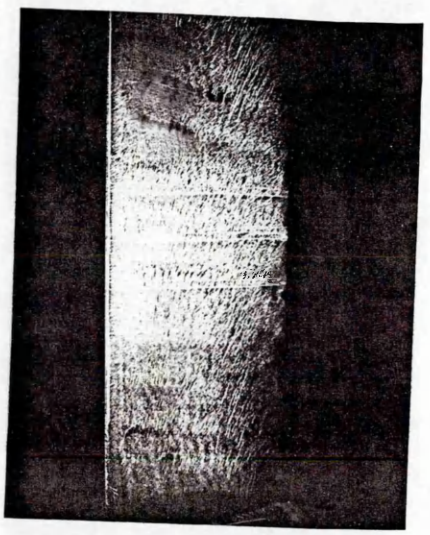

(x) approximately 26°

(wind blowing from left to right)

Figure 4.4 : Oil-flow characteristics for the NACA 23012C aerofoil at a Reynolds number of approximately 1.5×10^6. (continued)

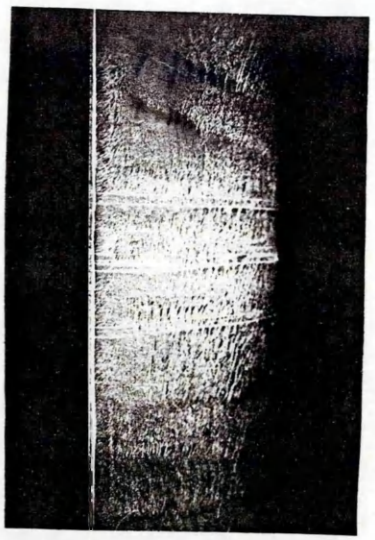

(y) approximately 26°
(taken from leading edge)

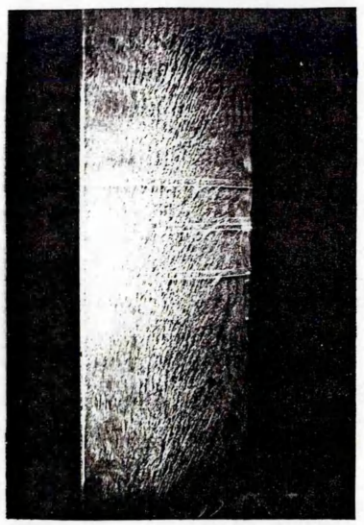

(z) approximately 32°

(wind blowing from left to right)

Figure 4.4 : Oil-flow characteristics for the NACA 23012C aerofoil at a Reynolds number of approximately 1.5×10^6. (concluded)

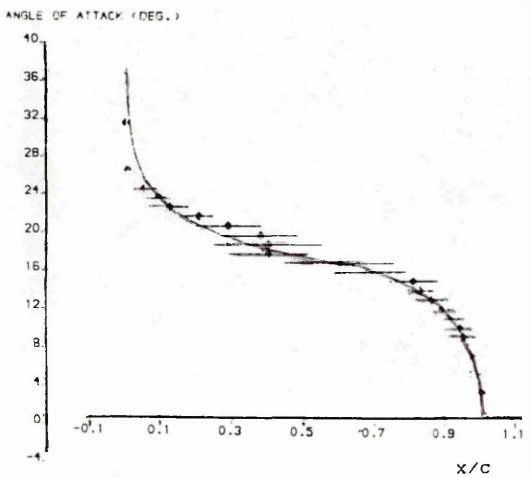

Figure 4.5 : Trailing-edge separation characteristics for the NACA 23012C aerofoil as determined from oil-flow visualisation.

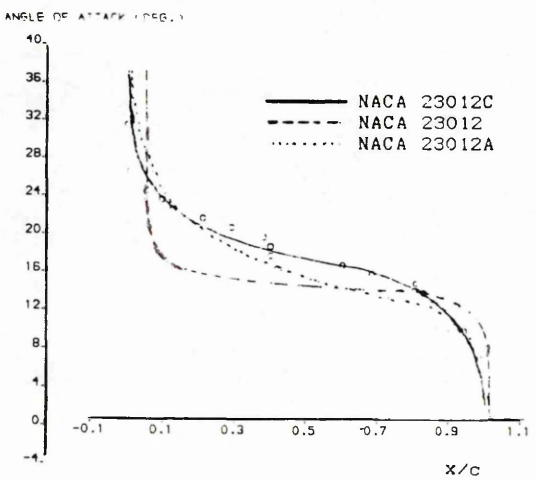

Figure 4.6 : Comparison of trailing-edge separation characteristics as determined from oil-flow visualisation for three aerofoils.

RUN REFERENCE NUMBER: 5341
REYNOLDS NUMBER = 1494846.
DYNAMIC PRESSURE = 1012.22 Nm^{-2}
NUMBER OF CYCLES = 1
MOTION TYPE: STATIC

DATE OF TEST: 12/12/88
MACH NUMBER = 0.119
AIR TEMPERATURE = 26.2°C
SAMPLING FREQUENCY = 100.00 Hz.
AVERAGED DATA OF 1 CYCLES

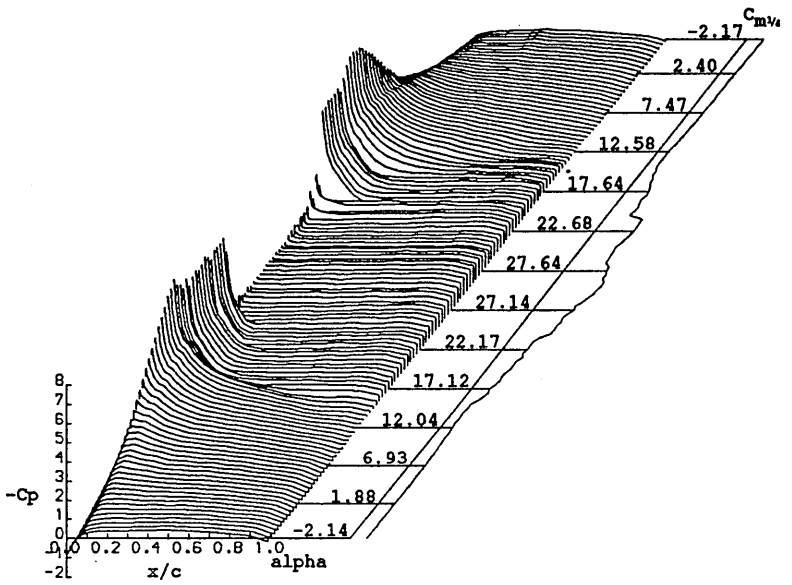

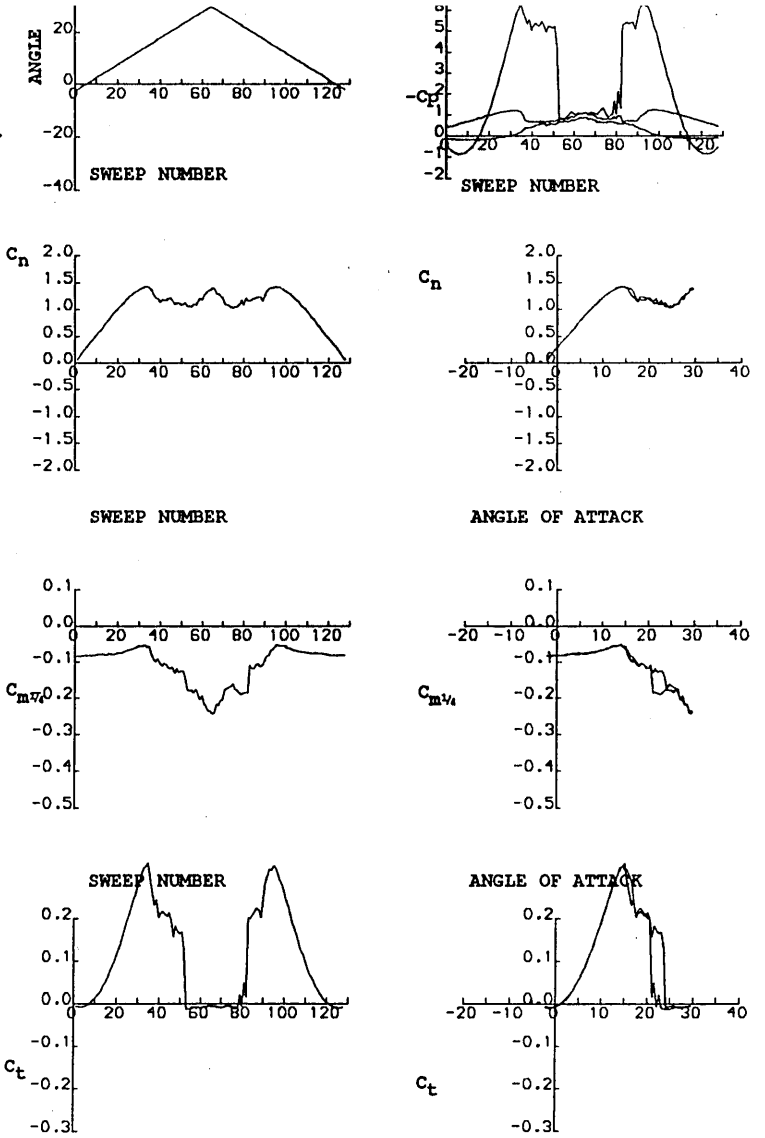

Figure 4.7 : Static characteristics of the NACA 23012C at a Reynolds number of approximately 1.5x10⁶.

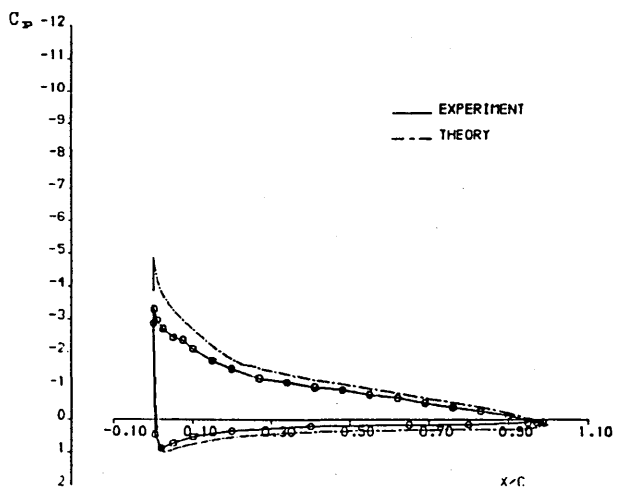

Figure 4.8 : Pressure coefficient distributions at an incidence of 10.00° for the NACA 23012C aerofoil from experimental data and potential-flow prediction.

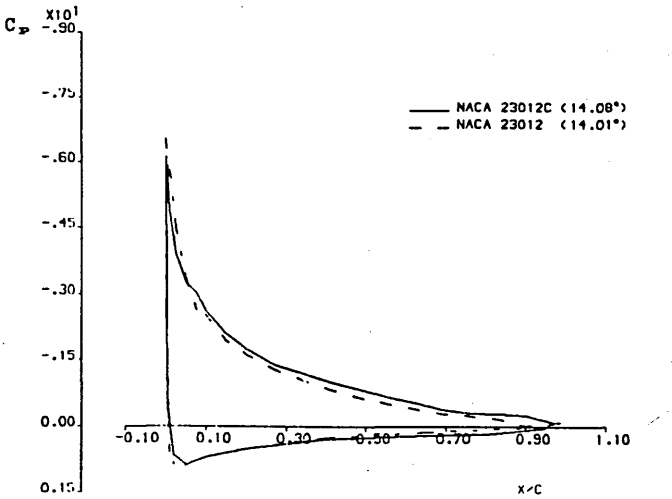

Figure 4.9 : Pressure coefficient distributions at an incidence of approximately 14° for the NACA 23012C and NACA 23012 aerofoils from experimental data.

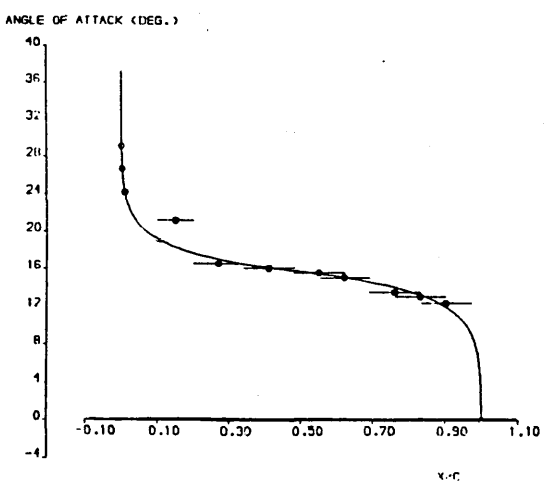

Figure 4.10 : Trailing-edge separation characteristics at a Reynolds number of approximately 1.5×10^6 for the NACA 23012C aerofoil as determined from pressure distribution.

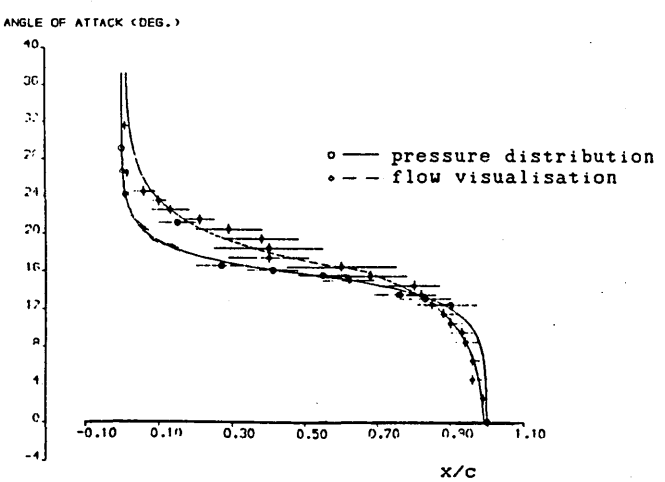

Figure 4.11 : Comparison of trailing-edge separation characteristics for the NACA 23012C aerofoil as determined from pressure distribution and oil-flow visualisation.

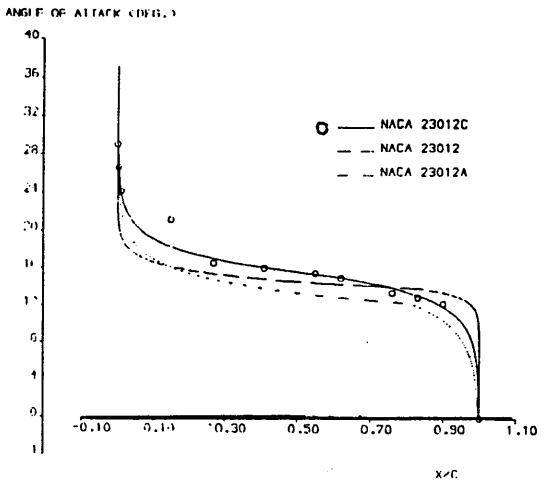

Figure 4.12 : Comparison of trailing-edge separation characteristics for three aerofoils as as determined from pressure distribution.

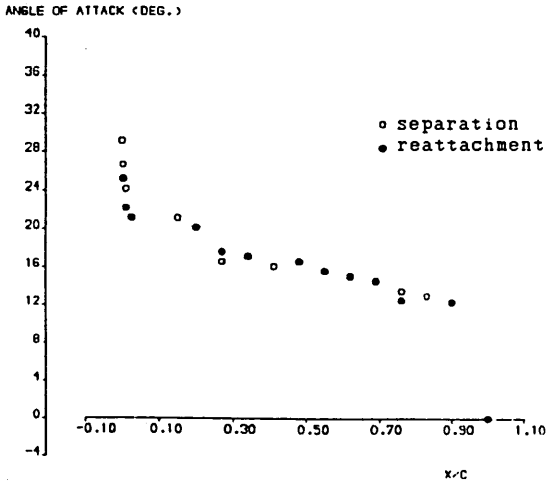

Figure 4.13 : Comparison of separation and reattachment characteristics for the NACA 23012C aerofoil as determined from pressure distribution.

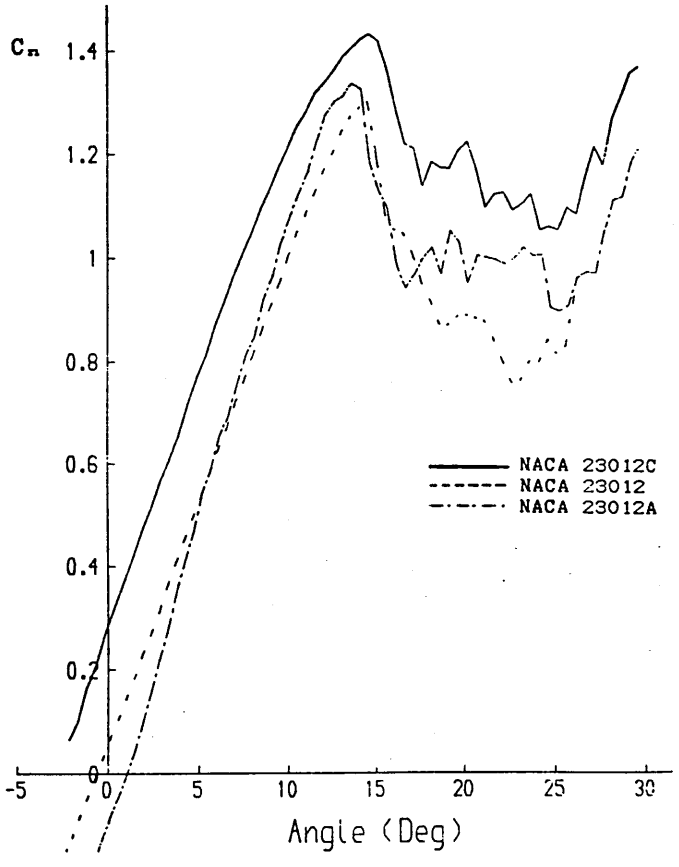

Figure 4.14 : Comparison of static normal force characteristics at a Reynolds number of approximately 1.5×10^6 for three aerofoils.

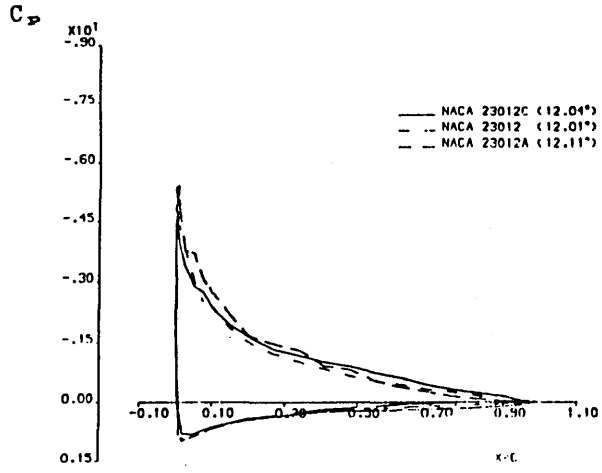

Figure 4.15 : Comparison of static pressure distributions for three aerofoils at an incidence and Reynolds number of approximately 12° and 1.5x10⁶ respectively.

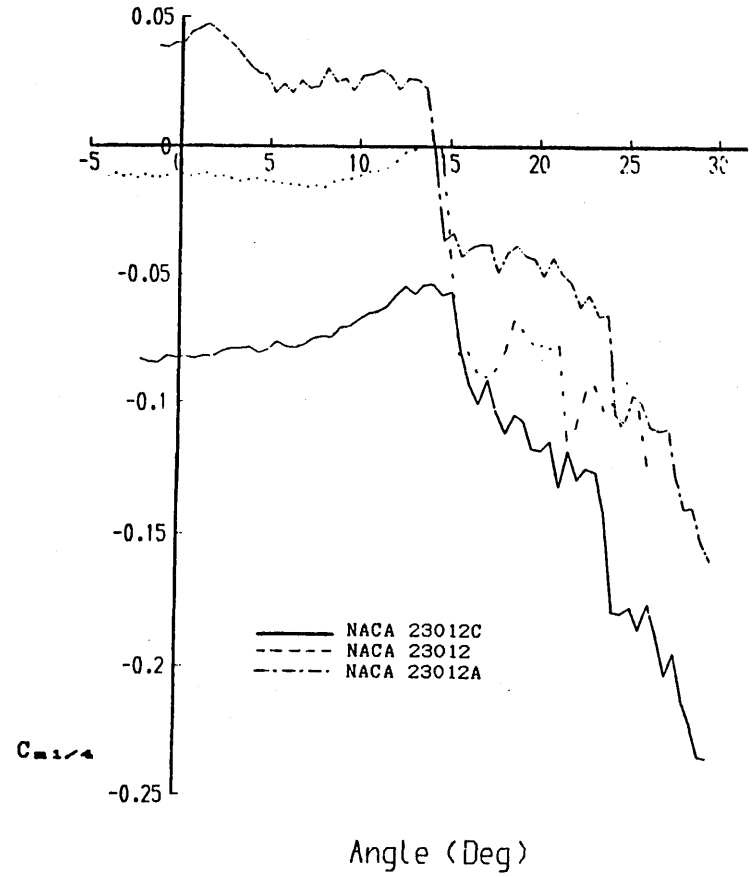

Figure 4.16 : Comparison of static pitching-moment characteristics at a Reynolds number of approximately 1.5x10⁶ for three aerofoils.

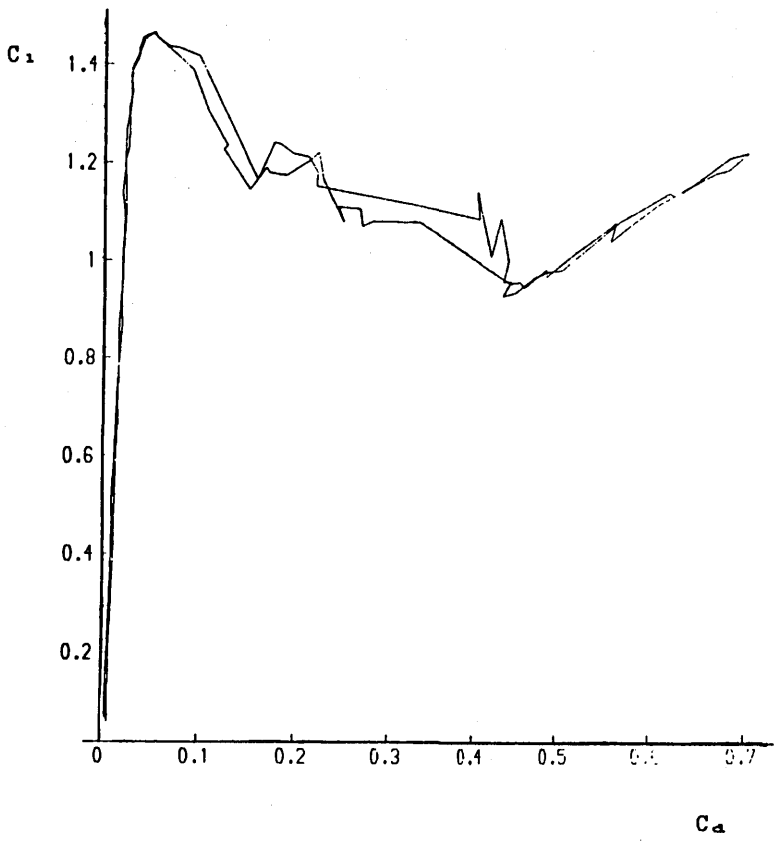

Figure 4.17 : Variation of lift with drag in steady conditions at a Reynolds number of approximately 1.5×10^6 for the NACA 23012C aerofoil.

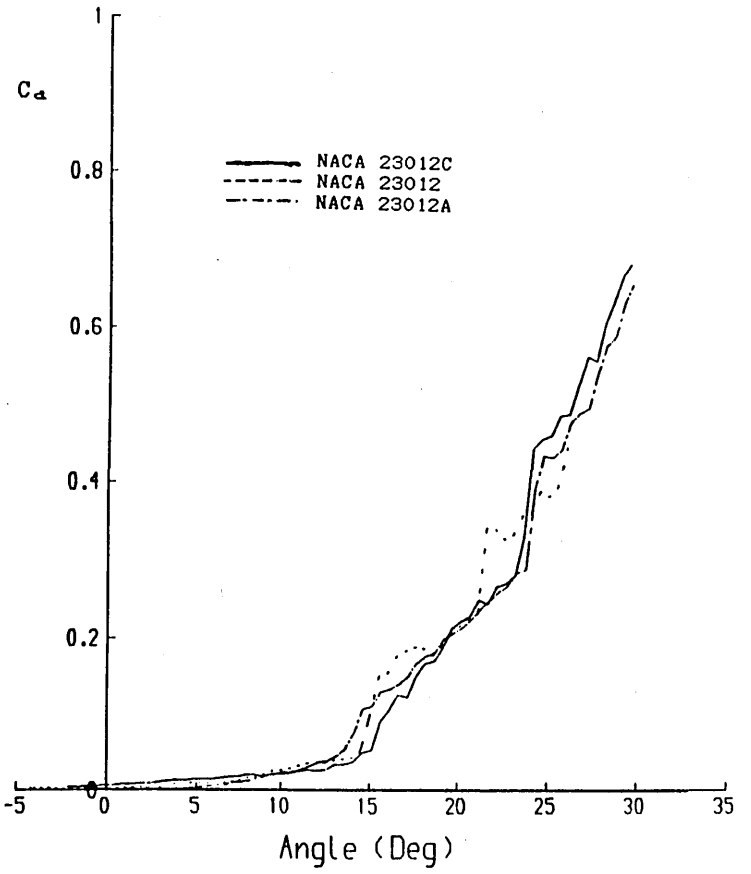

Figure 4.18 : Comparison of static drag force characteristics at a Reynolds number of approximately 1.5×10^6 for three aerofoils.

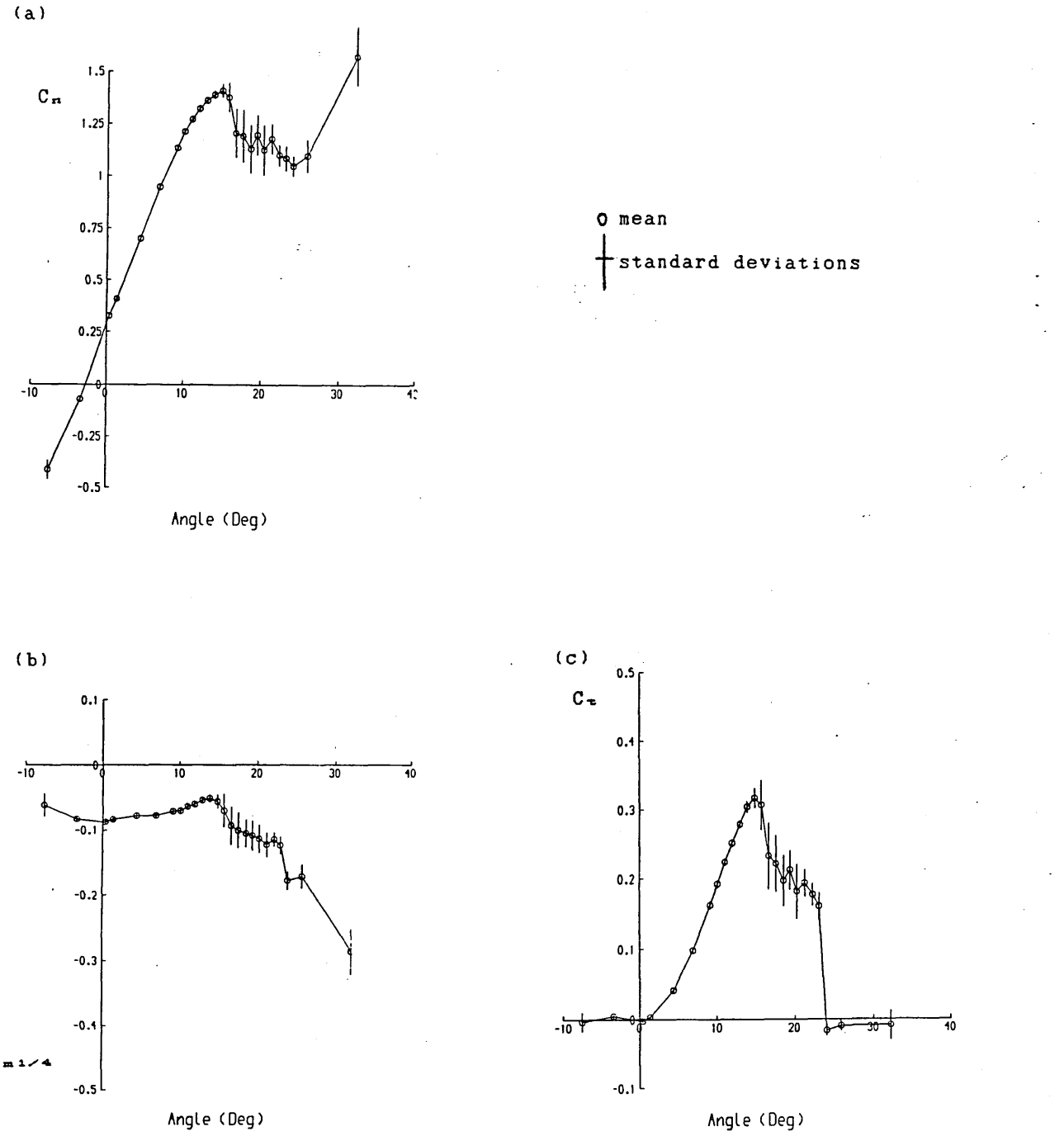

Figure 4.19 : Mean values and standard deviations of airloads and incidences from unsteady static experiments.

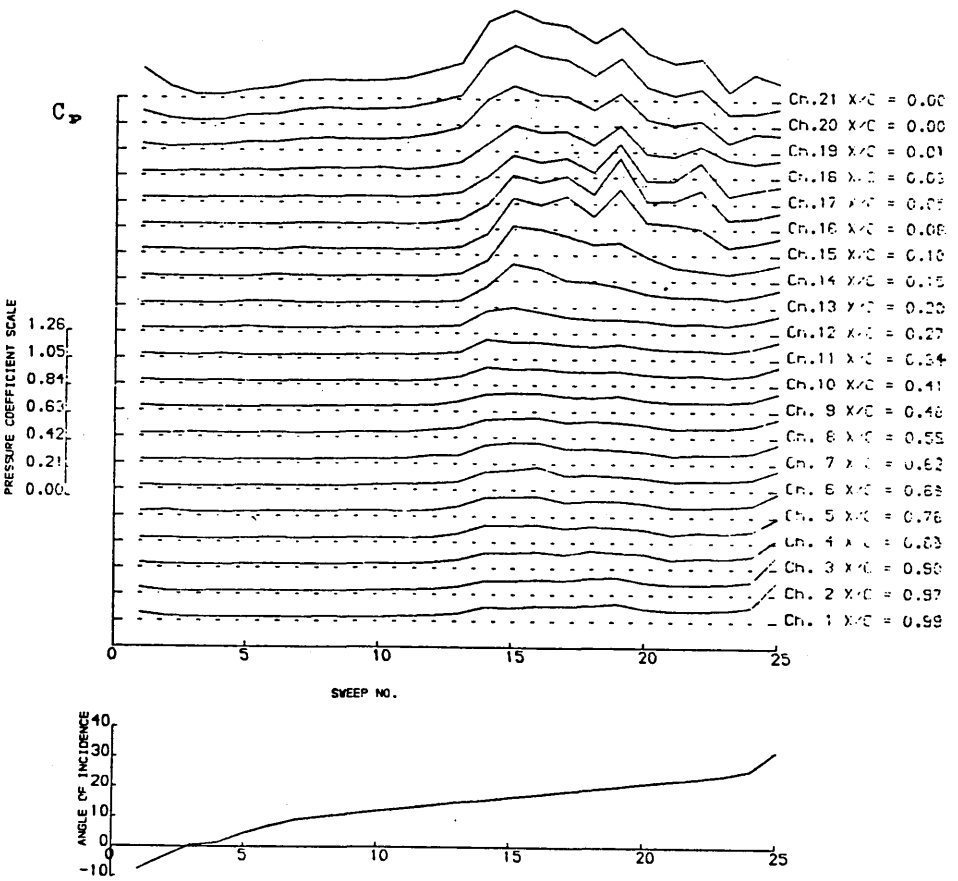

Figure 4.20 : Standard deviations of pressure coefficient traces from unsteady static experiments.

RUN REFERENCE NUMBER: 5351
REYNOLDS NUMBER = 1002922.
DYNAMIC PRESSURE = 459.54 Nm^{-2}
NUMBER OF CYCLES = 1
MOTION TYPE: STATIC

DATE OF TEST: 12/12/88
MACH NUMBER = 0.080
AIR TEMPERATURE = 27.2°C
SAMPLING FREQUENCY = 100.00 Hz.
AVERAGED DATA OF 1 CYCLES

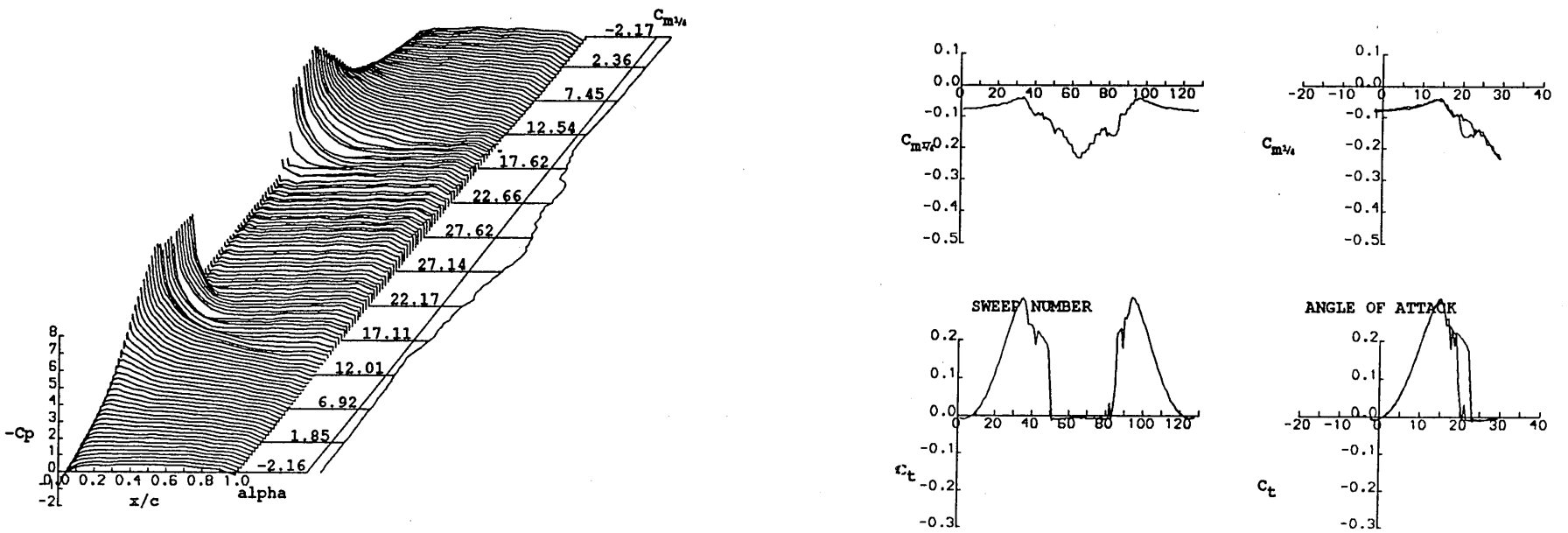

Figure 4.21 : Static characteristics of the NACA 23012C aerofoil at a Reynolds number of approximately 1.0×10^6.

RUN REFERENCE NUMBER: 5361
REYNOLDS NUMBER = 1970141.
DYNAMIC PRESSURE = 1770.30 Nm^{-2}
NUMBER OF CYCLES = 1
MOTION TYPE: STATIC

DATE OF TEST: 12/12/88
MACH NUMBER = 0.157
AIR TEMPERATURE = 27.0°C
SAMPLING FREQUENCY = 100.00 Hz.
AVERAGED DATA OF 1 CYCLES

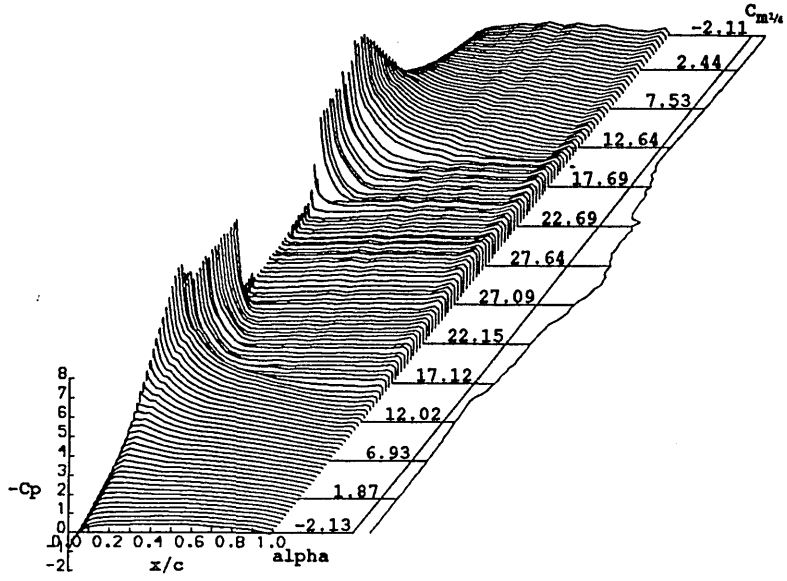

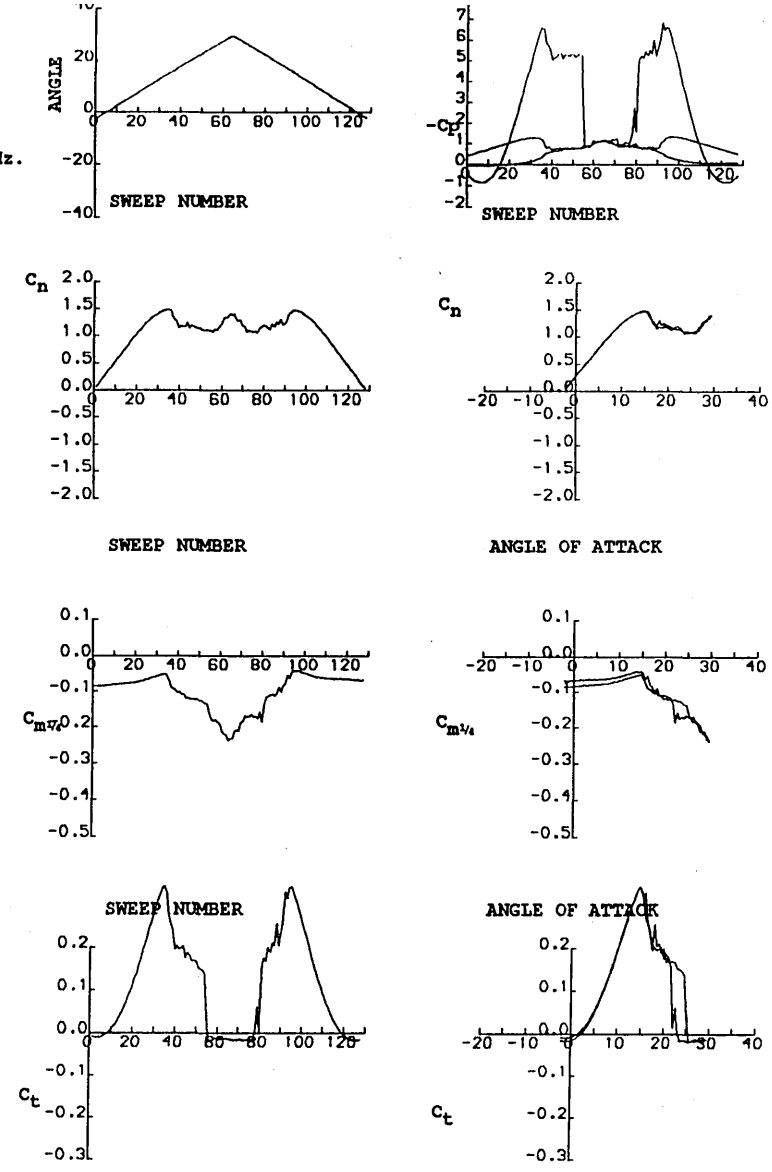

Figure 4.22 : Static characteristics of the NACA 23012C aerofoil at a Reynolds number of approximately 2.0×10^6.

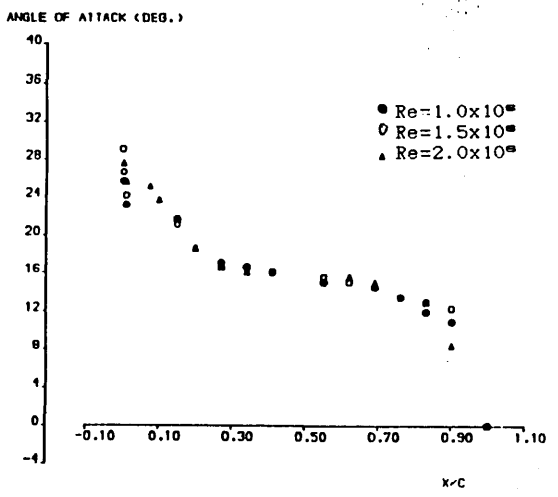

Figure 4.23 : Comparison of trailing-edge separation characteristics for the NACA 23012C aerofoil at three values of Reynolds number as determined from pressure distribution.

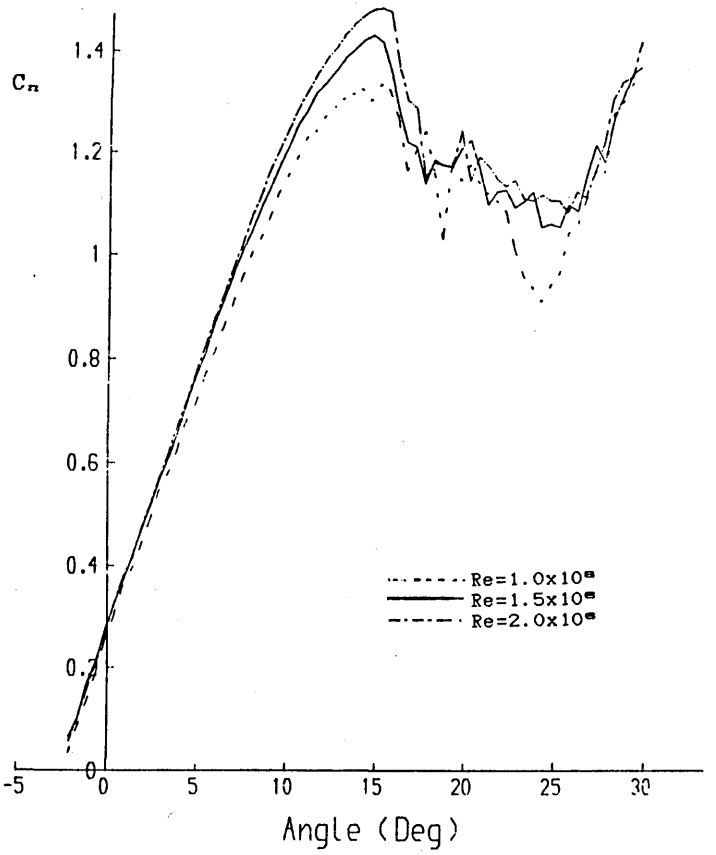

Figure 4.24 : Comparison of static normal force characteristics for the NACA 23012C aerofoil at three values of Reynolds number.

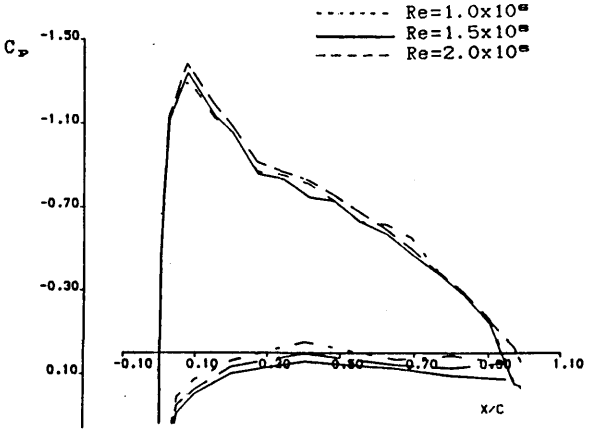

Figure 4.25 : Comparison of static pressure coefficient distributions for the NACA 23012C aerofoil at an incidence of 4.9° and three values of Reynolds number.

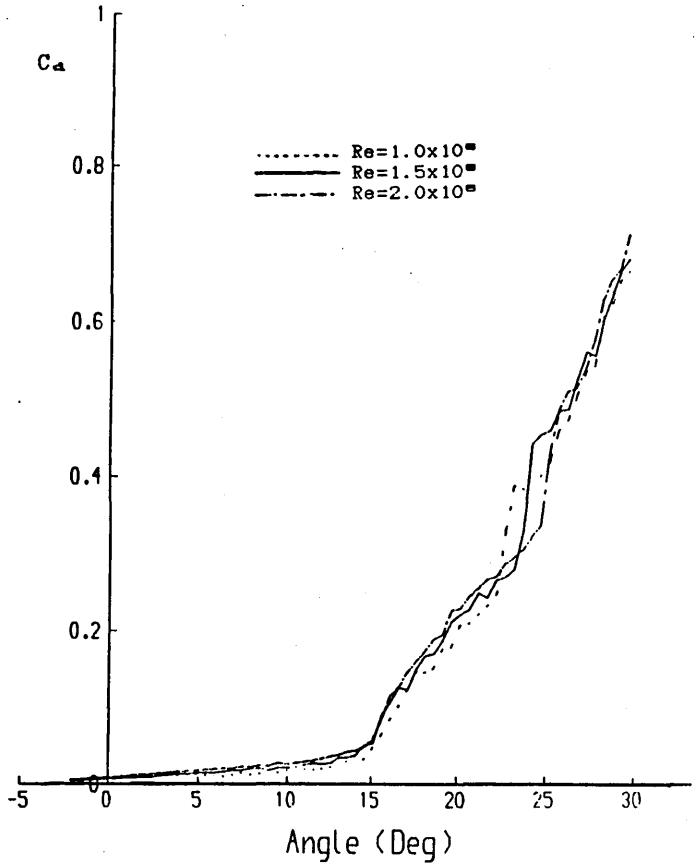

Figure 4.26 : Comparison of static drag force characteristics for the the NACA 23012C aerofoil at three values of Reynolds number.

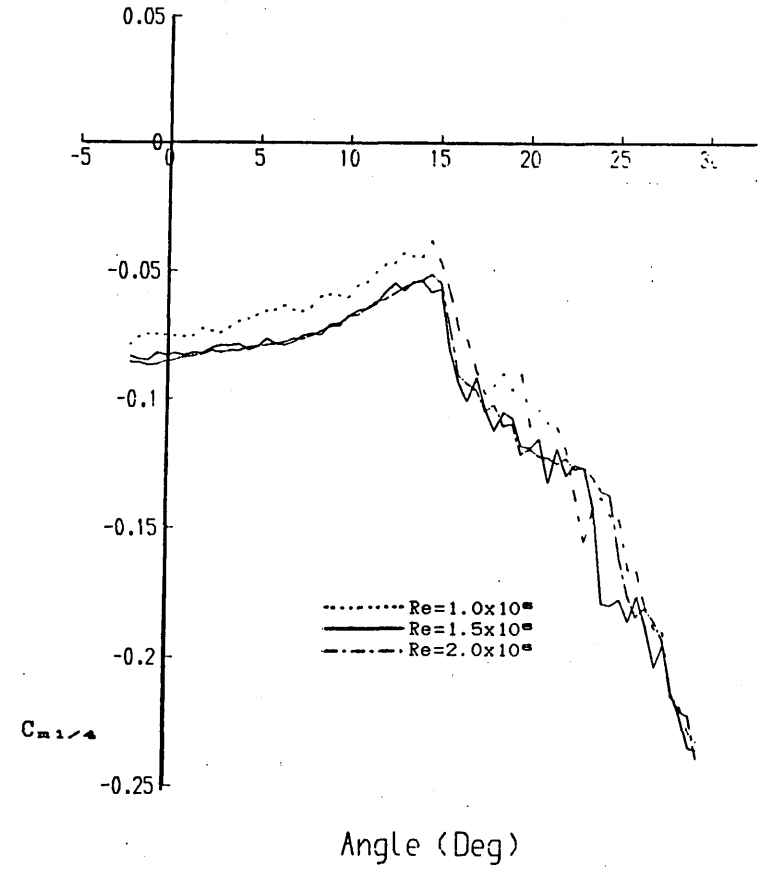

Figure 4.27 : Comparison of static pitching-moment characteristics for the NACA 23012C aerofoil at three values of Reynolds number.

DYNAMIC CHARACTERISTICS FOR THE NACA23012C MODEL04

RUN REFERENCE NUMBER: 16621
REYNOLDS NUMBER = 1499375.
DYNAMIC PRESSURE = 1016.39 Nm^{-2}
NUMBER OF CYCLES = 10
MOTION TYPE: SINUSOIDAL
MEAN ANGLE = 3.31°
OSCILLATION FREQUENCY = 2.414 Hz.
AVERAGED DATA OF 10 CYCLES

DATE OF TEST: 13/12/88
MACH NUMBER = 0.119
AIR TEMPERATURE = 26.2°C
SAMPLING FREQUENCY = 309.02 Hz.
REDUCED FREQUENCY = 0.101
AMPLITUDE = 8.21°

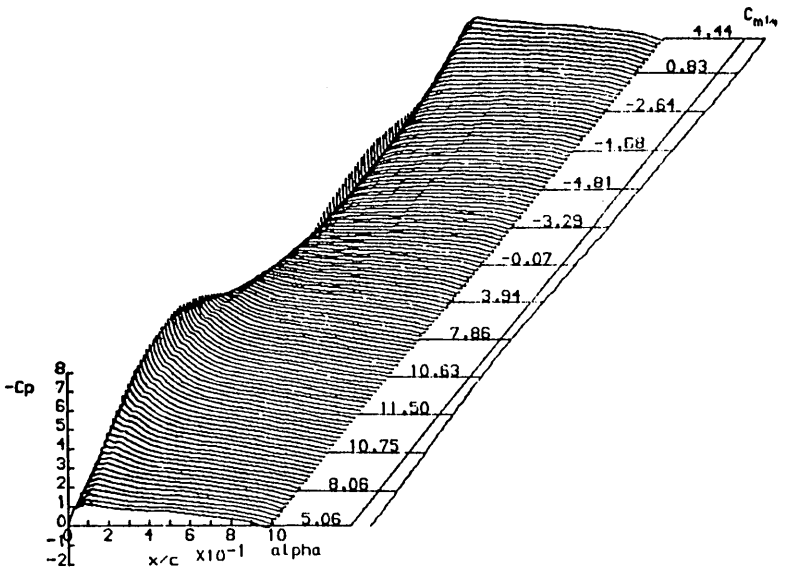

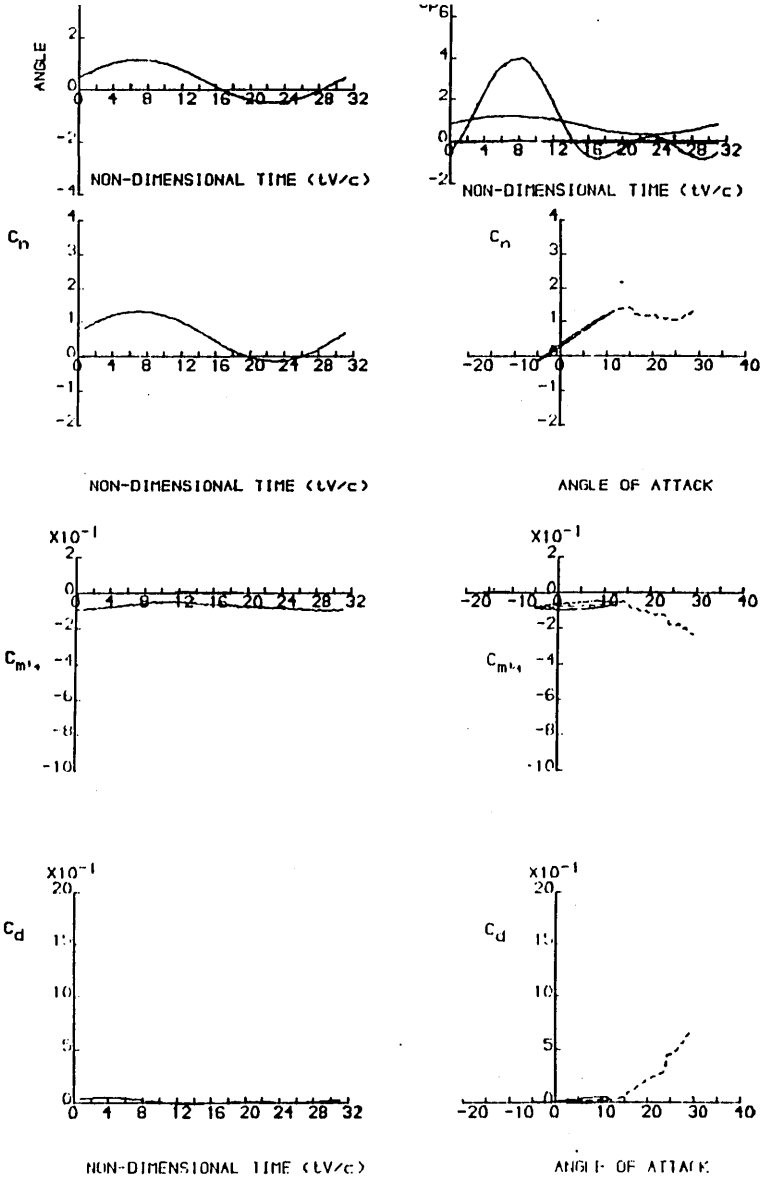

Figure 4.28 : Unsteady characteristics for the NACA 23012C aerofoil in the regime of no stall.

DYNAMIC CHARACTERISTICS FOR THE NACA23012C MODEL04

RUN REFERENCE NUMBER: 16681
REYNOLDS NUMBER = 1492985.
DYNAMIC PRESSURE = 1016.39 Nm^{-2}
NUMBER OF CYCLES = 10
MOTION TYPE: SINUSOIDAL
MEAN ANGLE = 9.80°
OSCILLATION FREQUENCY = 2.414 Hz.
AVERAGED DATA OF 10 CYCLES

DATE OF TEST: 13/12/88
MACH NUMBER = 0.119
AIR TEMPERATURE = 27.2°C
SAMPLING FREQUENCY = 309.02 Hz.
REDUCED FREQUENCY = 0.101
AMPLITUDE = 8.27°

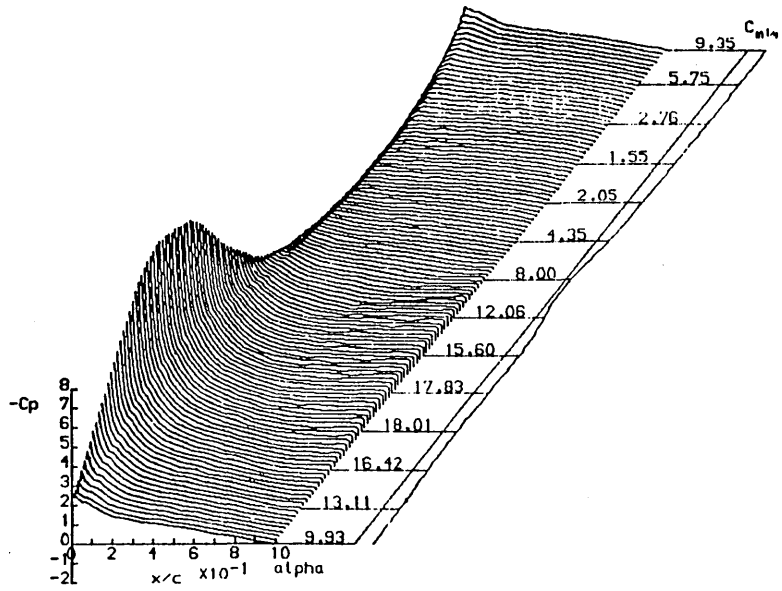

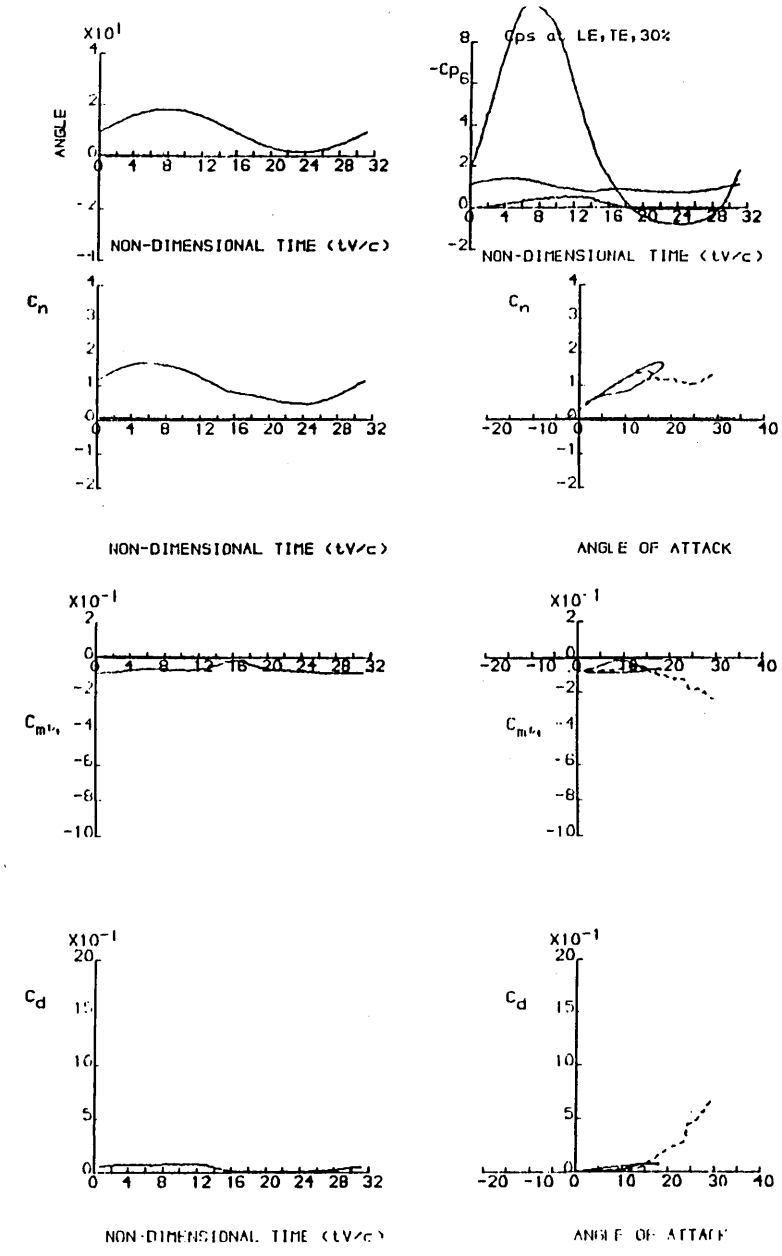

Figure 4.29 : Unsteady characteristics for the NACA 23012C aerofoil at incidence of stall onset.

DYNAMIC CHARACTERISTICS FOR THE NACA23012C MODEL04

RUN REFERENCE NUMBER: 16691
REYNOLDS NUMBER = 1492985.
DYNAMIC PRESSURE = 1016.39 Nm^{-2}
NUMBER OF CYCLES = 10
MOTION TYPE: SINUSOIDAL
MEAN ANGLE = 11.73°
OSCILLATION FREQUENCY = 2.414 Hz.
AVERAGED DATA OF 10 CYCLES

DATE OF TEST: 13/12/88
MACH NUMBER = 0.119
AIR TEMPERATURE = 27.2°C
SAMPLING FREQUENCY = 309.02 Hz.
REDUCED FREQUENCY = 0.101
AMPLITUDE = 8.27°

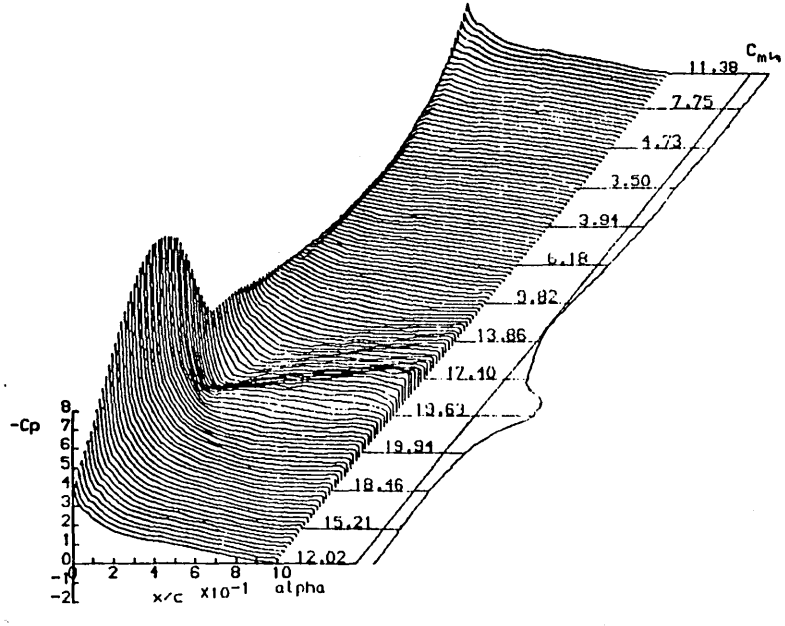

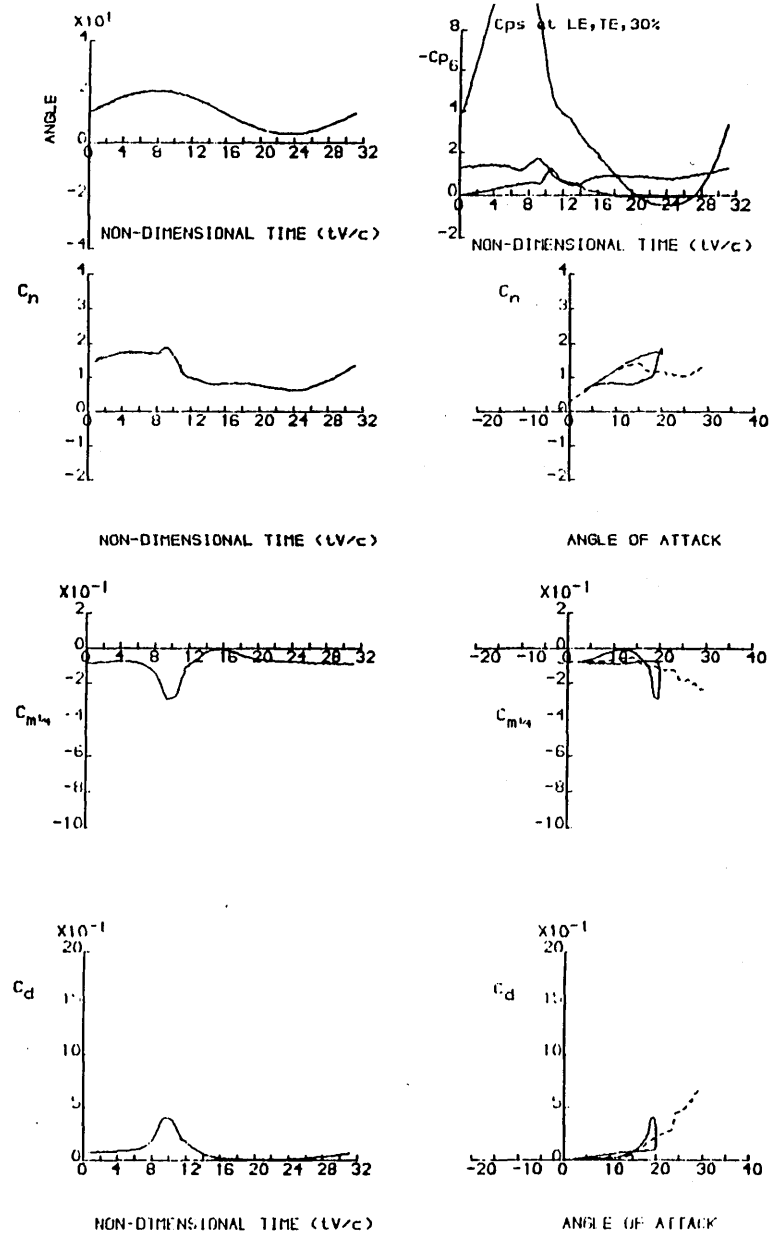

Figure 4.30 : Unsteady characteristics for the NACA 23012C aerofoil in the regime of light dynamic stall.

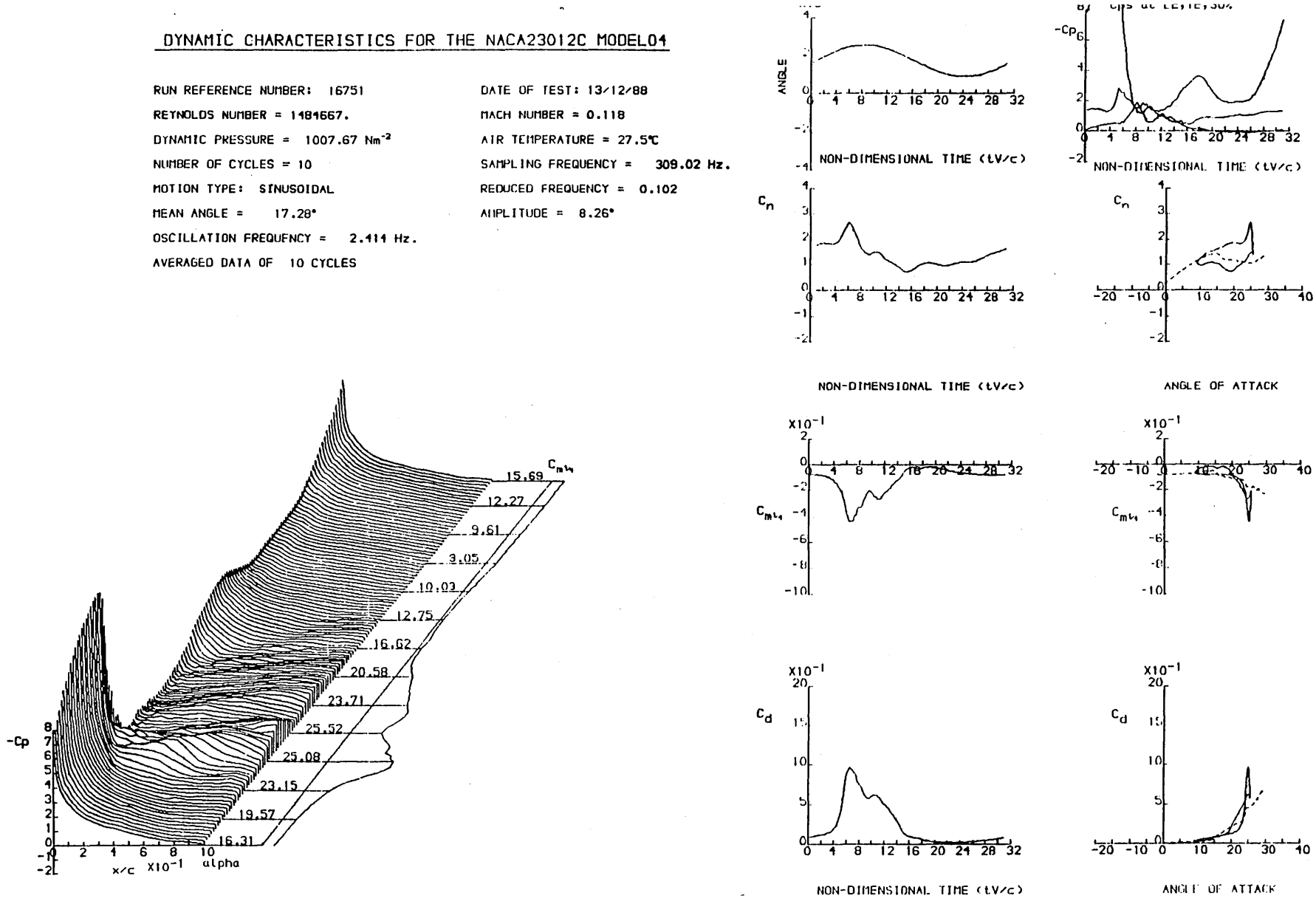

Figure 4.31 : Unsteady characteristics for the NACA 23012C aerofoil in the regime of deep dynamic stall.

DYNAMIC CHARACTERISTICS FOR THE NACA23012C MODEL04

RUN REFERENCE NUMBER: 16641
REYNOLDS NUMBER = 1494896.
DYNAMIC PRESSURE = 1016.39 Nm^{-2}
NUMBER OF CYCLES = 10
MOTION TYPE: SINUSOIDAL
MEAN ANGLE = 5.20°
OSCILLATION FREQUENCY = 2.414 Hz.
AVERAGED DATA OF 10 CYCLES

DATE OF TEST: 13/12/88
MACH NUMBER = 0.119
AIR TEMPERATURE = 26.9°C
SAMPLING FREQUENCY = 309.02 Hz.
REDUCED FREQUENCY = 0.101
AMPLITUDE = 8.25°

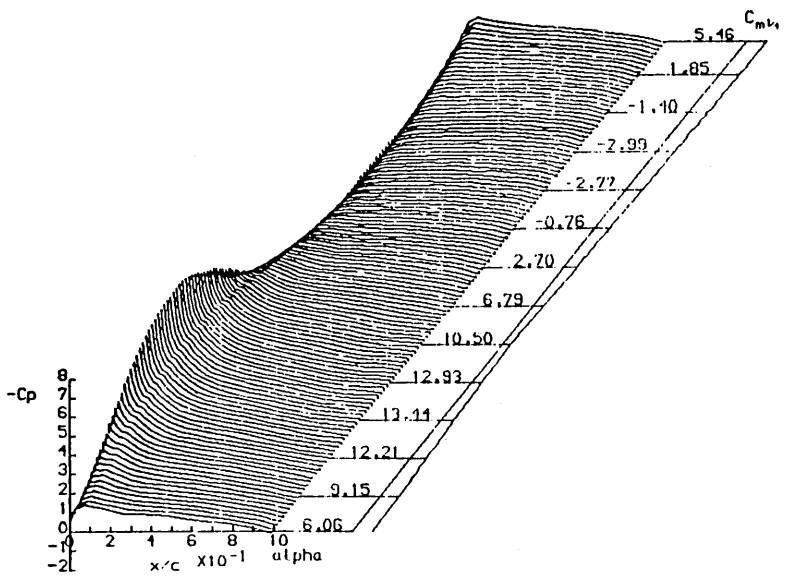

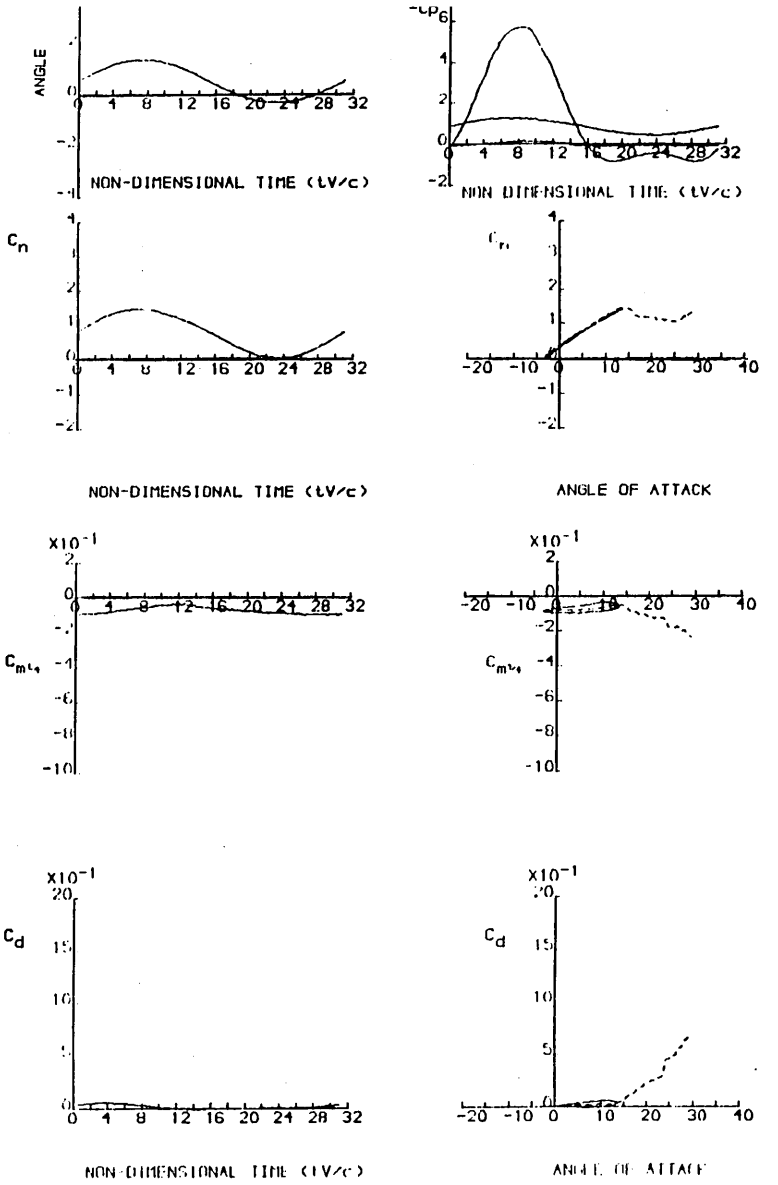

Figure 4.32 : Unsteady characteristics for the NACA 23012C aerofoil in the regime of no stall where the maximum incidence to be attained is 13.45°.

DYNAMIC CHARACTERISTICS FOR THE NACA23012C MODEL04

RUN REFERENCE NUMBER: 15861
REYNOLDS NUMBER = 1468798.
DYNAMIC PRESSURE = 1005.92 Nm^{-2}
NUMBER OF CYCLES = 10
MOTION TYPE: SINUSOIDAL
MEAN ANGLE = 13.61°
OSCILLATION FREQUENCY = 0.241 Hz.
AVERAGED DATA OF 10 CYCLES

DATE OF TEST: 12/12/88
MACH NUMBER = 0.118
AIR TEMPERATURE = 29.6°C
SAMPLING FREQUENCY = 30.85 Hz.
REDUCED FREQUENCY = 0.010
AMPLITUDE = 8.55°

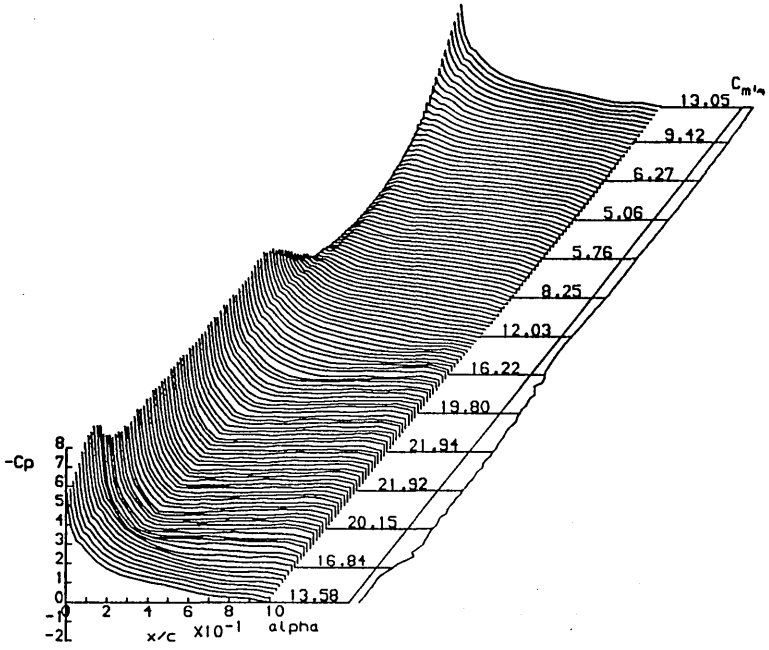

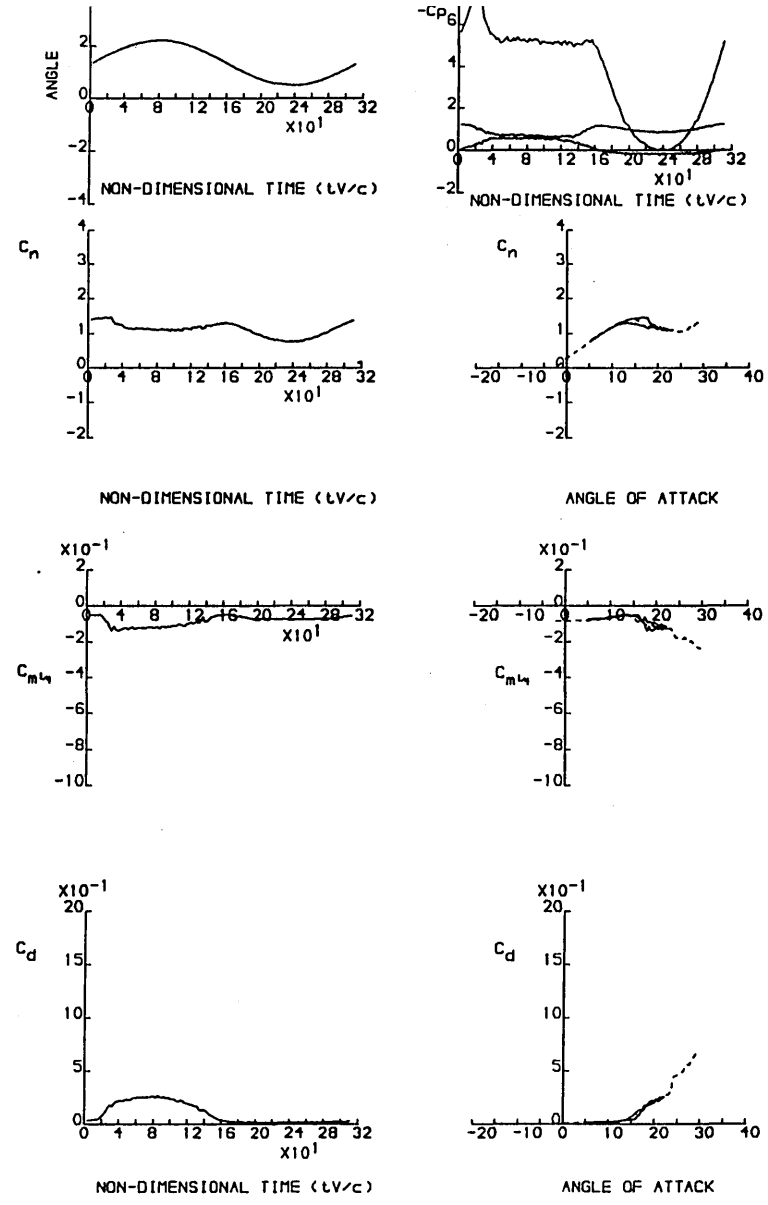

Figure 4.33 : Unsteady characteristics for the NACA 23012C aerofoil at a reduced frequency of 0.010.

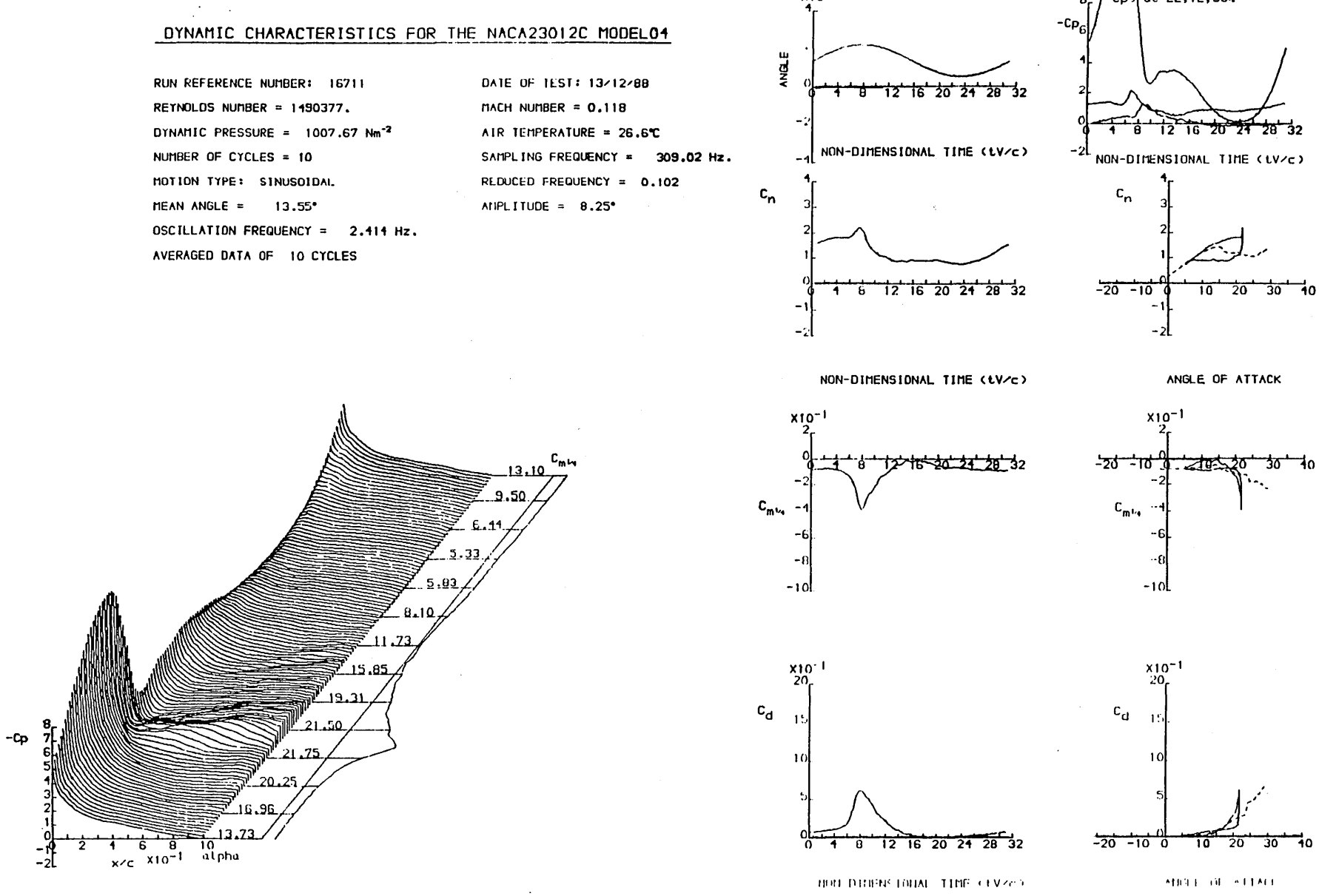

Figure 4.34 : Unsteady characteristics for the NACA 23012C aerofoil at a reduced frequency of 0.102.

DYNAMIC CHARACTERISTICS FOR THE NACA23012C MODEL04

RUN REFERENCE NUMBER: 17011
REYNOLDS NUMBER = 1489983.
DYNAMIC PRESSURE = 1020.09 Nm^{-2}
NUMBER OF CYCLES = 10
MOTION TYPE: SINUSOIDAL
MEAN ANGLE = 13.58°
OSCILLATION FREQUENCY = 3.624 Hz.
AVERAGED DATA OF 10 CYCLES

DATE OF TEST: 13/12/88
MACH NUMBER = 0.119
AIR TEMPERATURE = 28.1°C
SAMPLING FREQUENCY = 463.82 Hz.
REDUCED FREQUENCY = 0.151
AMPLITUDE = 8.12°

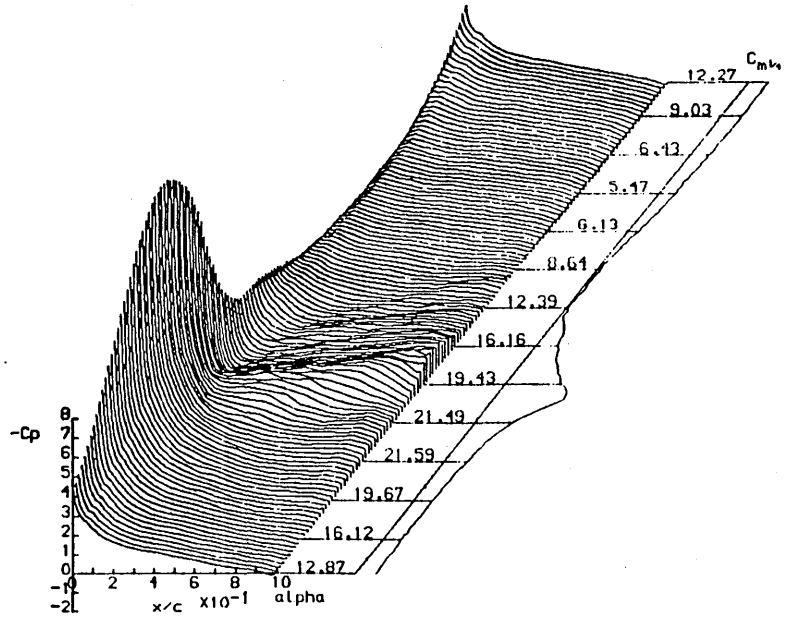

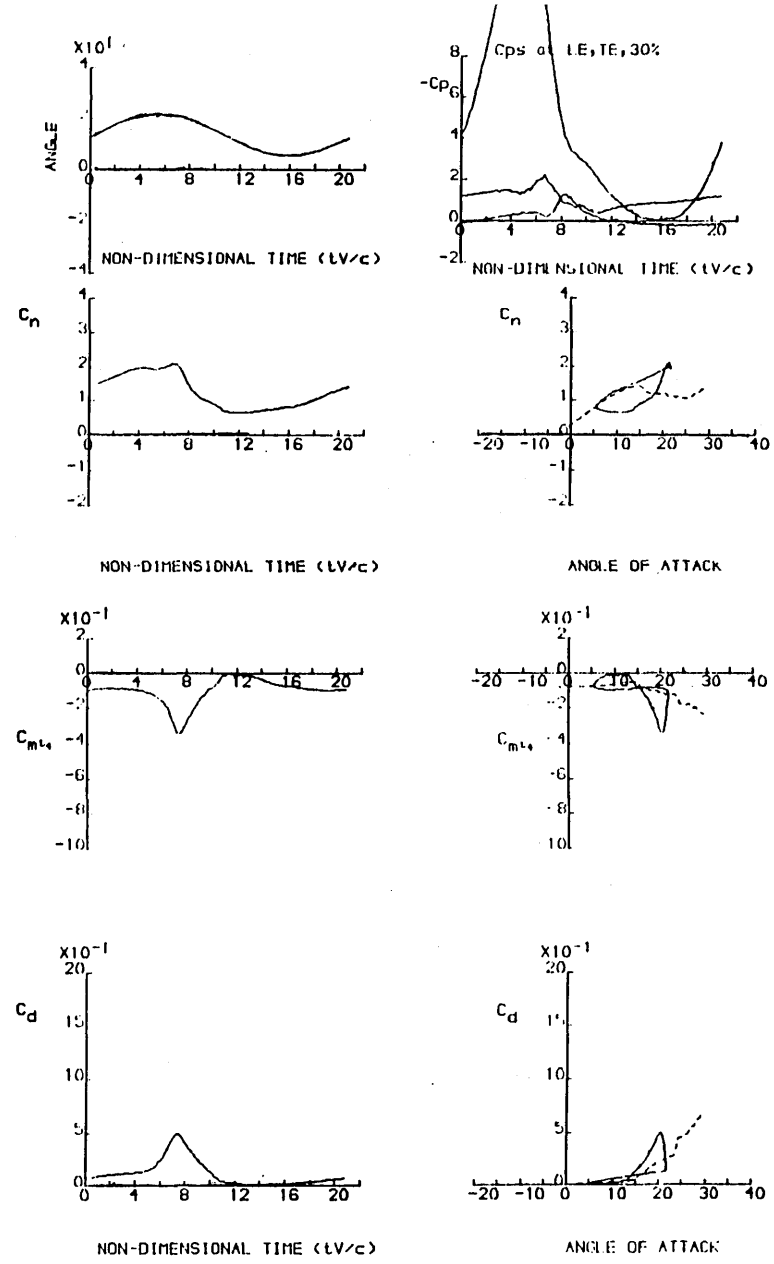

Figure 4.35 : Unsteady characteristics for the NACA 23012C aerofoil at a reduced frequency of 0.151.

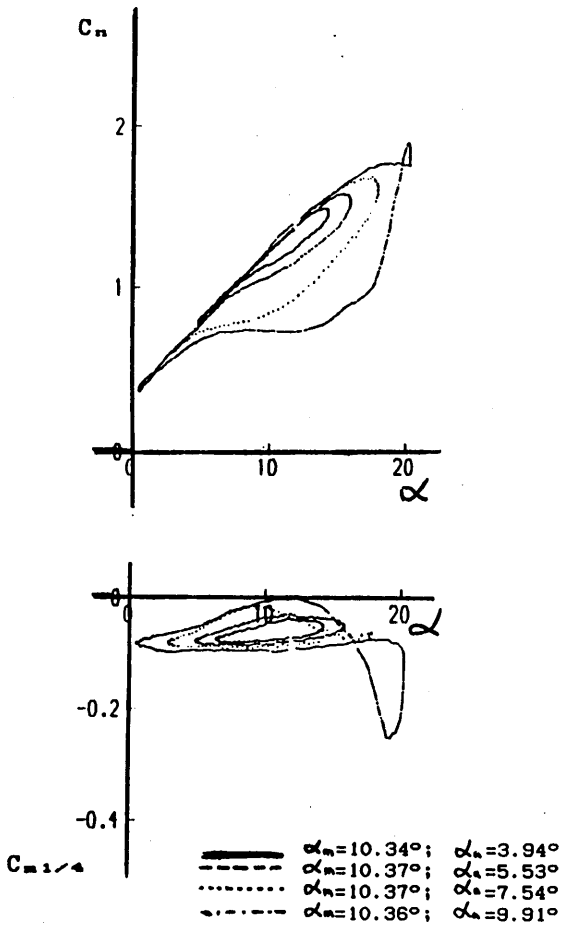

Figure 4.36 : Comparison of normal force and pitching-moment characteristics for the NACA 23012C aerofoil at a Reynolds number of 1.5×10^6 and a reduced frequency of 0.10.

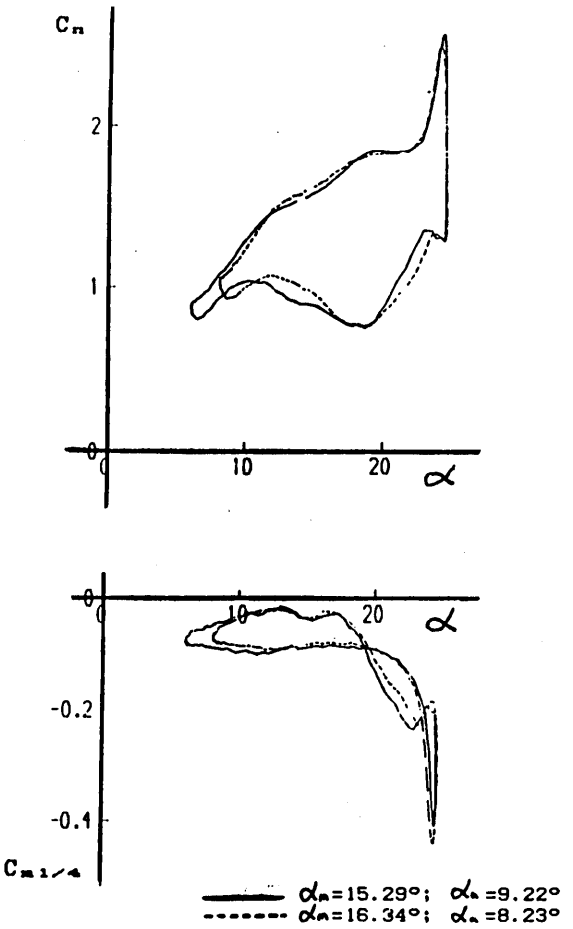

Figure 4.37 : Comparison of normal force and pitching-moment characteristics for the NACA 23012C aerofoil at a Reynolds number of 1.5×10^6 and a reduced frequency of 0.10.

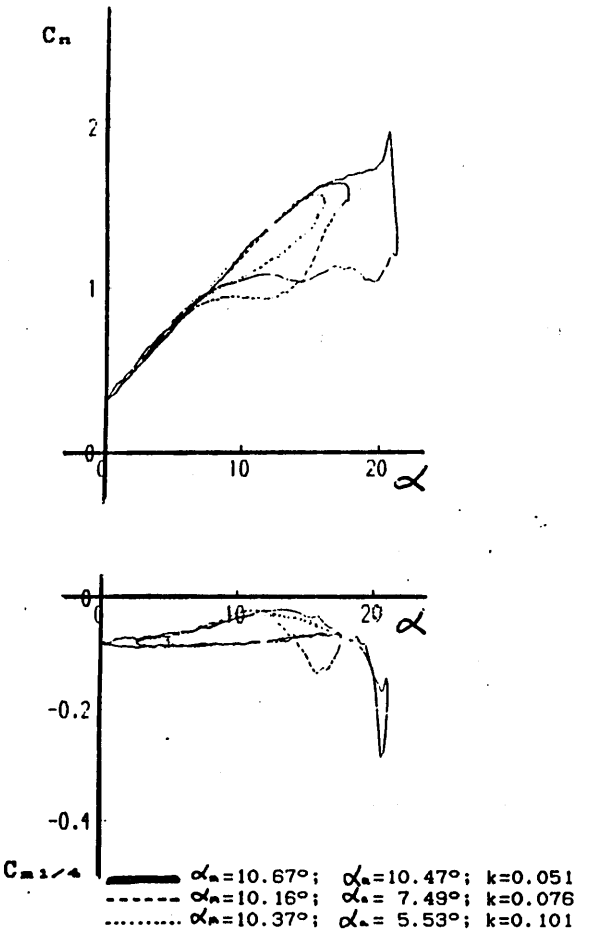

Figure 4.38 : Comparison of normal force and pitching-moment characteristics for the NACA 23012C aerofoil at a Reynolds number of 1.5×10^6 and three reduced frequencies.

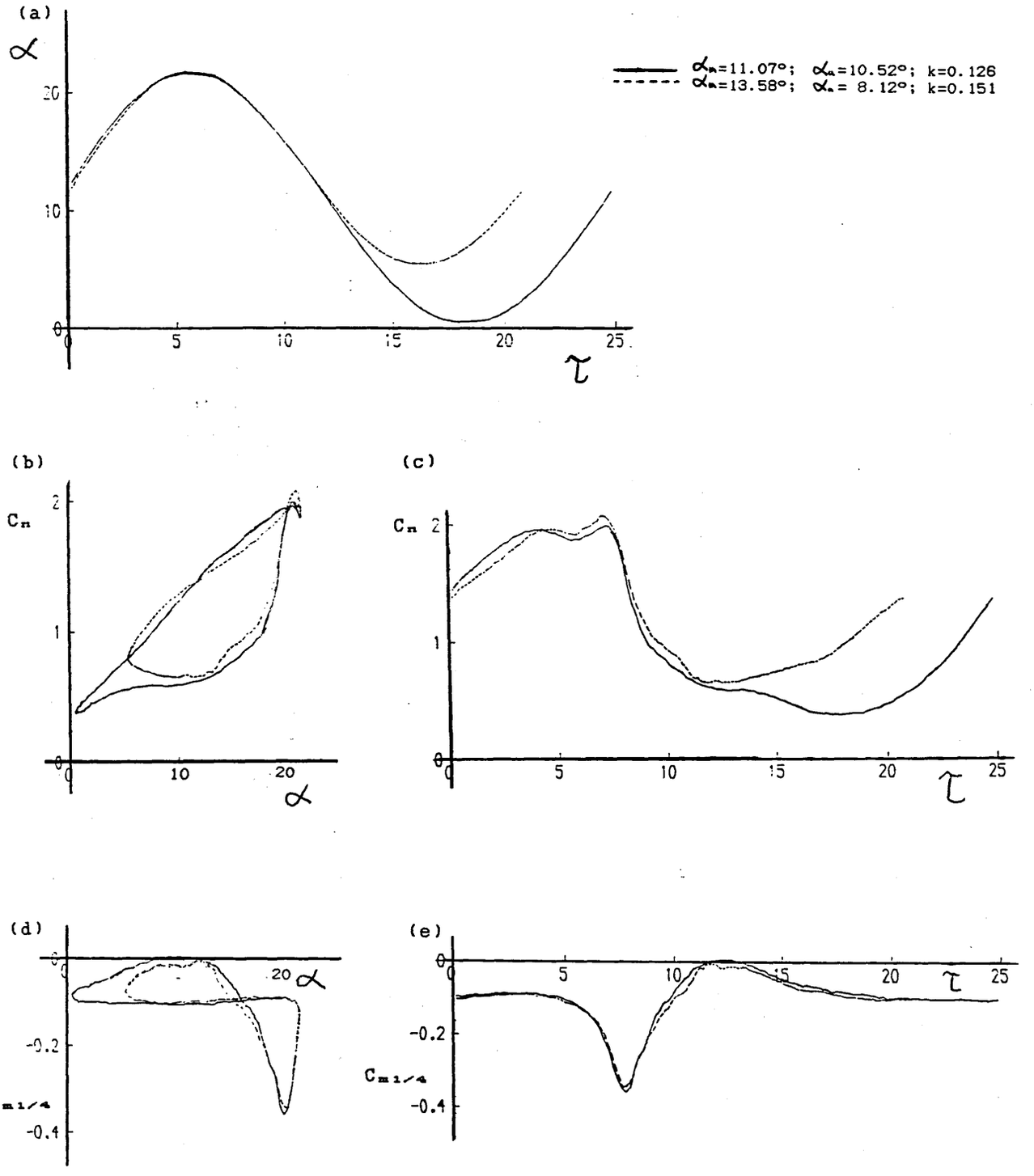

Figure 4.39 : Comparison of aerodynamic characteristics of the NACA 23012C aerofoil for two test cases possessing similar incidence traces on the upper half of the cycle.

DYNAMIC CHARACTERISTICS FOR THE NACA23012C MODEL04

RUN REFERENCE NUMBER: 16162
DATE OF TEST: 14/12/88
REYNOLDS NUMBER = 995852.
MACH NUMBER = 0.079
DYNAMIC PRESSURE = 450.37 Nm^{-2}
AIR TEMPERATURE = 27.1°C
NUMBER OF CYCLES = 10
SAMPLING FREQUENCY = 205.93 Hz.
MOTION TYPE: SINUSOIDAL
REDUCED FREQUENCY = 0.101
MEAN ANGLE = 11.69°
AMPLITUDE = 8.04°
OSCILLATION FREQUENCY = 1.609 Hz.
AVERAGED DATA OF 10 CYCLES

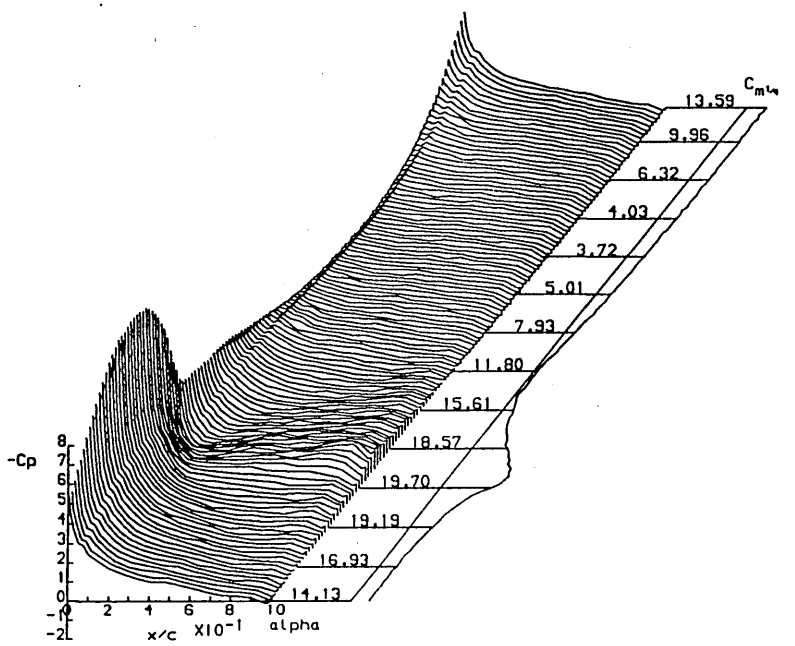

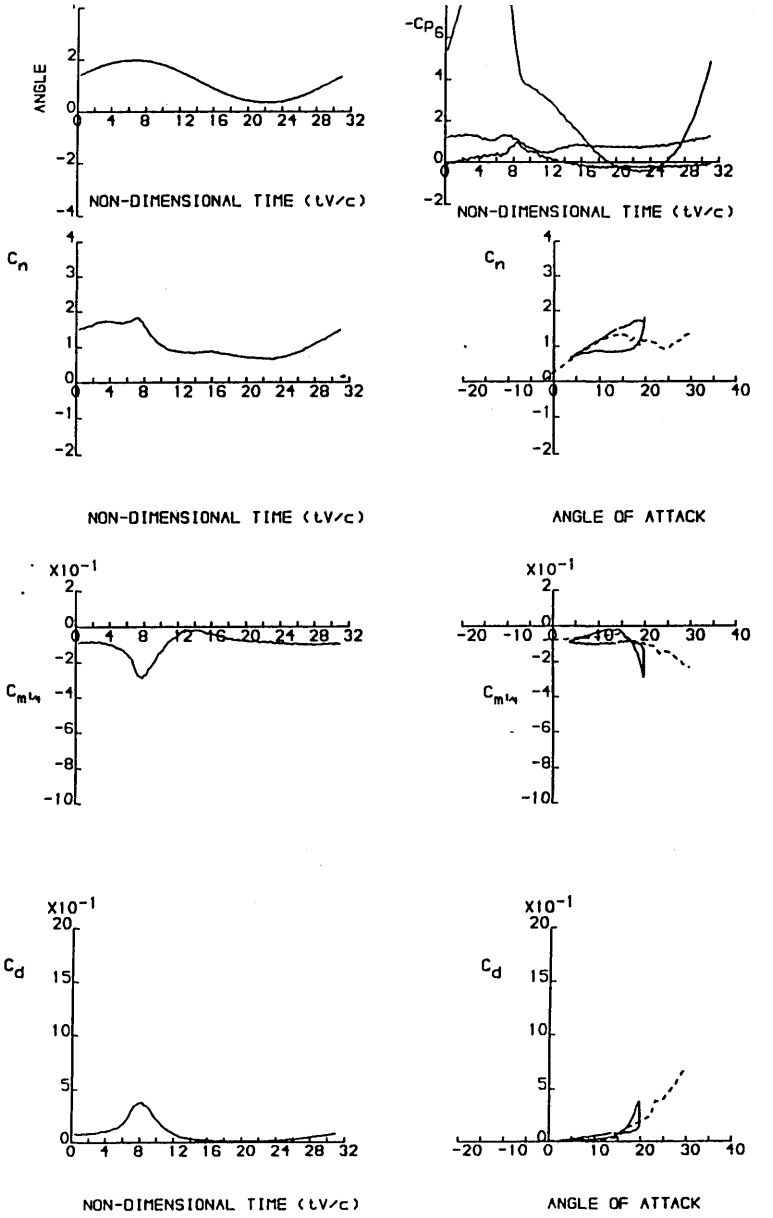

Figure 4.40 : Unsteady characteristics for the NACA 23012C aerofoil at a Reynolds number of 1.0×10^6 in the regime of light dynamic stall.

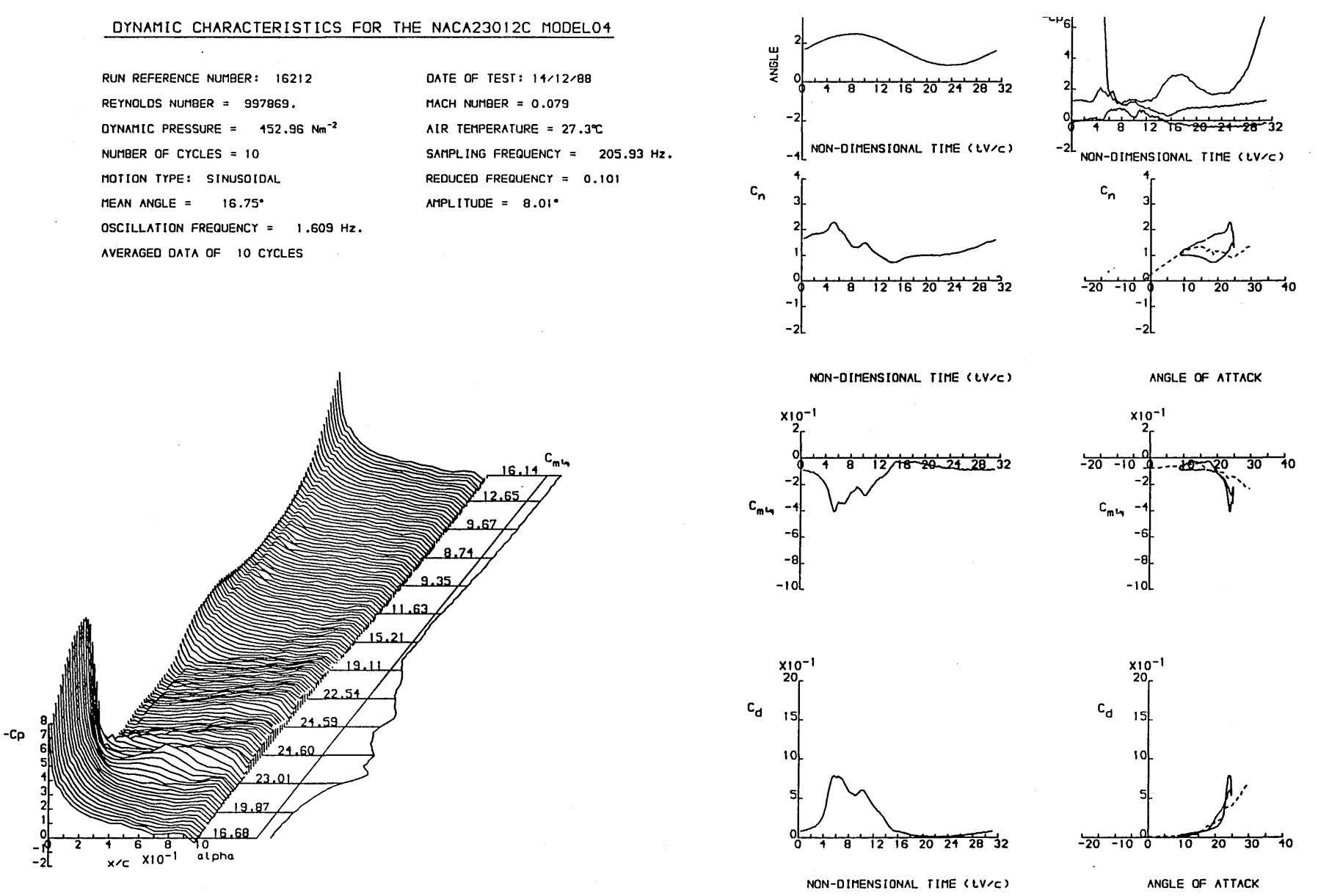

Figure 4.41 : Unsteady characteristics for the NACA 23012C aerofoil at a Reynolds number of 1.0×10^6 in the regime of deep dynamic stall.

DYNAMIC CHARACTERISTICS FOR THE NACA23012C MODEL04

RUN REFERENCE NUMBER: 16601
REYNOLDS NUMBER = 1919398.
DYNAMIC PRESSURE = 1758.68 Nm^{-2}
NUMBER OF CYCLES = 10
MOTION TYPE: SINUSOIDAL
MEAN ANGLE = 11.67°
OSCILLATION FREQUENCY = 3.223 Hz.
AVERAGED DATA OF 10 CYCLES

DATE OF TEST: 12/12/88
MACH NUMBER = 0.156
AIR TEMPERATURE = 32.1°C
SAMPLING FREQUENCY = 412.54 Hz.
REDUCED FREQUENCY = 0.102
AMPLITUDE = 7.80°

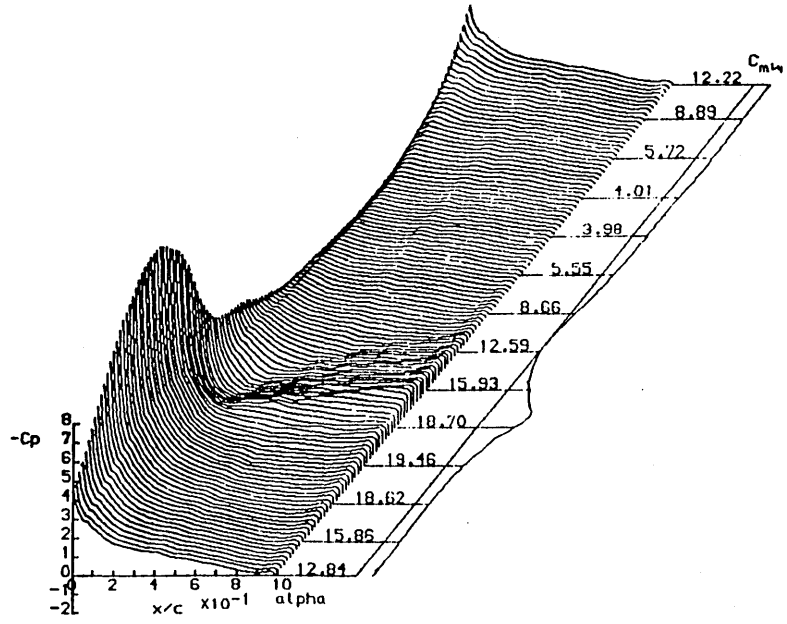

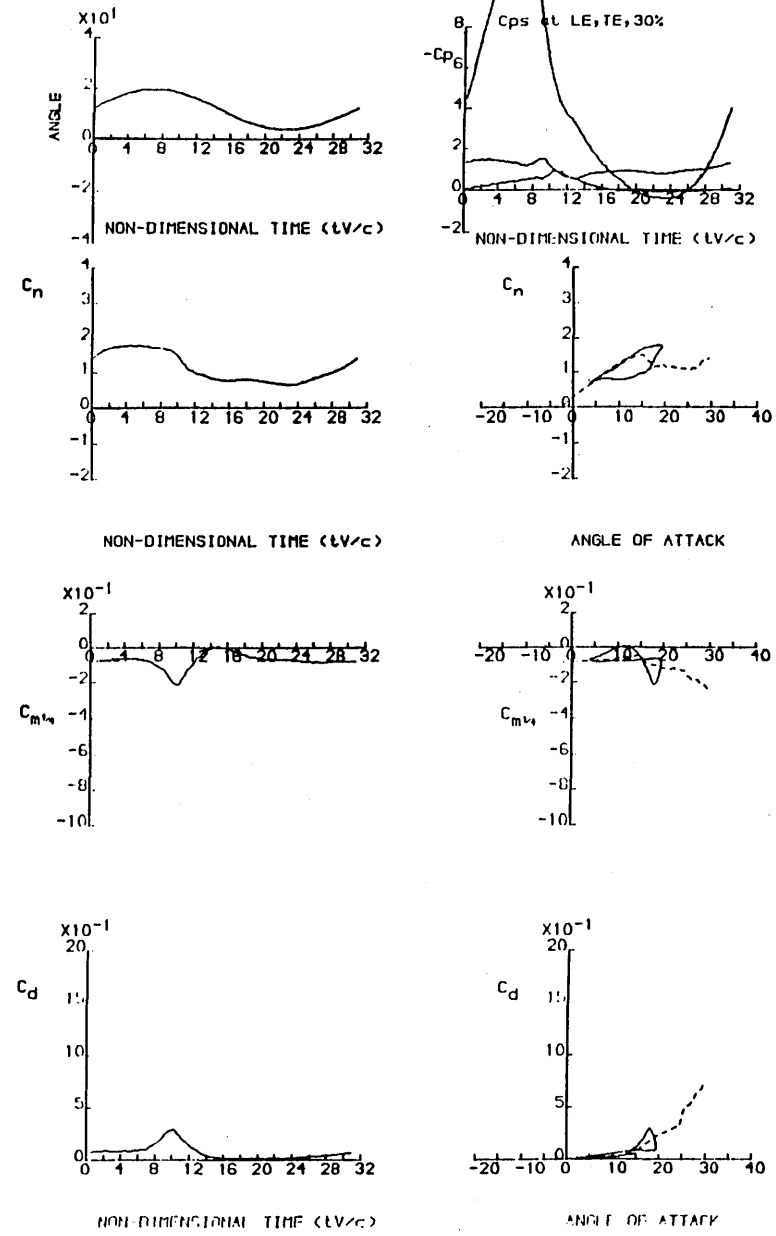

Figure 4.42 : Unsteady characteristics for the NACA 23012C aerofoil at a Reynolds number of 2.0×10^6 in the regime of light dynamic stall.

DYNAMIC CHARACTERISTICS FOR THE NACA23012C MODEL04

RUN REFERENCE NUMBER: 17521
REYNOLDS NUMBER = 1934973.
DYNAMIC PRESSURE = 1758.62 Nm^{-2}
NUMBER OF CYCLES = 10
MOTION TYPE: SINUSOIDAL
MEAN ANGLE = 17.10°
OSCILLATION FREQUENCY = 3.223 Hz.
AVERAGED DATA OF 10 CYCLES

DATE OF TEST: 13/12/88
MACH NUMBER = 0.156
AIR TEMPERATURE = 30.7°C
SAMPLING FREQUENCY = 412.54 Hz.
REDUCED FREQUENCY = 0.102
AMPLITUDE = 7.71°

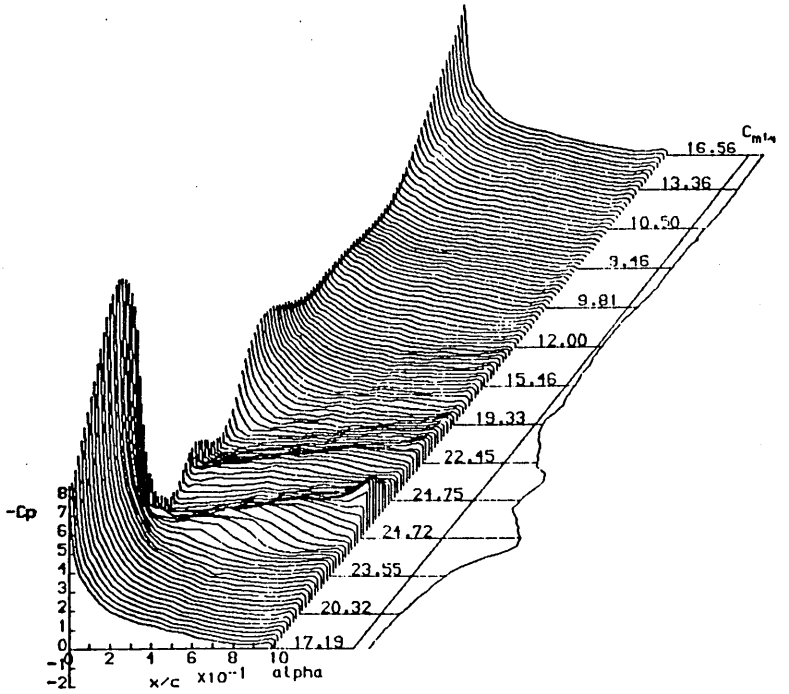

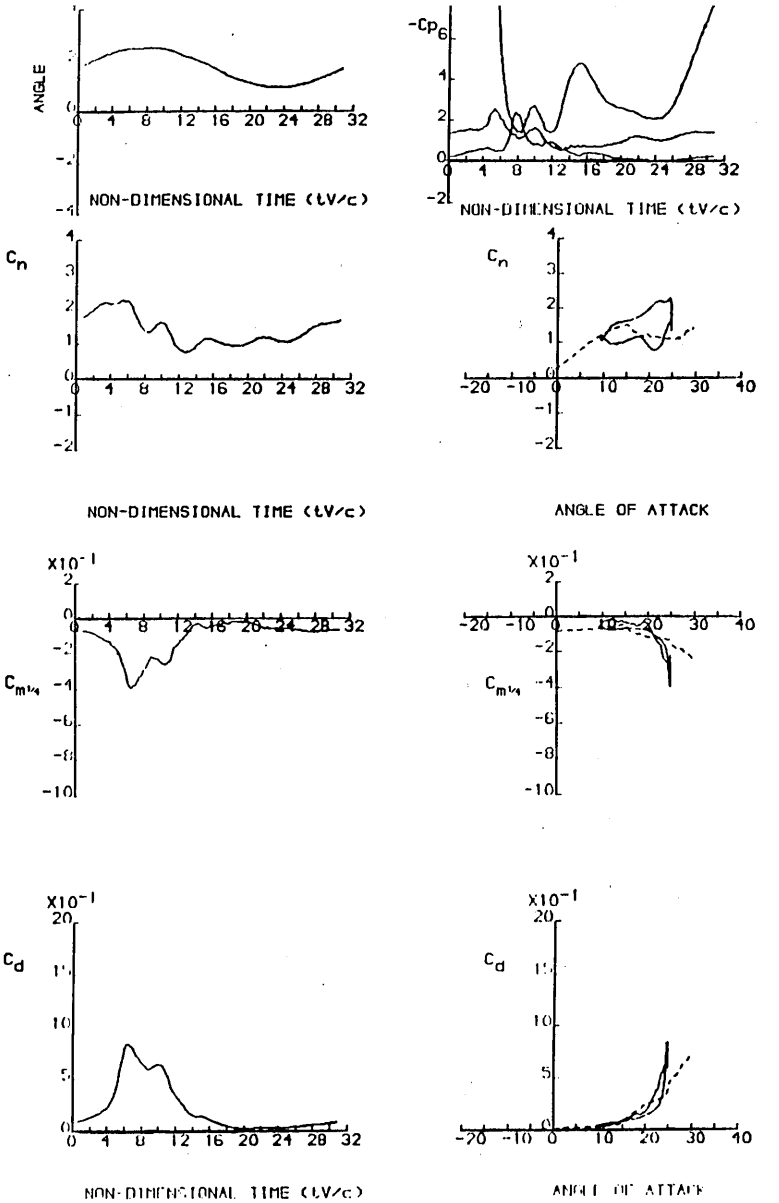

Figure 4.43 : Unsteady characteristics for the NACA 23012C aerofoil at a Reynolds number of 2.0×10^6 in the regime of deep dynamic stall.

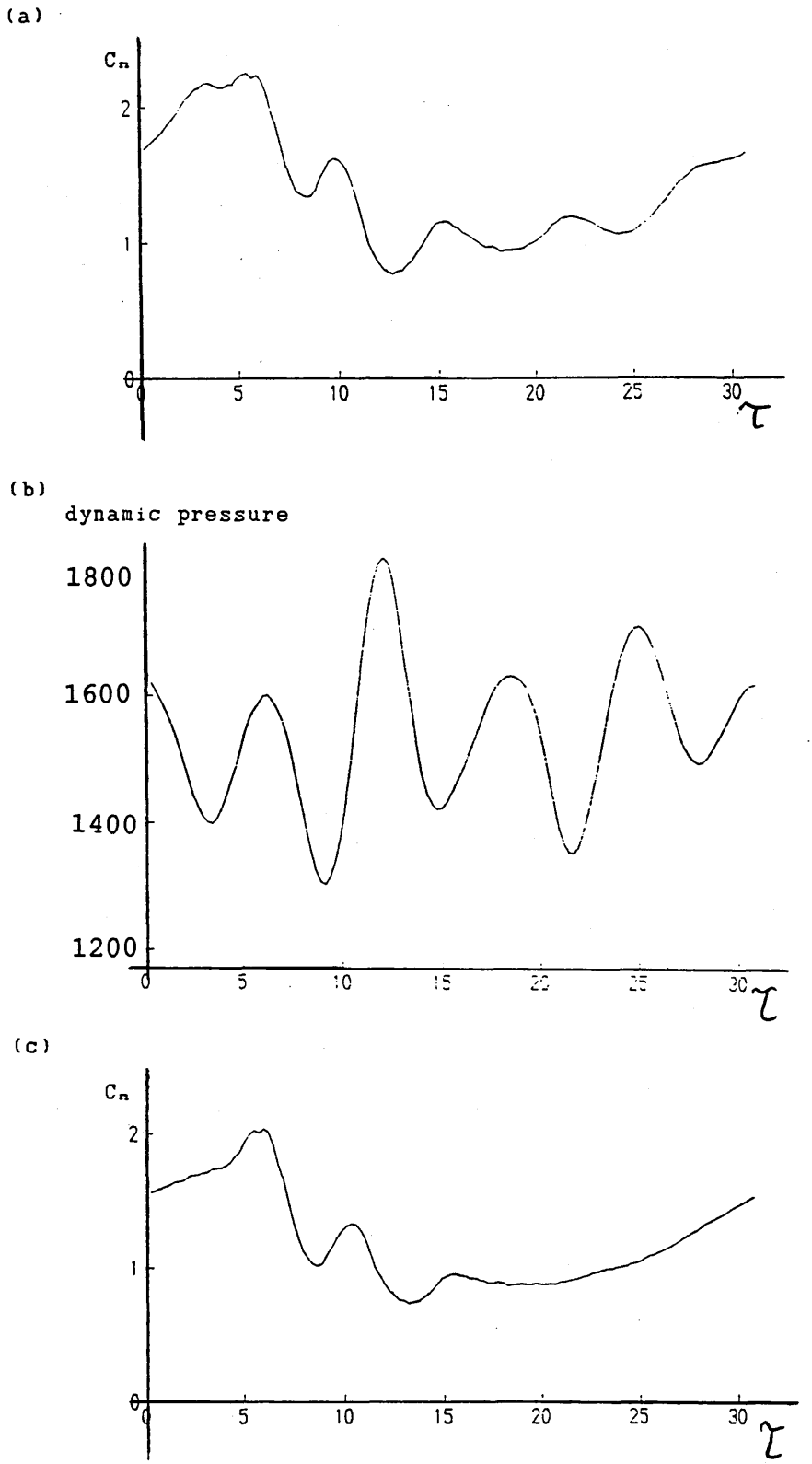

Figure 4.44 : Influence of variation of dynamic pressure on the normal force coefficient trace.

DYNAMIC CHARACTERISTICS FOR THE NACA 23012 MODEL01

RUN REFERENCE NUMBER: 13541
REYNOLDS NUMBER = 1524106.
DYNAMIC PRESSURE = 998.27 Nm^{-2}
NUMBER OF CYCLES = 10
MOTION TYPE: SINUSOIDAL
MEAN ANGLE = 6.49°
OSCILLATION FREQUENCY = 2.330 Hz.
AVERAGED DATA OF 10 CYCLES

DATE OF TEST: 16/6/83
MACH NUMBER = 0.112
AIR TEMPERATURE = 31.5°C
SAMPLING FREQUENCY = 298.24 Hz.
REDUCED FREQUENCY = 0.103
AMPLITUDE = 8.23°

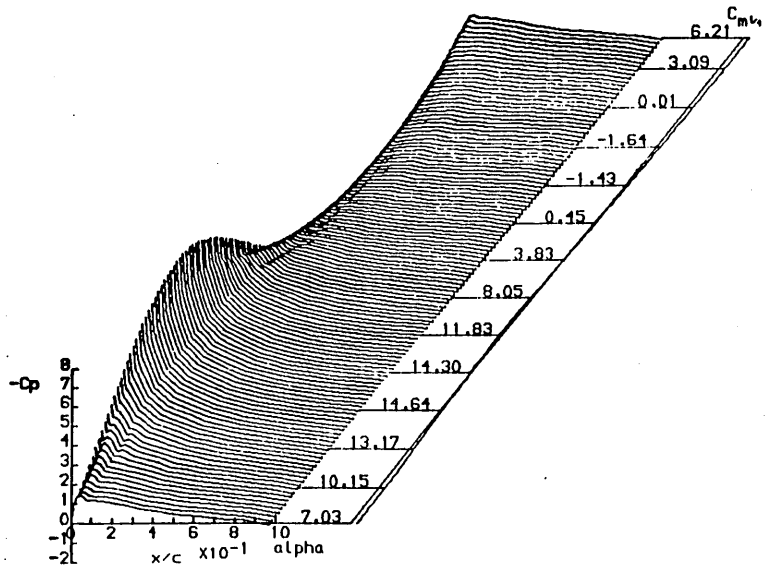

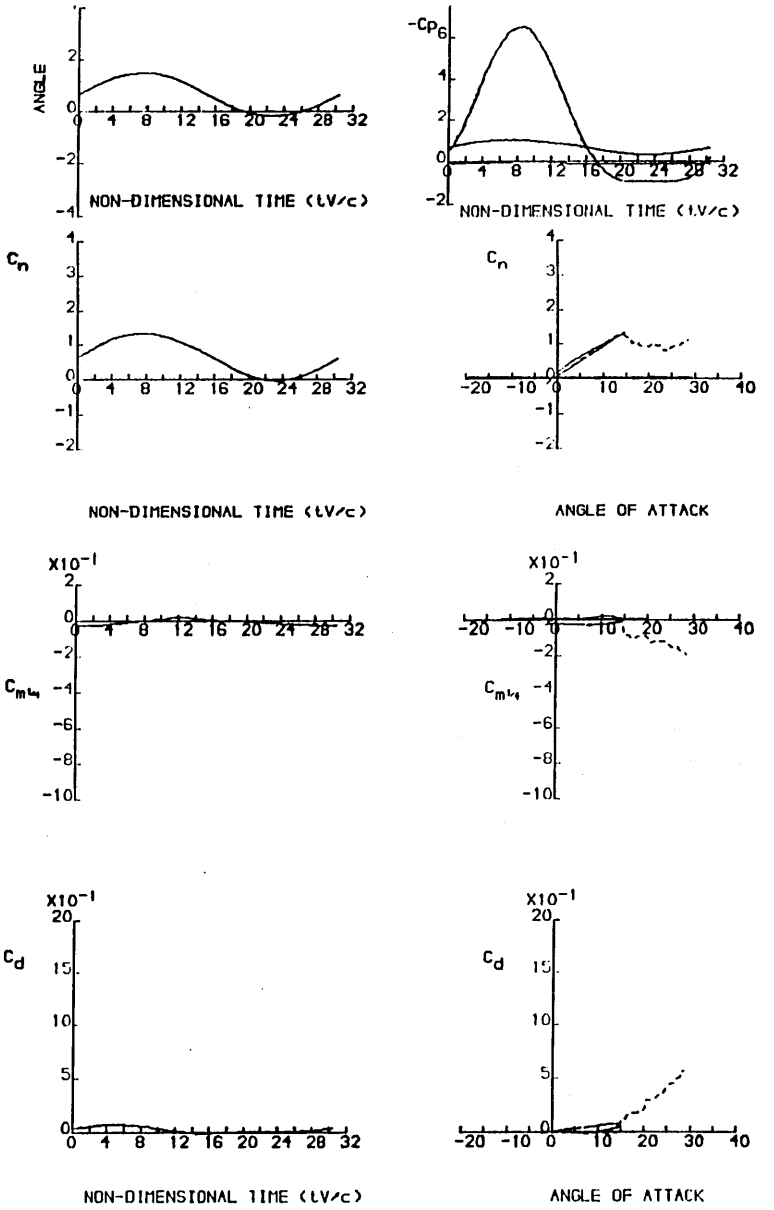

Figure 4.45 : Unsteady characteristics for the NACA 23012 aerofoil in the regime of no stall.

DYNAMIC CHARACTERISTICS FOR THE NACA 23012 MODEL01

RUN REFERENCE NUMBER: 13591
REYNOLDS NUMBER = 1529997.
DYNAMIC PRESSURE = 1014.27 Nm^{-2}
NUMBER OF CYCLES = 10
MOTION TYPE: SINUSOIDAL
MEAN ANGLE = 8.13°
OSCILLATION FREQUENCY = 2.330 Hz.
AVERAGED DATA OF 10 CYCLES

DATE OF TEST: 16/6/83
MACH NUMBER = 0.113
AIR TEMPERATURE = 33.0°C
SAMPLING FREQUENCY = 298.24 Hz.
REDUCED FREQUENCY = 0.102
AMPLITUDE = 8.21°

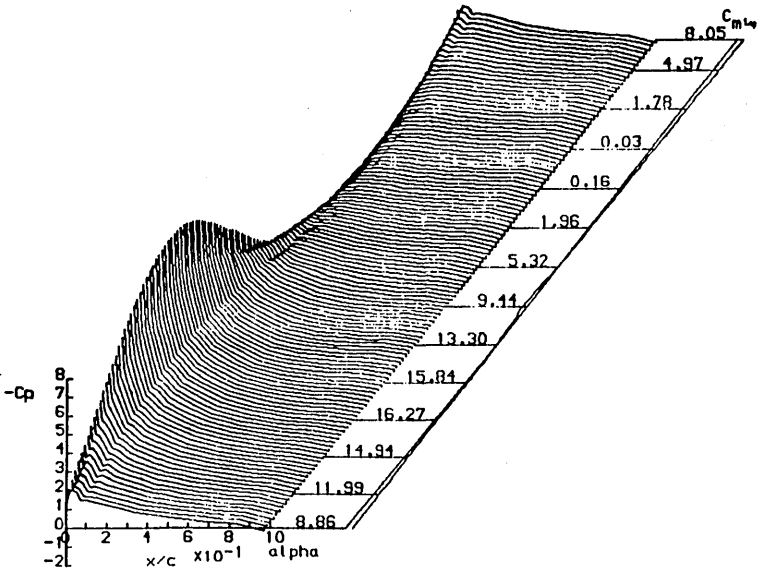

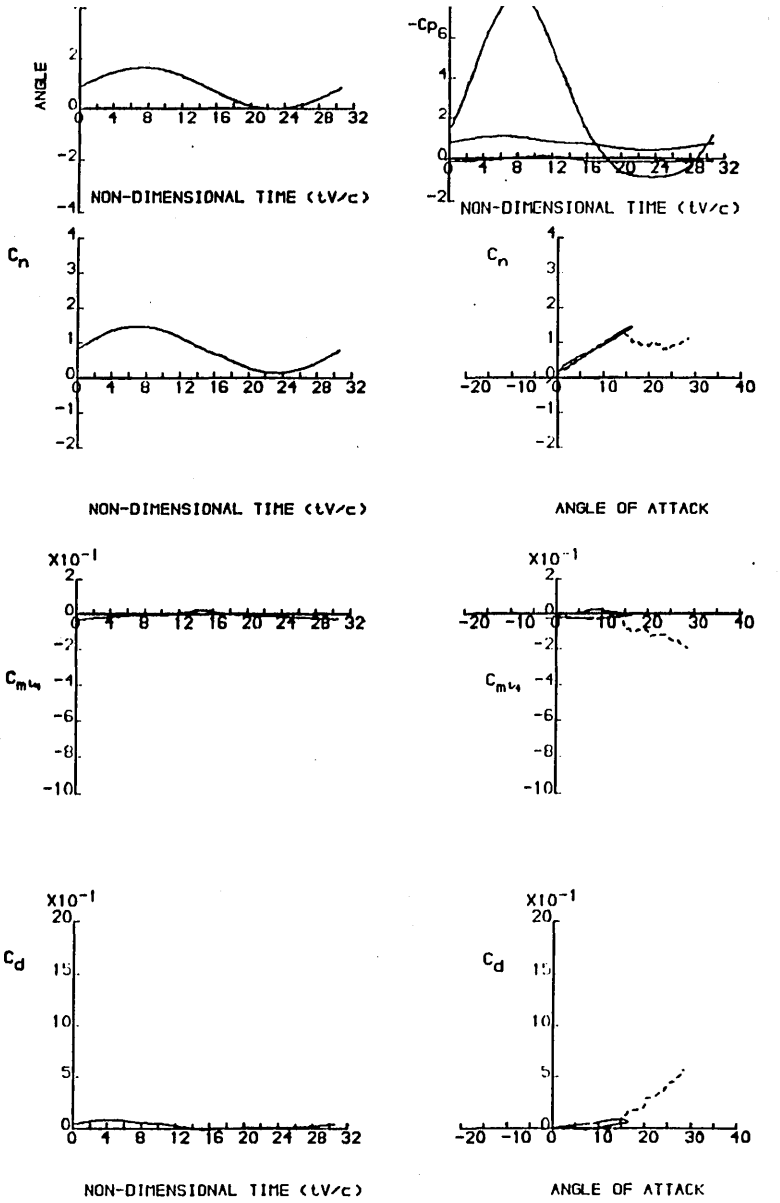

Figure 4.46 : Unsteady characteristics for the NACA 23012 aerofoil at incidence of stall onset.

RUN REFERENCE NUMBER: 13641

REYNOLDS NUMBER = 1530193.

DYNAMIC PRESSURE = 1020.01 Nm^{-2}

NUMBER OF CYCLES = 10

MOTION TYPE: SINUSOIDAL

MEAN ANGLE = 10.09°

OSCILLATION FREQUENCY = 2.330 Hz.

AVERAGED DATA OF 10 CYCLES

DATE OF TEST: 16/6/83

MACH NUMBER = 0.113

AIR TEMPERATURE = 31.0°C

SAMPLING FREQUENCY = 298.24 Hz.

REDUCED FREQUENCY = 0.101

AMPLITUDE = 8.37°

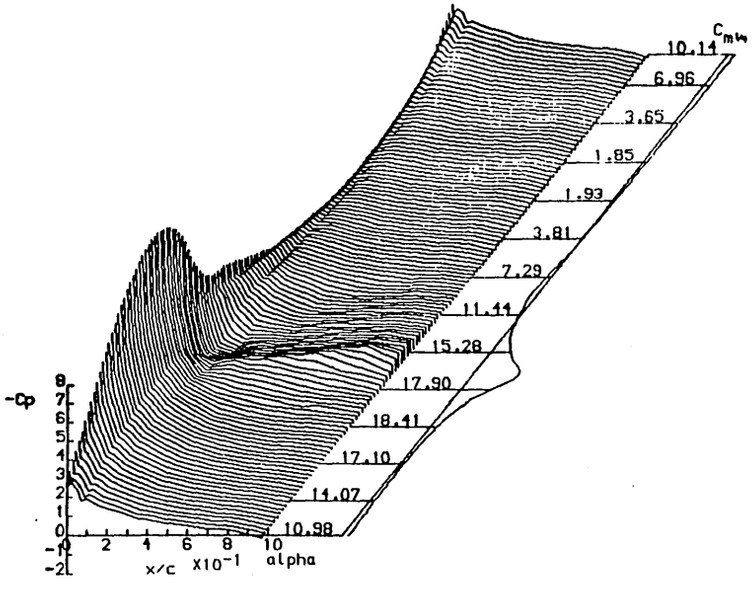

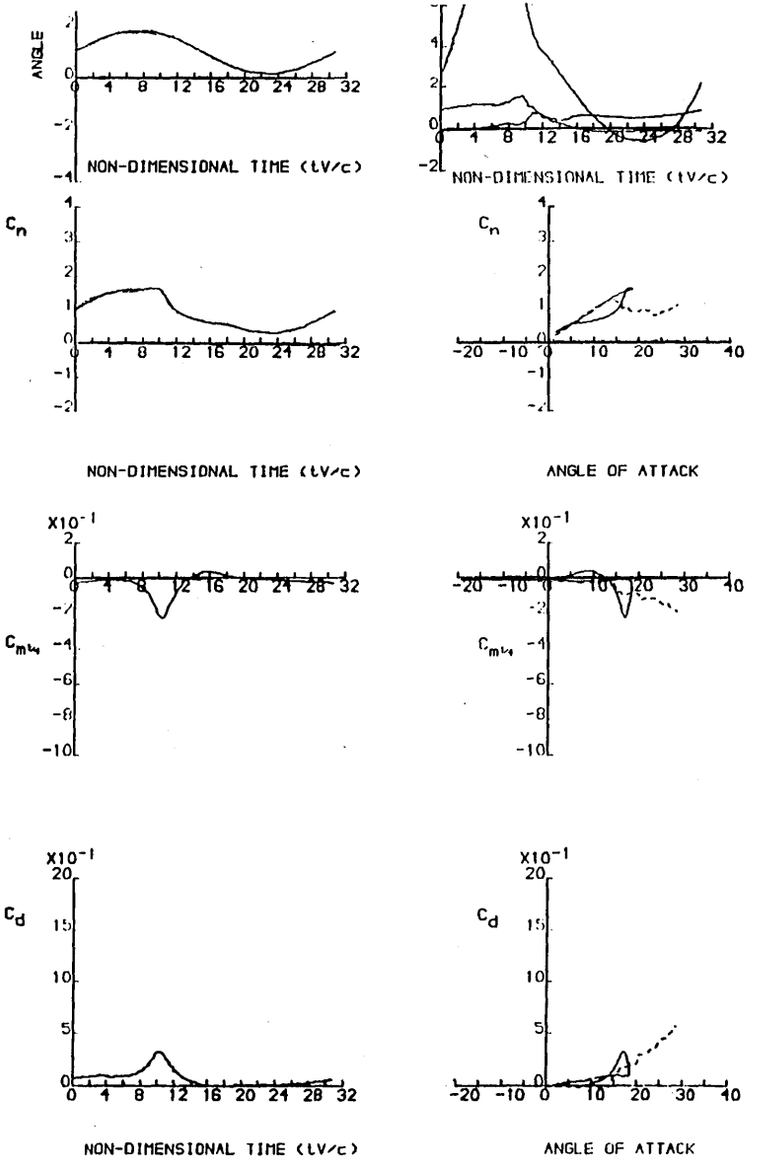

Figure 4.47 : Unsteady characteristics for the NACA 23012 aerofoil in the regime of light dynamic stall.

DYNAMIC CHARACTERISTICS FOR THE NACA 23012 MODEL01

RUN REFERENCE NUMBER: 13891
REYNOLDS NUMBER = 1520761.
DYNAMIC PRESSURE = 1000.76 Nm^{-2}
NUMBER OF CYCLES = 10
MOTION TYPE: SINUSOIDAL
MEAN ANGLE = 16.40°
OSCILLATION FREQUENCY = 2.330 Hz.
AVERAGED DATA OF 10 CYCLES

DATE OF TEST: 17/6/83
MACH NUMBER = 0.112
AIR TEMPERATURE = 33.0°C
SAMPLING FREQUENCY = 298.24 Hz.
REDUCED FREQUENCY = 0.103
AMPLITUDE = 8.53°

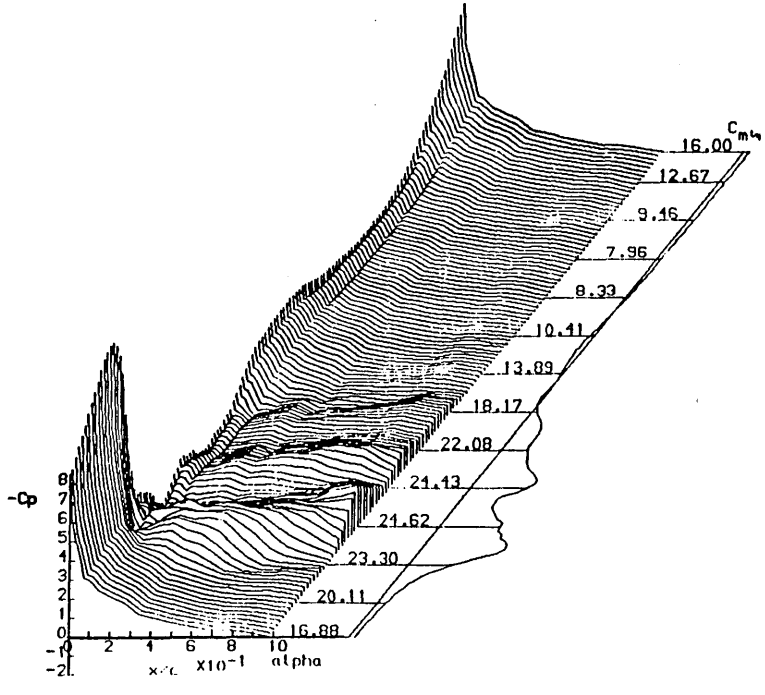

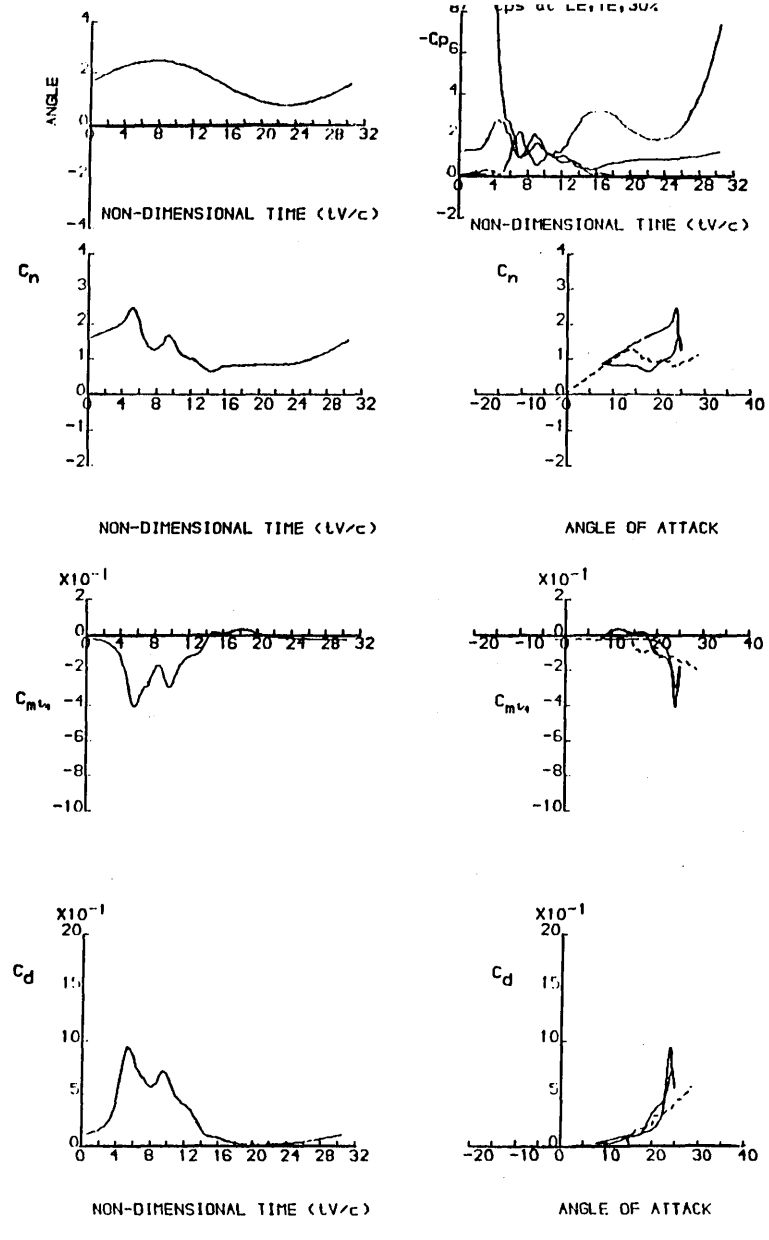

Figure 4.48 : Unsteady characteristics for the NACA 23012 aerofoil in the regime of deep dynamic stall.

DYNAMIC CHARACTERISTICS FOR THE NACA23012A MODEL02

RUN REFERENCE NUMBER: 10881
REYNOLDS NUMBER = 1507681.
DYNAMIC PRESSURE = 961.35 Nm^{-2}
NUMBER OF CYCLES = 10
MOTION TYPE: SINUSOIDAL
MEAN ANGLE = 4.07°
OSCILLATION FREQUENCY = 2.330 Hz.
AVERAGED DATA OF 10 CYCLES

DATE OF TEST: 24/7/85
MACH NUMBER = 0.112
AIR TEMPERATURE = 26.0°C
SAMPLING FREQUENCY = 298.24 Hz.
REDUCED FREQUENCY = 0.104
AMPLITUDE = 7.90°

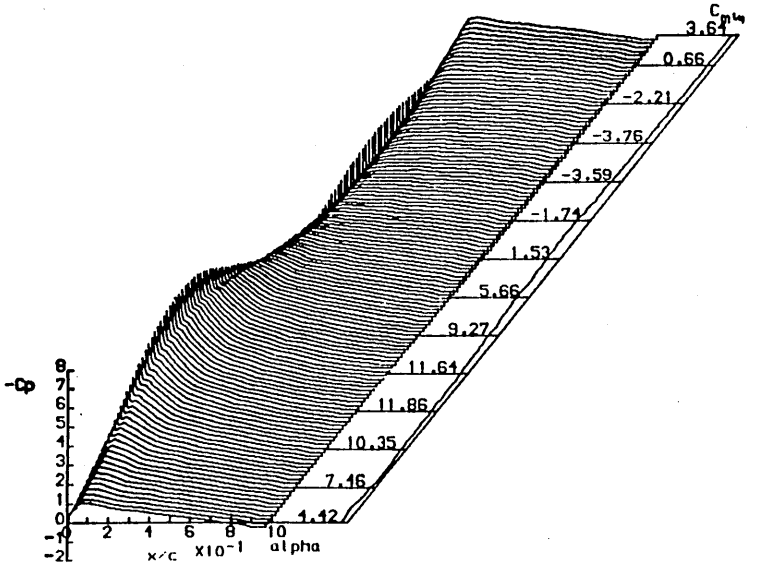

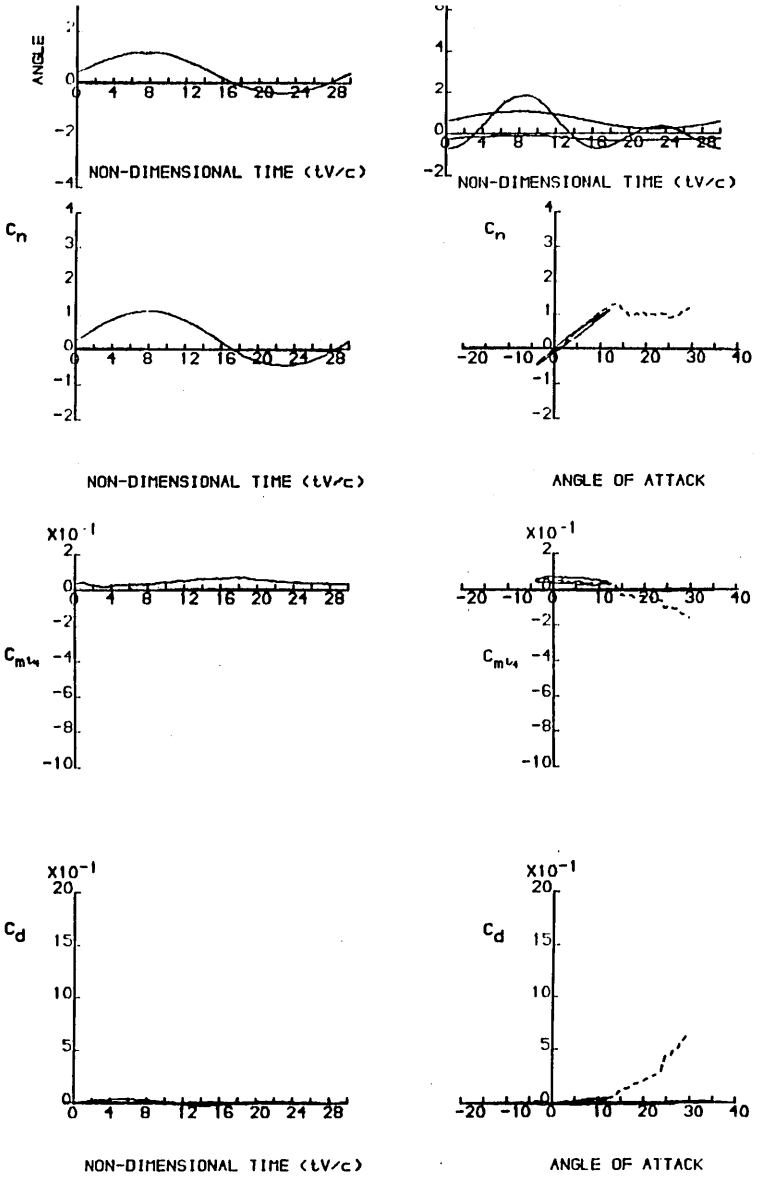

Figure 4.49 : Unsteady characteristics for the NACA 23012A aerofoil in the regime of no stall.

RUN REFERENCE NUMBER: 10891

REYNOLDS NUMBER = 1499009.

DYNAMIC PRESSURE = 950.32 Nm^{-2}

NUMBER OF CYCLES = 10

MOTION TYPE: SINUSOIDAL

MEAN ANGLE = 6.01°

OSCILLATION FREQUENCY = 2.330 Hz.

AVERAGED DATA OF 10 CYCLES

DATE OF TEST: 24/7/85

MACH NUMBER = 0.111

AIR TEMPERATURE = 26.0°C

SAMPLING FREQUENCY = 298.24 Hz.

REDUCED FREQUENCY = 0.105

AMPLITUDE = 8.11°

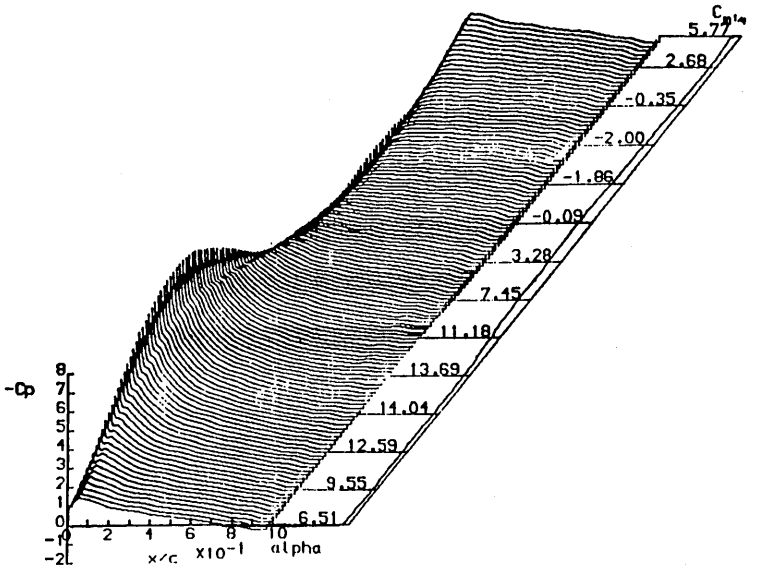

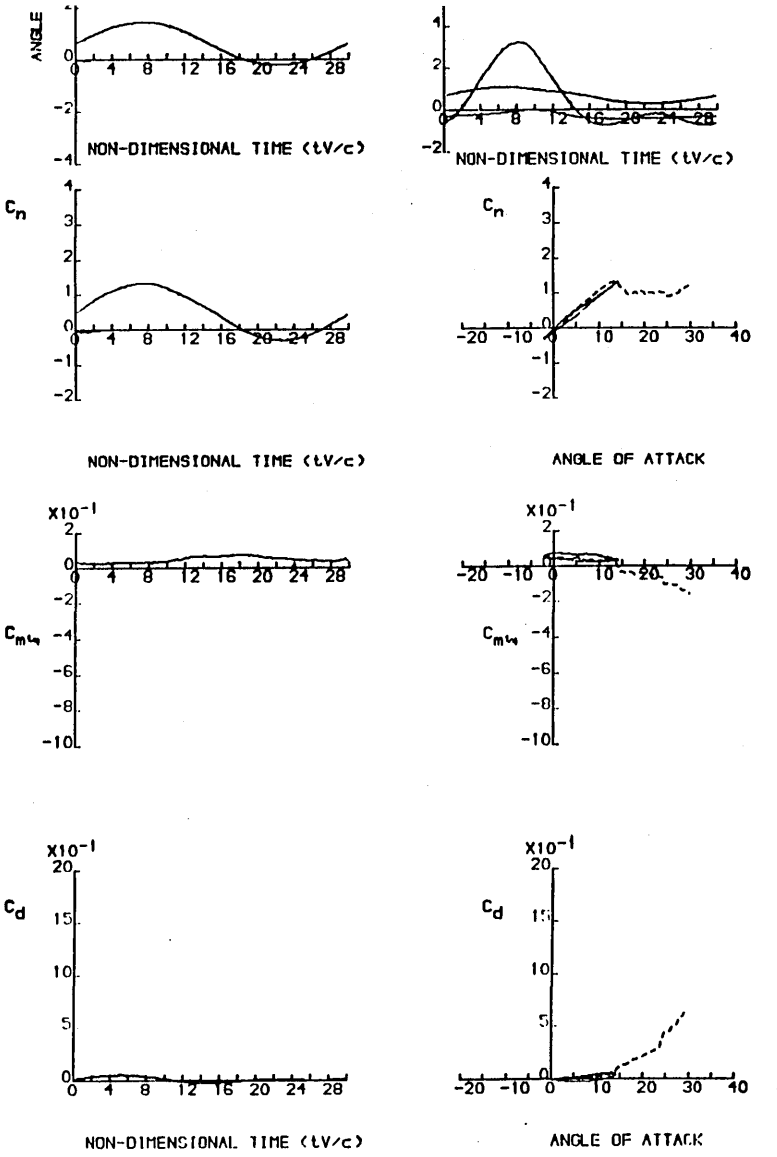

Figure 4.50 : Unsteady characteristics for the NACA 23012A aerofoil at incidence of stall onset.

DYNAMIC CHARACTERISTICS FOR THE NACA23012A MODEL02

RUN REFERENCE NUMBER: 10911
REYNOLDS NUMBER = 1542815.
DYNAMIC PRESSURE = 1006.67 Nm^{-2}
NUMBER OF CYCLES = 10
MOTION TYPE: SINUSOIDAL
MEAN ANGLE = 9.90°
OSCILLATION FREQUENCY = 2.330 Hz.
AVERAGED DATA OF 10 CYCLES

DATE OF TEST: 24/7/85
MACH NUMBER = 0.114
AIR TEMPERATURE = 26.0°C
SAMPLING FREQUENCY = 298.24 Hz.
REDUCED FREQUENCY = 0.102
AMPLITUDE = 8.39°

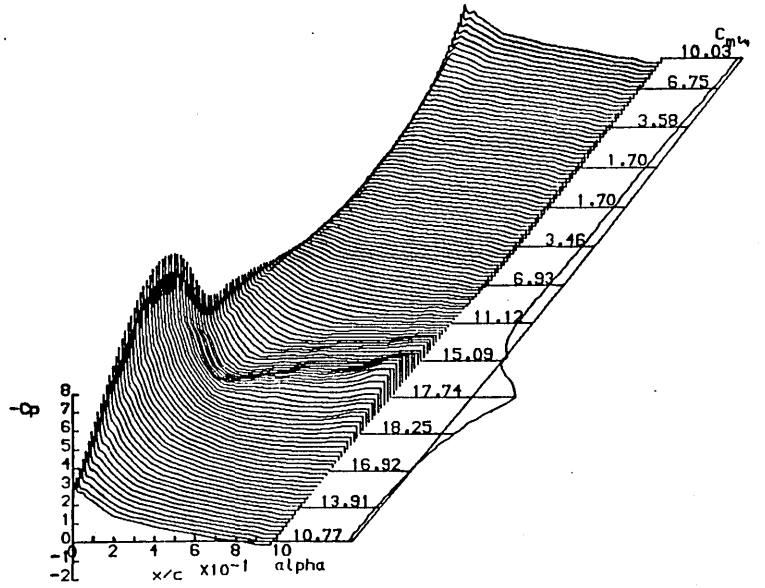

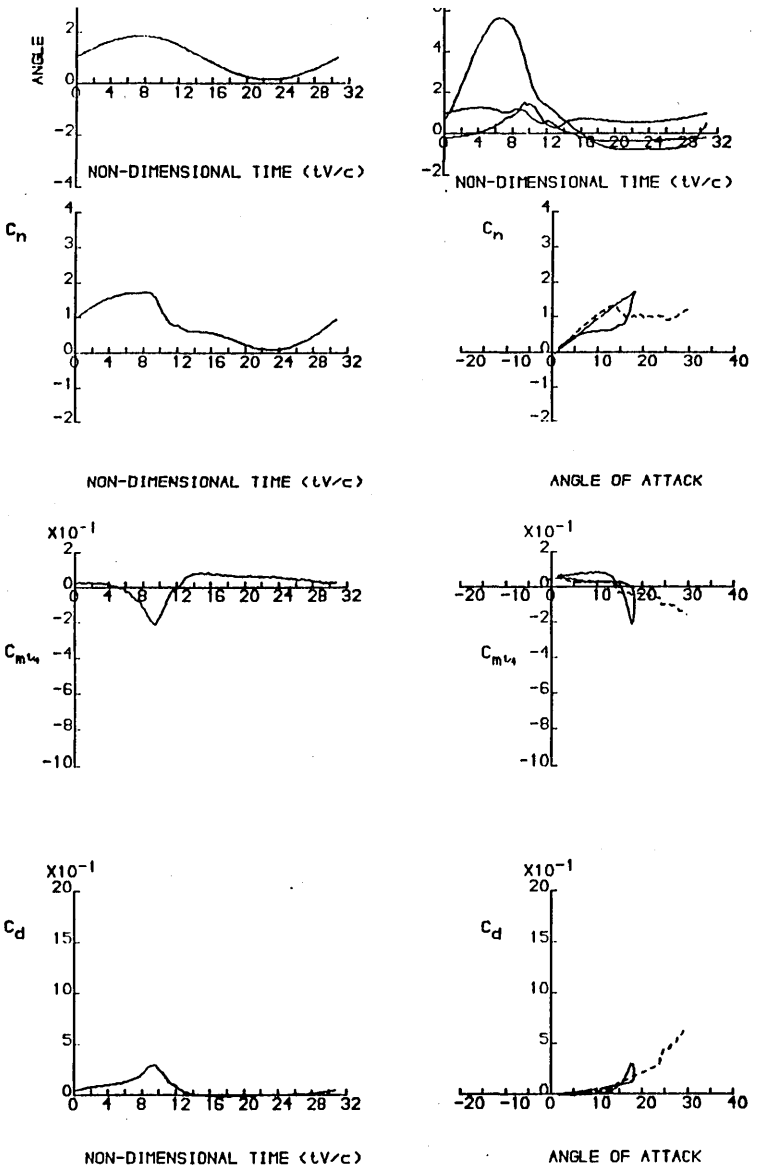

Figure 4.51 : Unsteady characteristics for the NACA 23012A aerofoil in the regime of light dynamic stall.

DYNAMIC CHARACTERISTICS FOR THE NACA23012A MODEL02

RUN REFERENCE NUMBER: 10931
REYNOLDS NUMBER = 1526851.
DYNAMIC PRESSURE = 985.95 Nm^{-2}
NUMBER OF CYCLES = 10
MOTION TYPE: SINUSOIDAL
MEAN ANGLE = 17.93°
OSCILLATION FREQUENCY = 2.330 Hz.
AVERAGED DATA OF 10 CYCLES

DATE OF TEST: 24/7/85
MACH NUMBER = 0.113
AIR TEMPERATURE = 26.0°C
SAMPLING FREQUENCY = 298.24 Hz.
REDUCED FREQUENCY = 0.103
AMPLITUDE = 7.66°

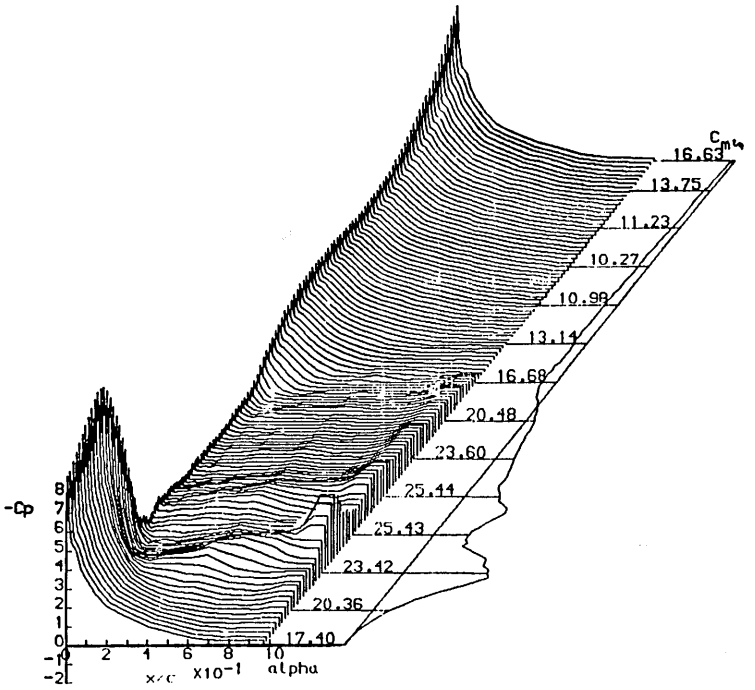

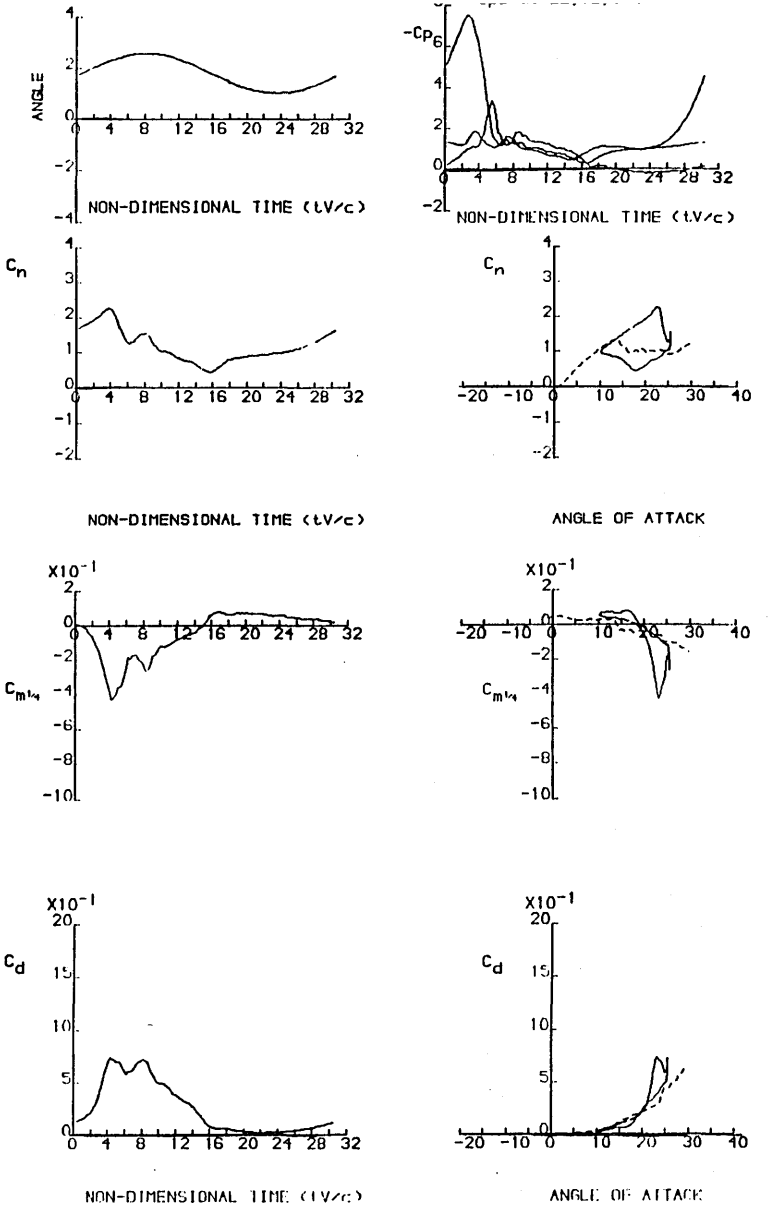

Figure 4.52 : Unsteady characteristics for the NACA 23012A aerofoil in the regime of deep dynamic stall.

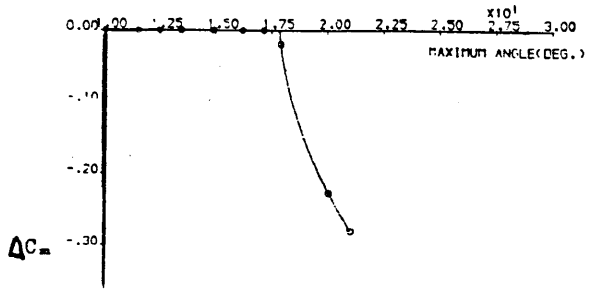

Figure 4.53 : Determination of critical angle of attack.

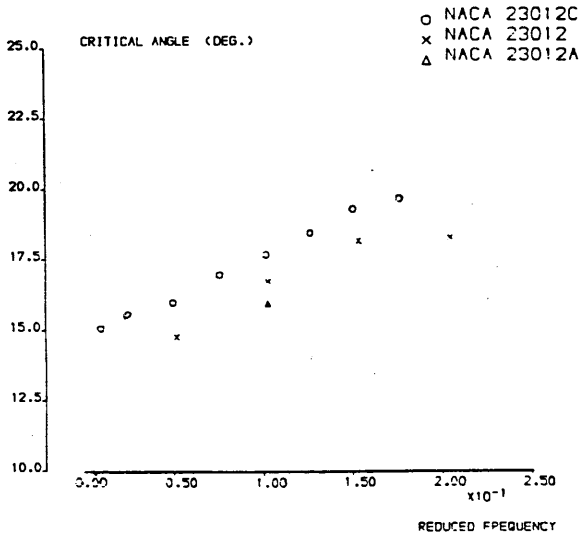

Figure 4.54 : Variation of critical angle of attack with reduced frequency for three aerofoils at a Reynolds number of approximately 1.5×10^6.

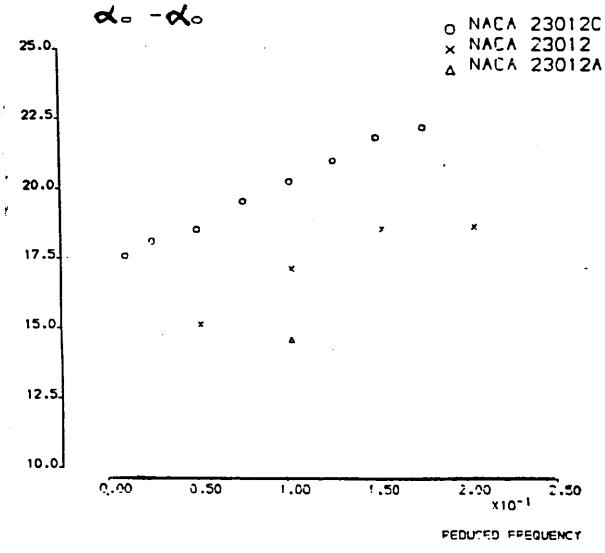

Figure 4.55 : Variation of difference between critical angle of attack and zero-lift incidence with reduced frequency for three aerofoils at a Reynolds number of approximately 1.5×10^6.

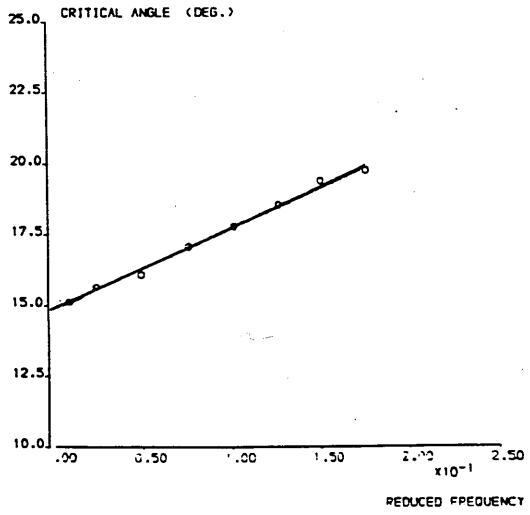

Figure 4.56 : Variation of critical angle of attack with reduced frequency for the NACA 23012C aerofoil at a Reynolds number of approximately 1.5×10^6.

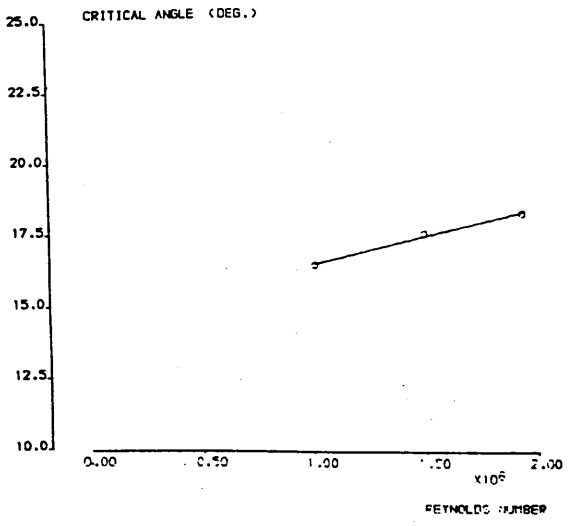

Figure 4.57 : Variation of critical angle of attack with Reynolds number for the NACA 23012C aerofoil at a reduced frequency of 0.10.

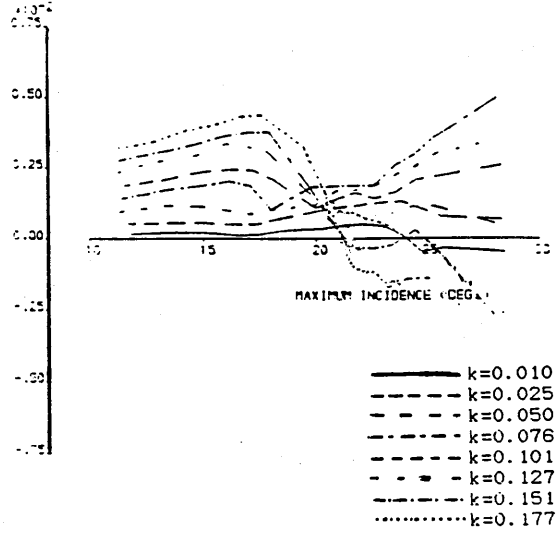

Figure 4.58 : Variation of pitch-damping parameter with maximum incidence for the NACA 23012C aerofoil at a Reynolds number of approximately 1.5×10^6 and over a range of reduced frequencies.

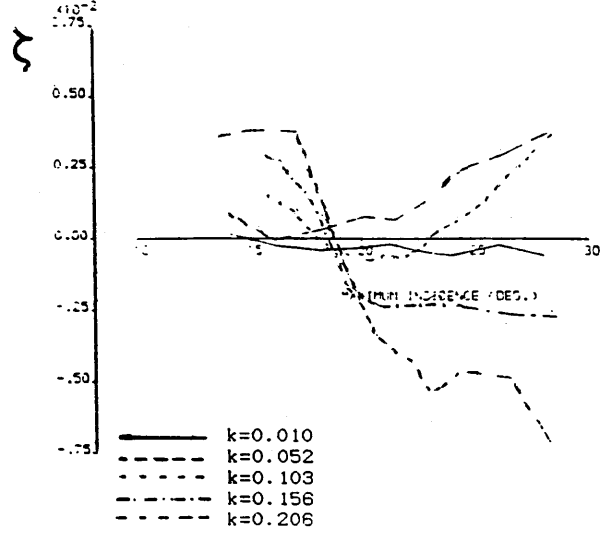

Figure 4.59 : Variation of pitch-damping parameter with maximum incidence for the NACA 23012 aerofoil at a Reynolds number of approximately 1.5×10^6 and over a range of reduced frequencies.

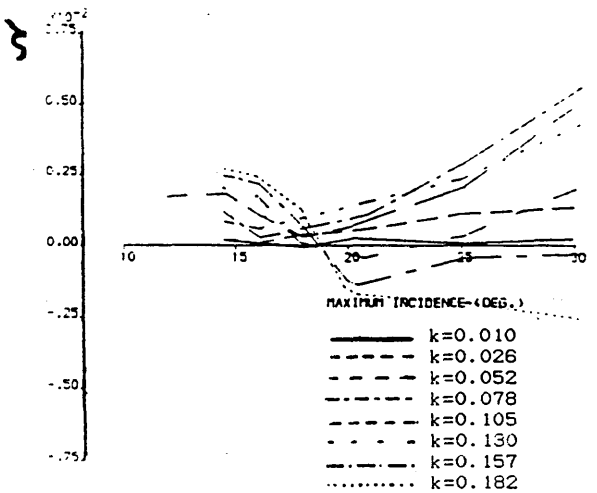

Figure 4.60 : Variation of pitch-damping parameter with maximum incidence for the NACA 23012A aerofoil at a Reynolds number of approximately 1.5×10^6 and over a range of reduced frequencies.

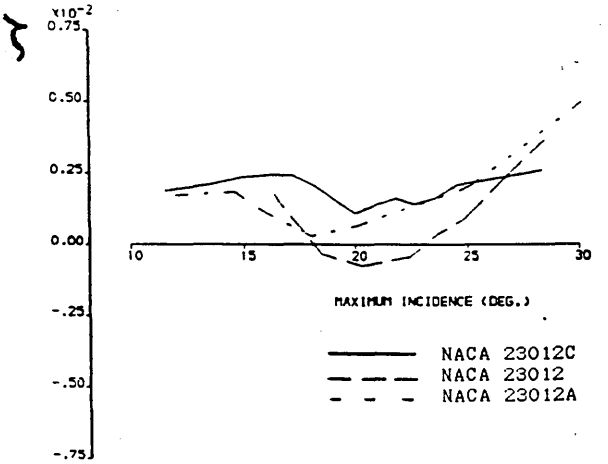

Figure 4.61 : Variation of pitch-damping parameter with maximum incidence for three aerofoils at a reduced frequency of 0.10 and a Reynolds number of approximately 1.5×10^6.

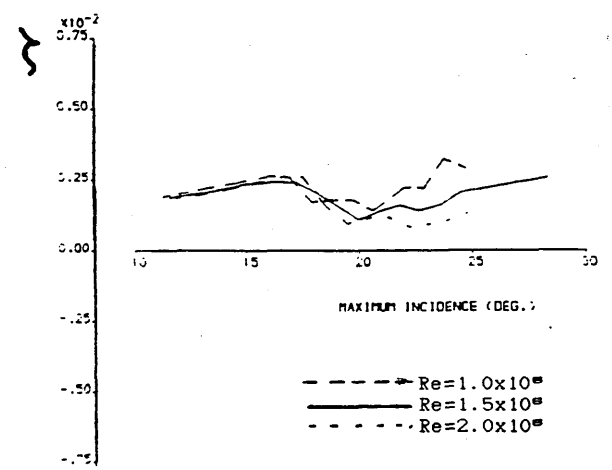

Figure 4.62 : Variation of pitch-damping parameter with maximum incidence for the NACA 23012C aerofoil over a range of Reynolds numbers at a reduced frequency of 0.10.

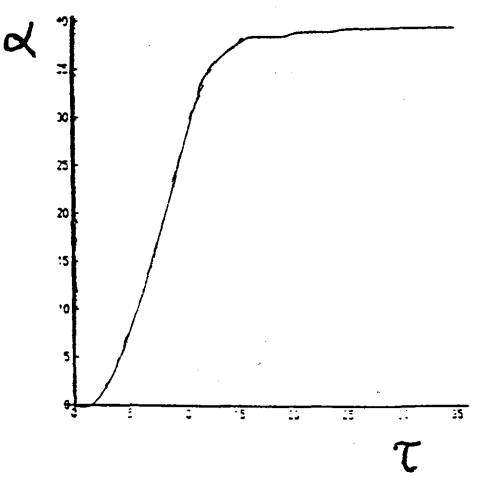

Figure 4.63 : Variation of incidence with non-dimensional time for a ramp at a nominal pitch-rate of approximately $290°s^{-1}$.

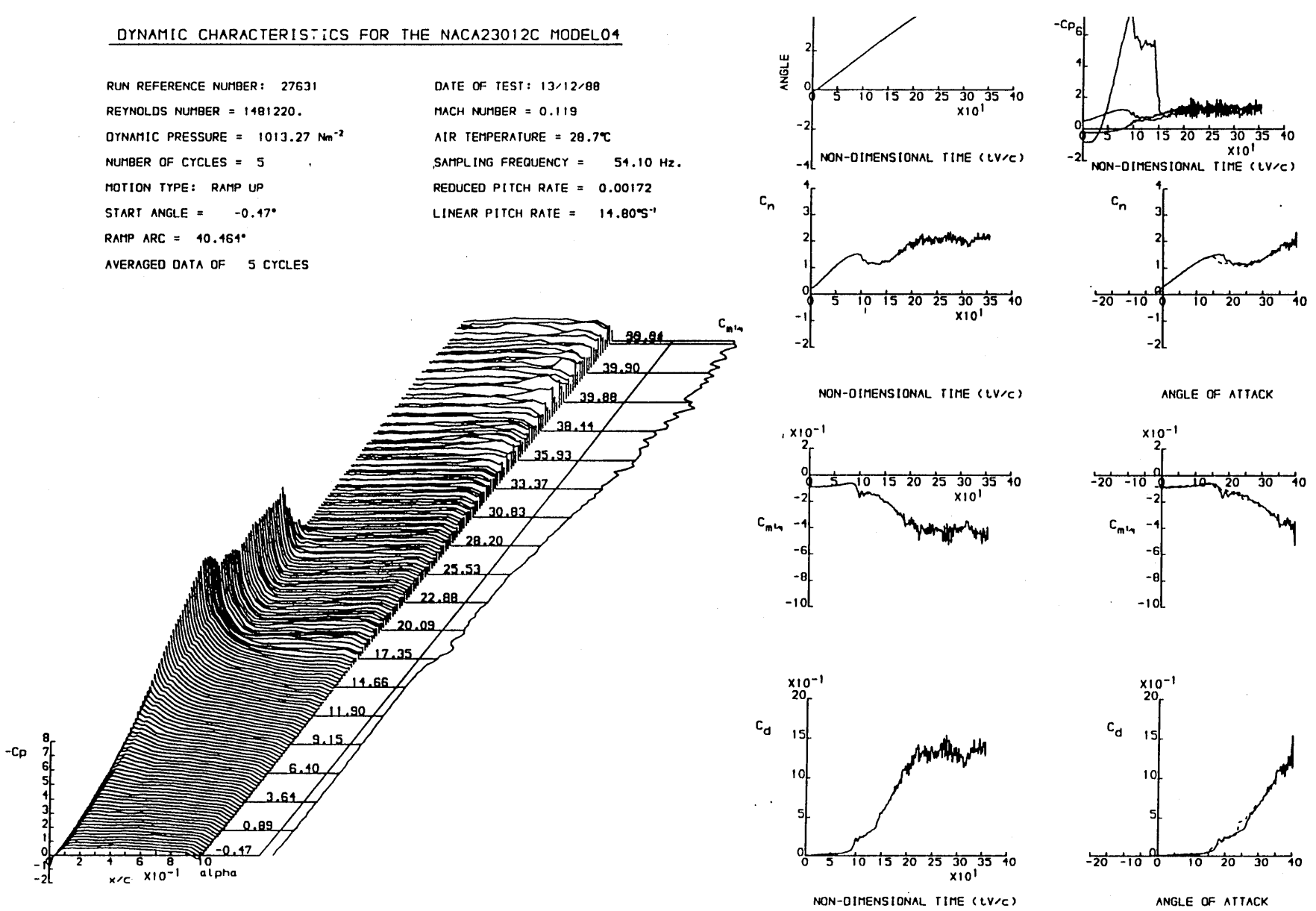

Figure 4.64 : Unsteady characteristics for the NACA 23012C aerofoil at a Reynolds number of 1.46×10^6 and a reduced pitch-rate of 0.002.

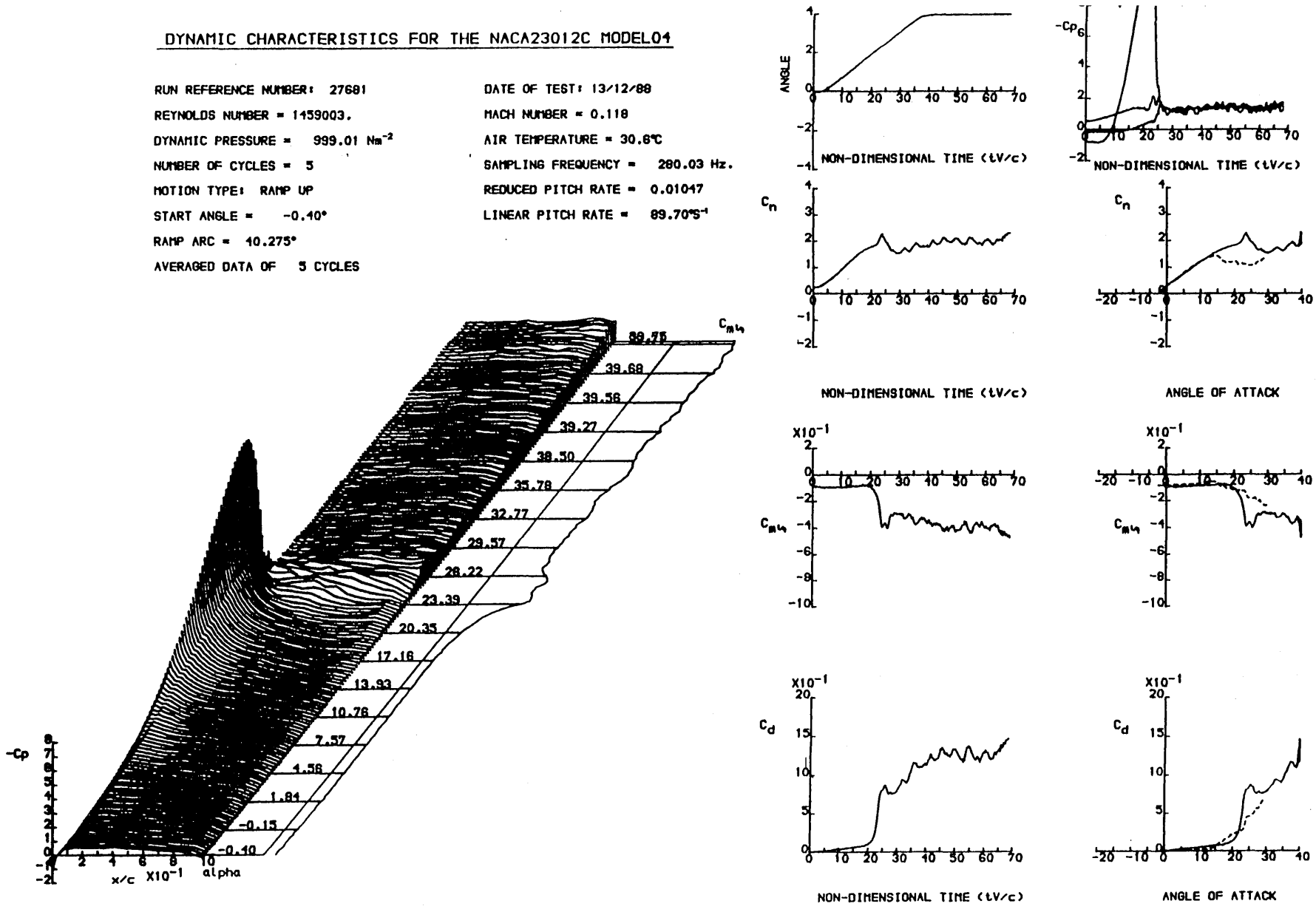

Figure 4.65 : Unsteady characteristics for the NACA 23012C aerofoil at a Reynolds number of 1.46×10^6 and a reduced pitch-rate of 0.010.

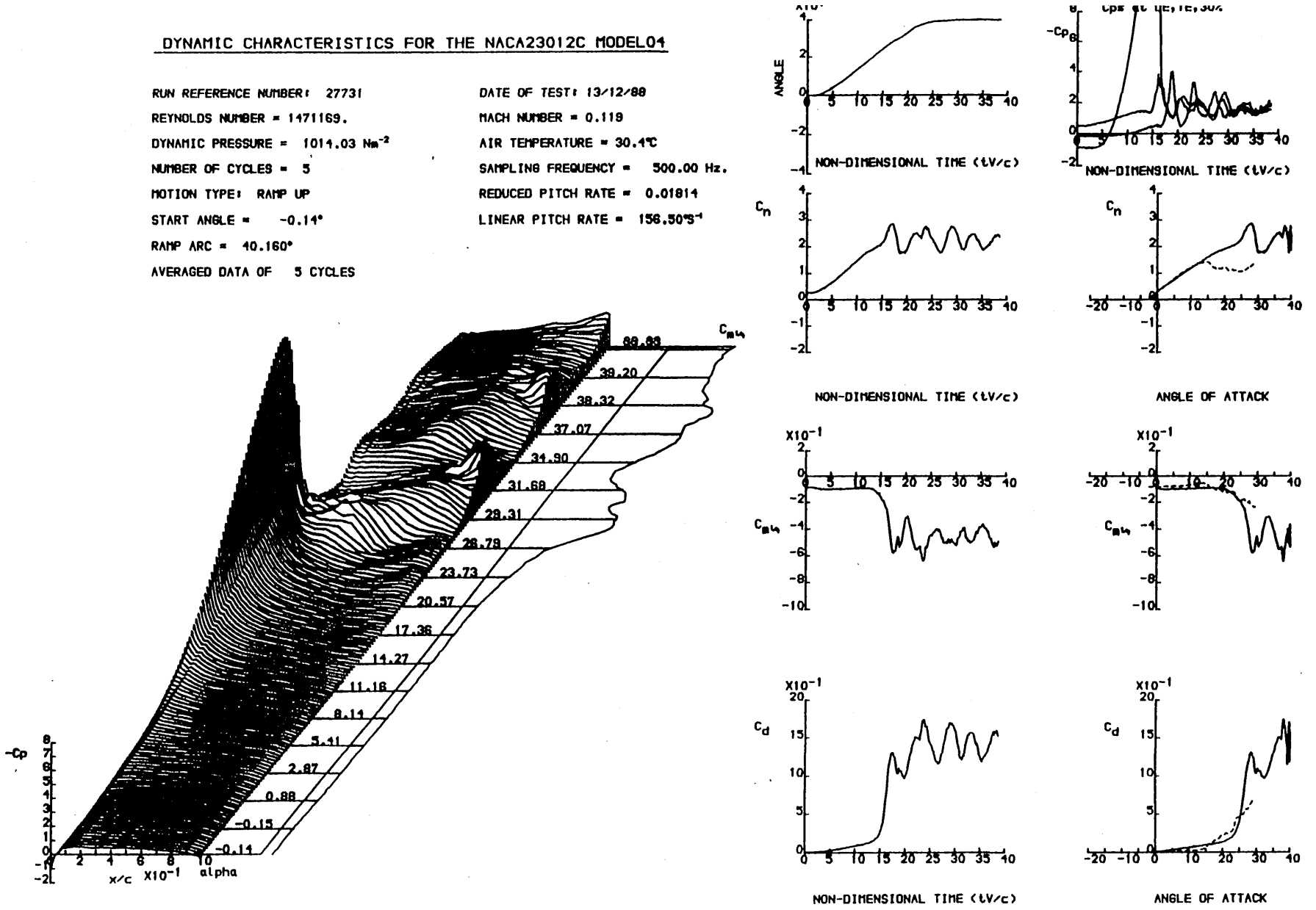

Figure 4.66 : Unsteady characteristics for the NACA 23012C aerofoil at a Reynolds number of 1.47×10^6 and a reduced pitch-rate of 0.018.

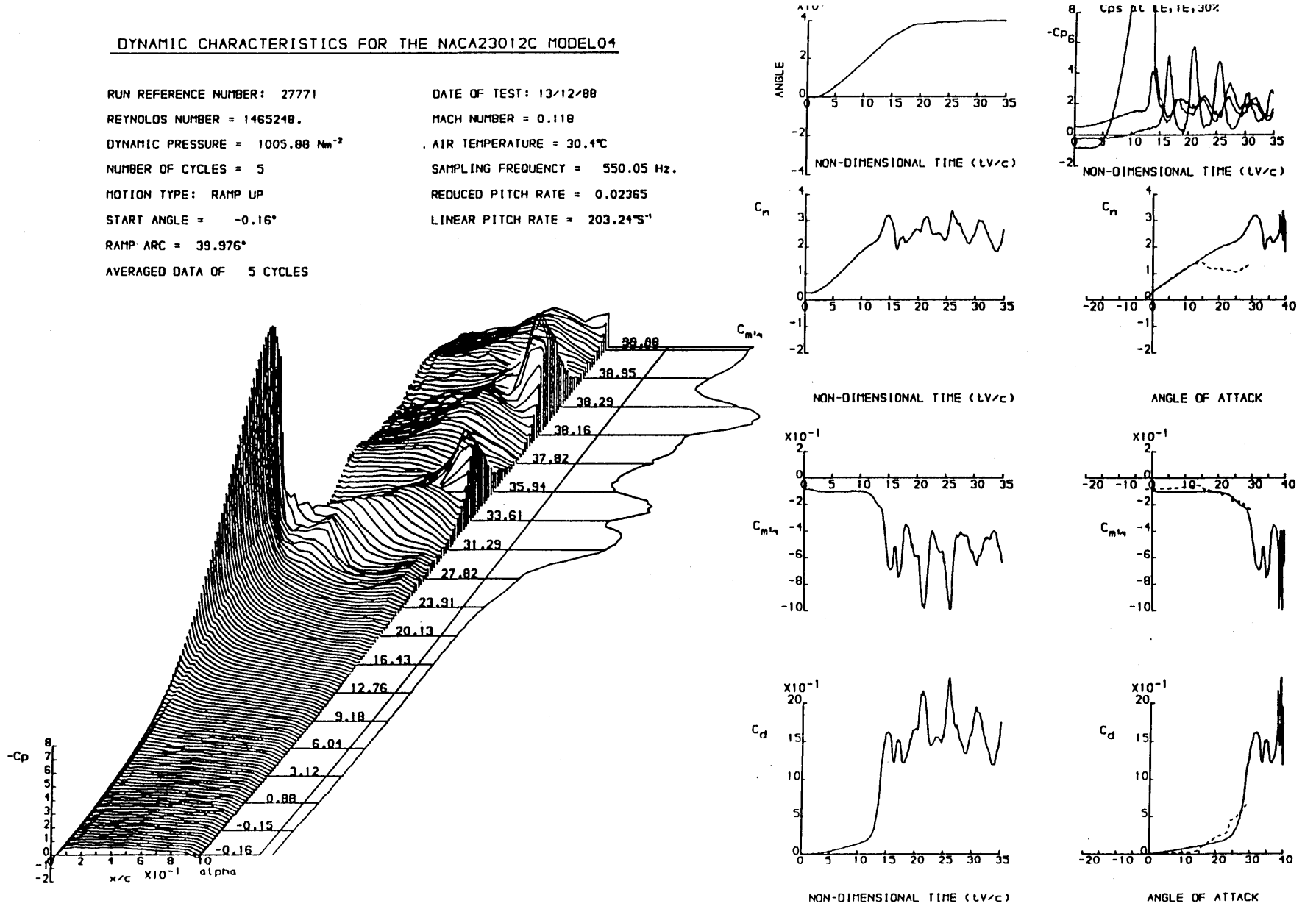

Figure 4.67 : Unsteady characteristics for the NACA 23012C aerofoil at a Reynolds number of 1.47×10^6 and a reduced pitch-rate of 0.024.

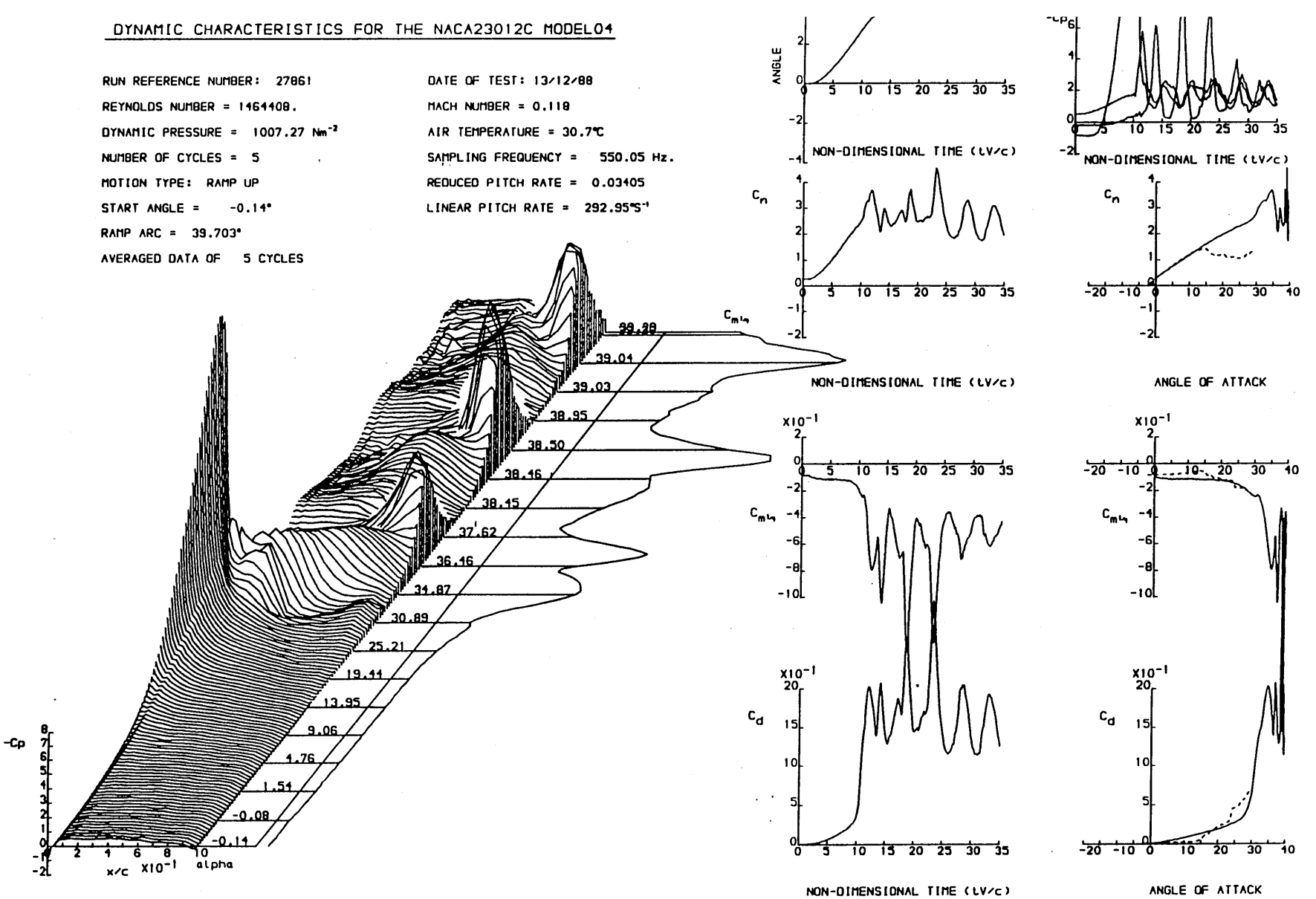

Figure 4.68 : Unsteady characteristics for the NACA 23012C aerofoil at a Reynolds number of 1.46×10^6 and a reduced pitch-rate of 0.034.

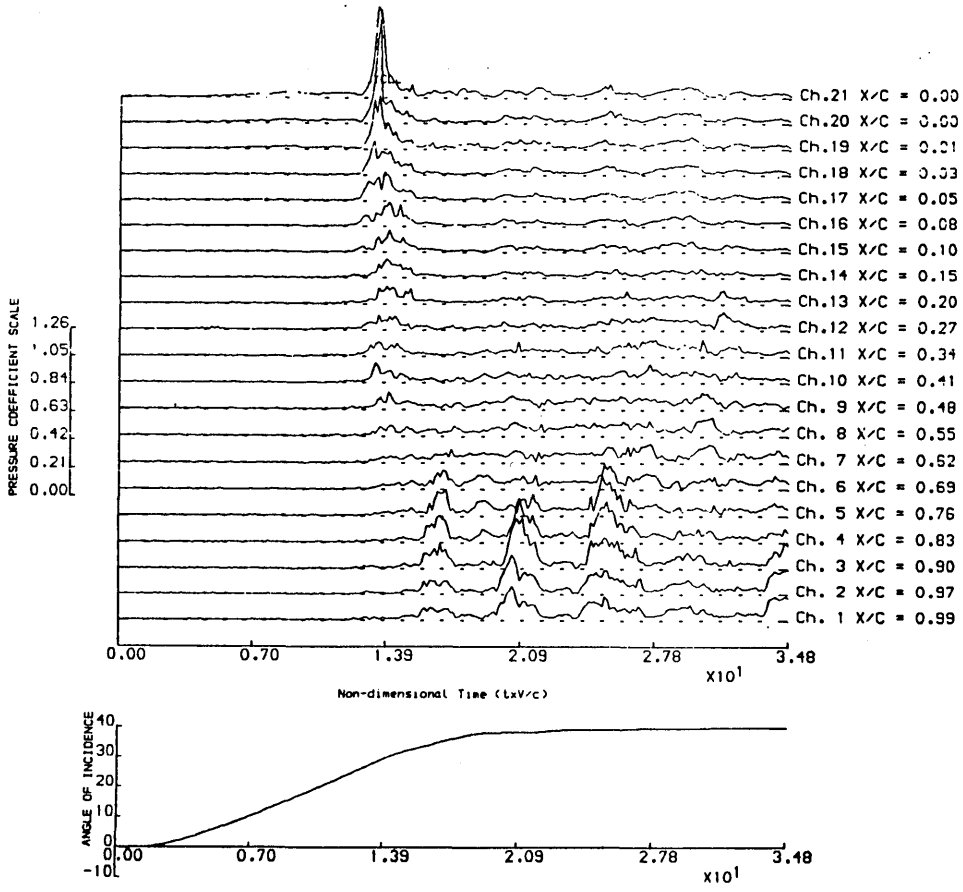

Figure 4.69 : Standard deviation in pressure traces for the NACA 23012C aerofoil at a Reynolds number of 1.47×10^6 and a reduced pitch-rate of 0.024.

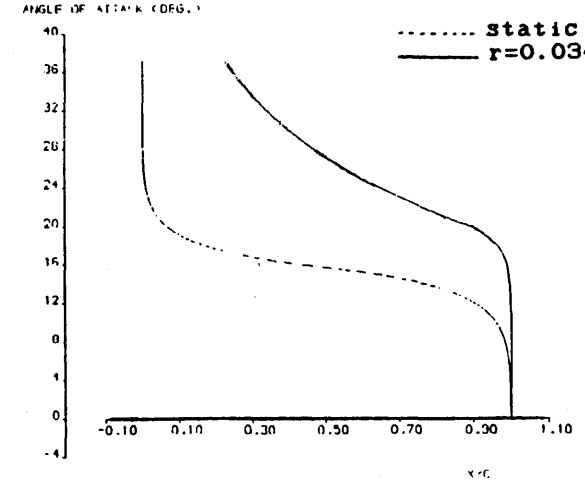

Figure 4.70 : Comparison of separation characteristics in steady conditions and at a reduced pitch-rate of 0.034 for the NACA 23012C aerofoil at a Reynolds number of approximately 1.5×10^6.

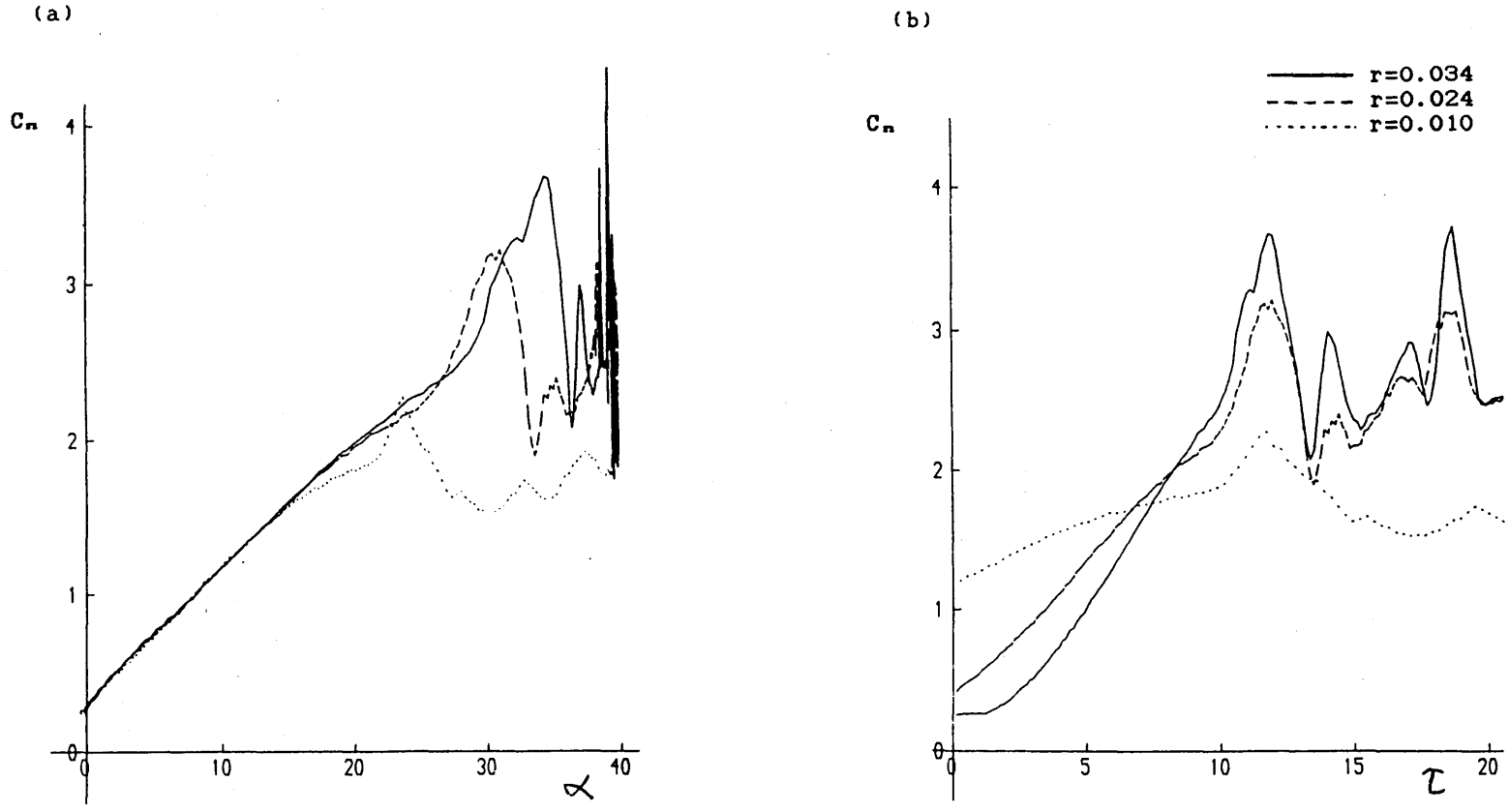

Figure 4.71 : Comparison of normal force characteristics for the NACA 23012C aerofoil at three reduced pitch-rates and a Reynolds number of approximately 1.5×10^6.

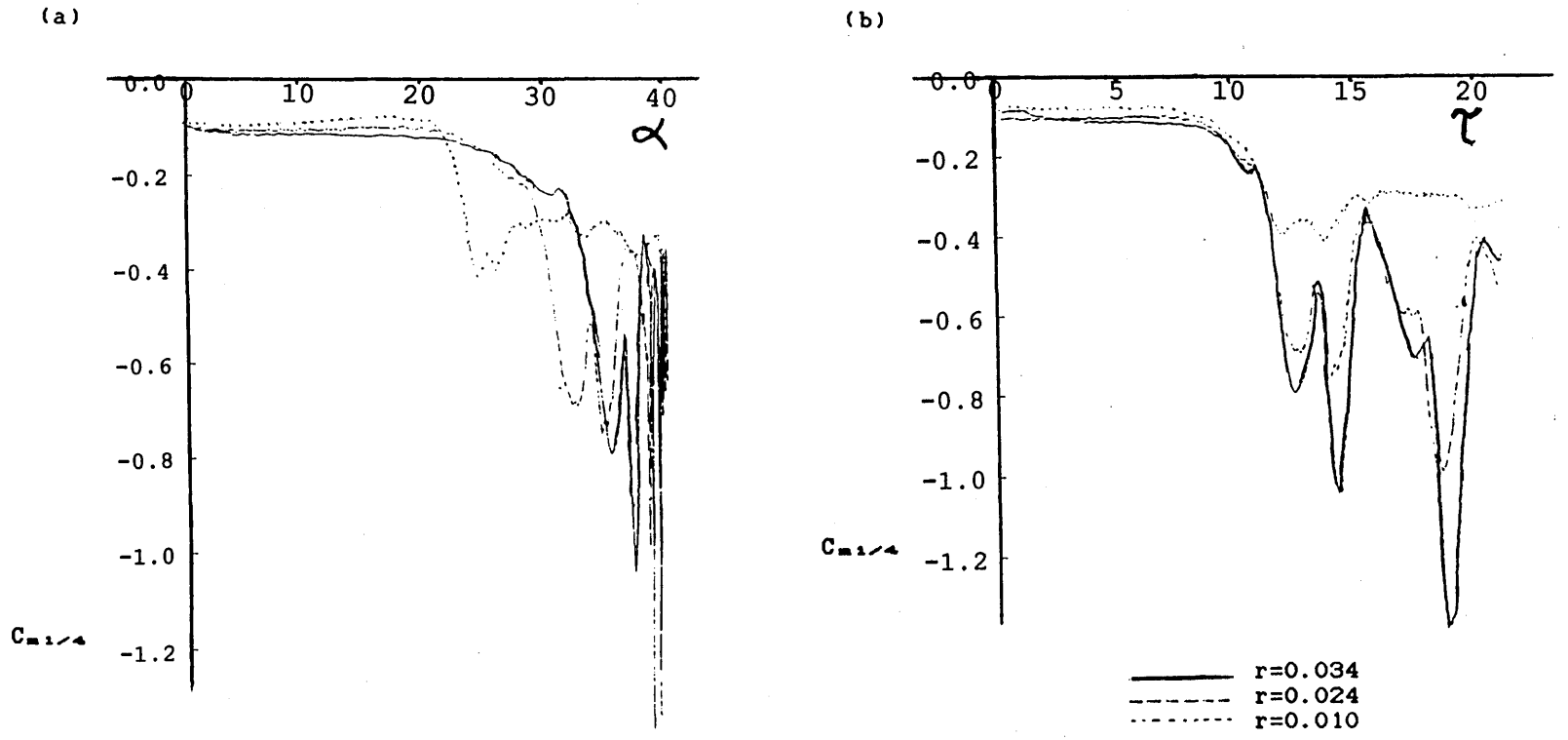

Figure 4.72 : Comparison of pitching-moment characteristics for the NACA 23012C aerofoil at three reduced pitch-rates and a Reynolds number of approximately 1.5×10^6.

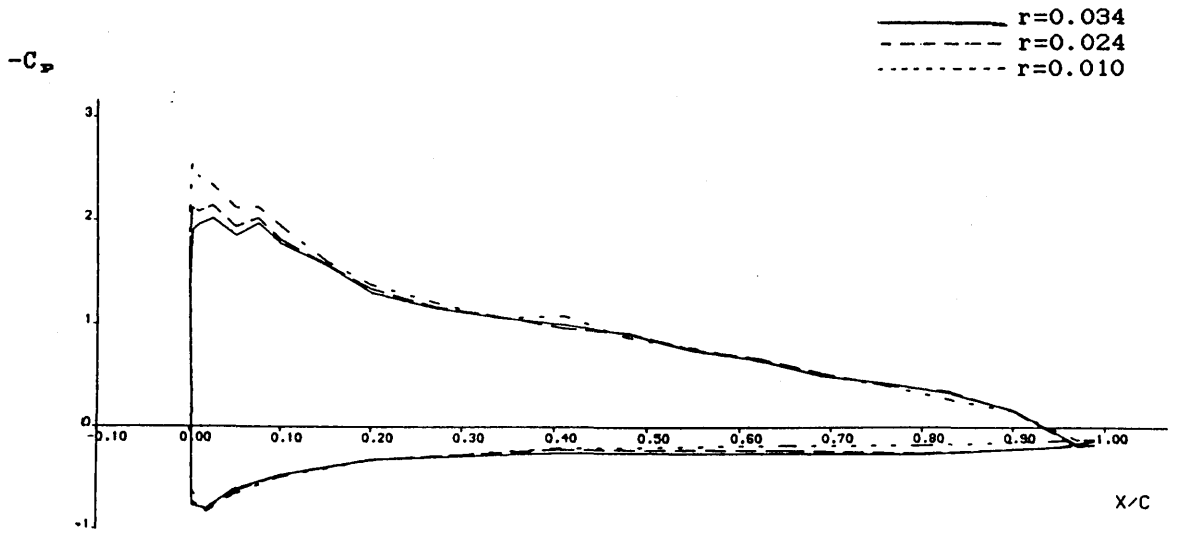

Figure 4.73 : Comparison of pressure distributions at an incidence of approximately 10° for the NACA 23012C aerofoil at three reduced pitch-rates and a Reynolds number of approximately 1.5×10^6.

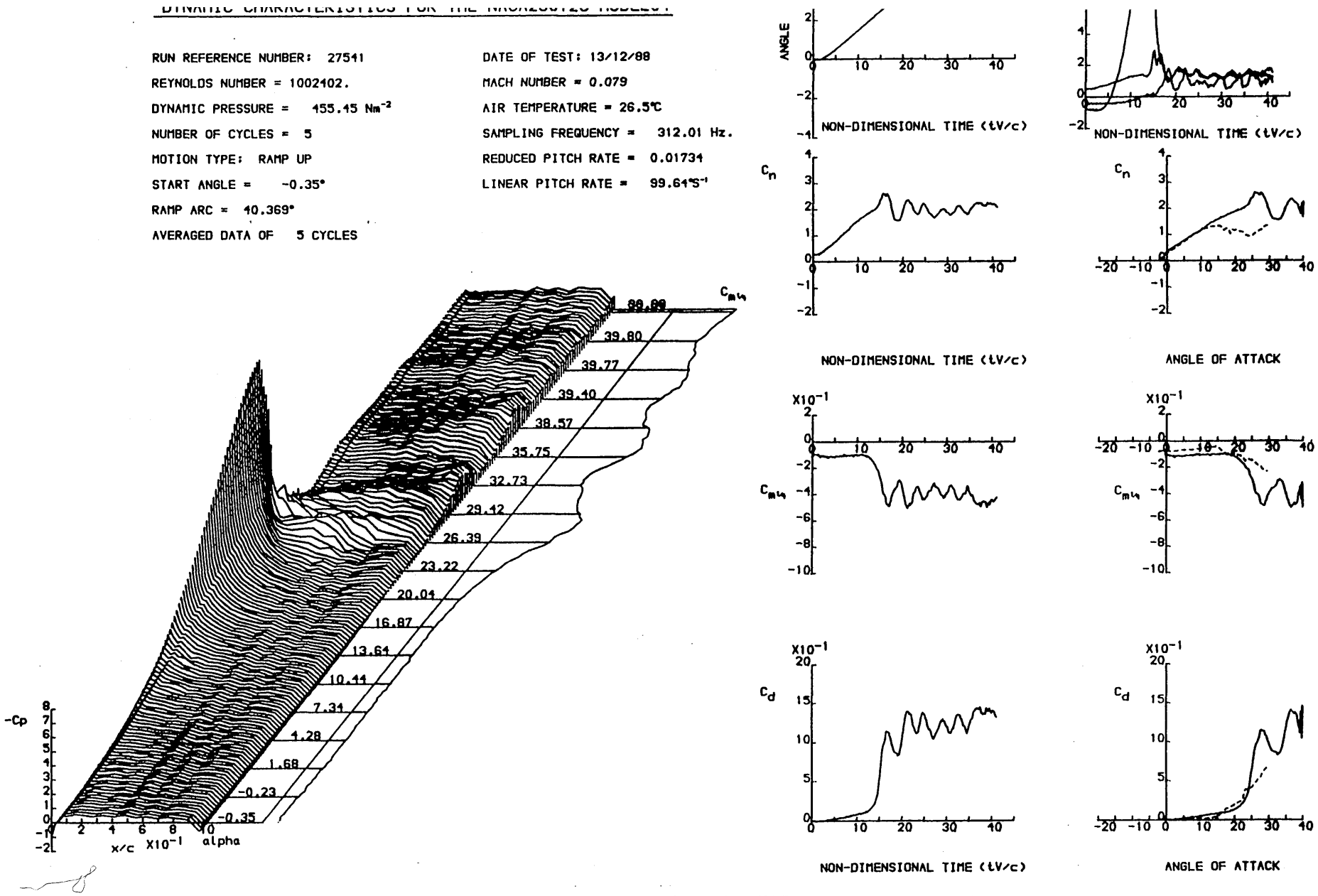

Figure 4.74 : Unsteady characteristics for the NACA 23012C aerofoil at a Reynolds number of 1.00×10^{6} and a reduced pitch-rate of 0.017.

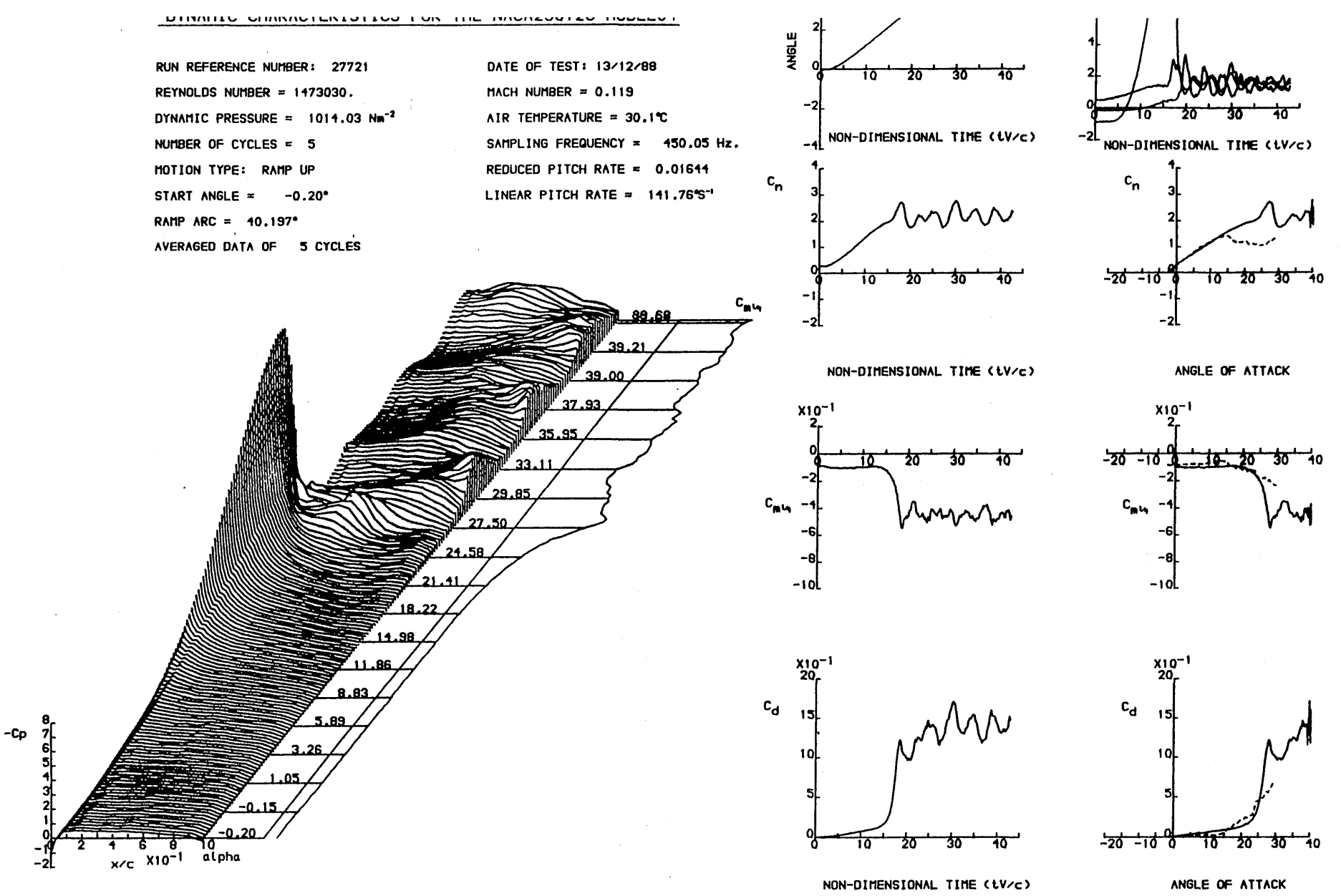

Figure 4.75 : Unsteady characteristics for the NACA 23012C aerofoil at a Reynolds number of 1.47×10^{6} and a reduced pitch-rate of 0.016.

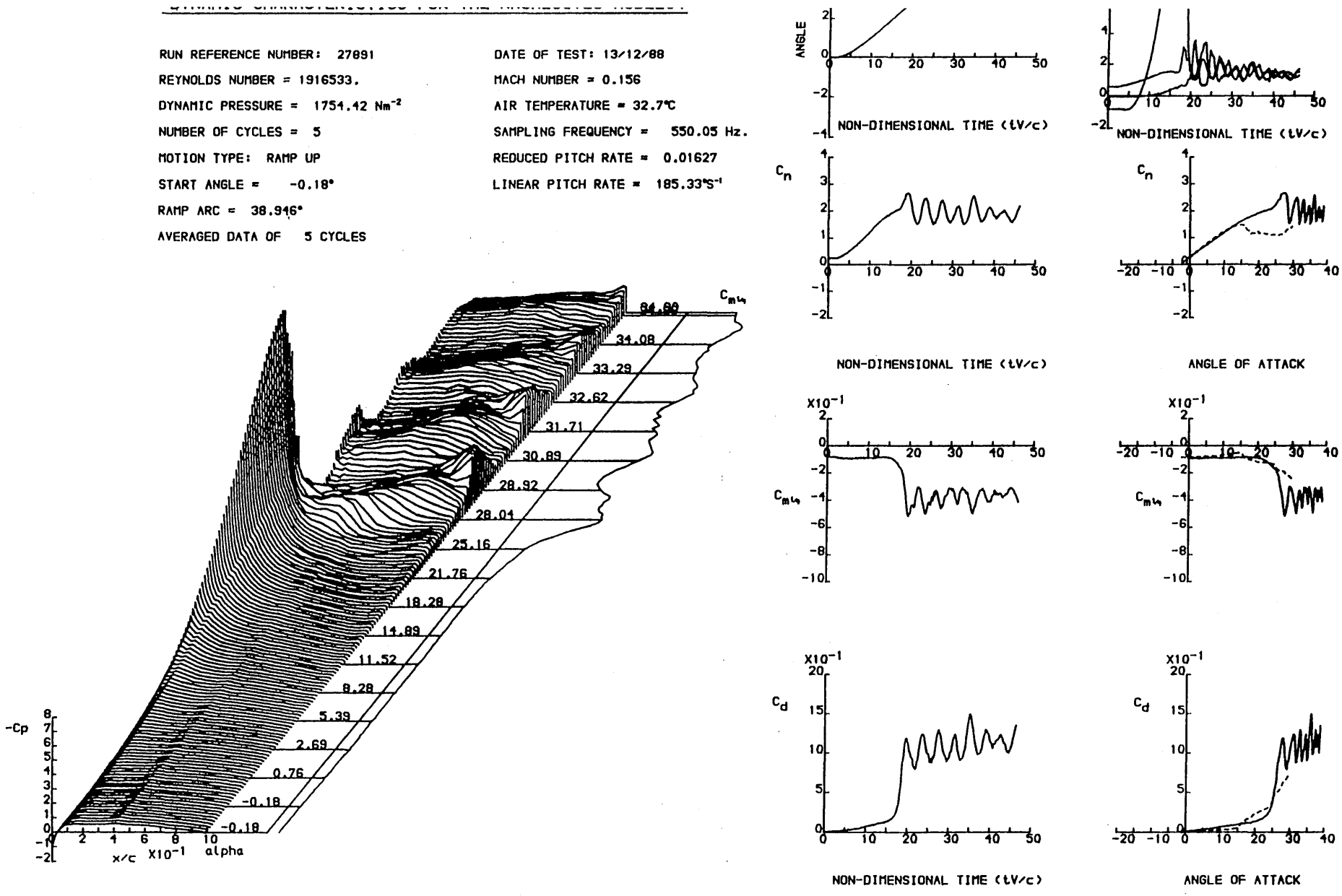

Figure 4.76 : Unsteady characteristics for the NACA 23012C aerofoil at a Reynolds number of 1.92×10^6 and a reduced pitch-rate of 0.016.

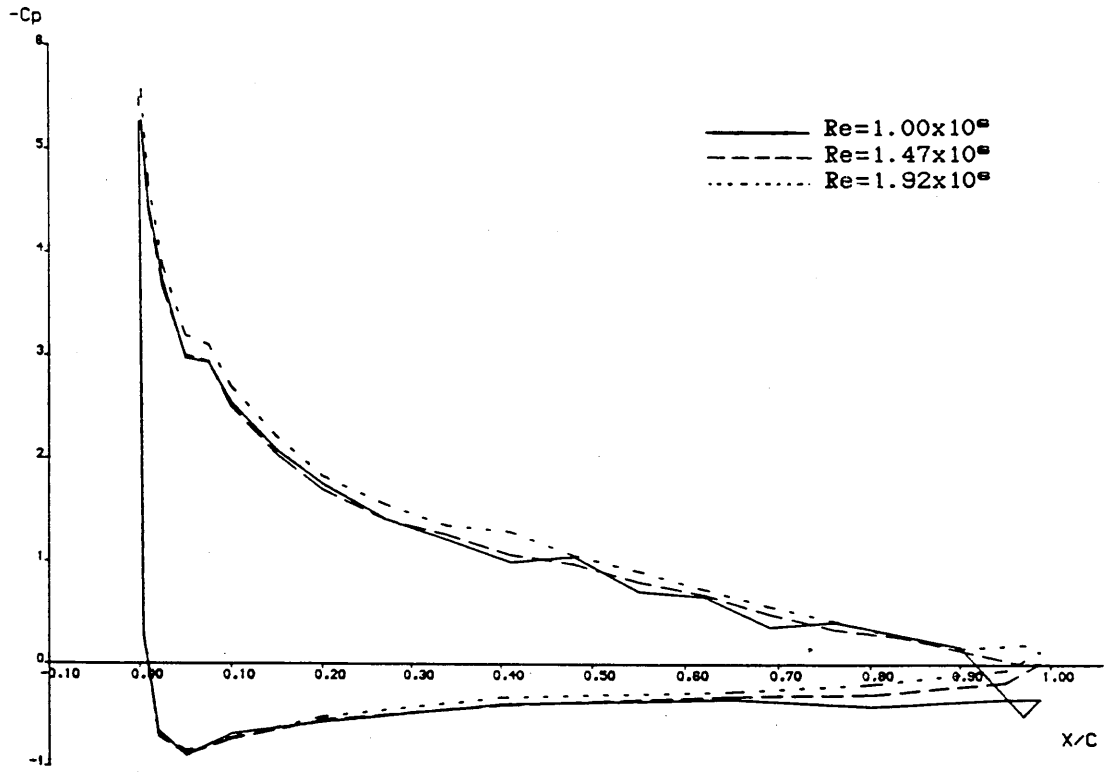

Figure 4.77 : Comparison of pressure distributions at an incidence of approximately 14° for the NACA 23012C aerofoil at three values of Reynolds number and a reduced pitch-rate of between 0.016 and 0.017.

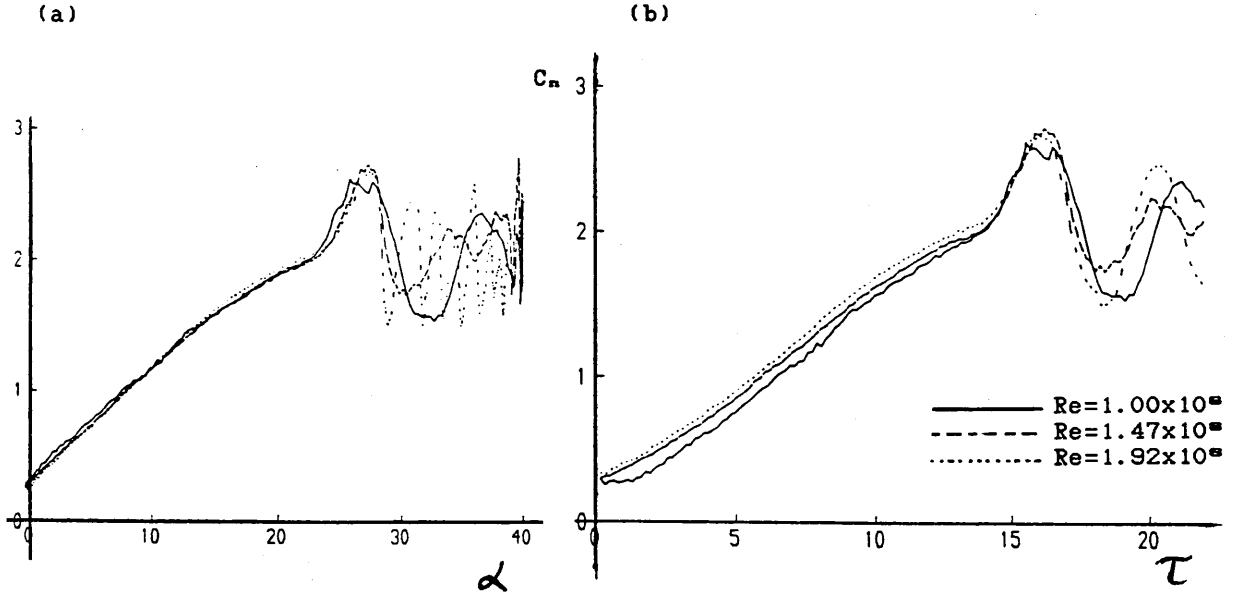

Figure 4.78 : Comparison of normal force characteristics for the NACA 23012C aerofoil at three values of Reynolds number and a reduced pitch-rate of between 0.016 and 0.017.

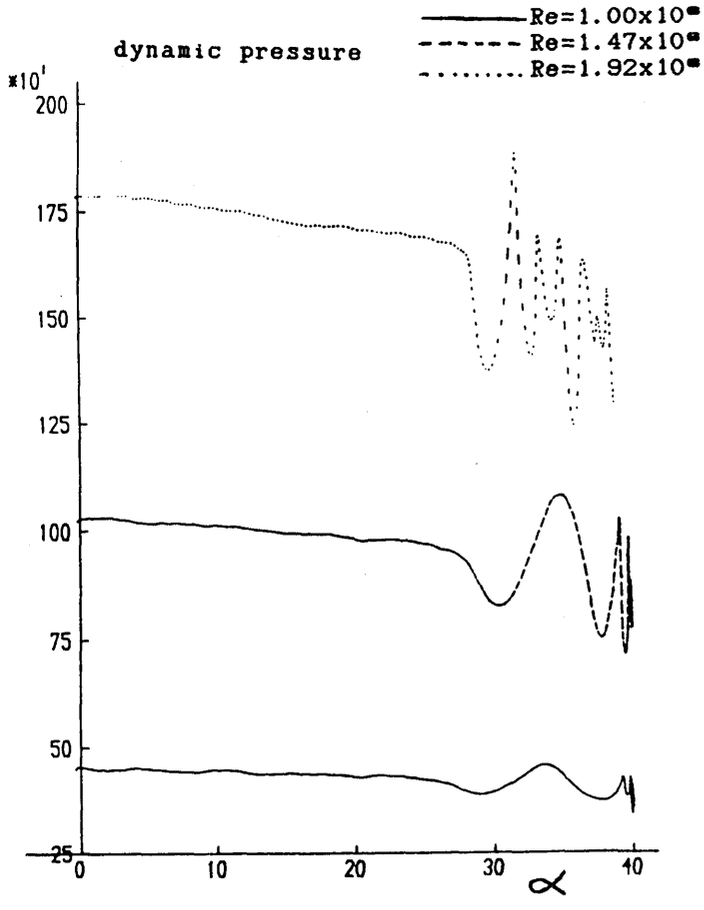

Figure 4.79 : Comparison of dynamic pressure distributions for the NACA 23012C aerofoil at three values of Reynolds number and a reduced pitch-rate of between 0.016 and 0.017.

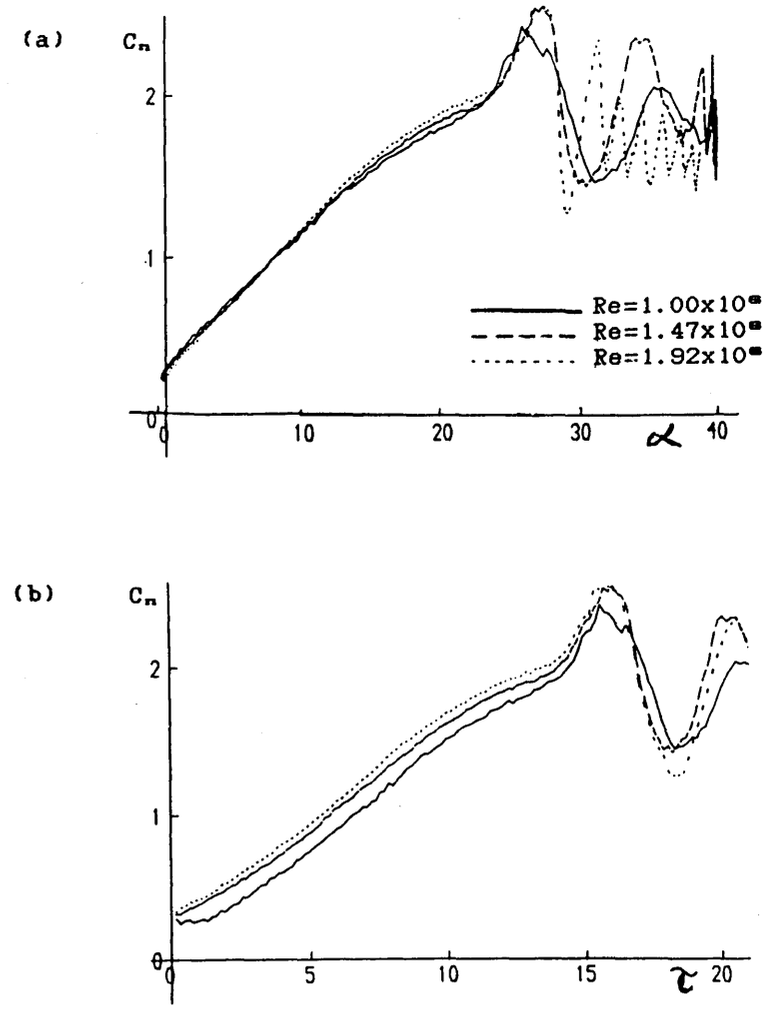

Figure 4.80 : Comparison of normal force characteristics for the NACA 23012C aerofoil at three values of Reynolds number, a reduced pitch-rate of between 0.016 and 0.017 and dynamic pressure determined from freestream velocity.

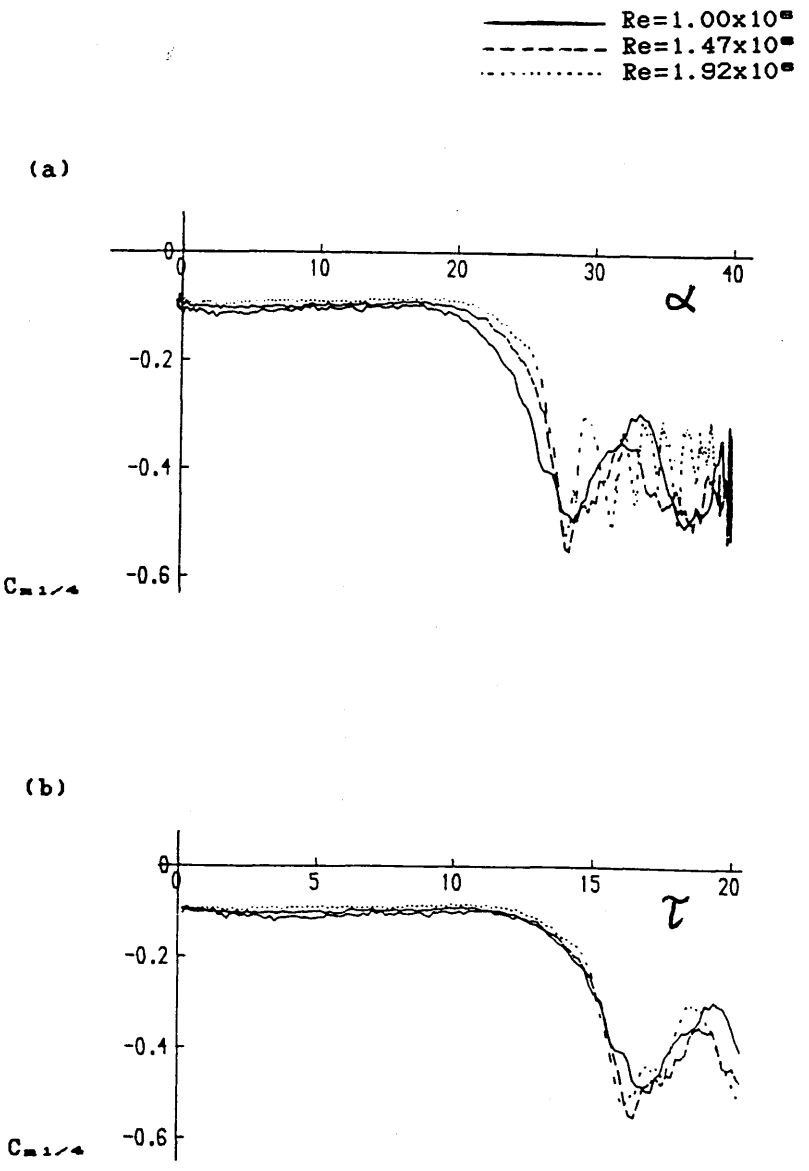

Figure 4.81 : Comparison of pitching-moment characteristics for the NACA 23012C aerofoil at three values of Reynolds number and a reduced pitch-rate of between 0.016 and 0.017.

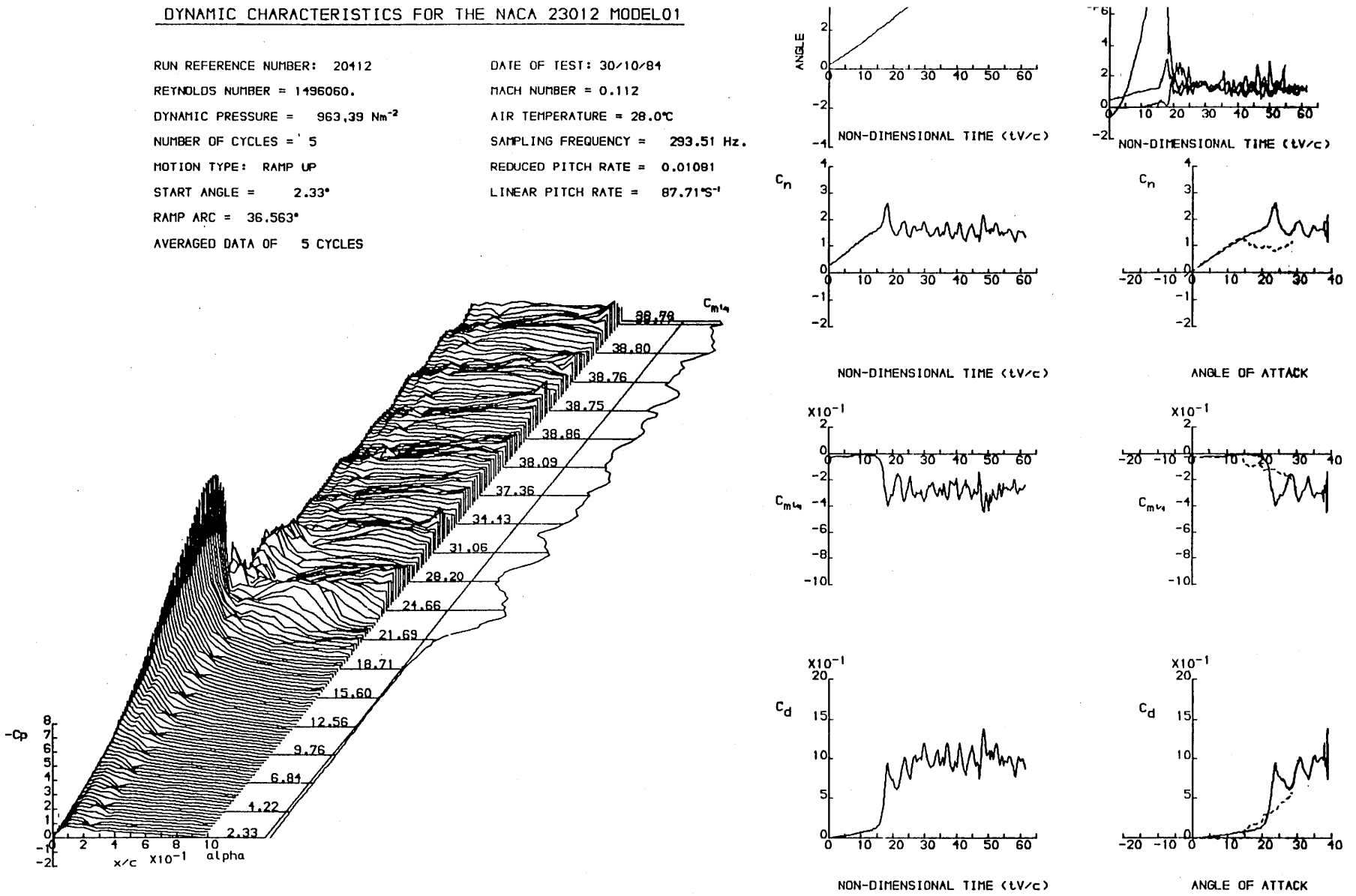

Figure 4.82 : Unsteady characteristics for the NACA 23012 aerofoil at a Reynolds number of 1.50×10^6 and a reduced pitch-rate of 0.011.

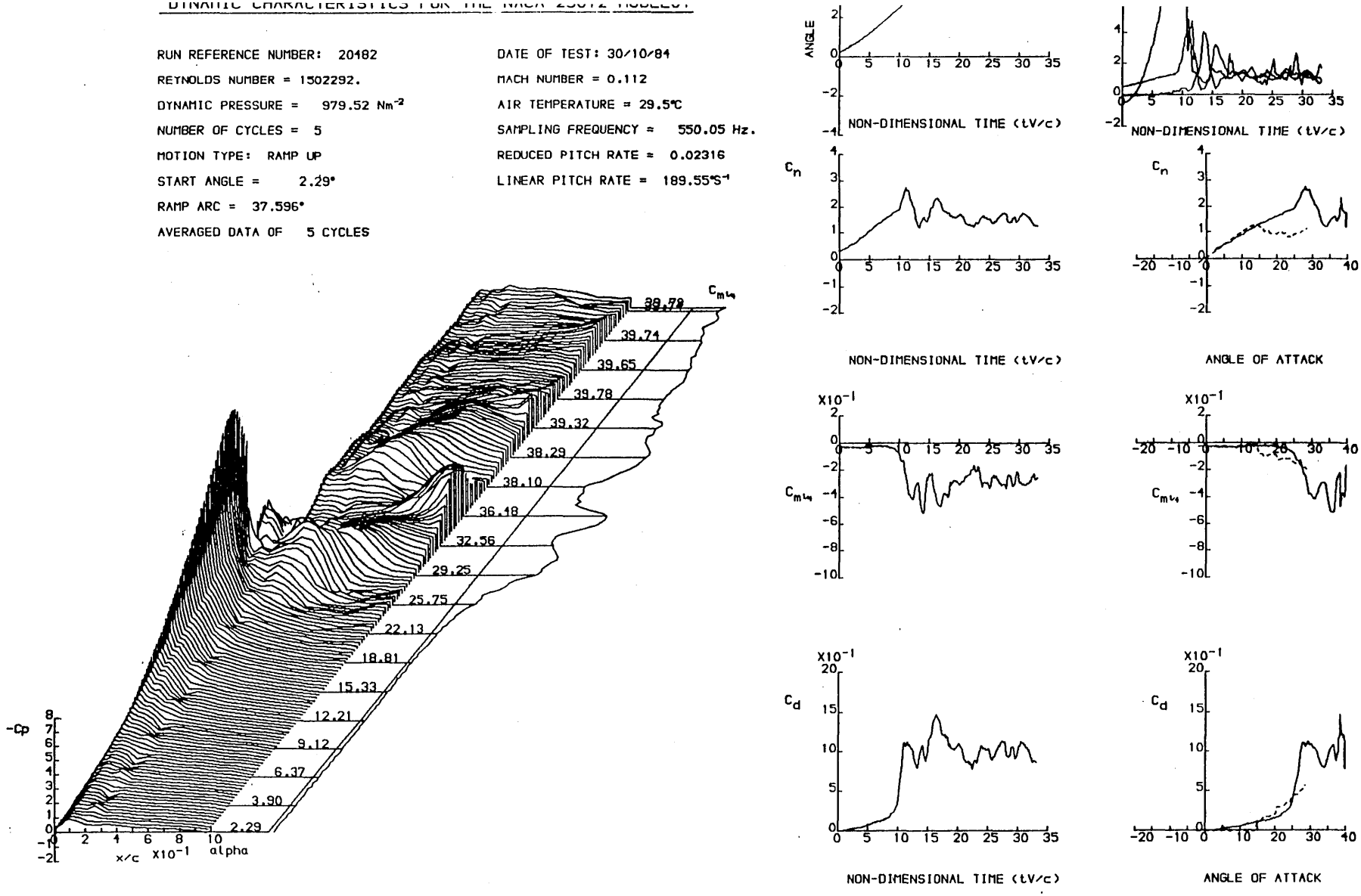

Figure 4.83 : Unsteady characteristics for the NACA 23012 aerofoil at a Reynolds number of 1.50×10^6 and a reduced pitch-rate of 0.023.

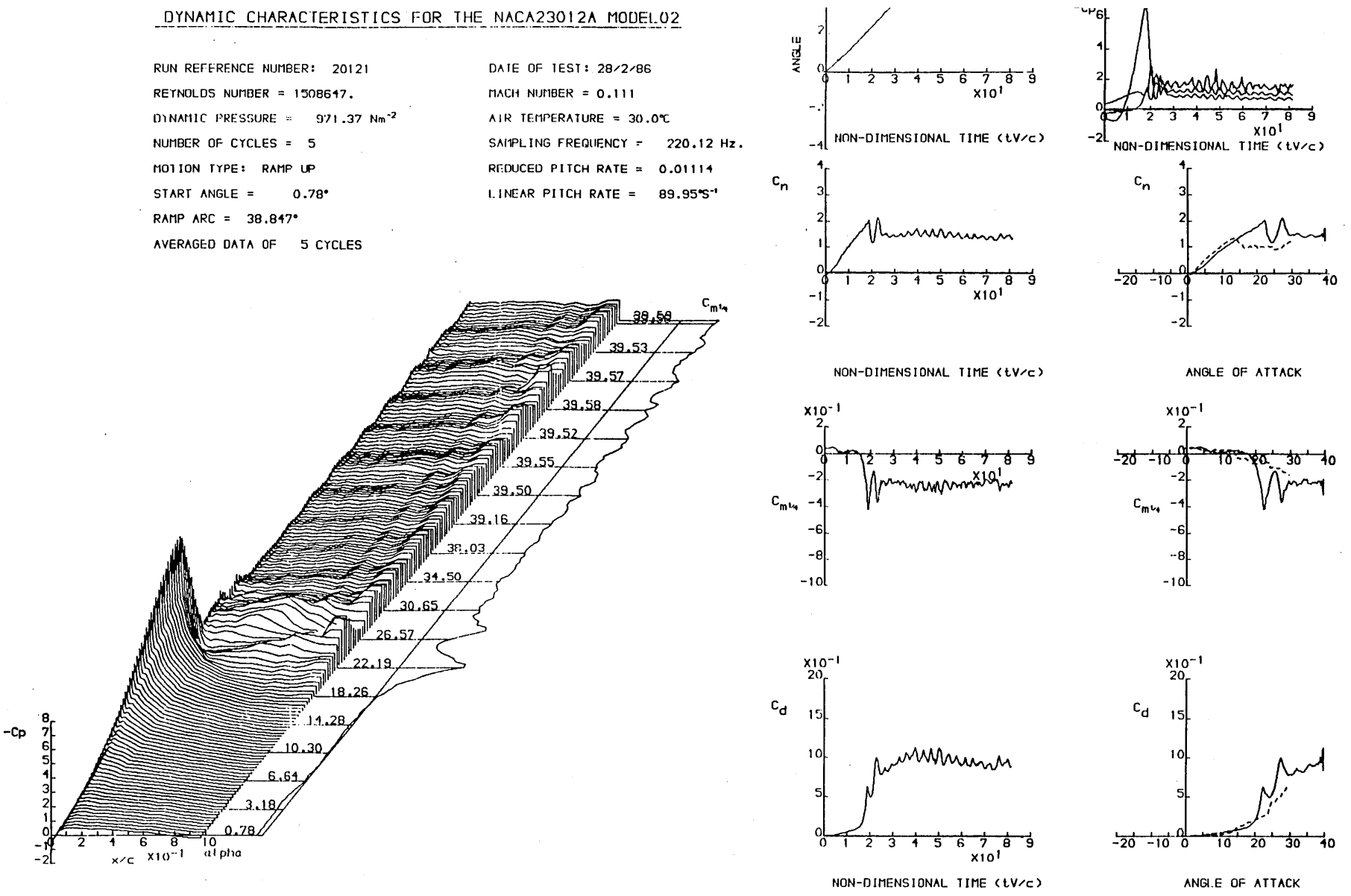

Figure 4.84 : Unsteady characteristics for the NACA 23012A aerofoil at a Reynolds number of 1.51×10^6 and a reduced pitch-rate of 0.011.

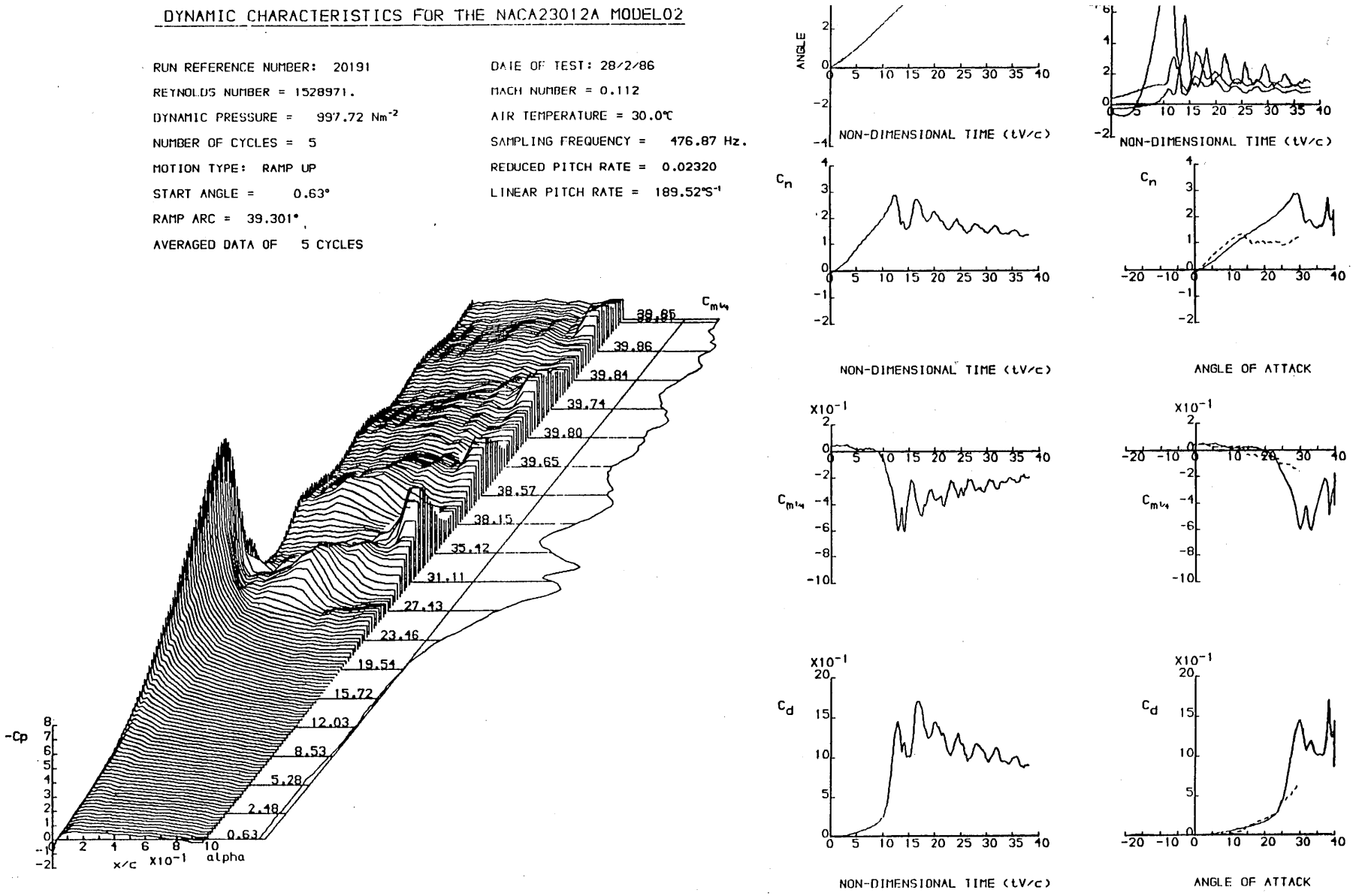

Figure 4.85 : Unsteady characteristics for the NACA 23012A aerofoil at a Reynolds number of 1.53×10^6 and a reduced pitch-rate of 0.023.

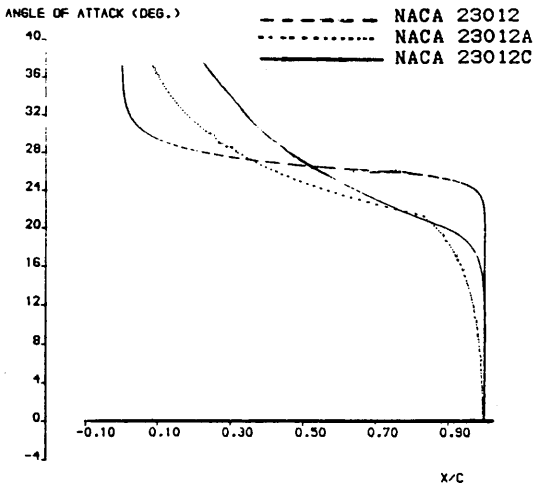

Figure 4.86 : Comparison of trailing-edge separation characteristics for three aerofoils at a reduced pitch-rate of 0.034 and a Reynolds number of 1.5×10^6.

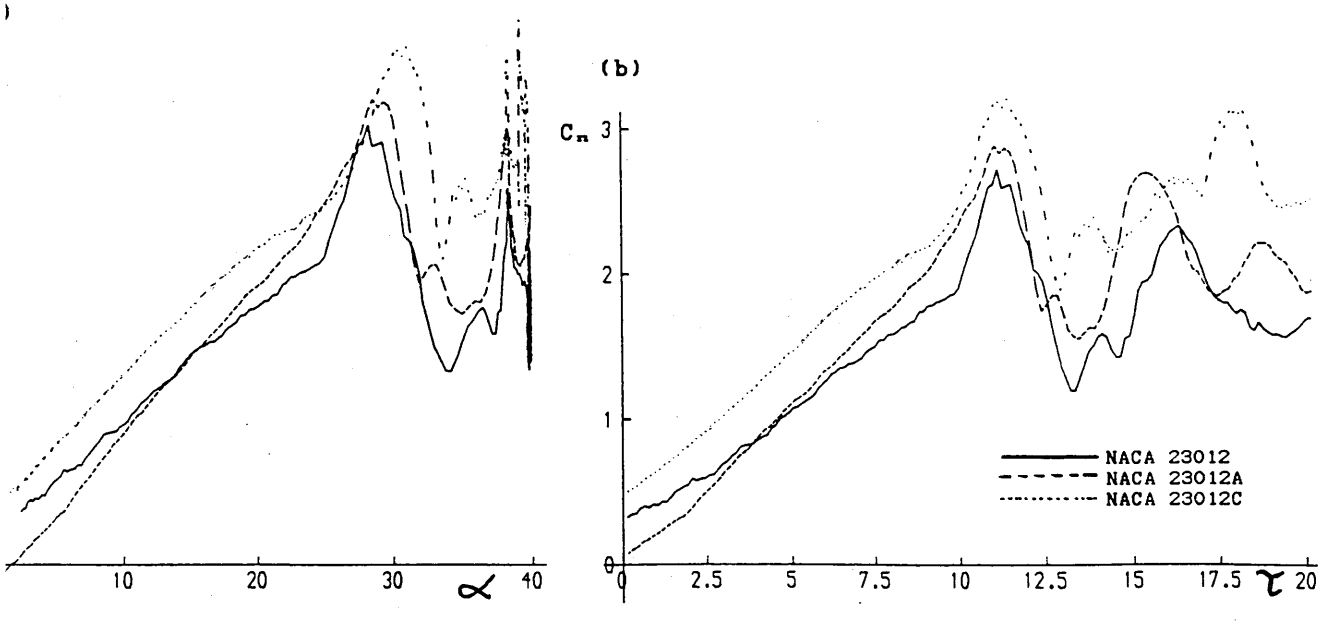

Figure 4.87 : Comparison of normal force characteristics for three aerofoils at a Reynolds number of 1.5×10^6 and a reduced pitch-rate of between 0.023 and 0.024.

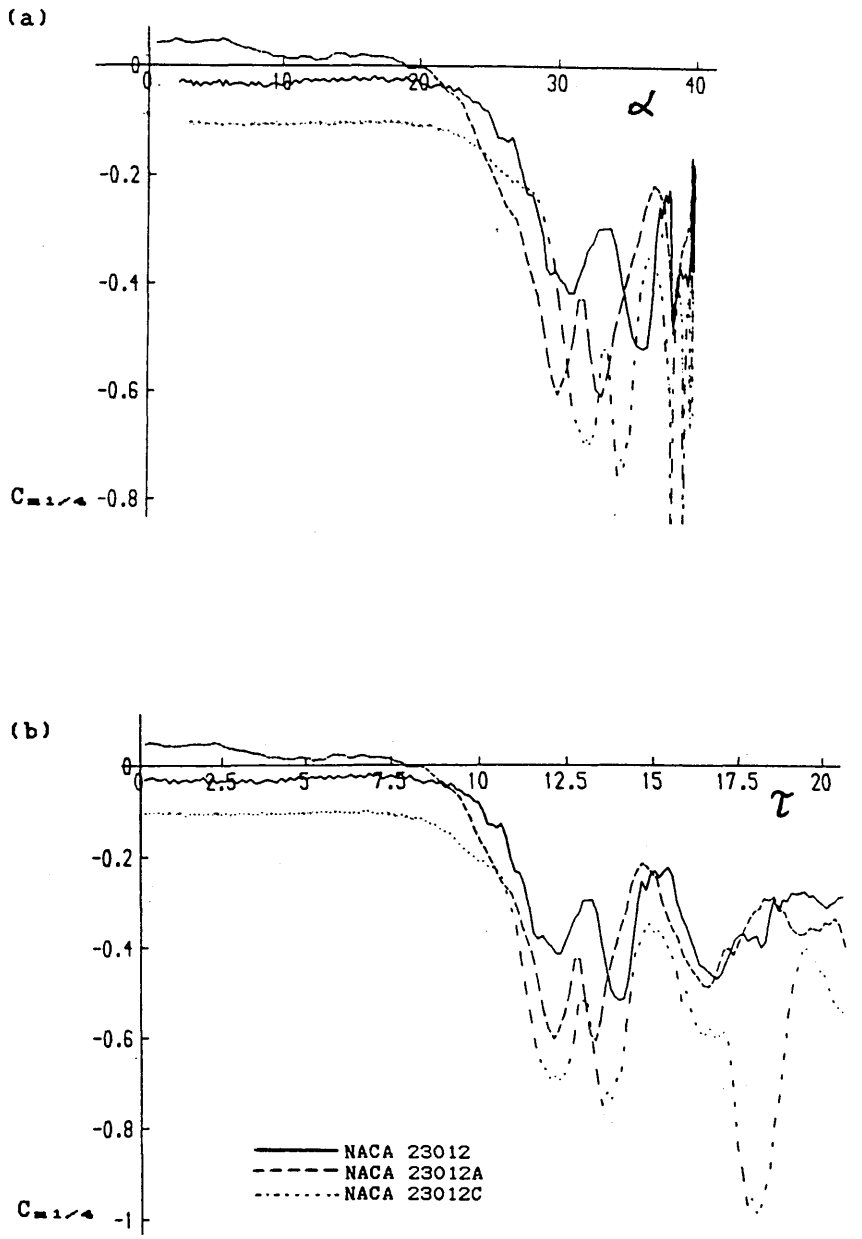

Figure 4.88 : Comparison of pitching moment characteristics for three aerofoils at a Reynolds number of 1.5×10^6 and a reduced pitch-rate of between 0.023 and 0.024.

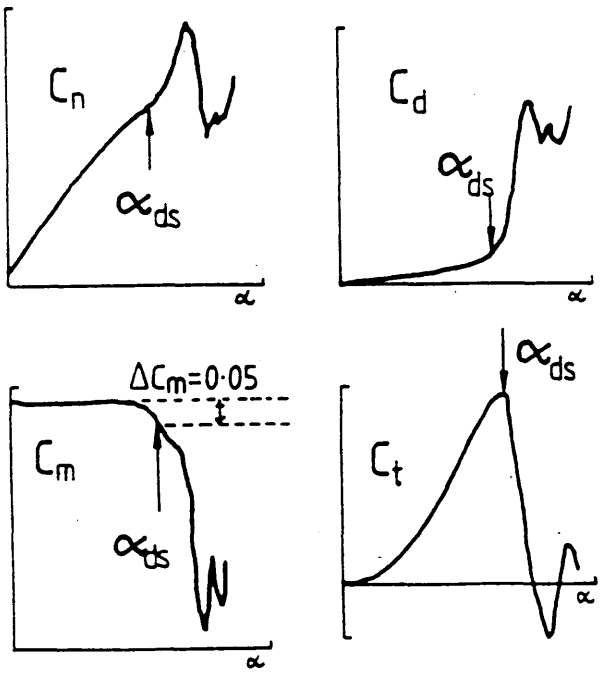

Figure 4.89 : Possible definitions of dynamic stall onset incidence from airloads at low Mach number.

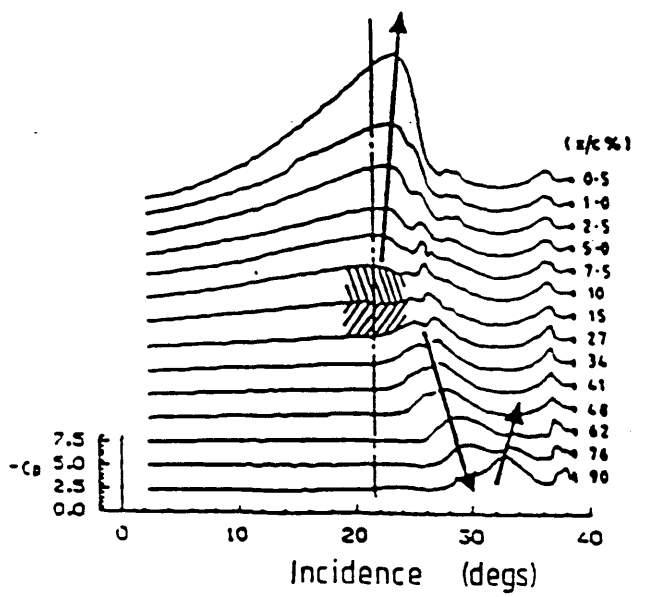

Figure 4.90 : Upper surface pressure variation for the NACA 23012 aerofoil at a reduced pitch-rate of 0.02 and a Reynolds number of 1.5×10^6. (from SETO AND GALBRAITH [84])

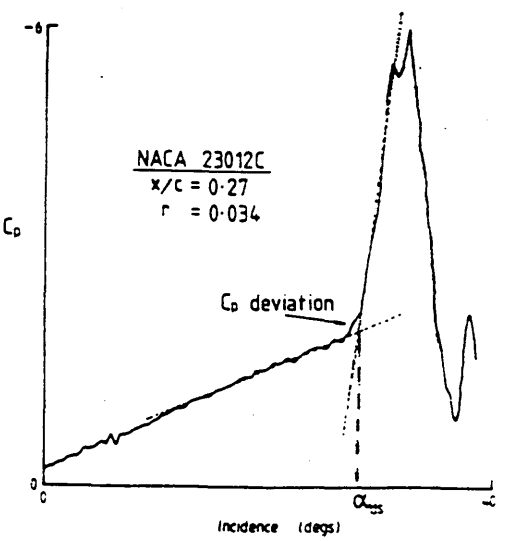

Figure 4.91 : Defined incidence of dynamic stall onset from pressure trace.

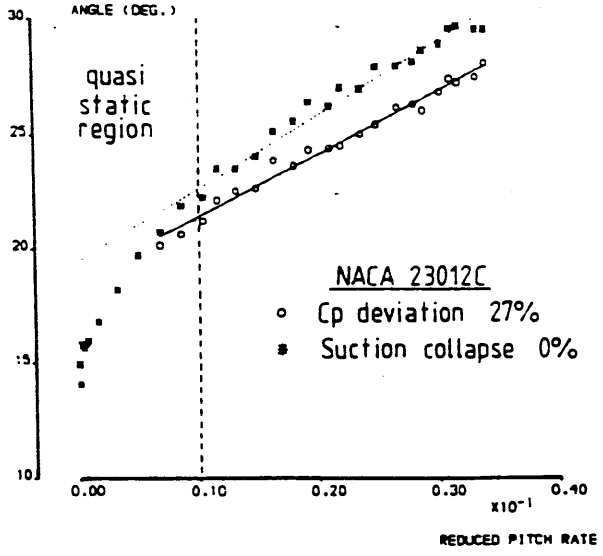

Figure 4.92 : Variation of C_p deviation incidence with reduced pitch-rate for the NACA 23012C aerofoil at a Reynolds number of 1.5×10^6.

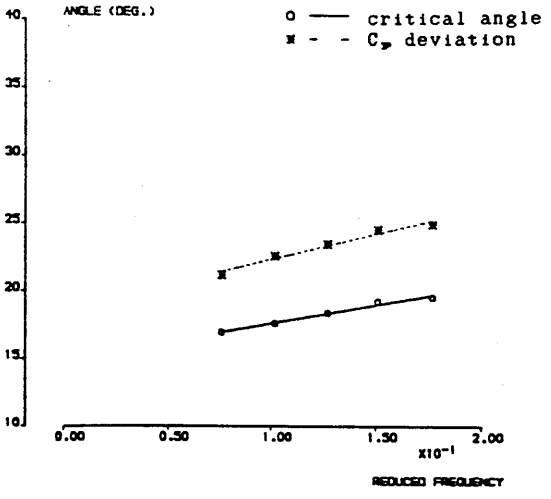

Figure 4.93 : Comparison of C_p deviation incidence with critical angle of attack for the NACA 23012C aerofoil at a Reynolds number of 1.5×10^6.

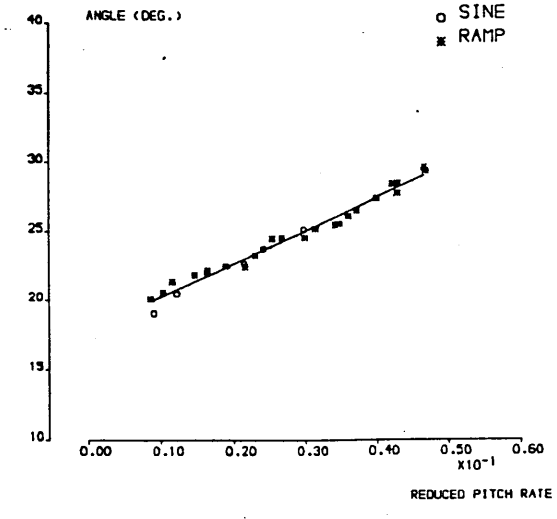

igure 4.94 : Variation of C_p deviation incidence with maximum reduced pitch-rate for the NACA 23012C aerofoil under both ramp and sinusoidal motions at a Reynolds number of 1.5×10^6.

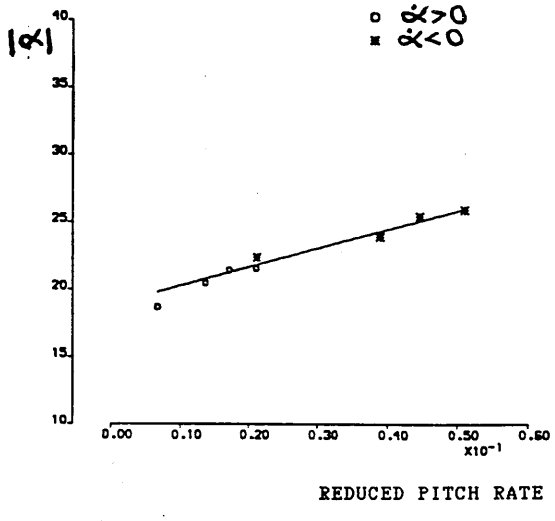

Figure 4.95 : Variation of C_p deviation incidence with maximum reduced pitch-rate for the NACA 0015 aerofoil under motion of VAWT function when incidence is both increasing and decreasing at a Reynolds number of 1.5×10^6.

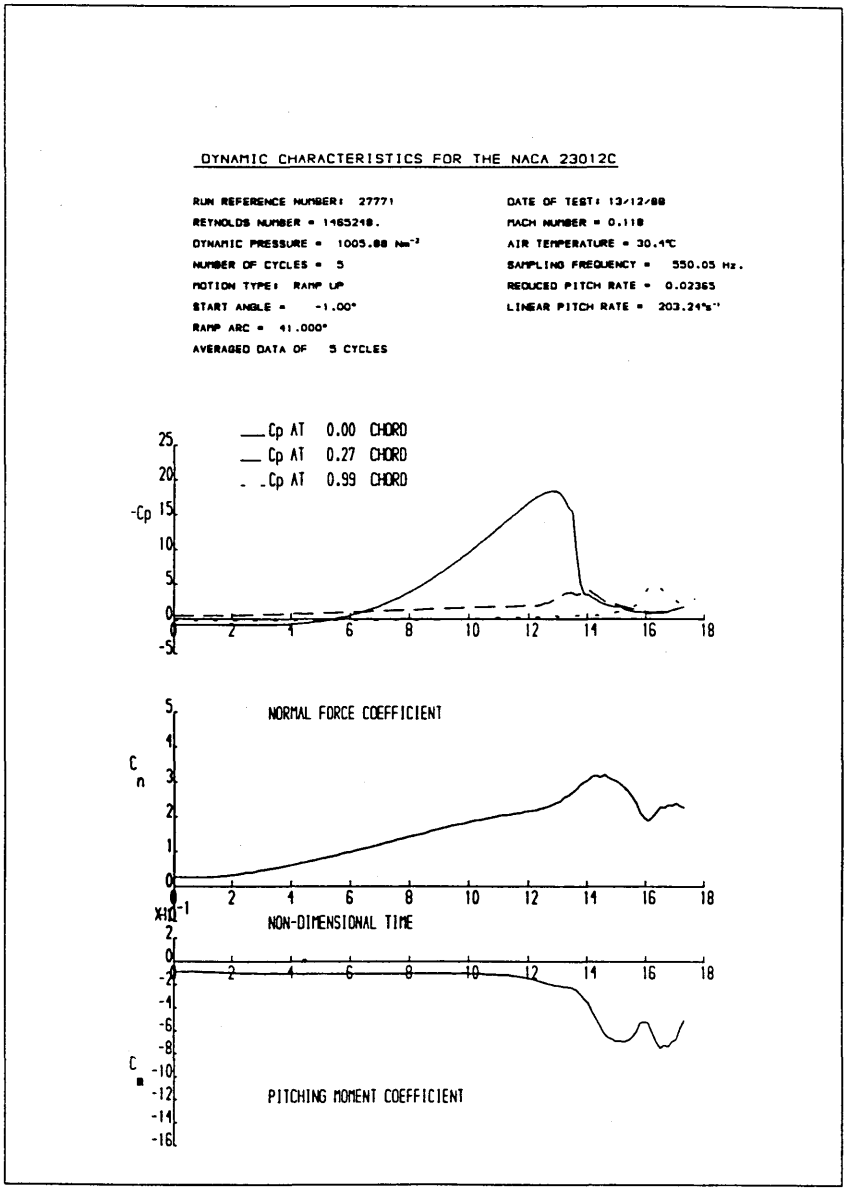

Figure 4.96 : Unsteady characteristics for the NACA 23012C aerofoil at a Reynolds number of 1.47×10^6 and a reduced pitch-rate of 0.024.

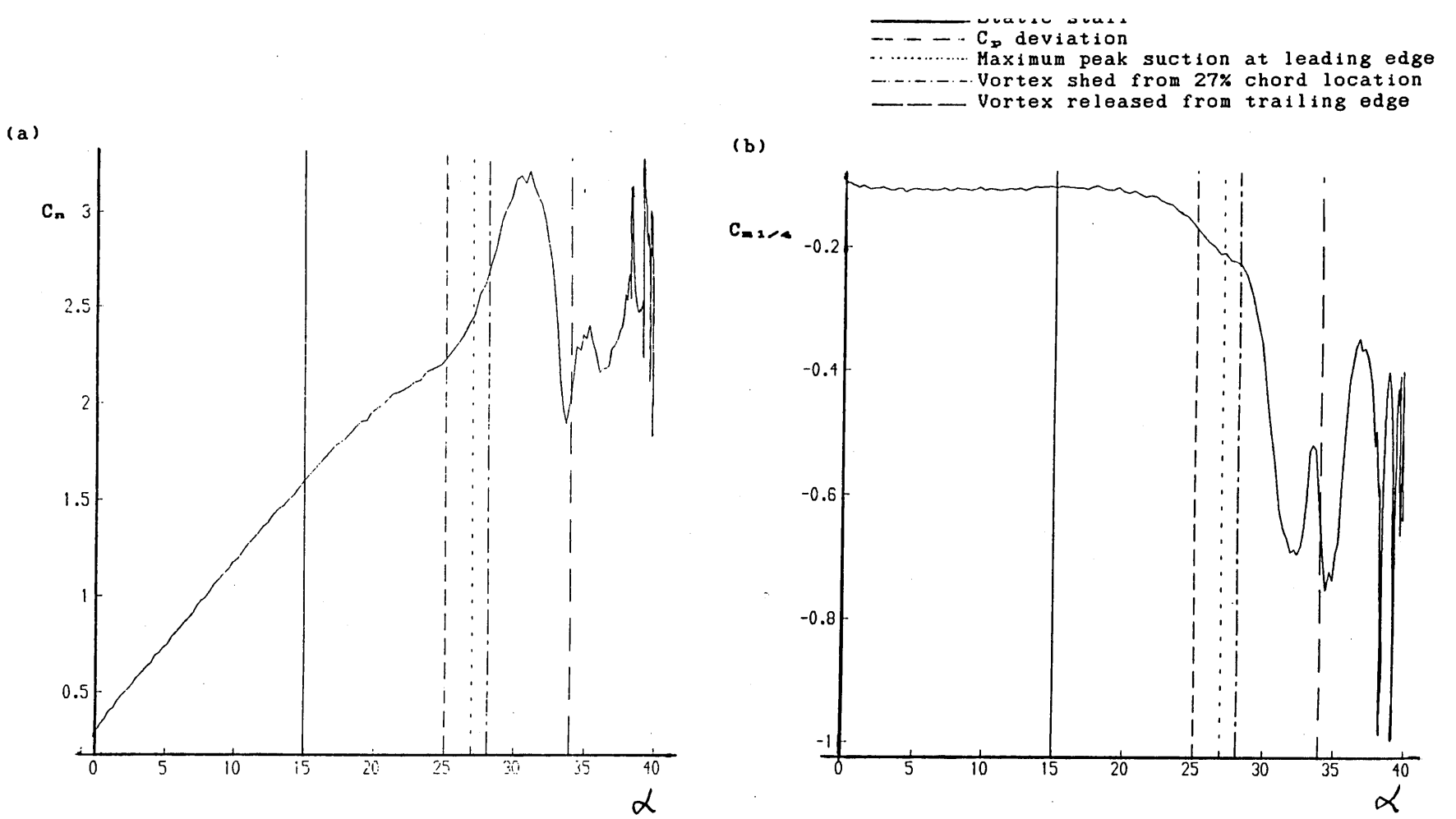

Figure 4.97 : Illustration of incidences of dynamic stall events in relation to normal force and pitching moment characteristics at a reduced pitch-rate of 0.024 and Reynolds number of 1.5×10^6.

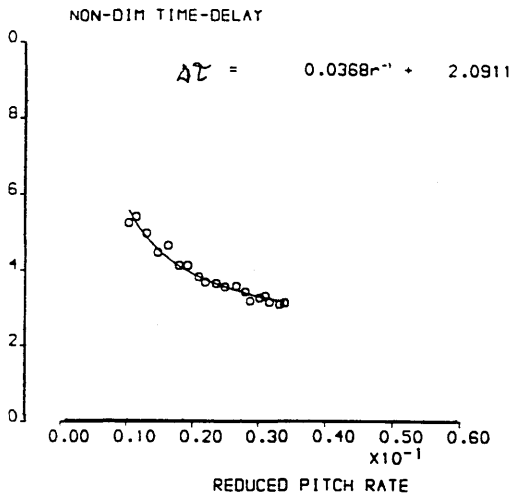

(a) Delay between static stall incidence and C_p deviation.

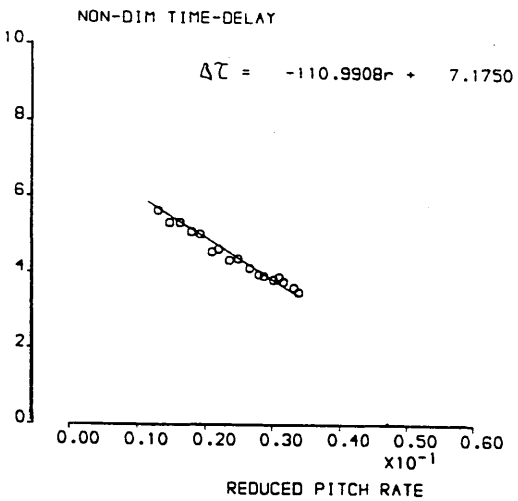

(b) Delay between static stall incidence and maximum peak leading-edge suction.

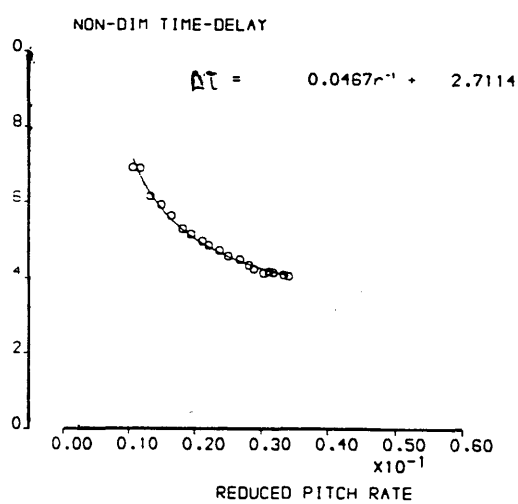

(c) Delay between static stall incidence and shedding of vortex from 27% chord.

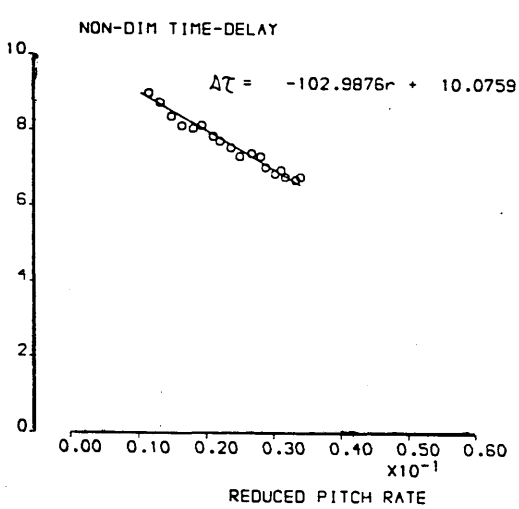

(d) Delay between static stall incidence and releasing of vortex from trailing-edge.

igure 4.98 : Variation of various time-delays with reduced pitch-rate for the NACA 23012C aerofoil at a Reynolds number of 1.5x10^6.

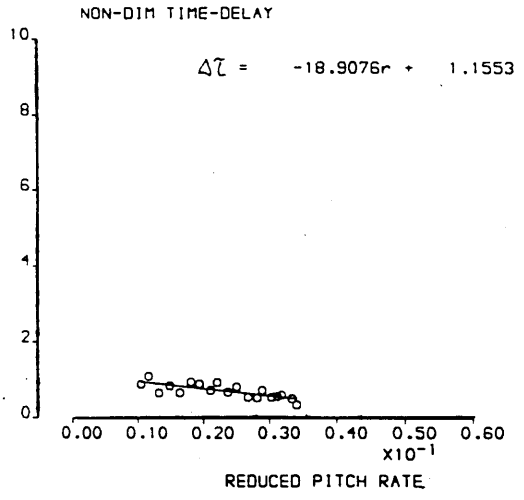

(e) Delay between C_p deviation and maximum peak leading-edge suction.

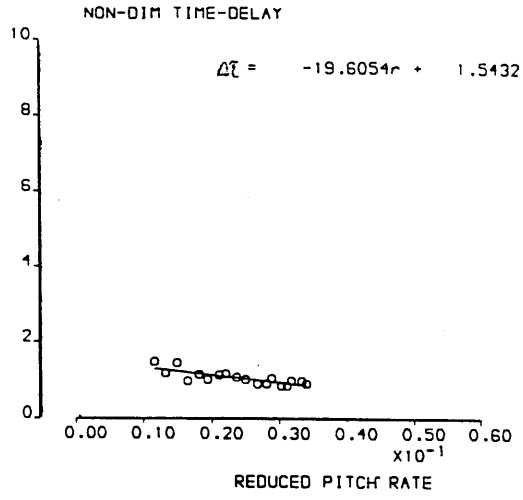

(f) Delay between C_p deviation and shedding of vortex from 27% chord.

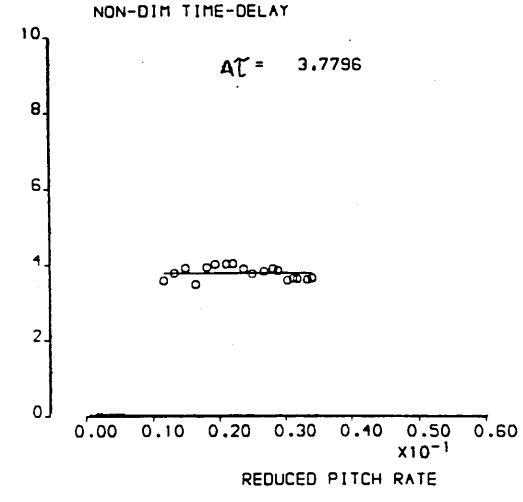

(g) Delay between C_p deviation and releasing of vortex from trailing-edge.

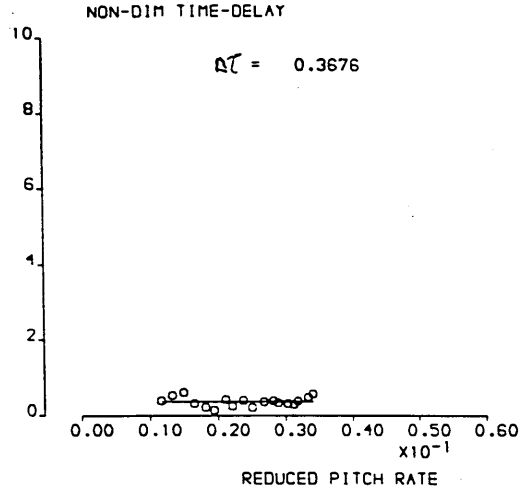

(h) Delay between maximum peak leading-edge suction and shedding of vortex from 27% chord.

Figure 4.98 : Variation of various time-delays with reduced pitch-rate for the NACA 23012C aerofoil at a Reynolds number of 1.5×10^6. (continued)

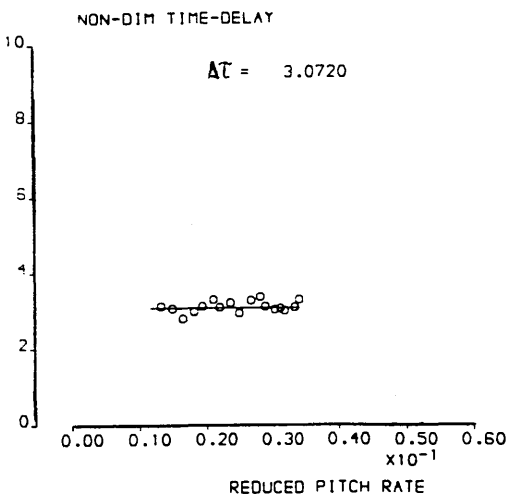

(i) Delay between maximum peak leading-edge suction and releasing of vortex from trailing-edge.

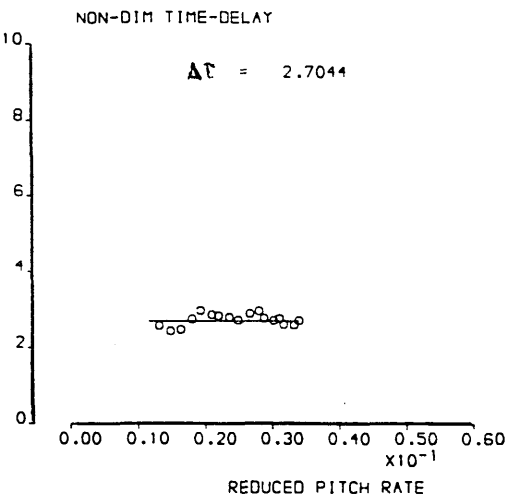

(j) Delay between vortex being shed from 27% chord and releasing of vortex from trailing-edge.

Figure 4.98 : Variation of various time-delays with reduced pitch-rate for the NACA 23012C aerofoil at a Reynolds number of 1.5×10^6. (concluded)

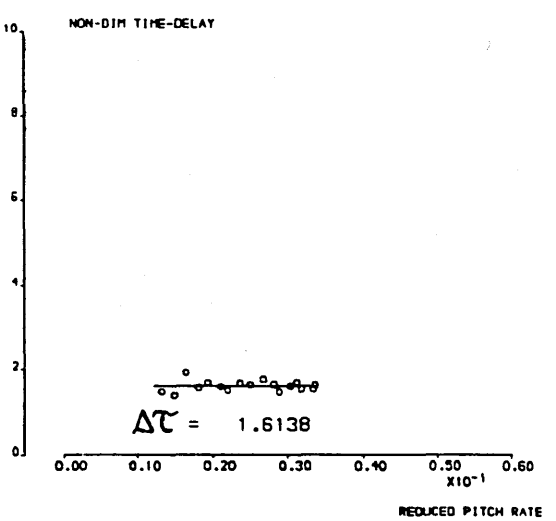

Figure 4.99 : Variation with reduced pitch-rate of the time-delay between Beddoes's definition of dynamic stall onset and C_p deviation for the NACA 23012C aerofoil at a Reynolds number of 1.5×10^6.

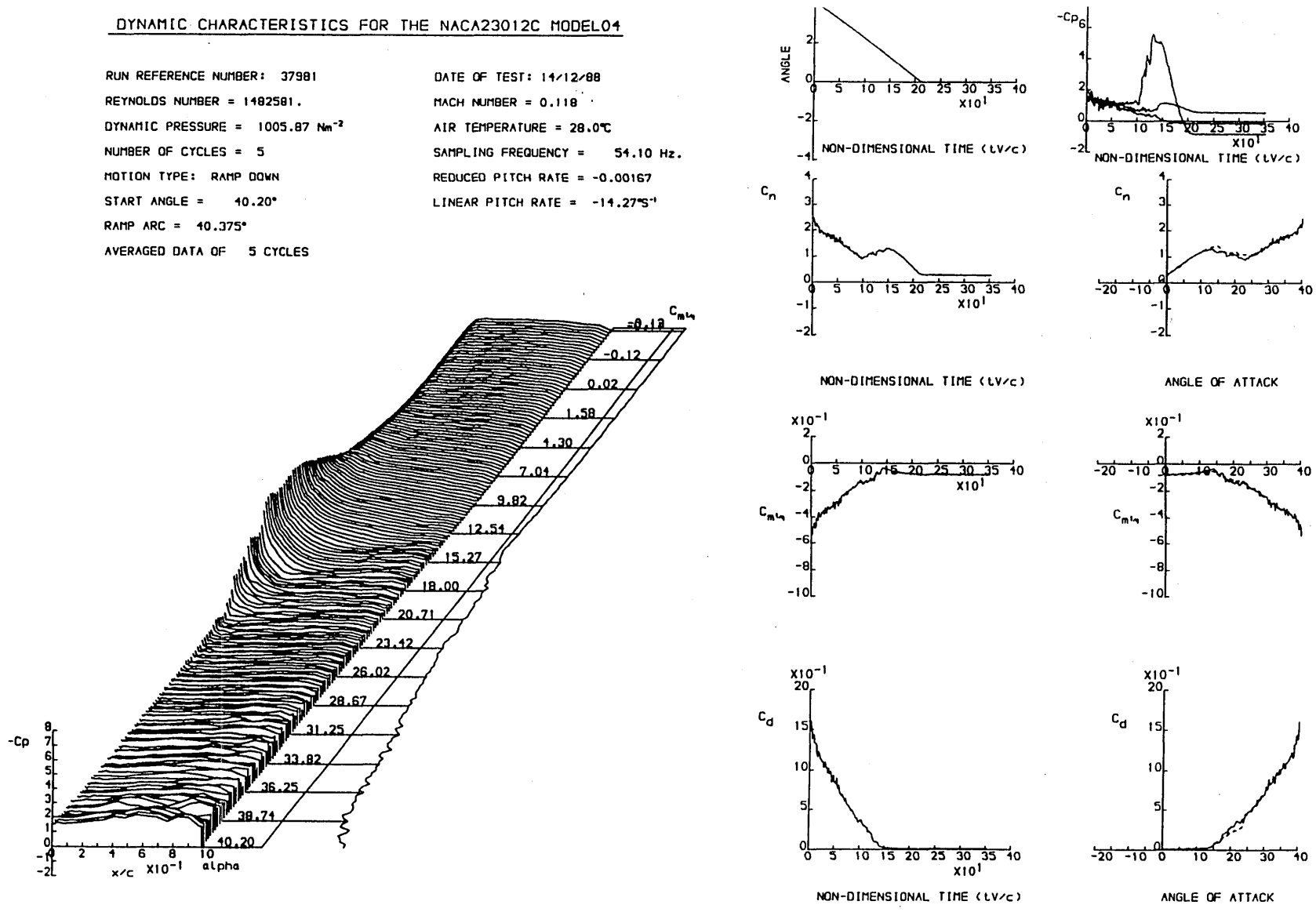

Figure 4.100 : Unsteady characteristics for the NACA 23012C aerofoil at a Reynolds number of 1.48×10^6 and a reduced pitch-rate of -0.002.

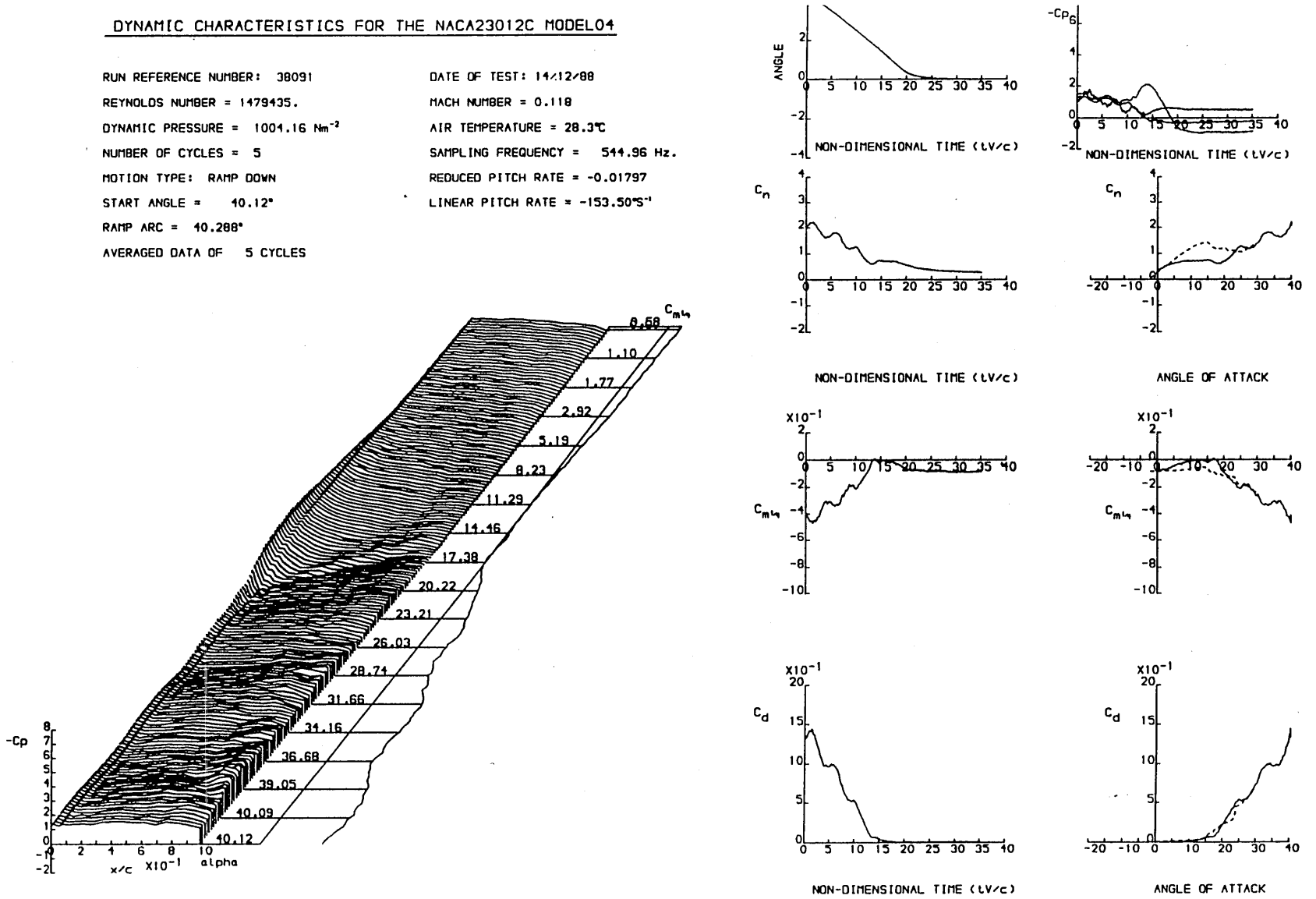

Figure 4.101 : Unsteady characteristics for the NACA 23012C aerofoil at a Reynolds number of 1.48×10^6 and a reduced pitch-rate of -0.018.

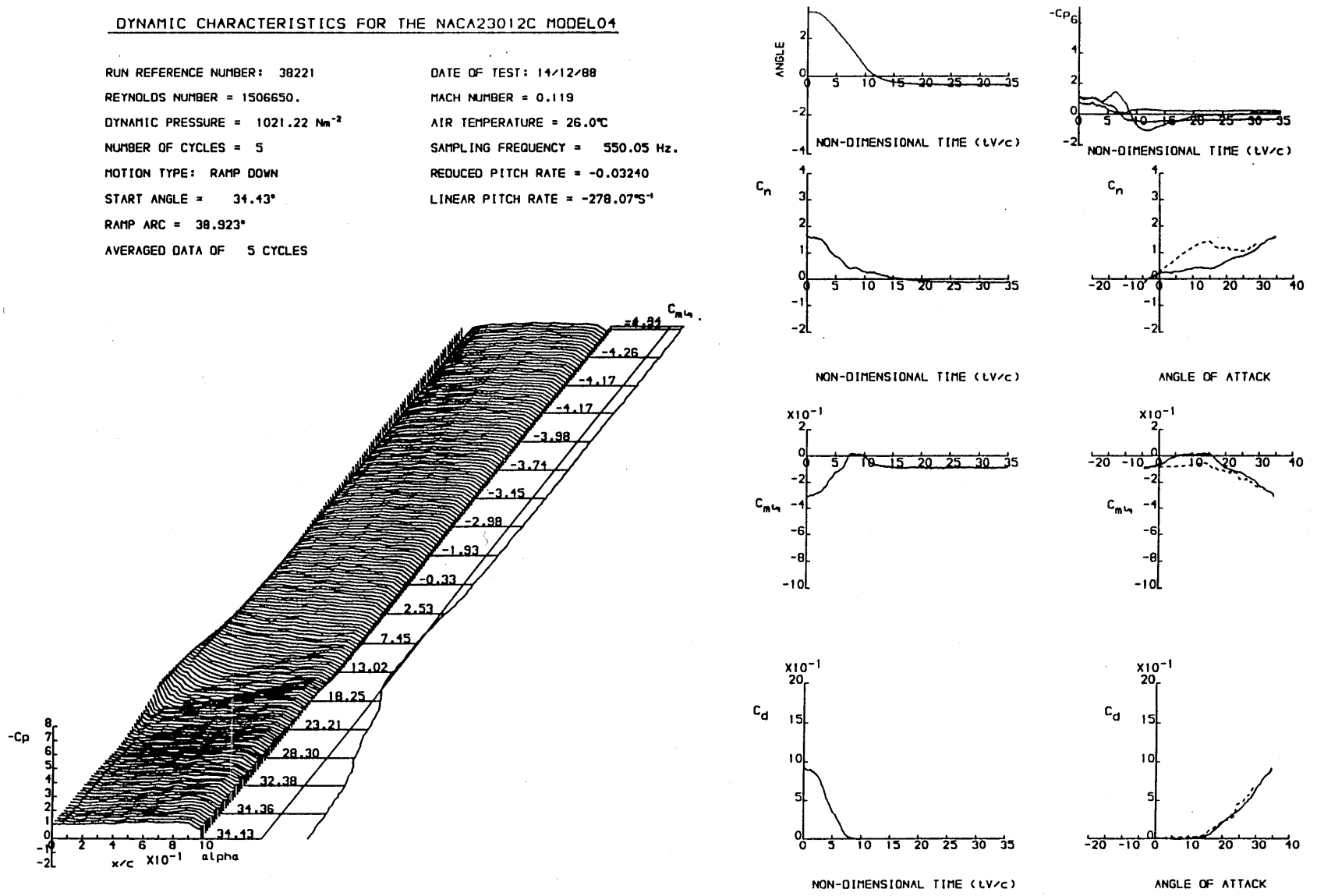

Figure 4.102 : Unsteady characteristics for the NACA 23012C aerofoil at a Reynolds number of 1.51×10^6 and a reduced pitch-rate of -0.032.

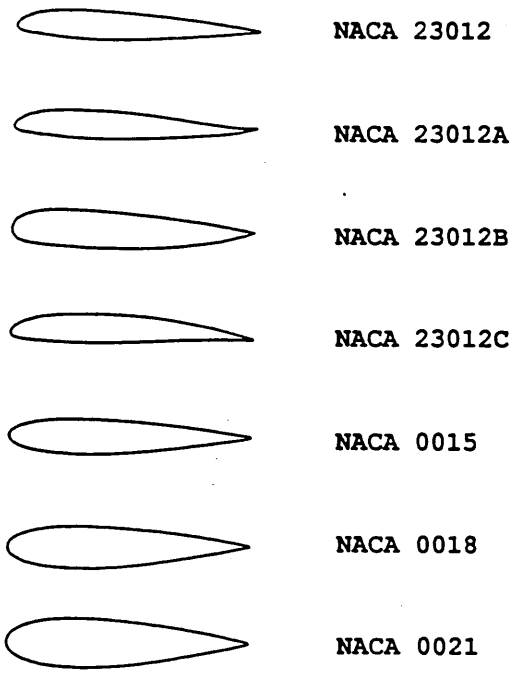

Figure 5.1 : Seven aerofoils tested at the University of Glasgow.

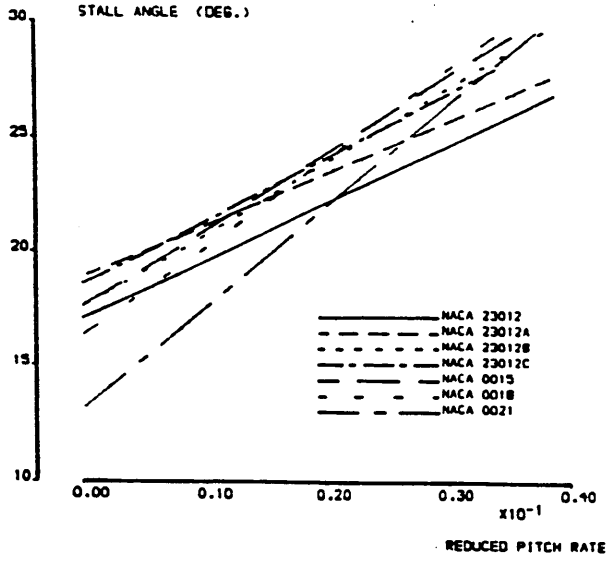

Figure 5.2 : Variation of C_p deviation incidence with reduced pitch-rate for seven aerofoils at a Reynolds number of 1.5×10^6.

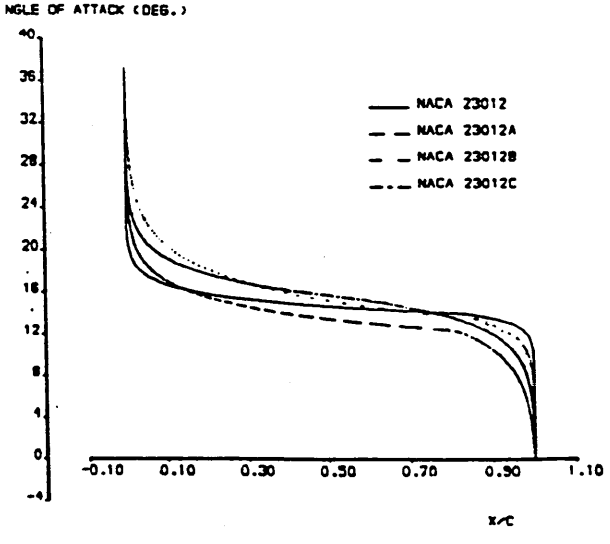

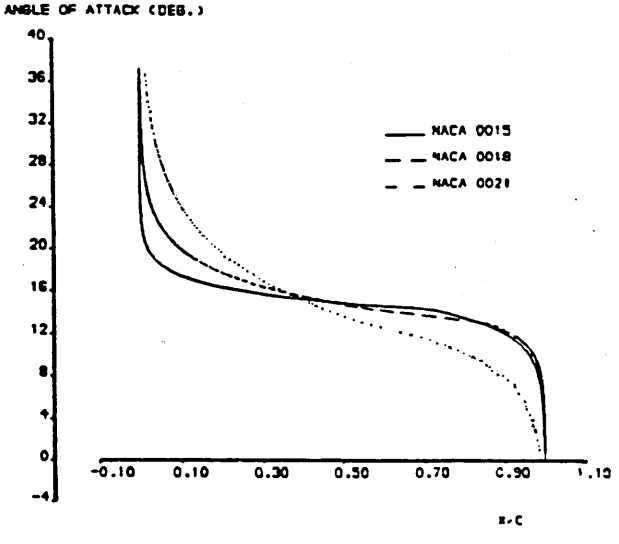

Figure 5.3 : Static trailing-edge separation characteristics for seven aerofoils at a Reynolds number of 1.5×10^6.

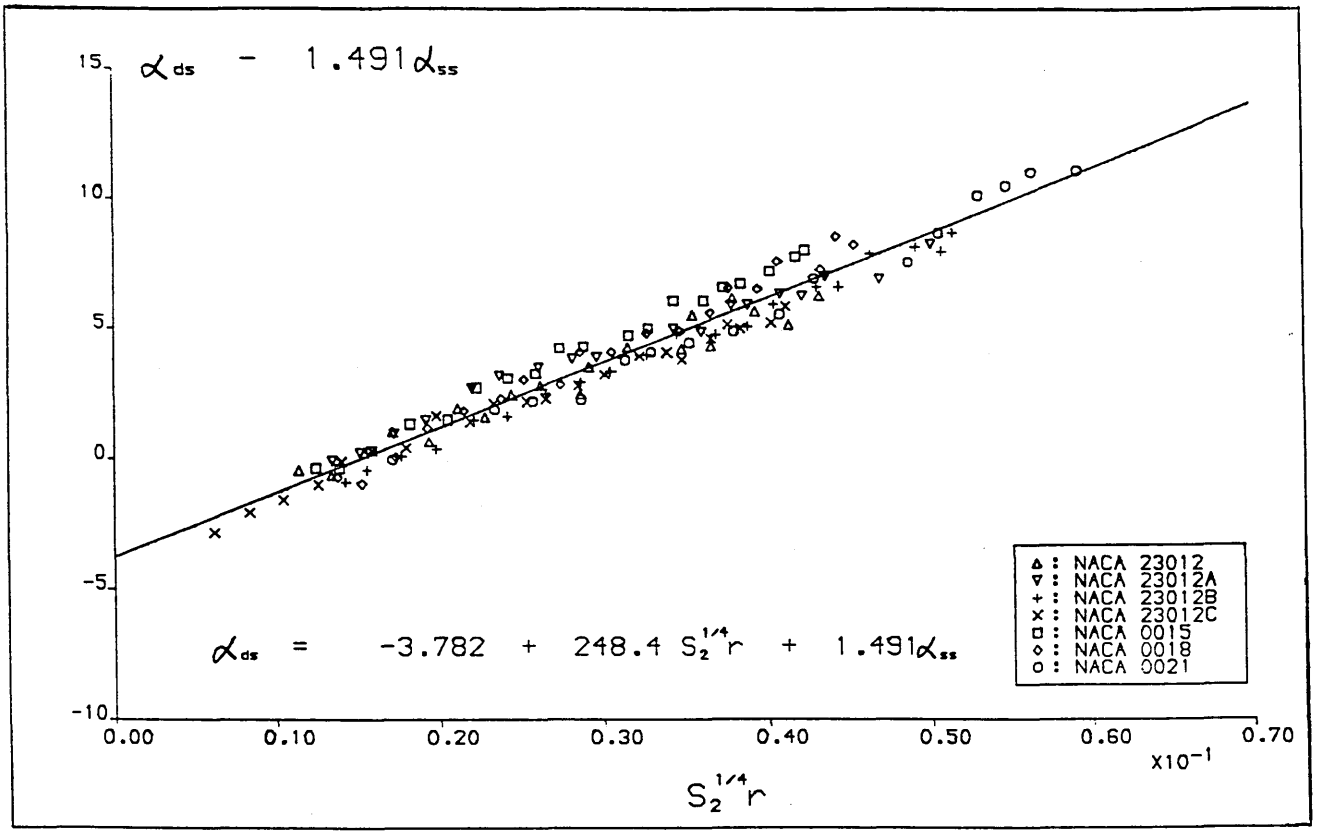

Figure 5.4 : Linear correlation of C_p deviation incidences at a Reynolds number of 1.5×10^6.

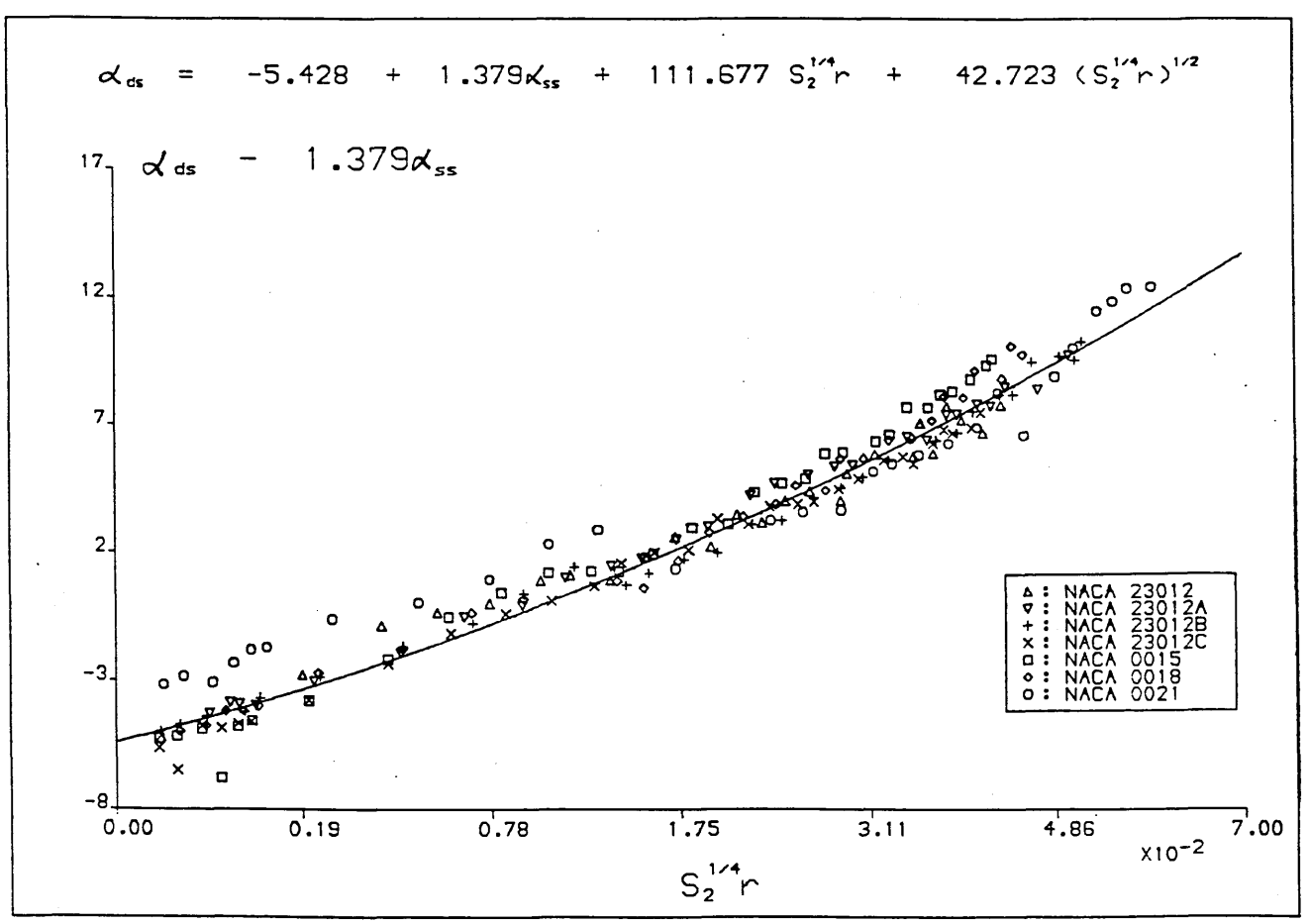

Figure 5.5 : Correlation of C_p deviation incidences at a Reynolds number of 1.5×10^6.

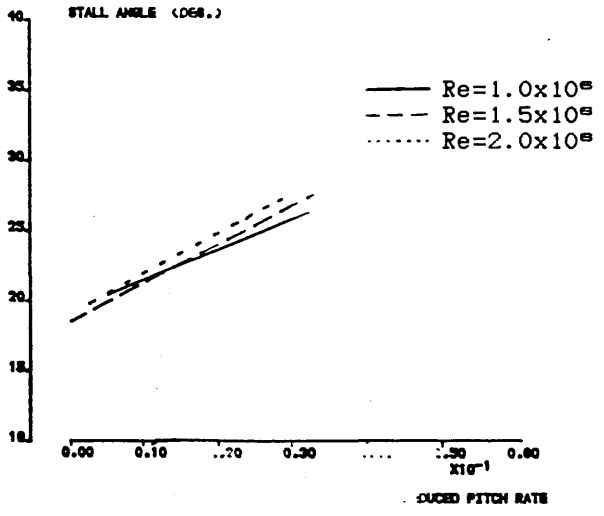

Figure 5.6 : Variation of C_p deviation incidence with reduced pitch-rate for the NACA 23012C aerofoil over a range of Reynolds numbers.

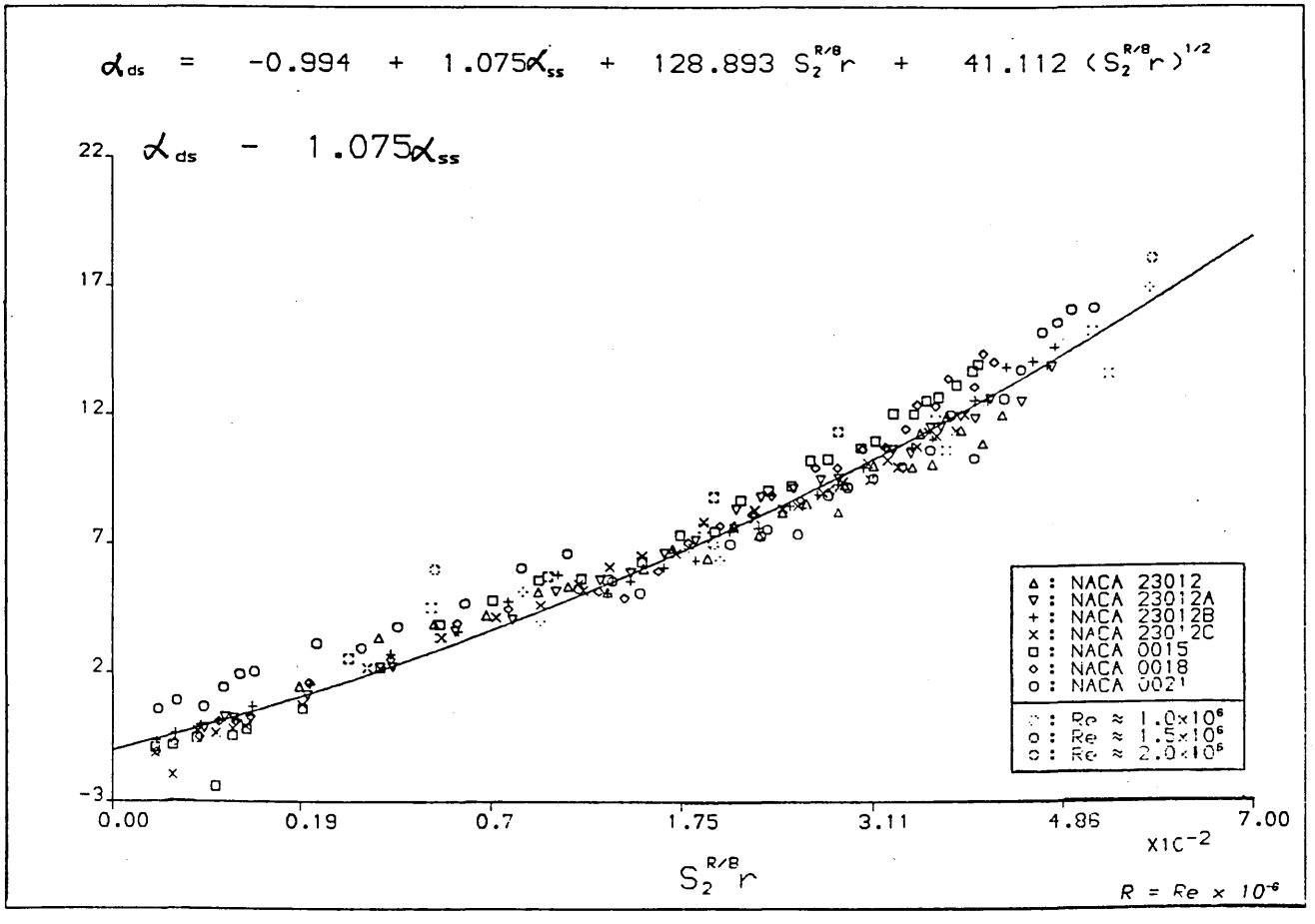

Figure 5.7 : Final correlation of C_p deviation incidences.

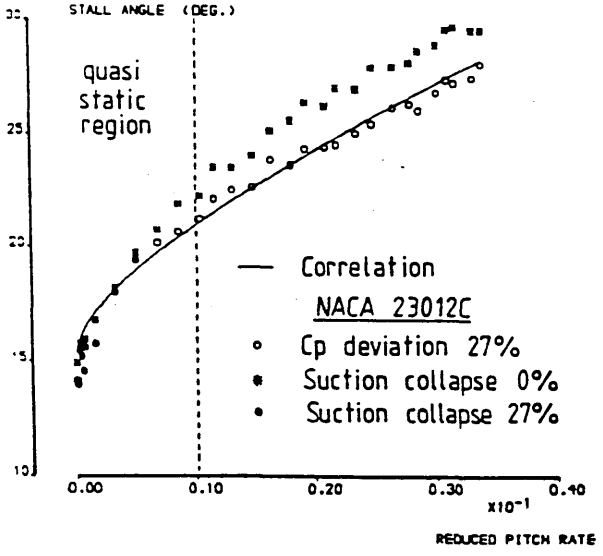

Figure 5.8 : Comparison between final dynamic stall correlation and incidences of various chordwise pressure events.

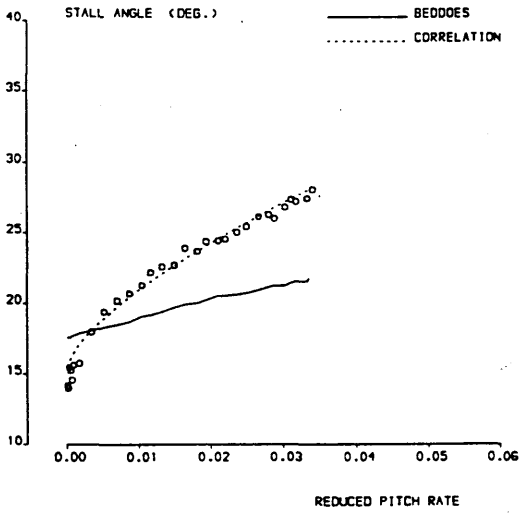

Figure 5.9 : Comparison between final dynamic stall correlation and incidences predicted by BEDDOES ET AL [13,56]

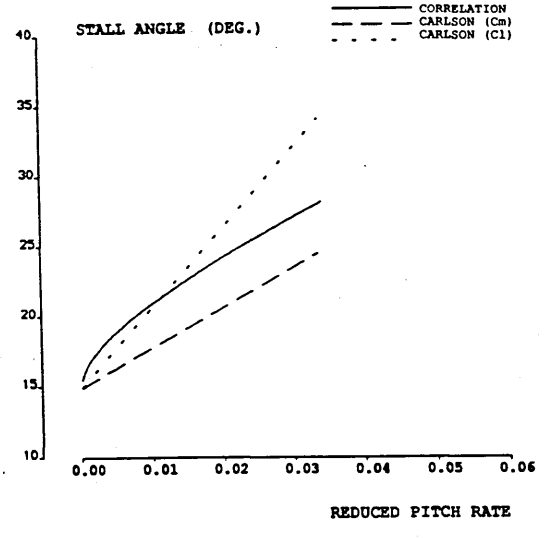

Figure 5.10 : Comparison between final dynamic stall correlation and incidences predicted by CARLSON ET AL [19].

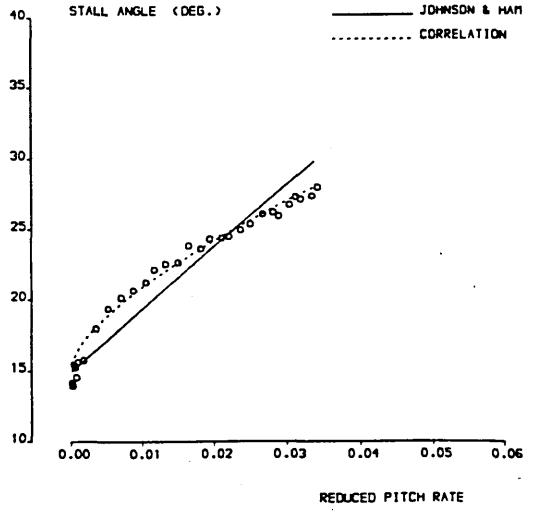

Figure 5.11 : Comparison between final dynamic stall correlation and incidences predicted by JOHNSON AND HAM [52].

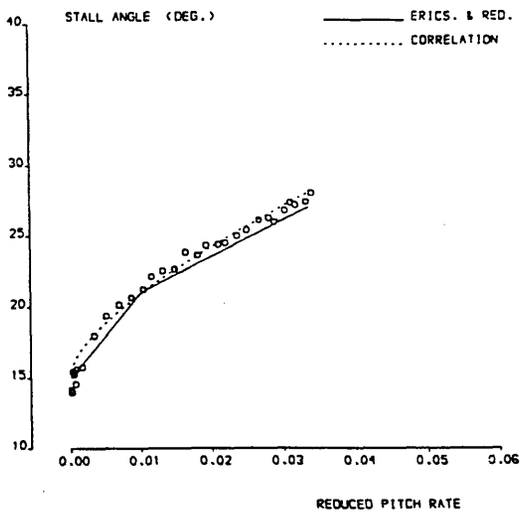

Figure 5.12 : Comparison between final dynamic stall correlation and incidences predicted by ERICSSON AND REDING [31].

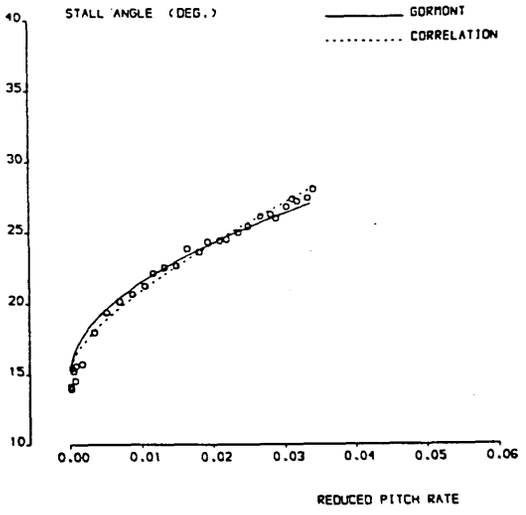

Figure 5.13 : Comparison between final dynamic stall correlation and incidences predicted by GORMONT [37].

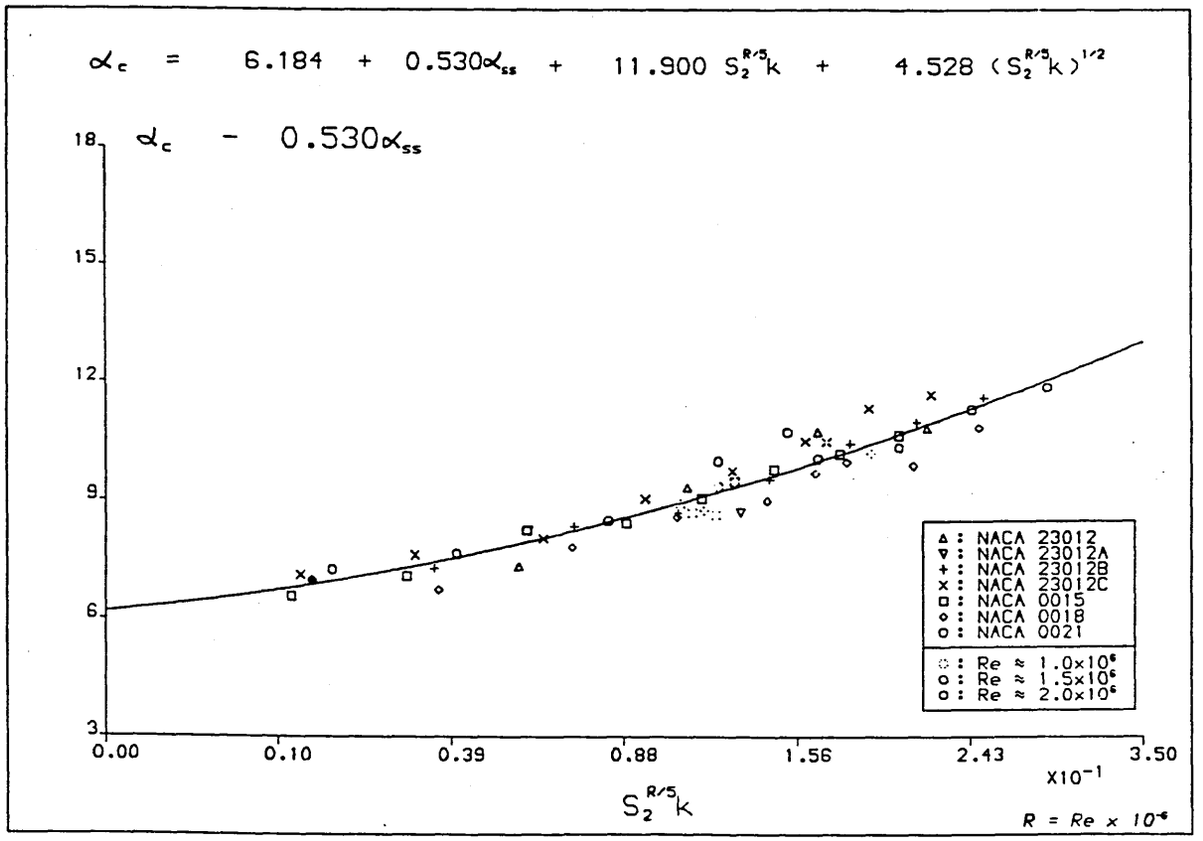

Figure 5.14 : Correlation of critical angles of attack.

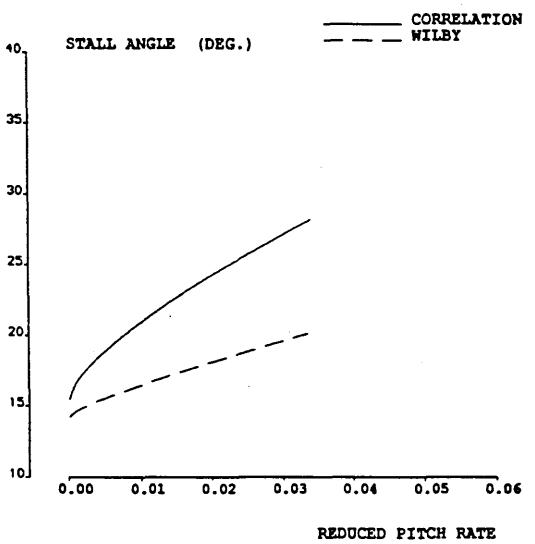

Figure 5.15 : Comparison between final dynamic stall correlation and incidences predicted for analogous critical angles of attack.

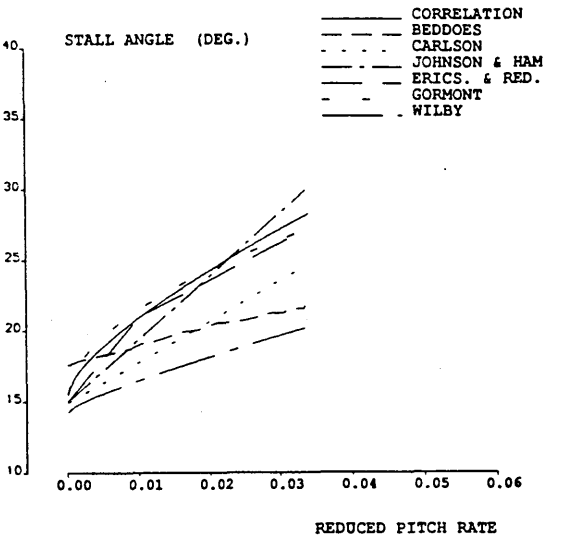

Figure 5.16 : Comparison of incidences predicted from seven criteria.

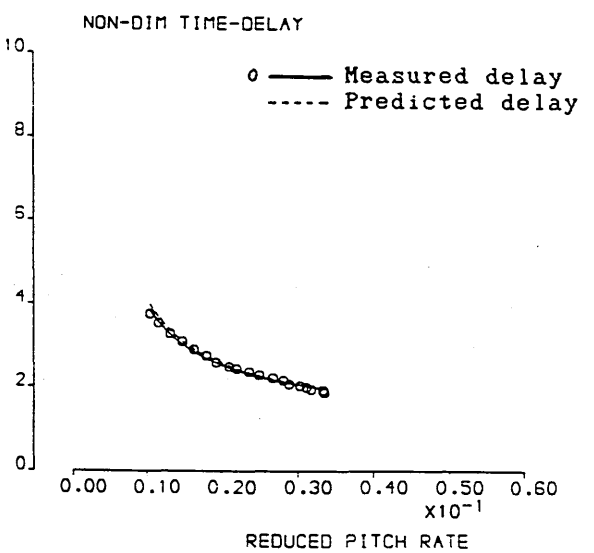

Figure 5.17 : Comparison of delays which were measured and predicted between analogous critical angle of attack and incidence of C_p deviation.

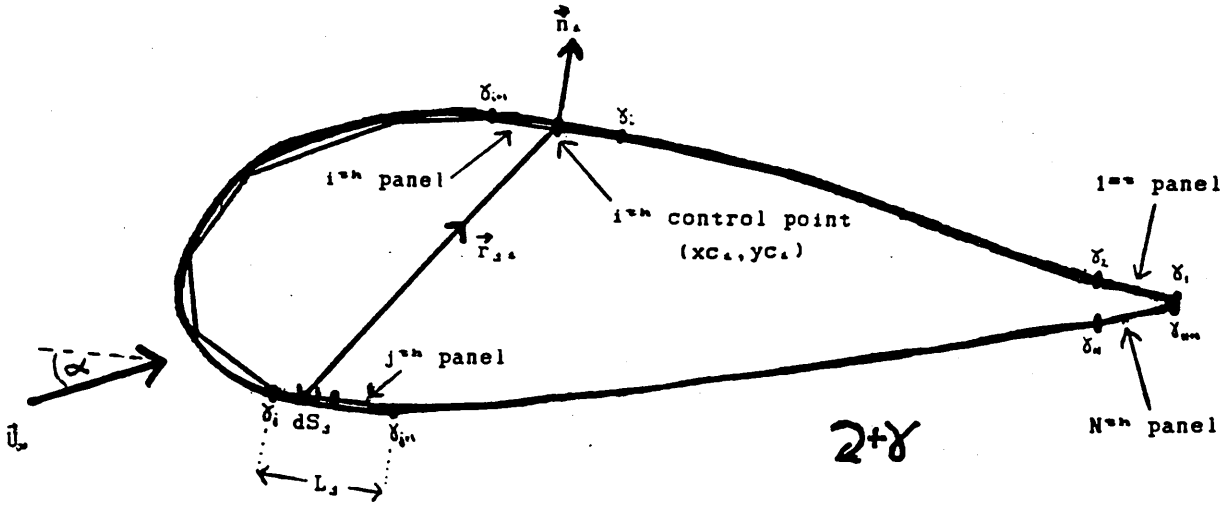

Figure A.1 : Illustration of variables employed in derivation of influence coefficients.

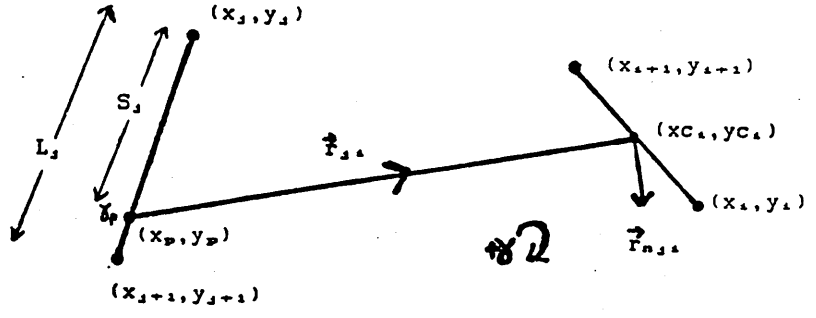

Figure A.2 : Induced velocity due to a point on a separate panel.